Synthesis of graphene using carbon ion implantation in copper

Von der Fakultät für Physik und Geowissenschaften
der Universität Leipzig
genehmigte
DISSERTATION
zur Erlangung des akademischen Grades

Doctor rerum naturalium

Dr. rer. nat.

vorgelegt von

Jan Lehnert, M.Sc.

geboren am 16.06.1989 in Borna

Erstgutachter:	Prof. Dr. Dr. h.c. Bernd Rauschenbach
Zweitgutachter:	Prof. Dr. Jörg K. N. Lindner

Tag der Verleihung:	21. Oktober 2019

Bibliographische Beschreibung

Jan Lehnert
Synthesis of graphene using carbon ion implantation in copper
Universität Leipzig, Dissertation
165 S., 248 Lit., 82 Abb., 4 Tab., 117 Glei.

Referat:

Im ersten Teil werden die Ergebnisse der Vorcharakterisierung der verwendeten Substrate für das Graphenwachstum vorgestellt. Zunächst werden die kommerziell verfügbaren Kupferfolien diskutiert, anschließend die Ergebnisse bezüglich der mittels physikalischer Gasphasenabscheidung auf Saphir hergestellten Cu(111)-Dünnschichten vorgestellt. Die Bestimmung der physikalischen Eigenschaften dieser Schichten wurde mittels AFM, SEM, XRD, Raman-Spektroskopie sowie XPS vorgenommen. Mit Hilfe von RBS-Messungen konnte eine Diffusion des Kupfers in das Saphir-Substrat hinein für Temperaturen von über 750 °C nachgewiesen werden. Im zweiten Teil der Arbeit wurden die auf Kupfer mittels Implantation von Kohlenstoffionen synthetisierten und unter Anwendung verschiedener Methoden auf SiO_2-Substrate transferierten Graphenschichten untersucht. Für den Transfer des Graphens von Kupferfolien wurde ein PMMA-freier chemischer Transferprozess entwickelt. Das auf den Cu(111)-Dünnschichten hergestellte Graphen wurde durch einen auf PMMA basierenden Transferprozess auf das Zielsubstrat übertragen. Mittels Raman-Bildgebung wurde die Homogenität des Graphens bestimmt sowie der Einfluss des Transferprozesses auf die Eigenschaften der Graphenschichten untersucht. Zur Auswertung der Raman Messungen wurde eine eigens dafür entwickelte Software in der Programmiersprache PYTHON verwendet. Mittels XPS wurden mögliche Verunreinigungen, die durch den Transferprozess hervorgerufen wurden, charakterisiert. Die Anzahl der Graphenlagen konnte über die Fluenz bei der Implantation beeinflusst werden. Außerdem war es möglich, $^{13}-\mathrm{C}$ Graphen durch entsprechende Auswahl der zu implantierenden Masse herzustellen. Die Oberflächenbeschaffenheit der Graphenschichten wurde mittels AFM analysiert. Durch SEM-Messungen konnten Zusammenhänge zwischen den Korngrößen der Graphenschichten und der Substrate aufgezeigt werden. Transporteigenschaften der Graphenschichten wurden mittels temperaturabhängiger Magnetowiderstandsmessung im Bereich 5 K bis 300 K bestimmt.

Abstract:

In the first part, the results from the pre-characterisation of the templates used for the graphene synthesis, first the commercially available Cu foils and second, via physical vapour deposition fabricated Cu(111) films on sapphire, are discussed. The physical properties were determined by SEM, AFM, XRD, Raman spectroscopy and XPS. RBS reveals a diffusion of Cu into sapphire substrate at temperatures above 750 °C. The second part contains the results of the characterisation of the graphene sheets synthesised on Cu templates via carbon ion implantation and transferred by different methods to SiO_2 wafers. For the transfer of graphene synthesised on Cu foils, a PMMA-free transfer process was developed, whereas the graphene synthesised on Cu(111) films was transferred by a standard wet-chemical PMMA-based approach. Using Raman mapping the homogeneity of the graphene and the influence of the different transfer methods on graphene's properties were investigated. For the evaluation of the Raman data, a specifically developed software based on PYTHON was used. With XPS, residuals from the transfer processes were analysed. The number of graphene layers can be controlled by the implanted carbon fluence. Furthermore, it was possible to synthesise $^{13}\mathrm{C}$ graphene by proper mass selection. The surface characterisation was done by AFM. Via SEM, a correlation between the grain size of the graphene and the used Cu templates was shown. Electrical and transport measurements were done at temperatures between 5 K and 300 K.

-Für meine Eltern-

Kein Erfolg der Welt ist etwas wert, wenn man ihn mit niemandem teilen kann.

-For my parents-

Everything is nothing if you got no one.

Contents

Introduction and motivation

By the recent discovery of graphene [1, 2], an atomically thin layer of hexagonally arranged sp^2 hybridised carbon atoms, a fruitful period of scientific and technological research has started. In recent years, graphene has been subject of enormous research efforts because of its unique physical, mechanical and electronic properties [1,2]. The carbon atoms are covalently bonded and form the strongest bonds in nature which gives graphene its remarkable mechanical properties [3, 4]. For example, a suspended single layer of graphene has a YOUNGs modulus of $\sim 1\,\mathrm{TPa}$ and is therefore one of the stiffest materials known [4]. Moreover, graphene is attractive for a wide variety of applications including sensors [5], semiconductor and high frequency devices [6–8], optoelectronics [9] and spintronics [8,10] or even catalysis [8,11]. Some of the physical properties, for example the behaviour as a conductor or a semiconductor, depend on the number of graphene layers [12, 13].

Despite substantial effort in recent years and a variety of approaches [14], the synthesis of monolayer graphene with large domains is one of the remaining challenges [15]. One approach is the mechanical exfoliation of highly oriented pyrolytic graphite [16]. High-quality graphene films of up to $100\,\mu$m domain diameter can be obtained. However, after fabrication the regions with monolayer graphene need to be identified, i.e. control and homogeneity of the number of graphene layers are poor and yields are typically low. Other approaches are, for example, the chemical reduction of graphene oxide [17], exfoliation of graphite [18] or the epitaxial growth on SiC surfaces [19, 20].

The most widely used route for graphene synthesis is chemical vapor deposition (CVD) [21–24] by which the growth of graphene on several substrates like Ni [25–27], Cu [28–30] or Ir [31] has been demonstrated. Careful control of the purity of the precursor gases as well as residuals in the CVD reactor is required for high-quality graphene growth [32].

An alternative approach for graphene synthesis is carbon ion implantation into metallic substrates. This is a high-vacuum process typically done at room temperature followed by subsequent annealing. Ion implantation uses a mass-selected ion beam of the implant species which not only allows extreme levels of purity but also to produce isotopically pure graphene, e.g. consisting of ^{12}C or even ^{13}C (or any mixture) that might be of interest for spintronic applications, without the need of isotopically enriched or even pure source materials.

The commercially available graphene shows a large variation in terms of quality [15]. Therefore, the improvement of the quality and reproducible production are two of the goals of this work. To date, only a few studies using ion implantation for graphene synthesis can be found in the literature. As substrates, mostly Ni [33–38] and Cu [37, 39, 40] were used. For the growth of large domains of graphene, Cu is the more suitable substrate, because it forms much larger grains under thermal treatment than Ni. The Cu foils in these studies had a Cu(200) orientation which results in a lattice mismatch of 19.9% between graphene and the underlying Cu substrate. In contrast, Cu(111) substrates would allow for a lattice mismatch of only 3.8% [41–44] and are therefore desirable for growth of high quality graphene.

In order to fully exploit the strengths of ion implantation as a technique for the graphene synthesis, it is essential to start with a carbon-free substrate, in order to have full control on the layer number of the synthesised graphene and therefore on its physical properties. Any additional contribution from intrinsic carbon that may have been incorporated into the Cu substrate during its preparation process has to be avoided. In case of the Cu thin films, prepared by physical vapour deposition, this carbon mostly comes from the residual gas within the deposition chamber. It is mentioned in the literature, that the Cu foils used for graphene synthesis so far may also not be free of carbon [39].

The goal is to develop a procedure for the synthesis of large area, high-quality monolayer graphene sheets which is based on ion implantation, a technique which is already established within the semiconductor industry. This includes also the investigation of the properties of the substrates used because they strongly influence the properties of the grown graphene.

For this purpose, commercially available Cu foils and Cu(111) thin films on c-plane Al_2O_3 prepared by different physical vapour deposition methods, were used as templates. They have to be characterised regarding purity, crystalline quality and grain sizes in order to increase the quality of the grown graphene. As the synthesis of graphene usually requires high temperatures around 1000 °C, the influence of this thermal treatment on the physical properties of the templates has to be investigated as well. One main issue addressed in this work is the preparation of carbon free templates.

The transfer process is a crucial step within the graphene synthesis pathway. Normally, this is done by PMMA coating of the samples followed by a wet chemical etching process [44]. Due to the difficulties with spin-coating of the Cu foils, a novel PMMA-free transfer process has been established and the influence of the transfer process on graphene properties investigated.

Another aim beside the fabrication of monolayer graphene is to investigate the possibility of synthesising multilayer graphene by changing the amount of the implanted carbon ions. Also a proof that the implanted carbon indeed forms the graphene should be provided which has been done by implantation of ^{13}C. By this, growing isotopically labelled graphene becomes possible. In order to achieve a good statistics about the graphene properties on a large scale which are usually measured by RAMAN spectroscopy, the spectra evaluation had to be improved and automated. Due to the strong dependence of the spectral position and also the peak shape of the RAMAN signals on the physical properties of graphene, it is important to comprehend and control all the steps within the spectra evaluation process.

Finally, the electrical properties of the synthesised graphene are of interest. For this purpose, the graphene has been structured and contacted in order to perform temperature dependent electrical resistivity and magneto-resistivity measurements which give information about the transport properties of the charge carriers in the graphene.

Part I

Theoretical fundamentals and experimental methods

Chapter 1

Graphene - Properties and synthesis methods

This chapter gives an overview on the properties and synthesis of graphene. This includes mechanical and electrical properties as well as transport phenomena within graphene. Furthermore, the synthesis methods for graphene which are used nowadays will be explained.

1.1 Basic properties of graphene

1.1.1 Band structure and stacking orders of graphene

In general the term graphene is used for sp^2 hybridised, covalent-bonded carbon (C) atoms forming a hexagonal 2D network as illustrated in figure 1.1a. The unit cell is built up of two carbon atoms, illustrated by (🟧) and (■), which are displaced from each other by the C-C bond length $a_{\mathrm{C-C}} = 0.142\,\mathrm{nm}$ [45]. Each carbon atom shares one σ bond with each of the three neighbours. The fourth bond is a π bond which is oriented out of plane. This situation is illustrated in picture 1.1b, there the π orbitals are visualised by a pair of symmetric lobes orientated out of plane. These bonds, one from each atom, hybridise and form the so called π and π^* bands in the electronic band structure.

The lattice vectors denoted in figure 1.1a are given by

$$\vec{a}_1 = \frac{3a}{2}\hat{a} + \frac{\sqrt{3}a}{2}\hat{y}, \qquad \vec{a}_2 = \frac{3a}{2}\hat{a} - \frac{\sqrt{3}a}{2}\hat{y}, \tag{1.1}$$

with a as the lattice constant mentioned above. The reciprocal vectors are given by (see figure 1.2)

$$\vec{b}_1 = \frac{2\pi}{3a}\hat{k}_x + \frac{2\sqrt{3}\pi}{3a}\hat{k}_y, \qquad \vec{b}_2 = \frac{2\pi}{3a}\hat{k}_x - \frac{2\sqrt{3}\pi}{3a}\hat{k}_y. \tag{1.2}$$

The band structure of graphene is calculated using the nearest-neighbour-tight-binding (NN-TB) approximation [47, 48] which results in the analytical expression for the eigenvalues of the tight-binding Hamiltonian [49, 50]

$$E_{\pm}(k_x, k_y) = \pm t_0 \left[1 + 4\cos\left(\frac{3}{2}k_x a\right)\cos\left(\frac{\sqrt{3}}{2}k_y a\right) + 4\cos^2\left(\frac{\sqrt{3}}{2}k_y a\right)\right]^{1/2}, \tag{1.3}$$

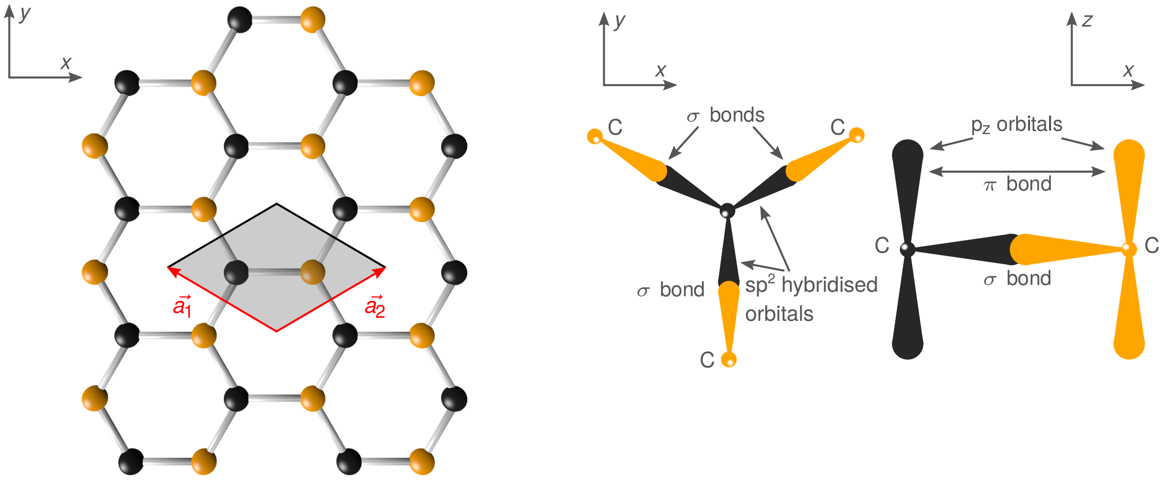

(a) (b)

Fig. 1.1: (a) Two sublattices form the hexagonal network of graphene. The C-C bond length is $a_{\mathrm{C-C}} = 0.142\,\mathrm{nm}$. (b) sp^2 hybridised orbitals of carbon atoms symmetrically orientated in the molecular plane at angles of 120 °. The three nearest neighbours form σ bonds. The remaining electrons form orbitals oriented perpendicular to the molecular plane which leads to the formation of π bonds to the nearest neighbours (modified after [45, 46]).

with the + or − sign corresponding to the valence and conduction band, respectively. The parameter t_0 is the nearest neighbour hopping energy ($\approx 2.8\,\mathrm{eV}$) [50].

A plot of equation (1.3) and a slice along the high symmetry points of the first BRILLOUIN zone is shown in figure 1.2. The valence band and the conduction band touch at the six K-points. Thus, graphene is a zero band gap semiconductor. The bands are symmetric as seen from equation (1.3). The K-points are also known as DIRAC points. Near these points, the energy dispersion relation can be written as (for small displacements $\vec{q}$ from K, total wave vector $\vec{k} = \vec{K} + \vec{q}$)

$$E_{\pm}(\vec{q}) = \pm\hbar v_{\mathrm{F}}|\vec{q}|, \tag{1.4}$$

with v_{F} as the FERMI velocity ($\approx 10^6\,\mathrm{m/s}$) [51, 52].

A more accurate band structure of graphene can be obtained by use of the third-nearest-neighbour-tight-binding approximation (3NN-TB). This approximation breaks the symmetry of the conduction and valence band. The parameter t_0 splits then into two different parameters t_+ and t_- for the conduction and valence band, respectively [47].

Due to the linear energy-momentum relationship given by equation (1.4), the charge carriers become a constant velocity. Due to the zero bandgap at the DIRAC-points it is possible to tune the conductivity of graphene from electron-like to hole-like by adding an external gate [53] or through doping [50].

If more than one layer is present, graphene is usually called two-layer, three-layer or simply multi-layer (or few-layer) graphene, according to the number of present layers. These layers can be stacked together in different forms (AA, AB, ABA, ABC-stacking) illustrated for ABA stacking in figure 1.3 [54–58]. Also random stacking or rotational disorder in the stacking has been observed [59, 60]. A detailed description of the stacking mechanism is given in reference [45][1].

---

[1] Note, within this thesis the main emphasis is the fabrication of monolayer graphene.

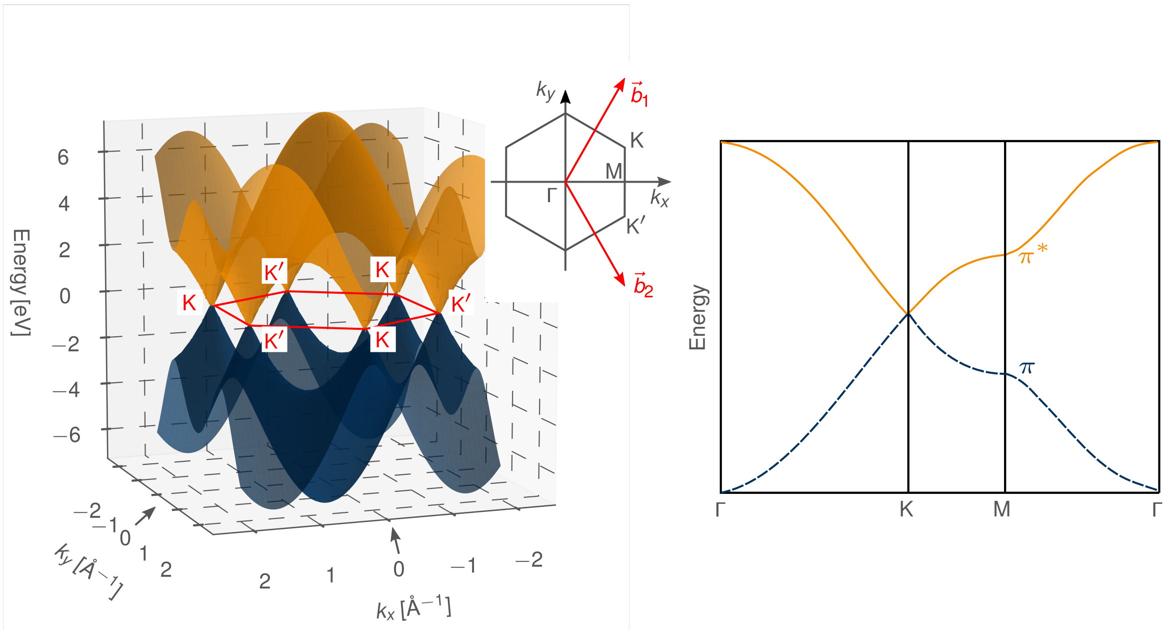

(a) **(b)**

Fig. 1.2: (a) Graphene band structure calculated by nearest neighbour tight binding approximation (equation (1.3)), with a sketch of the unit cell in the reciprocal space with the base vectors $\vec{b}_{1,2}$ and (b) a simplified plot of the band structure of graphene using cut-lines along high symmetry directions.

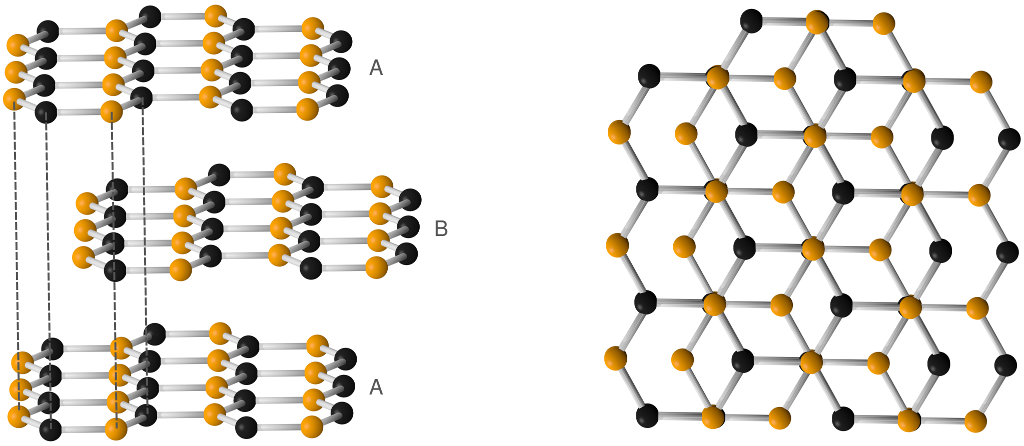

Fig. 1.3: ABA stack of three layers of hexagonal graphene, (left) side view, (right) top view (modified after [45]).

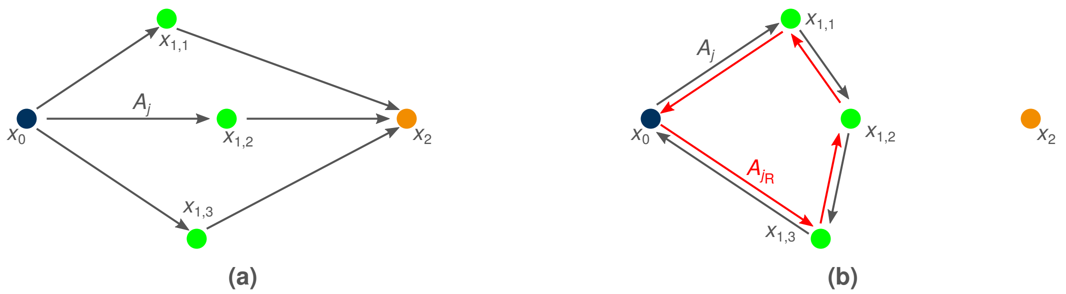

Fig. 1.4: Different FEYNMAN paths $x_{1,j}$ on which the electron can move from position x_0 to x_2 (a) and on which the electron becomes backscattered to the initial position x_0 (b), which can happen also in the reversed path (red arrows).

1.1.2 Charge carrier mobility and optical transparency

The very high carrier mobility of clean suspended graphene lies in the range of $10^5\,\mathrm{cm}^2/\mathrm{Vs}$ near room temperature [61, 62] and $10^7\,\mathrm{cm}^2/\mathrm{Vs}$ at liquid helium temperature [63]. These high mobilities are due to the high FERMI velocity. However, the carrier mobility is sensitive to the supporting substrate of the graphene due to electron-phonon scattering [64]. For comparison, the electron mobility in Si at 300 K is around $1400\,\mathrm{cm}^2/\mathrm{Vs}$ [65].

Another unique property of graphene is the optical transparency. For photon energies between 0.5 eV ($\sim$ 2478 nm) and 3 eV ($\sim$ 413 nm) it has a constant absorption of around 2.3% [66–68] which makes it suitable for applications in which optically nearly transparent devices are needed.

1.1.3 Transport properties in graphene, weak localisation and negative magnetoresistance

Regarding the transport properties of graphene, the concept of weak localisation and the phenomenon of a negative magnetoresistance are of importance [69, 70]. Hence, its theoretical background is described in the following.

Weak localisation

In general, the electrical resistance originates from the scattering of the electrons with impurities within the crystal lattice. At low temperatures, the impurities consist of vacancies or impurity atoms. Additionally, at high temperatures the thermal motion of the atoms (thermally activated phonons) act as scattering centres as well [71, 72]. However, due to the wave character of the electrons, there are quantum corrections to the electrical resistance. One of these corrections is the so called enhanced backscattering, which leads to weak localisation.

The probability P of the electron moving from an initial position x_0 (at time t_0) to a final position x_2 (at time t_2) can be derived by adding all FEYNMAN paths which can be taken by the electron. Thus,[2]

$$P(x_0 \to x_2) = \left|\sum_j A_j\right|^2 = \sum_j |A_j|^2 + \sum_{j\neq k} A_j A_k^*. \tag{1.5}$$

The first term of the right side in equation (1.5) is the sum of the squared amplitudes of each path and corresponds to the probability for a classical particle. The second term is

---

[2] A complete derivation for formula (1.5) is given in appendix A.2.

an interference term which gives the quantum correction. That only applies as long as phase coherence on the way from x_0 to x_2 is maintained. The phase coherence may break due to inelastic scattering (e.g. at phonons which are thermally activated if $T > 0\,\mathrm{K}$) and is only conserved if the phase coherence length $l_\phi \sim v_\mathrm{F}\tau_\phi$ is much larger than the mean free path of the electron $l_\mathrm{el} = v_\mathrm{F}\tau_\mathrm{el}$[3].

Thus, the probability $P(x_0 \to x_2)$ that an electron is deflected from x_0 to x_2 is obtained by squaring the sum of the amplitudes for all paths connecting the initial state x_0 and the final state x_2, so it can be written as

$$P(x_0 \to x_2) = |A_1(x_0 \to x_2) + A_2(x_0 \to x_2) + ...|^2. \tag{1.6}$$

The phase acquired on a path A_j is given by [73]

$$\Delta\phi = \frac{1}{\hbar}\int_{\mathrm{path}\,j} \vec{p}\cdot\mathrm{d}\vec{r} = \int_{\mathrm{path}\,j} \vec{k}\cdot\mathrm{d}\vec{r}. \tag{1.7}$$

In most cases, the paths have a different length (see figure 1.4a, the lengths of $x_{1,j}$ are different). Therefore, the electrons acquire randomly distributed phases which vanish on the average [74]. Thus, the square of the sum is equal to the sum of squares, the phases can be neglected and the probability can be obtained by adding probabilities instead of probability amplitudes.

This does not apply, however if the initial and final states are the same (or the trajectories cross themselves). If the path starts and ends at x_0, the electron can take a way like

$$x_0 \to x_{0,1} \to x_{0,2} \to x_{0,3}... \to x_{0,N-1} \to x_{0,N} \to x_0,$$

as indicated in figure 1.4b. For each path like this, there is a time reversed path (red arrows in 1.4b)

$$x_0 \leftarrow x_{0,1} \leftarrow x_{0,2} \leftarrow x_{0,3}... \leftarrow x_{0,N-1} \leftarrow x_{0,N} \leftarrow x_0,$$

which has to be added as well, because all possible paths contribute to the sum. The probability $P(x_0 \to x_0)$ becomes therefore

$$P(x_0 \to x_0) = |(A_1(x_0 \to x_0) + A_2(x_0 \to x_0) + ...) \tag{1.8}$$

$$+(A_{1\mathrm{R}}(x_0 \to x_0) + A_{2\mathrm{R}}(x_0 \to x_0) + ...)|^2 \tag{1.9}$$

$$\equiv |A + A_\mathrm{R}|^2. \tag{1.10}$$

Here, A is the sum of the amplitudes of all the paths of the first set and A_R is the sum of the amplitudes of all the paths of the time reversed set. For a isotropic space and no magnetic field, in equation (1.7), $\vec{p}$ changes to $-\vec{p}$ and $\mathrm{d}\vec{r}$ to $-\mathrm{d}\vec{r}$ in case of the time reversed path. Thus, the phase $\Delta\phi$ is not changing and the probability amplitudes interfere always constructivelyy . This also means that the probability amplitudes are the same for the two paths, so $A = A_\mathrm{R}$ [74]. Hence, the probability becomes

$$P(x_0 \to x_0) = |A + A|^2 = |2A|^2 = 4|A|^2. \tag{1.11}$$

---

[3] $v_\mathrm{F} = p_\mathrm{F}/m$ is the FERMI velocity and τ_ϕ and τ_el the mean free times between two scatter events.

This is called enhanced (or coherent) backscattering which leads to so called weak-localisation [75]. Due to the increase of the probability for the electron to end up at the starting point, the probability to reach the point x_2 has to decrease due to the conservation of the net probability. This leads to a lower measurable current (at the same voltage) and therefore to an increase of electrical resistance.

If a magnetic field is present, the amplitudes $A_{j\mathrm{R}}$ along the time reversed paths do not accumulate phase identical to A_j. The amplitude A_j associated with any path j acquires an additional phase proportional to the line integral of the vector potential $\vec{A}$ along this path [74][4]. For this phase difference calculation, in equation 1.7, $\vec{p}$ has to be replaced by $\vec{p} - e\vec{A}$, where $\vec{A}$ is the vector potential [74]. If the direction of the movement for electron is reversed, $\vec{p}$ changes to $-\vec{p}$, but the vector potential is not changed. Thus, the magnetic field causes a phase change for these two paths which can be calculated by

$$\Delta\phi_{\mathrm{M}} = \frac{2}{\hbar} \oint_{\mathrm{path}\, j} e\vec{A} \cdot \mathrm{d}\vec{r} = \frac{2e}{\hbar} \int_{\mathrm{Area}} \nabla \times \vec{A} \mathrm{d}\vec{F} = \frac{2e}{\hbar} \int_{\mathrm{Area}} \vec{B} \mathrm{d}\vec{F} = 2\pi \frac{\Phi}{\Phi_0}. \tag{1.12}$$

Here, Φ is the magnetic flux through the area F which is created by the closed path j. $\Phi_0 = h/2e$ is the magnetic flux quantum.

Due to the different orientation of the magnetic field relative to the different paths, the electrons acquire different phases also in case of backscattering to the same point in space. On average, this cancels the interference term again. Thus the probability for backscattering of the electron decreases. Therefore, the probability for the electron to move to x_2 has to increase, which yields in a decrease of electrical resistance[5].

This influence of a magnetic field on electrical resistance can be determined by measuring the magnetoresistance.

Magnetoresistance

The magnetoresistance is defined as

$$\frac{\Delta R}{R} = \frac{R(B) - R(B=0)}{R(0)}, \tag{1.13}$$

with $R(B)$ as the resistance with magnetic field B and $R(0)$ as the resistance without the magnetic field. As described above, the external magnetic field can lead to a decrease of the electrical resistance due to weak localisation. This phenomenon occurs normally at weak magnetic fields below 1 T.

However, in case of stronger magnetic field (> 1 T), the LORENTZ-force $F_{\mathrm{L}} = q \cdot (\vec{v} \times \vec{B})$ which acts on the electrons becomes dominant and increases the path through the conductor. Due to this increase, the probability to scatter is also increased and the electrical resistance rises. This is called LORENTZ Magneto Resistance (LMR) and is usually a positive contribution to the magnetoresistance [77]. This phenomenon becomes stronger with increasing magnetic field strength.

For the LMR, there are two types, the longitudinal and the transversal LMR. The first one is nearly independent of the applied magnetic field. The second one shows a B^2 behaviour [77,78].

---

[4] This can be obtained by solving the SCHRÖDINGER equation for a charged particle within a vector potential and leads to the magnetic AHARONOV-BOHM effect [76].

[5] The probability to get backscattered is half as large as without the magnetic field. This is shown in appendix A.2.

For the measurements in this thesis, the magnetic field was perpendicular to the graphene plane and therefore the transversal LMR has to be considered here.

Note that there are other effects beside the LMR which contribute to the magnetoresistance [79] like the domain-wall resistance [80], the anisotropic magnetoresistance [81], the giant magnetoresistance [82] and the electron-electron interaction [83].

1.1.4 Overview of graphene synthesis methods

There are several methods for the synthesis of graphene, each with their advantages and disadvantages. The first approach is the synthesis by mechanical exfoliation. This is also the first recognised technique of graphene synthesis [84]. Graphene sheets of different thickness can be created by peeling off layers from a graphitic material like highly ordered pyrolytic graphite (HOPG) by scotch tape [16]. The lateral size can be in the cm range with a good quality but with a very small production yield [16, 84]. Another approach is the chemical exfoliation which can produce single layer and few layer graphene with lateral dimensions up to $500 - 700\,\mathrm{nm}$ [84], but with high costs for the ionic liquids which are needed for this approach [85]. Also direct sonication of graphite can be used to obtain single and multiple layers with lateral dimensions in the μm range but with a low production yield [18, 86].

Reduction of CO yields also multiple graphene layers with sub μm lateral dimension [87]. Unzipping of carbon nanotubes gives multiple layers of graphene with a lateral size depending on the size of the nanotubes [88,89]. Large areas of very pure graphene can be obtained by epitaxial growth on SiC. The thickness can be varied from single layer to few layer graphene with lateral dimensions in the cm range [90–95]. Highly focused research was done on the fabrication of graphene by chemical vapour deposition (CVD) [21–24]. The graphene growth by this approach can be done on several substrates like Cu [28–30], Co [96], MgO [97], Ir [31] or Ni [25–27]. The graphene domains can reach a few cm in size with high quality [28]. Nevertheless, a careful control of the purity of the precursor gases as well as residuals in the CVD reactor is required for high-quality graphene growth [32].

The possibility of the usage of ion implantation technique for the synthesis of graphene was already shown in literature. As substrates, mostly Ni [33–38] and Cu [37, 39, 40] were used. The details for this process are given in section 2.1.

Chapter 2

Preparation and experimental methods

In this chapter, an overview about the experimental methods relevant for this work is given. It starts with a description of the novel pathway of graphene synthesis by ion implantation as it was developed within this thesis. Also, the different methods used for the transfer of the graphene from the template on which it was synthesised to the final SiO_2/Si substrates are presented. Furthermore, the basics of ion implantation and investigation methods using this technique will be presented. Subsequently, the techniques used for the thin film preparation of the template for graphene growth are explained. The RAMAN spectroscopy as a tool for investigation of the graphene properties will be explained in more detail. At the end, an overview of the characterisation methods for thin films and also for the graphene will be given.

2.1 Pathway for the graphene synthesis by ion implantation and transfer methods

Employing of an ion beam for the synthesis of graphene has multiple benefits. The first one is the excellent process control. Ion implantation is an integral part in semiconductor processing. Therefore, the synthesis of graphene by this technique has the potential for integration in the CMOS fabrication line. It is a low temperature process [98], thus the substrate on which the graphene is to be synthesised is not exposed to a process gas at high temperatures with the increased risk of contamination. The layer number of the graphene can be adjusted by the ion fluence (number of ions per area). The second benefit concerns the purity of the graphene. Due to mass selection (see section 2.2.3) used in ion implantation the implanted species is very pure. By this mass selection, even a production of isotopically pure ^{13}C or ^{12}C graphene becomes possible.

2.1.1 Established pathway for graphene synthesis by ion implantation

The synthesis of graphene by ion implantation is done in multiple steps. The pathway is shown in figure 2.1 for Cu foils and in figure 2.2 for Cu thin films. For graphene synthesis on Cu foils, the steps are as follows. The first step is usually the cleaning of the substrate by thermal treatment (step (a)). This also changes the morphology of the substrate, for example the roughness and the grain size. The next step is the ion implantation. Here, with the fluence of implanted carbon ions, the layer number can be adjusted (step (b)). After this, the so called activation annealing is performed, where due to the high temperature, the carbon atoms become mobile and diffuse to the surface of the substrate (step (c)). In general, after this procedure, graphene is formed

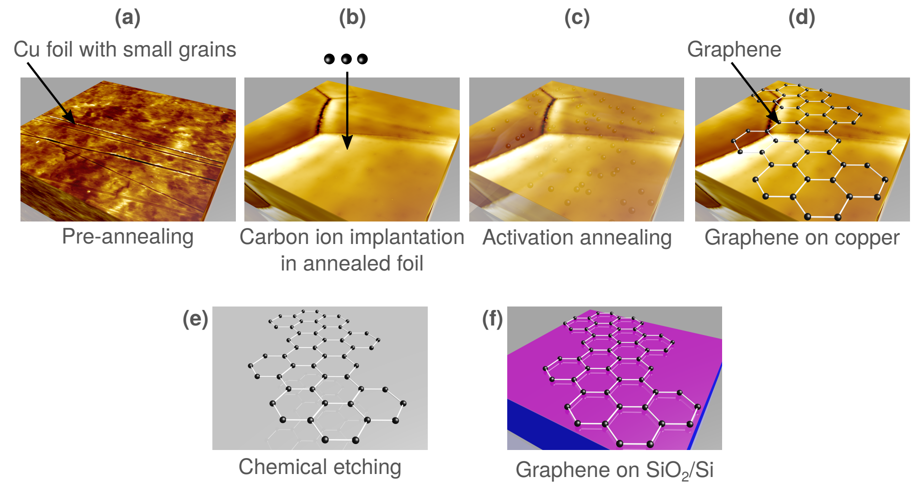

Fig. 2.1: Pathway for the synthesis of graphene by ion implantation and subsequent annealing. The first step is the annealing of the substrate for cleaning and improving of the material. After that, the carbon ions are implanted and the activation annealing is performed in which the graphene is formed on the surface of the substrate (here Cu foil). The graphene can then be transferred to other substrates like SiO_2/Si.

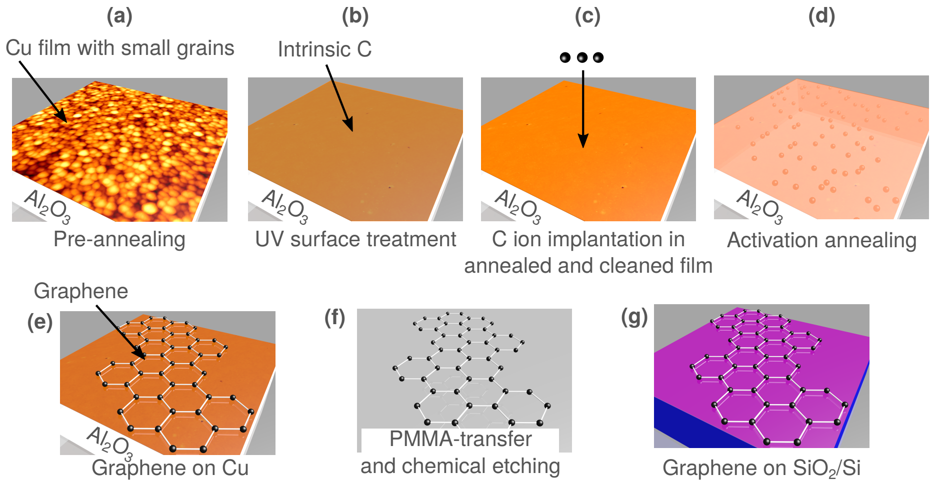

Fig. 2.2: Pathway for the synthesis of graphene on Cu films. The steps are the same as for the Cu foils, but with an additional step (b) for surface cleaning.

(step (d)) which can be characterised by several methods or transferred (step (e,f)) to another substrate, for example SiO_2/Si. For the Cu thin films, an additional cleaning step is necessary in order to remove residual carbon from the surface after the pre-annealing step (see section 3.2.4).

2.1.2 Methods for graphene transfer to SiO_2/Si

The transfer process is a crucial step within the whole graphene synthesis [99]. In general, the central issue is the separation of the graphene from the substrate (here Cu) on which it was synthesised.

A first approach is based on a polymer support layer [100–103]. The conventional PMMA-assisted graphene transfer process includes the following steps. First the substrate with the graphene on top receives a PMMA spin-coated film. Subsequently, the sample is plasma etched (O_2 plasma) in order to remove graphene which was formed on the backside of the substrate[1].

---

[1] Note that in a typical CVD process (which is mostly used) graphene grows on both sides of the Cu foil [99].

Then, the substrate is chemically etched (for example with $FeCl_3$ for Cu substrate). Then the graphene is washed by millipore water and transferred (by scoop out method) to the final substrate. At the end, the PMMA is removed chemically, in most cases by acetone [99]. The spin-coating of the foils is one main problem within this process because of handling issues. Furthermore, this transfer method leaves residuals from the PMMA within the graphene [99]. Instead of using PMMA as a support layer, thermal release tape can be used [104–107]. This tape has specific adhesives that act depending on the temperature. It adheres to the substrate at room temperature while losing adhesion at high temperature (above 100 °C) [99].

A second approach is to transfer the graphene without a support layer. Here, a problem is that the surface tension of the etching solution used to remove the substrate can destroy the graphene layer. It is also known that the support layer not only prevent the graphene from shrinking or rolling, but also protects it during the metal etching process [108–110].

Graphene transfer from Cu foils to SiO_2/Si

In order to reduce the handling issues in case of the Cu foils and to reduce the contamination from the PMMA, a PMMA-free transfer method was established. The experimental setup is shown in figure 2.3.

Fig. 2.3: Experimental setup for the PMMA-free graphene transfer of graphene on Cu foils.

The etchant (see section 4.1.2 for more details on the etchants investigated) was gently poured into a crystallising dish where the graphene on Cu sample was allowed to float on the etchants surface, carried by surface tension forces. A glass cylinder with open ends and a slightly smaller radius than the crystallizing dish was inserted into the dish, forming a double-walled cylinder, however, suspended in order to leave a small gap between cylinder and the bottom of the dish (see figure 2.3). After a certain time, the dissolution of the Cu foil was complete and the etchant was removed by flowing 10 l millipore water at a flow rate of 2 l/h through the inter-wall region between the crystallising dish and the glass cylinder. This setup allows exchange of the etchant by the millipore water without turbulent flow close to the graphene layer and hence avoids ripples and folding. As a final step, the graphene layer was scooped up with a pre-cleaned SiO_2/Si wafer and dried under gentle nitrogen flow [111]. For Cu etching, different etchants were investigated (section 4.1.2).

Graphene transfer from Cu thin films to SiO_2/Si

For the transfer of the graphene from the Cu thin films, a standard wet chemistry approach was used. Figure 2.4 shows the different steps for this method. At the very beginning, the graphene is on top of the Cu film (fig. 2.4a). In the first step, a thin PMMA film is deposited on top of the as-grown graphene (fig. 2.4b) by spin coating 2 ml of a PMMA-chlorobenzene solution (Sigma Aldrich, Mw = 996 kDa by GPC-Alfa Aesar, HPLC 99.5%) at 3000 rpm for 1 minute. The sample was allowed to dry under ambient conditions for 12 h. Concentrated nitric acid (millipore, 65%) was used in order to remove the Cu and separate the PMMA/graphene from the Al_2O_3 substrate. For this purpose, the whole stack was allowed to float until the Cu was removed completely (fig. 2.4c). Note that the concentration of the acid is not only important for the etching time, but also to prevent the stack from sinking due to the increased surface tension compared to a lower concentrated acid solution. After the Cu is removed, the Al_2O_3 substrate sinks down whereas the PMMA/graphene stack still floats on the surface (fig. 2.4d). This is vital, otherwise the graphene cannot be retrieved for transfer. The PMMA/graphene, still floating on the surface, is washed with millipore water, analogous to the washing process within the transfer method for the Cu foils. After the etchant has been removed, the free floating PMMA/graphene stack is scooped out and transferred to the SiO_2/Si wafer (fig. 2.4f). In the final step, pure acetone (VWR, for HPLC) is used to remove the PMMA layer followed by drying using dry nitrogen (fig. 2.4g). This transfer method was used for all graphene samples, synthesised on Cu films.

Note, there are many other transfer methods or modifications of them like the up-side-down approach in which the graphene/PMMA stack is transferred to SiO_2/Si with the graphene on top and without removal of the PMMA [112].

2.2 Basics of ion implantation and RBS-channelling

This section describes the basics of ion implantation and the interaction of the ions with the target material. Also the SRIM [113, 114] simulation software will be explained which can be used to calculate ranges of ions and damage they produce during the stopping within the target material[2]. Rutherford backscattering spectrometry (RBS) and channelling will be briefly described in order to evaluate the damage produced by the ion implantation process and to investigate the change of the template for the graphene synthesis during annealing at high temperatures (diffusion and contamination). Subsequently, the accelerator which was used for the implantation process will be described including the creation of ions with a certain energy and mass.

2.2.1 Ion-solid interaction and SRIM simulation

When an ion with a certain energy and certain mass hits the target material, several processes occur. Here, the kinetic energy E_{kin} of the ions should be high enough so that they are getting implanted ($E_{\mathrm{kin}} > 1\,\mathrm{keV}$). There are several other methods which can be realised with ion beams such as smoothing or roughening of the target surface (ion beam etching) or layer deposition (ion beam sputtering, see for example section 2.3) [115, 116]. Also ion beams can be used to perform material analysis like particle induced X-ray emission (PIXE), particle induces Gamma-Ray emission (PIGE) and RBS [117]. RBS was used to determine the crystal structure and quality of the used graphene templates. The technique will be described in section 2.2.2.

In general, the interaction between the atoms in a solid forming the lattice can be described by the Lennard-Jones potential [118][3]

$$V(d) = 4\varepsilon\left[\left(\frac{\sigma}{d}\right)^{12} - \left(\frac{\sigma}{d}\right)^{6}\right]. \tag{2.1}$$

Here, ε is the depth of the potential, σ is the finite distance at which the inter particle potential becomes zero (the equilibrium distance between neighbouring atoms) and d is the distance

---

[2] Note, there is an important difference between ions and electrons, especially regarding the energy transfer mechanisms [98]. Within this thesis only ions will be discussed.

[3] Also called L-J potential, 6-12 potential, or 12-6 potential.

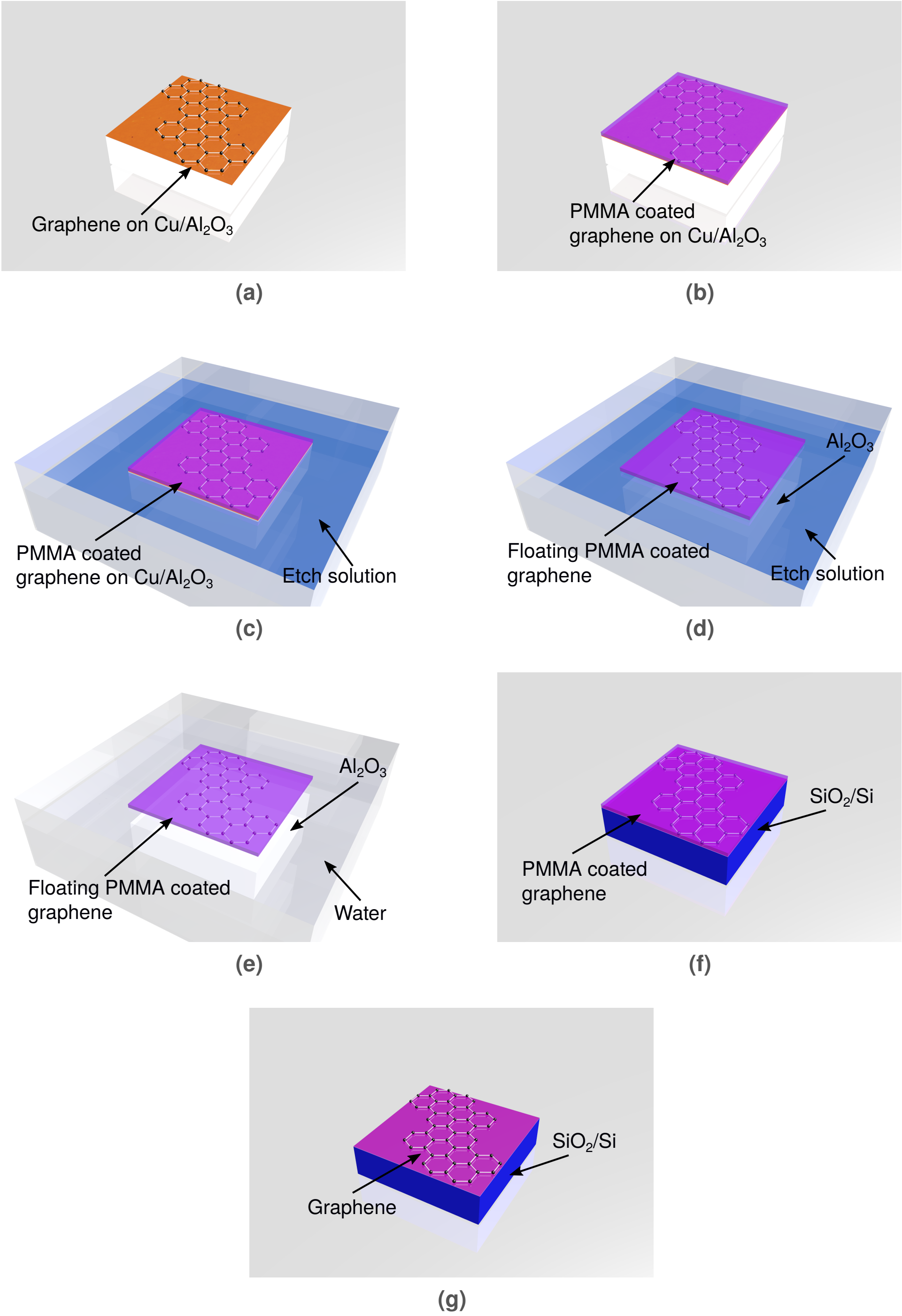

Fig. 2.4: Illustration of the different steps of the graphene transfer process. In the first step, the sample receives a PMMA-film on top of the graphene (a). Subsequently, the sample is floating on the etch solution (b) until the Cu is chemically removed and the Al_2O_3 substrate sinks down on the ground of the solution (d). Afterwards, the PMMA/graphene is washed with millipore water (e). Then, the PMMA/graphene stack is scooped out and transferred to the SiO_2/Si wafer (f). Finally, the PMMA is removed by acetone (g).

between the particles [98]. The energy of the ions is normally much higher than the thermal motion energy of these target atoms in equilibrium. This leads to a interaction distance d which is less than the equilibrium distance σ from equation (2.1).

Using $a_0 = 0.053\,\mathrm{nm}$ (BOHR radius of the hydrogen atom) and $\sigma \approx 0.25\,\mathrm{nm}$ (distance between atoms in a solid lattice), three scenarios can be distinguished [98]. In case of $d \gg \sigma$, the LENNARD-JONES potential (2.1) can be used to approximate the atomic interaction. Every individual atom energy state is occupied by electrons according to the PAULI principle. If the atoms are brought close to each other, the outer valence bands will overlap and form bonds. If $d \ll a_0$, the COULOMB interaction due to the charge of the nuclei becomes dominant. Then, this repulsive interaction can be described by

$$V(d) = \frac{1}{4\pi\varepsilon_0}\frac{Z_1 Z_2 e^2}{d}, \tag{2.2}$$

with Z_1 and Z_2 being the atomic number of target atom and ion, respectively, and e the elementary charge [98]. For intermediate distances $a_0 < d < \sigma$ the electron clouds screen the COULOMB potential of the nuclei from each other. Therefore, the repulsive potential can be described by multiplying the COULOMBic repulsion between the bare nuclei with a screening function $\chi(d/a)$ containing a as the screening parameter. Thus, equation (2.2) becomes

$$V(d) = \frac{1}{4\pi\varepsilon_0}\frac{Z_1 Z_2 e^2}{d}\chi(d/a). \tag{2.3}$$

This screening function should modify the COULOMB potential in a way that it becomes zero for large distances between the particles, and tend to one for very small distances. If so, the potential (2.3) describes the entire collision process. There are several screening functions obtained by theory calculations like the ZIEGLER-BIERSACK-LITTMARK (ZBL) repulsive potential [119]. A deeper explanation of screening functions is given in reference [98].

Due to the interactions between the incoming ion and the target atoms, the ion looses energy on its way through the solid. This energy loss rate (or stopping power) $\mathrm{d}E/\mathrm{d}x$ consists of two different mechanisms [98]. The first is the interaction of the ion with the electrons in the target which is called electronic stopping. In this process, the ion can excite the atom or even eject electrons from the electron shell. The second mechanism are collisions with the atomic nuclei of the target material. This process is called nuclear stopping and the main reason for the production of defects in the lattice by the displacement of atoms from their initial positions [98, 117]. The energy loss rate can therefore be calculated by

$$\frac{\mathrm{d}E}{\mathrm{d}x} = \left.\frac{\mathrm{d}E}{\mathrm{d}x}\right|_{\mathrm{e}} + \left.\frac{\mathrm{d}E}{\mathrm{d}x}\right|_{\mathrm{n}} \tag{2.4}$$

with e and n as indicator for the electronic and nuclear stopping term. Figure 2.5a gives a schematic illustration for the way of an ion through the solid. Figure 2.5b shows the range R of the ion in the solid which can be calculated by

$$R = \int_{E_0}^{0} \frac{1}{\mathrm{d}E/\mathrm{d}x}\mathrm{d}E, \tag{2.5}$$

with E_0 beeing the energy of the ion with which it enters the target. In practise, the projected range R_P (or the penetration depth) is used which is the projection of R normal to the surface as indicated in figure 2.5b. In general, nuclear stopping is dominant for low energies of the incident particle and high Z_1 values, whereas electronic stopping becomes important for high particle energies and small Z_1 values [98, 117].

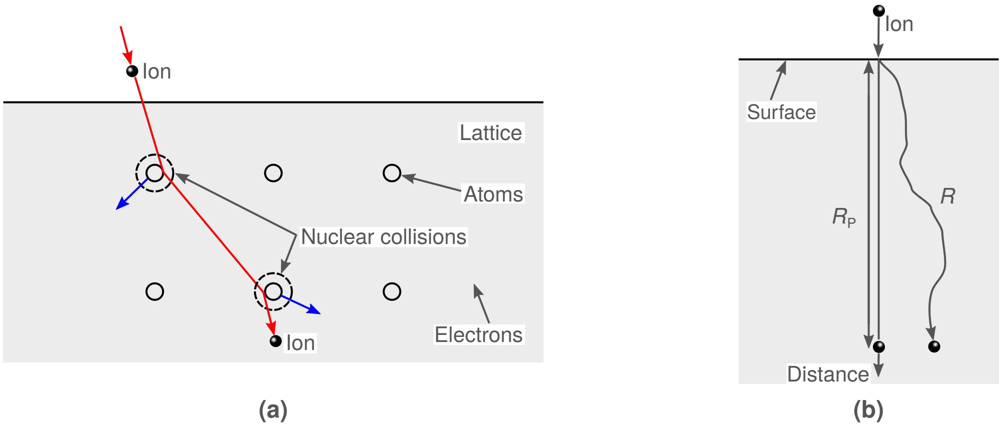

Fig. 2.5: Schematic illustration of the way of an ion through the solid in which it looses energy via collisions with the electrons (electronic stopping) as well as with the target atoms (nuclear stopping). The trajectory of the ion deviates from a straight line due to these collisions. (b) Illustration of the ion range R and the projected range R_P (modified after [98]).

The stopping power for ions in matter can be calculated by help of the simulation software THE STOPPING AND ION RANGE IN MATTER (SRIM) [113, 114]. This is a Monte-Carlo based simulation tool. Within these simulations, the target is assumed to be amorphous, therefore crystal orientations are ignored in the calculations [98] which become important for channelling experiments. Due to this channelling, the range of the ion can be increased (see section 2.2.2). Also the damage of the crystal lattice made by prior incident ions is ignored for the next ion trajectory simulation.

The software is based on semiempirical formula for the stopping power $\mathrm{d}E/\mathrm{d}x$ [120] which are based on experimentally data [121, 122]. The number of displacements per atom which can be calculated, the range and the straggling of the incoming ions depend on the displacement energy of a target atom which is different for different materials. This displacement energy can be set manually within the software.

Electronic stopping for ions in copper

The stopping power for protons ions in Cu over a large energy range is shown in figure 2.6a. The nuclear stopping can be neglected in the high energy regime (as mentioned above). The electronic stopping has a maximum, which is called the BRAGG peak. Here, the energy loss rate reaches its maximum in the target material. For high energies, the stopping power is described by the BETHE-BLOCH theory [123]. This requires that the ion is fully ionised and the velocity of the target electrons is much lower than the velocity of the ion. These conditions are given for $E > E_\eta$ with [124]

$$E_\eta = 24.98 M_1 Z_2 \,\mathrm{keV/amu}. \tag{2.6}$$

For protons in Cu, $E_\eta \approx 730\,\mathrm{keV}$.

For $E < E_\eta$ the ion is not fully ionised anymore [124] and the stopping process cannot treated by the BETHE-BLOCH theory. Near the BRAGG peak, the velocity of the ion becomes equal to the velocity of the target electrons. Then, a quasi molecule is formed within the collision process.

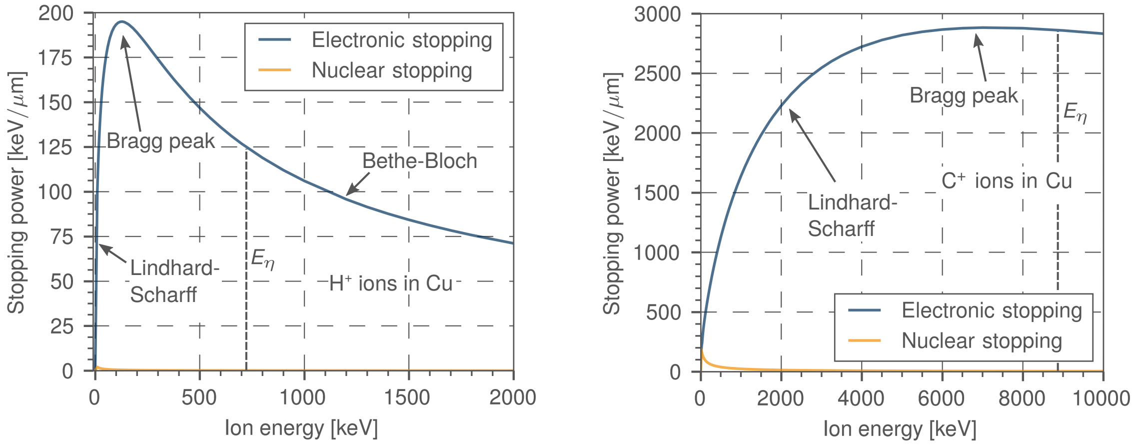

(a) **(b)**

Fig. 2.6: SRIM simulations for the nuclear and electronic stopping power $\left.\frac{\mathrm{d}E}{\mathrm{d}x}\right|_{\mathrm{e,n}}$ for (a) protons and (b) carbon ions in Cu. The nuclear stopping in case of carbon ions becomes much larger, especially for low energies. The theory which can be applied for the respective energy region is marked.

An electron gets exchanged which transfers energy from the ion to the target atom [125]. A theoretical description for this energy regime below the Bragg peak is given by Lindhard and Scharff [126]. In this case, the electrons are moving faster than the ion which now feel some sort of viscosity. Within this theory, the electronic stopping power is related to the energy by

$$\left.\frac{\mathrm{d}E}{\mathrm{d}x}\right|_{\mathrm{e}} \propto \sqrt{E}. \tag{2.7}$$

For the RBS-channelling experiments, He^+ ions with around 2 MeV were used. For these ions with this energy, only the electron stopping is important (see figure 2.6a). Therefore, within this measurement no significant damage is introduced into the sample within the first few hundred nanometres[4].

Figure 2.6b show the stopping power of carbon ions in copper. The Bragg peak becomes broader and moves to higher energies. Relation (2.6) gives for carbon ions in copper a value of $E_\eta = 8693\,\mathrm{keV}$. Therefore, C^+ energies $< 100\,\mathrm{keV}$ cannot be explained by the Bethe-Bloch theory and have to be treated by e.g. Lindhard Scharff [126].

Nuclear stopping for ions in copper

Within this thesis, only energies in the range of a few tenths of keV were used for the carbon ion implantation process. Figure 2.7a shows the stopping power for carbon ions in copper for the lower energy range. The nuclear stopping power which creates defects in the target lattice [98] becomes the important process. Figure 2.7b shows the stopping power as function of the penetration depth. Most of the energy is deposited within the first 60 nm.

---

[4] Note that the RBS-experiments were only performed for the 200 nm Cu films. Thereby the He^+ ions reaches the low energy regime which is relevant for the nuclear stopping only within the $\mathrm{Al_2O_3}$ substrate on which the Cu film was sputtered.

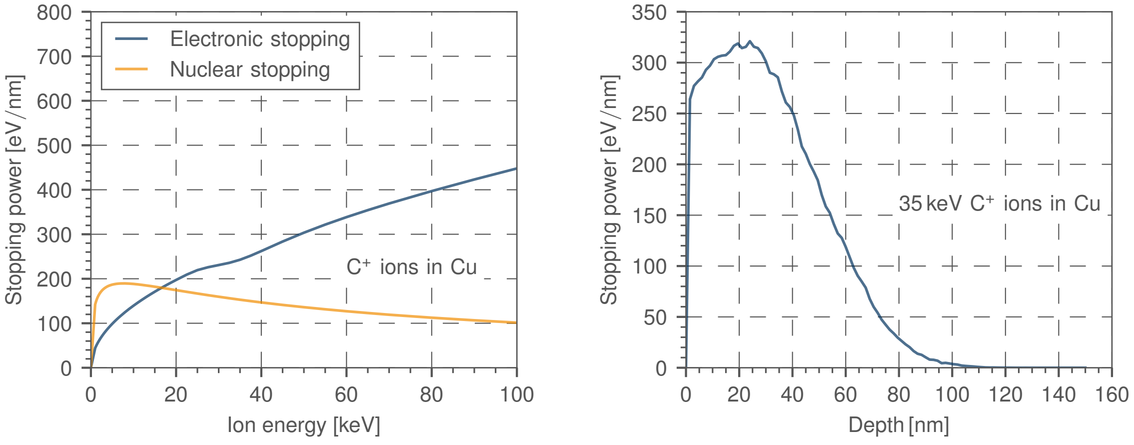

(a) **(b)**

Fig. 2.7: (a) SRIM simulation for the stopping power of C^+ ions into a Cu target within the lower energy region. In this region, the nuclear stopping becomes an important process. (b) The stopping power of 35 keV C^+ ions in Cu as function of the penetration depth. Most of the energy is deposited in the first 60 nm.

2.2.2 Basics of RBS spectroscopy and channelling

In order to determine the crystal quality after the implantation process to estimate the damage produced by the carbon ions in the copper foil or in the copper thin film, RBS-channelling measurements were performed. Here, the fact that the target material is crystalline and not amorphous, as assumed in the previous section for the SRIM calculations, is exploited. Within a crystalline target, not only the energy and type of the ions as well as the target atomic mass are important for the range of the ions, but also the target orientation with respect to the ion beam and the vibrations of the target atoms and therefore the temperature [98].

The backscatter yield and the energy of the backscattered ions can be measured. This measurement is called RBS-spectrometry [117]. Here, only the basic principle of this method is explained. A more detailed explanation of backscattering spectrometry can be found in reference [127].

When an ion on its way through the solid comes close to an atom it may become backscattered due to the Coulomb interaction with the nucleus. Within this interaction the incoming ion (mass M_1, atomic number Z_1) with energy E_0 transfers a part E_2 of its energy to the nucleus (M_2, Z_2) which is assumed to be initially at rest. After the scattering by the angle θ the ion has the energy E_1. This scattering process is elastic as long there are no nuclear reactions, resonances or excitations and is called Rutherford scattering. The relation E_1/E_0 is called the kinematic factor K. With energy and momentum conservation it yields for $M_1 \leq M_2$ [127]

$$K_{M_2} = \frac{E_1}{E_0} = \left[\frac{\sqrt{1-(M_1/M_2)^2\sin^2(\theta)} + (M_1/M_2)\cos(\theta)}{1+(M_1/M_2)}\right]^2 . \tag{2.8}$$

Due to the dependence of the kinematic factor K on M_2 (mass of the nucleus on which the ion is scattered) it is possible to identify the atomic species in the sample. The mass separation is best for light target elements and $\theta = 180\,^\circ$.

Schematically this process is shown in figure 2.8a. The probability for an ion to become scattered in a solid angle $\mathrm{d}\Omega$ is given by the differential cross section which is in the case of Rutherford scattering [127]

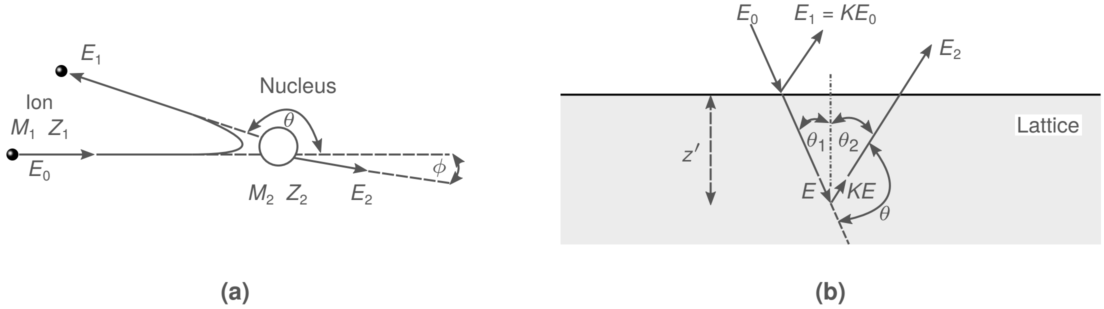

Fig. 2.8: Schematic illustration of (a) the backscattering of an ion on an atom and (b) the geometrical relations for the layer thickness determination (modified after [117]).

$$\frac{\mathrm{d}\sigma}{\mathrm{d}\Omega} = \left(\frac{Z_1 Z_2 e^2}{16\pi\varepsilon_0 E}\right) \frac{4}{\sin^4(\theta)} \frac{\left(\sqrt{1-[(M_1/M_2)\sin(\theta)]^2}\cos(\theta)\right)^2}{\sqrt{1-[(M_1/M_2)\sin(\theta)]^2}}, \tag{2.9}$$

with E as the energy of the ion prior scattering. For constant θ the cross section increases with $(Z_1 Z_2)^2$ and decreases with $1/E^2$. Therefore, RBS is most sensitive for heavy elements. Note that for light elements, the complementary technique to RBS is the elastic recoil detection analysis (ERDA) [128].

For high energetic ions or light target atoms the cross section may become non-RUTHERFORD due to the small distance of the incoming ion to the target nucleus. Therefore, nuclear forces cannot be neglected anymore. In this case equation (2.9) cannot be applied anymore.

As already mentioned, the ion loses energy on its way through the solid. With the kinematic factor K, the energy of an ion which was scattered in a depth $z' > 0$ of the sample becomes $E_2 < KE_0$ which can be measured with the detector. Figure 2.8b shows this schematically. E is the energy before the scattering process and KE the energy after the scattering. E_0 is the energy with which the ion enters the solid. Assuming a constant stopping power $\mathrm{d}E/\mathrm{d}x$ all the way of the ion in the solid, it yields

$$E = E_0 - \frac{z'}{\cos(\theta_1)} \left.\frac{\mathrm{d}E}{\mathrm{d}x}\right|_{\mathrm{in}} \tag{2.10}$$

and

$$E_2 = KE - \frac{z'}{\cos(\theta_2)} \left.\frac{\mathrm{d}E}{\mathrm{d}x}\right|_{\mathrm{out}}. \tag{2.11}$$

Therefore, the measured energy range for ions backscattered on a specific atomic species becomes

$$\Delta E = KE_0 - E_2 = \left(\frac{K}{\cos(\theta_1)} \left.\frac{\mathrm{d}E}{\mathrm{d}x}\right|_{\mathrm{in}} + \frac{1}{\cos(\theta_2)} \left.\frac{\mathrm{d}E}{\mathrm{d}x}\right|_{\mathrm{out}}\right) \cdot z', \tag{2.12}$$

which makes it possible to determine layer thicknesses.

The evaluation of the measured RBS spectra was carried out with the software RUMP developed by L. DOOLITTLE [129].

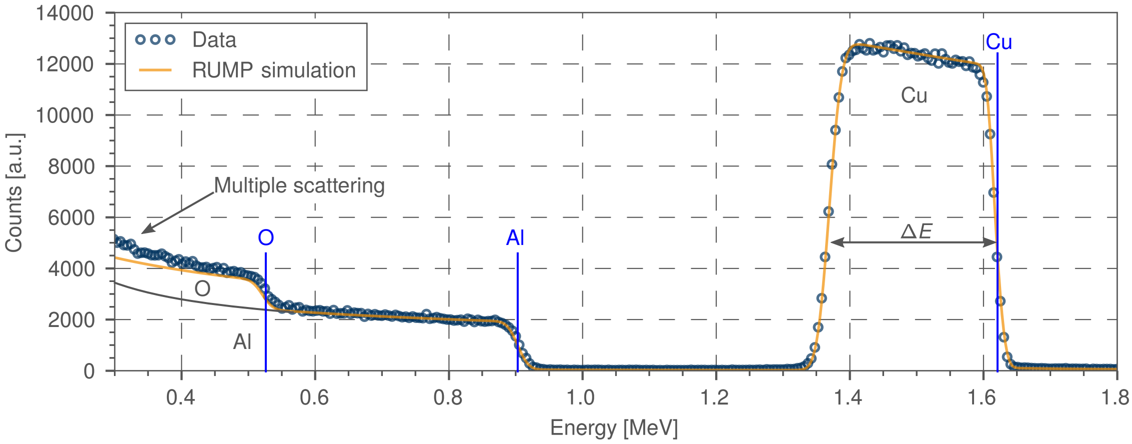

Fig. 2.9: RBS spectrum and RUMP simulation of a 200 nm film on Al_2O_3 substrate. The blue lines are the backscattering edges for the indicated elements. The deviation for small energies is due to multiple scattering within the sample which is not considered by RUMP. The thickness of the film is given by the energy loss range ΔE.

Evaluation of RBS spectra with RUMP

Figure 2.9 shows a RBS spectrum measured with a 2 MeV He^+ ion beam. As the energy of the backscattered ion depends on the mass of the target atom (equation (2.8)), the element analysis can be done by evaluating the backscattering edge (blue lines). The backscattered yield gives in principle the concentration of the element.

For the quantitative analysis, the spectra were imported in RUMP. The analysis is done by comparing the measured spectra with simulated ones. At the very beginning an energy-channel calibration has to be done[5]. Subsequently, a layer structure is assumed and simulated until a good agreement between the measured and the simulated curves is achieved [117]. Note, also non RUTHERFORD cross sections can be imported into RUMP for simulations.

The layer thickness is according to equation (2.12) related to the energy loss ΔE, indicated in figure 2.9 for the Cu film. The thickness will be obtained from the simulation in atoms per cm^2. To obtain a geometrical thickness, i.e. in nm, the mass density of the layer is required.

Determination of the crystal quality by RBS-channelling

Figure 2.10 shows schematically the ion channelling process. If the target crystal axes (or planes) are aligned to the ion beam within a critical angle ψ_c ion channelling will occur. This critical angle depends on the ion energy, the ion species and the target material. In general it is less than 5 ° [98][6].

The crystal quality of the sample can be obtained by measuring the backscattered yield $Y_r(E)$ with random orientation of the sample with respect to the ion beam and $Y_a(E)$ of an aligned spectrum (see figure 2.10). As a measure of the crystal quality, the normalised backscattered yield $\chi(E) = Y_a(E)/Y_r(E)$ is used. This curve has its minimum χ_{min} near the surface peak. The value of χ_{min}, normally in the range of a few percent, gives information about the crystal quality. The channelling method was used only to obtain information about the crystal quality of Cu thin films before and after implantation and annealing. Therefore, a detailed explanation will not be given here. This can be found in [117, 127]. The channelling experiments were

---

[5] The measured spectra is only the counts over channels, the energy calibration has to be done with a standard sample, i.e. a gold film on carbon.

[6] For that reason, substrate holders for ion implantation are often inclined with 7 ° with respect to the ion beam to avoid the channelling effect.

carried out at the Lipsion laboratory at the University of Leipzig. A detailed description of this accelerator is given in reference [117].

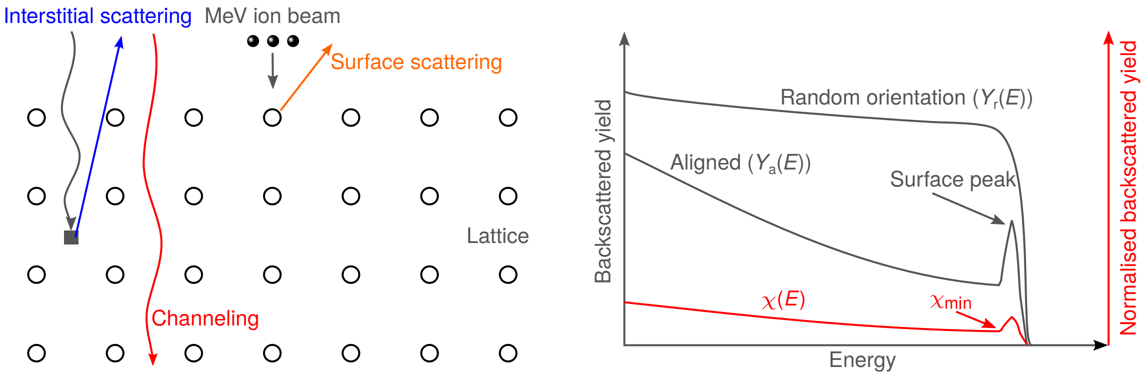

Fig. 2.10: Schematic illustration of the channelling process. The ion beam is aligned to the target lattice which allows the ions to channel into the lattice. Some of the ions are backscattered on the surface (surface peak). Others may scatter back by interstitials within the lattice or by defects. The penetration depth in general increases due to the channelling process and the yield of the backscattered ions decreases in contrast to the non aligned case (modified after [98]).

2.2.3 Ion accelerator and energy-mass selection

For the ion implantation an IMC 200 Ion Implanter from the company IBS (ion beam services) was used. In general, an accelerator for ion implantation, schematically shown in figure 2.11, consists of an ion source with pre-acceleration, an electromagnet for energy and mass selection, an accelerator tube and a scanning and focussing unit These parts are shortly described in the following.

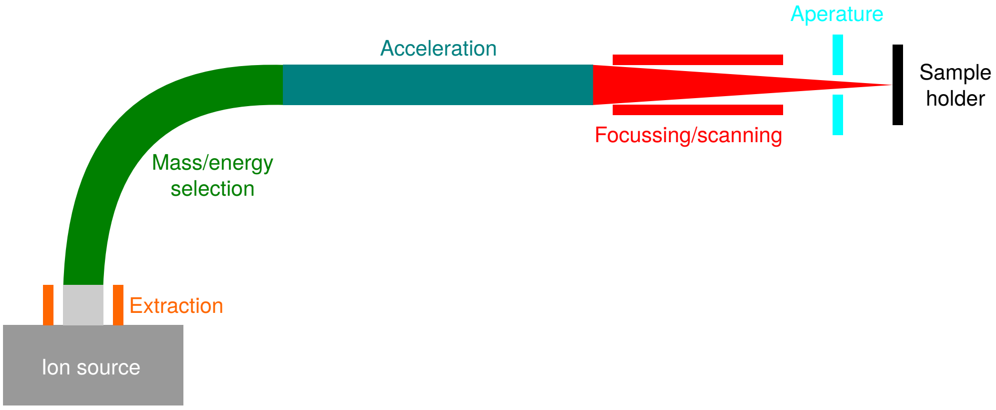

Fig. 2.11: Schematic illustration of the implanter. Starting from a gaseous ion source containing the atomic species to be implanted the created ions are extracted by an electric field applied at the exit of the source. The ions travel through an electromagnet for energy and mass selection (see text for details). Then the mass selected ion beam is accelerated, focused and finally swept over the surface of the sample.

Ion source and extraction unit

The used ion implanter is equipped with a Freeman arc discharge ion source [130]. The filament is heated by the filament current. When the emission temperature is reached, electrons can escape from that filament. A potential is applied to accelerate these free electrons. The gas which contains the elements for implantation (e.g. CO_2 for carbon ions) is injected through a mass flow controller (MFC). The gas molecules become ionised by collision with the energetic electrons. A magnetic field applied within the source increases the mean path of the electrons and therefore the probability to hit and ionise a gas atom/molecule. A plasma of positively charged ions and electrons is formed. A so called extraction voltage U_{extract} is applied (usually 15 kV) to extract the ions from the source into the analyser unit. After this extraction, the ions have the energy $E_{\text{kin}} = q \cdot U_{\text{extract}}$. This is schematically shown in figure 2.12. Note, that there additional components required in the ion source like water cooling, venting ports or power supplies which are not shown for simplicity.

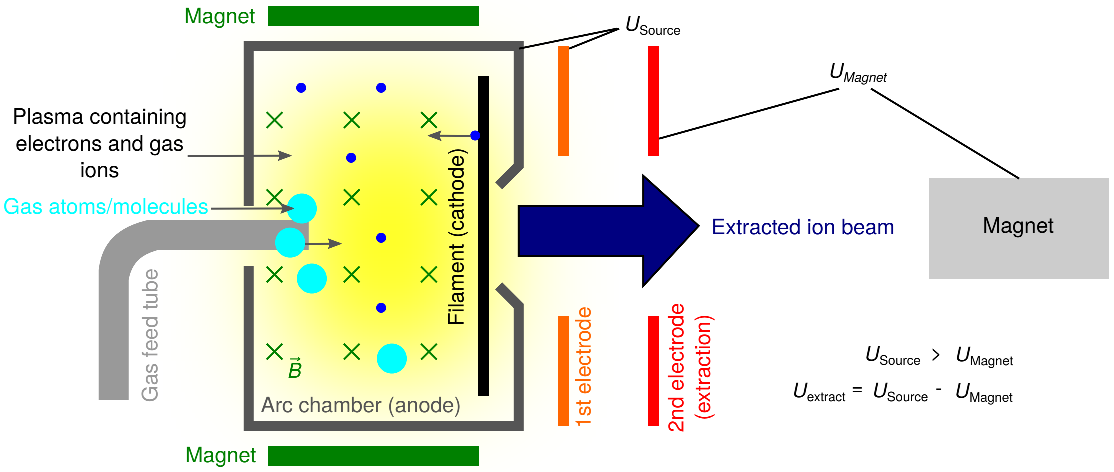

Fig. 2.12: Schematic illustration of the ion source of the implanter. Electrons are extracted from the hot filament (cathode), collide with gas molecules/atoms and produce ions that are extracted by the extraction voltage. The magnetic field increases the path of the electrons (modified from [130]).

Analyser magnet and mass-energy selection

For the selection of the ion species with specific mass m to be implanted, a 90°-magnet is used. The magnetic field B is perpendicular to the moving direction of the ions (charge q, velocity v and mass m) resulting in a LORENTZ force $F_{\text{L}} = q \cdot v \cdot B$ that bends the ions on a circular path of radius R. By use of the centripetal force it yields

$$R = \frac{1}{qB}\sqrt{2mE_{\text{kin}}}, \tag{2.13}$$

with $E_{\text{kin}} = \frac{m}{2}v^2$ being the kinetic energy of the ions[7].

The mass uncertainty for the used magnet is specified as $\frac{m}{\Delta m} = 100$ [130]. Therefore, every elemental mass or isotope can be separated, e.g. ^{12}C and ^{13}C. However, a separation of ^{13}C and ^{12}CH is not possible.

Acceleration unit, beam focussing and scanning

After ion type selection, the ions are accelerated within the acceleration unit (see figure 2.11) by the acceleration voltage. After this, the ions have the energy $E_{\text{kin}} = q \cdot (U_{\text{extract}} + U_{\text{accel}})$ with U_{extract} and U_{accel} as the extraction and acceleration voltage, respectively. The beam shaping

---

[7] For velocities much smaller than the speed of light c which is the case for the used ion energies.

(or focussing) is done by an electrostatic quadrupole doublet. The scanner plates scan the beam over the whole sample which can be up to 6 inch in diameter. The beam is also scanned over FARADAY cups to measure the beam current and therefore the fluence during the implantation process. The sample holder can be equipped with four 6 inch (≈ 15.2 cm) wafers which are inclined 7° with respect to the ion beam to avoid channelling [130].

2.3 Cu thin film deposition

Beside the graphene synthesis on Cu foils, within this thesis graphene was also synthesised on thin films. For the production of these films, magnetron sputtering and ion beam sputtering were used. Both methods are physical vapour deposition methods (PVD) [115, 116].

2.3.1 Magnetron sputtering

A scheme of the magnetron sputtering process is shown in figure 2.13a. The Ar^+ ions, created by collisions of electrons with the argon atoms (gas discharge), are accelerated towards the target (on negative potential) which is made of the material to be deposited on the substrate. All this is done in Ar-atmosphere at a pressure of $\approx 10^{-3}$ mbar. Ar^+ ions that hit the target surface lead to the ejection of target atoms. They can move to the substrate, condensate and form the first monolayers of the thin film. Also secondary electrons are created near the target during this sputter process. In a magnetron sputter system, a strong magnetic field $\vec{B}$ is applied close to the target surface. Thereby, the ejected electrons are moving on spirals along the field lines which enlarges their mean travelled distance. In this way, an increase of the ionisation probability for the Ar atoms is achieved. A higher density of Ar^+ ions means a higher sputter yield from the target which leads to a faster deposition rate. Moreover, the absence of electrons or highly energetic Ar^+ ions near the substrate improves the quality of the deposited film by avoiding ion beam damage.

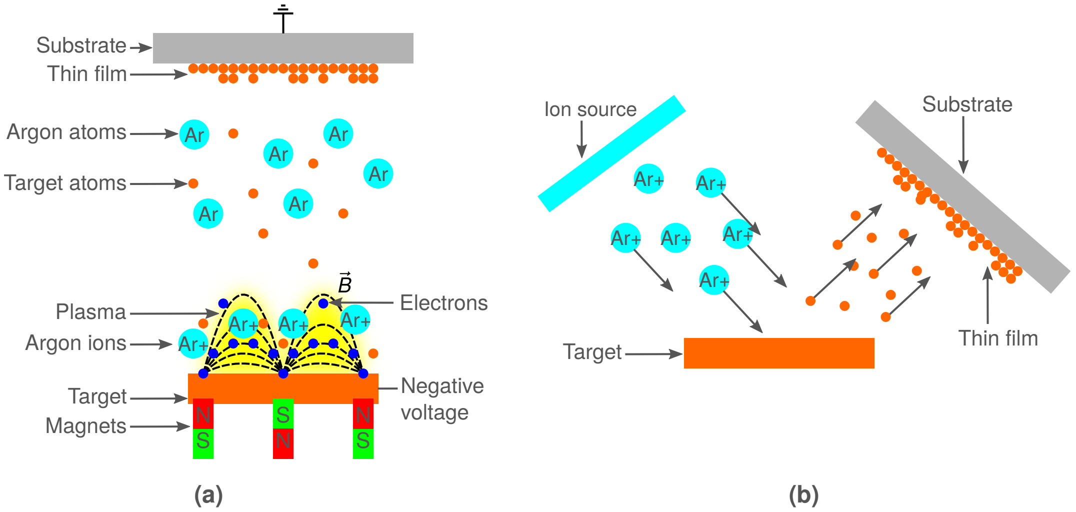

Fig. 2.13: (a) Schematics of the magnetron sputter process. Due to the magnetic field, the electrons trajectories are extended leading to a more efficient ionisation of the argon atoms. The target atoms which are sputtered from the target by the argon ions form the layer on the substrate. (b) Ion beam sputtering process where the argon ions are created within the ion source and accelerated onto the target. There, the atoms become sputtered and form the film on the substrate.

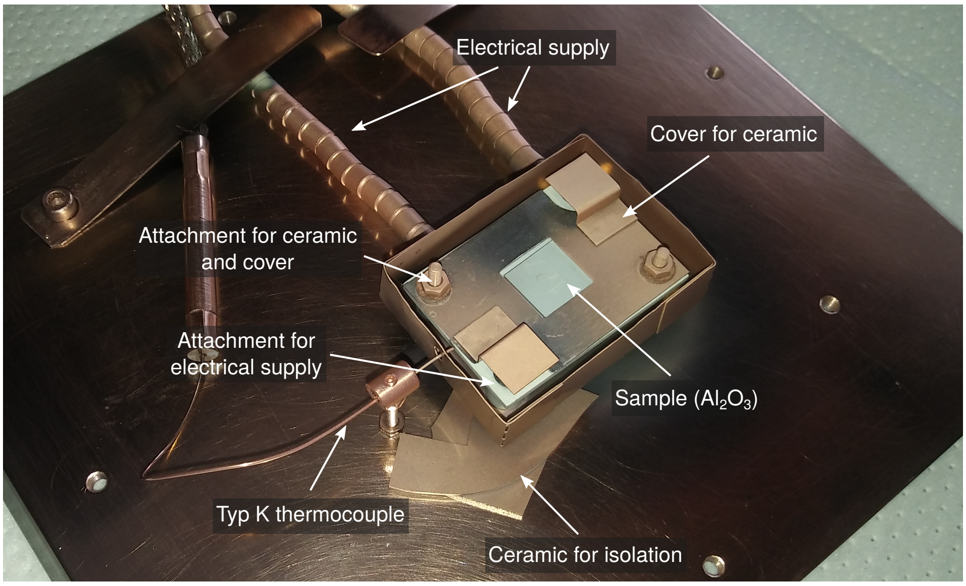

Fig. 2.14: Sample holder for the magnetron sputter chamber, with the heater stage attached on it.

Heater stage for Cu film deposition at high temperature

In order to increase the quality of the sputtered Cu films, a custom heater stage was designed and installed inside the magnetron sputter chamber. For this purpose, a TECTRA HTR-1-100 sample heater stage was modified and attached to the conventional sample holder of the magnetron sputter chamber, as shown in figure 2.14.

The electrical supply for the heating current was realised by copper wires isolated by small ceramic pieces. This current flows through a thin wire within a ceramic which acts as sample holder. On this, the sample was mounted and fixed by a thin metal plate which also acts as a cover of the ceramic in order to protect it from the sputtered Cu and therefore to avoid formation of an electrical short circuit. Plates made from ceramic act as isolators below the screws that fix the wire for the current flow. A type K thermocouple was used for temperature measurement. The heating stage was controlled by a TECTRA HC3500-LV.

2.3.2 Ion beam sputtering

Another technique used for the synthesis of Cu thin films is ion beam sputter deposition. The process is shown schematically in figure 2.13b. An ion source provides Ar^+ ions, already accelerated within the grid system of the ion source. These ions move to the target and sputter the target material which forms the thin film on the substrate. In the used sputter chamber [131], the target as well as the substrate is on ground potential.

2.4 Thermal treatment of Cu foils and Cu films

Before the implantation of carbon ions, an annealing procedure is performed. This leads to bigger grain sizes and in case of the Cu foils also to a smoother surface [132–134].

All annealing steps were performed with a XERION XRETORT UHV 1100. This oven is equipped with a rough pump, a turbo-pump as well as an ion getter pump system to reach a vacuum in the range 10^{-7} mbar at around 1000 °C (usually $p < 8 \cdot 10^{-7}$ mbar). A mass flow controller allows to heat the sample not only in vacuum but under specific gas atmosphere and pressure. During the annealing process, the sample lies on a quartz glass tube in vacuum, surrounded by insulting wool. Also a mass spectrometer allows to determine the residual gas composition.

The temperature is measured via a type K thermocouple (materials NiCr-Ni) which is positioned under the sample. The time to achieve 1000 °C is around 20 min. The cooling rate is 1 °C per second at high temperature. For temperatures below ≈ 500 °C, the cooling rate decreases. Note, no active cooling was applied.

2.5 Basics of Raman spectroscopy as a tool for probing properties of graphene

In this part, the RAMAN spectroscopy method in general and its use for probing the properties of graphene will be presented. Because this method was used very intensively within this thesis, it is described in more detail, especially the shape of the RAMAN bands and the influences on them.

The determination of the number of the graphene layers on a substrate can be done by different approaches beside RAMAN spectroscopy (see section 2.6.1). It is advisable to apply different methods to unambiguously determine the number of graphene layers on a given substrate.

2.5.1 Classical concept for the Raman scattering process and its limitations

RAMAN spectroscopy is based on the inelastic scattering of light in solids or molecules [46,135]. The incoming photon has the energy $\hbar\omega_\mathrm{i}$ and excites the molecule from the initial state i with energy E_i to another, final energy state E_f which can be a vibrational state with an energy E_vib. Due to this excitation the scattered photon with the frequency ω_s looses the energy

$$\Delta E = E_\mathrm{f} - E_\mathrm{i} = \hbar\left(\omega_\mathrm{i} - \omega_\mathrm{s}\right). \tag{2.14}$$

The energy ΔE can represent rotational, oscillation or electronic energy of the molecule. In case of solids which show a band structure due to the periodic lattice, phonons can be created within this scatter process. The transient energy state

$$E_\mathrm{virt} = E_\mathrm{i} + \hbar\omega_\mathrm{i} \tag{2.15}$$

of the system during the scattering process is called a virtual state. Note, this virtual state is not a stationary state of the system. It is also not a solution of the time-independent SCHRÖDINGER equation [136]. The energy is not conserved within this absorption process. Therefore, this process is called virtual absorption. Within the quantum mechanical treatment of RAMAN scattering this virtual state is not needed. The transition between the energy levels is then described by the transition matrix elements [137].

Beside of that, the RAMAN effect can be described classically by the theory of electromagnetism. For simplicity, the RAMAN effect on molecules is described here. In case of solids, the process of changing the polarisability due to the external electric field is analogous.

An electric field $\vec{E} = \vec{E}_0 \cos\left(\omega t\right)$ which is applied to a molecule (or solid) induces an oscillating dipole moment

$$\vec{P}_\mathrm{ind} = \bar{\bar{\alpha}} \cdot \vec{E}, \tag{2.16}$$

which may overlap with a permanent dipole moment $\vec{\mu}$ to

$$\vec{P} = \vec{\mu} + \bar{\bar{\alpha}} \cdot \vec{E} \tag{2.17}$$

$$= \vec{\mu} + \bar{\bar{\alpha}} \cdot \vec{E}_0 \cos(\omega t), \tag{2.18}$$

where $\bar{\bar{\alpha}}$ is the polarisability which is in general a 3×3 matrix (or a second rank tensor). Its components are functions of the molecule symmetry and the position of the atomic nuclei [135]. Thus, the dipole moment $\vec{P}$ and the polarisability $\bar{\bar{\alpha}}$ are functions of the electron and atomic nuclei coordinates. If the molecule is oscillating, the displacements of the nuclei from the equilibrium position can be expressed with the generalised coordinates q_n. If the displacements of the nuclei due to the polarisation of the electron shell is small, it yields in case of $(3\mathrm{Q} - \mathrm{f})$ possible normal oscillation modes [138]

$$\vec{\mu}(q) = \vec{\mu}(0) + \sum_{n=1}^{3\mathrm{Q}-\mathrm{f}} \left(\frac{\partial \vec{\mu}}{\partial q_n}\right)_0 q_n \tag{2.19}$$

for the dipole moment and

$$\alpha_{ij}(q) = \alpha_{ij}(0) + \sum_{n=1}^{3\mathrm{Q}-\mathrm{f}} \left(\frac{\partial \alpha_{ij}}{\partial q_n}\right)_0 q_n \tag{2.20}$$

for the polarisation. Here, Q is the number of atomic nuclei. The degrees of freedom are $(3\mathrm{Q} - \mathrm{f})$ with $\mathrm{f} = 5$ for linear and $\mathrm{f} = 6$ for non-linear molecules. The terms $\vec{\mu}(0)$ and $\alpha_{ij}(0)$ are the dipole moment and polarisation at the equilibrium position $q_n = 0$. For small deflections, q_n can be linearly approximated by a harmonic oscillation

$$q_n(t) = q_{n_0} \cos(\omega_n t), \tag{2.21}$$

where q_{n_0} is the equilibrium position and ω_n the frequency of the n-th normal oscillation.

With equation (2.20) and (2.19) together with (2.18) it yields for the total time dependent dipole moment[8]

$$\begin{aligned}\vec{P}(t) = \overbrace{\vec{\mu}_0}^{1} &+ \overbrace{\sum_n \left(\frac{\partial \vec{\mu}}{\partial q_n}\right)_0 q_{n0} \cos(\omega_n t)}^{2\,(\mathrm{IR})} + \overbrace{\alpha_{ij}(0) \vec{E}_0 \cos(\omega t)}^{3\,\mathrm{Rayleigh}} \\ &\underbrace{+ \frac{E_0}{2} \sum_n \left(\frac{\partial \alpha_{ij}}{\partial q_n}\right)_0 q_{n0} \left[\cos((\omega - \omega_n) t) + \cos((\omega + \omega_n) t)\right]}_{4\,\text{Raman Stokes, Raman Anti–Stokes}}.\end{aligned} \tag{2.22}$$

The first term describes the permanent dipole moment, the second the part of the dipole moment which is oscillating. This one is responsible for the infra-red (IR) spectrum. The third term depends on the polarisability and describes the induced dipole moment due to the incoming electromagnetic wave (see equation (2.16)). This oscillating dipole moment emits electromagnetic waves, with the same frequency ω as the incoming wave. Therefore, every molecule gives off

---

[8] With the cosine rule $\cos \mathrm{A} \cos \mathrm{B} = \frac{1}{2} [\cos(\mathrm{A} + \mathrm{B}) + \cos(\mathrm{A} - \mathrm{B})]$.

elastically scattered light which is called the Rayleigh scattering. The fourth term describes the Raman scattering which occurs at the shifted frequencies $(\omega - \omega_n)$ (Stokes scattering) and $(\omega + \omega_n)$ (Anti-Stokes scattering). These three processes are illustrated in figure 2.15. The Anti-Stokes process happens if the molecule is in an excited vibrational and/or rotational state before the scattering process, for example, due to thermal excitation [136]. Within this process, a phonon is annihilated.

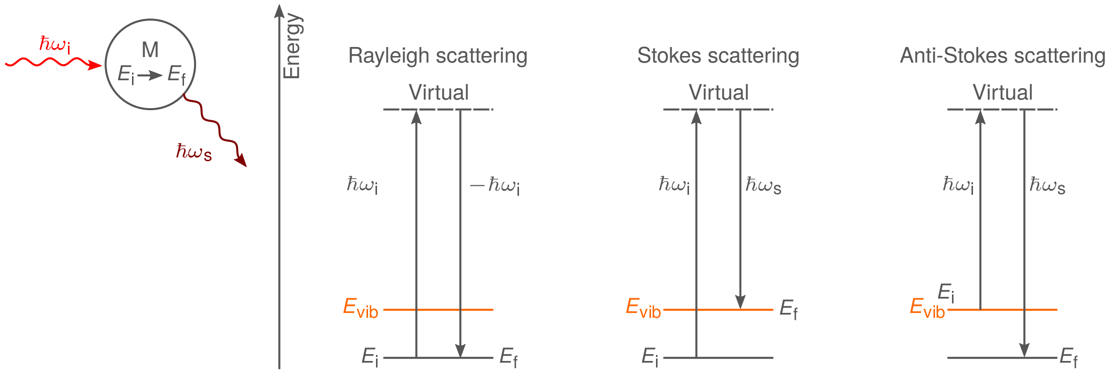

Fig. 2.15: Energy scheme for the scattering processes of light in a sample or molecule. (a) Elastic scattering from the ground state back to the ground state (Rayleigh scattering, $E_\mathrm{i} = E_\mathrm{f}$), (b) inelastic scattering with $E_\mathrm{i} < E_\mathrm{f}$ (Stokes scattering) and (c) inelastic scattering with $E_\mathrm{i} > E_\mathrm{f}$ (Anti-Stokes scattering). E_vib is the first excited vibrational state (modified after [135]).

Equation (2.22) shows that the intensity of the Raman scattering depends on the change of polarisability with respect to the displacement of the nuclei $\partial\alpha_{ij}/\partial q_n$, whereas the IR absorption depends on the change of the dipole moment with respect to the displacement of the nuclei $\partial\vec{\mu}/\partial q_n$. Thus, homonuclear two atomic molecules have no IR active modes, but a Raman mode. For heteronuclear molecules it depends on the symmetry of the displacement motion. The Raman active oscillation modes for graphene are discussed in section 2.5.2.

This classical treatment of the Raman scattering processes gives the correct frequency dependence for the Rayleigh scattering and the vibrational Raman scattering. To obtain characteristic molecular vibrational frequencies (and use them as a signature) this explanation is reasonable as well. However, the classical concept does not treat rotational modes of the molecules, because in this frame they cannot be discretised [136]. Also, energy diagrams like figure 2.15 give no information about the mechanisms of the photon-molecule interactions or the probability of their occurrence [136]. Furthermore, the intensity ratio of the Stokes and Anti-Stokes bands is incorrect [136]. The excited vibrational state is only thermally populated according to the Boltzmann distribution and the Stokes intensity will, therefore, be much larger than the Anti-Stokes intensity.

Raman intensity and laser energy dependence

In general, the Raman intensity shows a ω^4 dependence with ω as the excitation wavelength of the laser [139, 140]. This dependence arises from the general theory about dipole radiation [46]. Let $\vec{d} = e\vec{r}$ be a dipole moment with e as the electric charge and $\vec{d}$ as the connecting vector between the positive and negative charges in the dipole. If the electric charge is accelerated, radiation will be emitted which means that the $\vec{E}$ field is proportional to the second time derivative of the dipole momentum, so $\vec{E} \propto \ddot{\vec{d}} = e\ddot{\vec{r}}$. This equation can be solved with $\vec{r} = \vec{r}_0 e^{i\omega t}$ which gives $\ddot{\vec{d}} = -\omega^2\vec{d}$. The scattering intensity I is related to the energy flux which can be obtained from the POYNTING vector $\vec{S}$ for which in case of plane waves $I \propto |\vec{S}| \propto \vec{E}^2 \propto \left(\ddot{\vec{d}}\right)^2$. Therefore, the light emission (or the "intensity of scattering") is dependent on ω^4. For the assumption that the energy difference of the incoming and scattered photon within the RAMAN process is small, $\hbar\omega_\mathrm{i} \approx \hbar\omega_\mathrm{s}$, it is a good approximation to state that the absolute RAMAN intensity increases with E^4_Laser [137, 141]. However this is only true if the frequency ω is far from the band gap (for semiconductors) or more general any energy difference between an occupied initial state and an unoccupied final state[9]. If the induced dipole moment $\vec{P}_\mathrm{ind}$ is not proportional to the electric field $\vec{E}$, this is called non-linear (or non-resonant) RAMAN scattering, hyper-RAMAN scattering and hyper-RAYLEIGH scattering which is described in detail in reference [135, 136, 142]. To obtain the right intensities for the different RAMAN modes, the RAMAN scattering cross sections have to be calculated by quantum mechanical perturbation theory [143]. This is done very intensively in reference [46, 136].

Raman lineshape and Raman spectral linewidth

In order to obtain quantitative information about the specimen it is required to fit the spectra with the appropriate type of functions. In general, the photon excitation can be represented by a harmonic oscillator which is damped by the interaction with other excitations from the medium [46]. This is similar to a mass spring system inside a liquid system. Thus, the intensity peak shape of the RAMAN signal is the same as from a damped harmonic oscillator with eigenfrequency ω_0 which is forced by an external field (here $\vec{E}$) with the frequency ω.

If the damping factor is denoted with γ, the signal has a LORENTZian shape (see appendix A.1) and is given by

$$I(\omega) = I_0 \left[\frac{\gamma^2}{(\omega-\omega_0)^2+\gamma^2}\right] = I_0 \left[\frac{1}{1+\left(\frac{\omega-\omega_0}{\gamma}\right)^2}\right]. \tag{2.23}$$

The peak height then is I_0 and the full width at half maximum is $\Gamma_\mathrm{L} = 2\gamma$.

In spectroscopy, normally a DOPPLER broadening occurs due to a distribution of the velocities of the oscillating molecules which originate from different masses or the temperature (thermal DOPPLER broadening). This broadening can be taken into account for the spectral lineshape by convoluting the LORENTZian peak shape (2.23) with a GAUSSian profile. This gives the socalled VOIGT profile which is defined as

$$V(\omega-\omega_0) = (G * L)(\omega-\omega_0) = \int_{-\infty}^{\infty} G(\tau)L((\omega-\omega_0)-\tau)\mathrm{d}\tau. \tag{2.24}$$

This integral has no analytical solution but, can be expressed by the real part of the FADDEEVA function $X(z)$. Thus, the VOIGT profile becomes

$$V(\omega, P_0, \omega_0, \sigma, \gamma) = \frac{P_0 \mathrm{Re}[X(z)]}{\sigma\sqrt{2\pi}} \tag{2.25}$$

with

$$z = \frac{\omega-\omega_0+i\gamma}{\sigma\sqrt{2}}$$

---

[9] If so, the virtual state in which the electron becomes excited after light absorption is not virtual any more.

and

$$X(z) = e^{-z^2}\mathrm{erfc}(-\mathrm{i}z),$$

where erfc(−iz) is the complementary error function[10]. Here as above, P_0 is the amplitude of the signal, ω_0 is the center position. The full width at half maximum Γ_V of the VOIGT profile can be approximated with an accuracy of 0.02 % by [144]

$$\Gamma_\mathrm{V} \approx 0.5346\Gamma_\mathrm{L} + \sqrt{0.2166\Gamma_\mathrm{L}^2 + \Gamma_\mathrm{G}^2}, \tag{2.26}$$

with $\Gamma_\mathrm{L} = 2\gamma$ as the full width at half maximum of the LORENTZ part and $\Gamma_\mathrm{G} = 2\sigma\sqrt{2\ln(2)}$ as the full width at half maximum of the GAUSSian part.

For a faster calculation it is also common to use a Pseudo-VOIGT profile which is a linear combination of both, LORENTZ and GAUSS profile and given by

$$V_\mathrm{P}(x) = I_0 \cdot (\nu \cdot L(\omega) + (1-\nu) \cdot G(\omega)), \tag{2.27}$$

with $0 < \nu < 1$. If $G(\omega)$ and $L(\omega)$ are set to

$$G(\omega) = \exp\left[-\ln(2) \cdot \left(\frac{\omega - \omega_0}{\gamma}\right)^2\right] \tag{2.28}$$

and

$$L(\omega) = \frac{1}{1 + \left(\frac{\omega-\omega_0}{\gamma}\right)^2}, \tag{2.29}$$

I_0 in equation (2.27) becomes the amplitude of the signal and 2γ again the full width at half maximum [46]. This makes the calculation faster than the convolution approach. Note, the spectra within this thesis were fitted with the real VOIGT profile (2.25) unless otherwise stated[11].

Figure 2.16 shows the different fit models for a measured 2D peak of monolayer graphene. For the VOIGT fit function (2.25), for the GAUSSIAN fit (2.28) and for the LORENTZ fit equation (2.29) was used. For all three, the residual sum of squares $RSS = \sum_{i=1}^{n}(y_i - f(x_i))^2$ was calculated which shows that the VOIGT profile fits best with the measured data. Also the full widths at half maxima are changing for the different models. This value is important to obtain properties of graphene like the layer number, as described in section 2.6.1, so it is essential to fit the spectra accurately[12].

2.5.2 Raman spectroscopy on graphene

For a correct interpretation of the RAMAN spectra, the phonon dispersion of graphene becomes important. Figure 2.17a shows the phonon dispersion relation for graphene calculated by ab initio methods [146], figure 2.17b the Dirac cones (see section 1.1.1) [45], figure 2.17c a RAMAN spectrum of graphene with indication of the most prominent bands and figure 2.17d the associated vibrations of the sublattices with respect to each other.

---

[10] The complimentary error function is defined as $\mathrm{erfc}(x) = 1 - \mathrm{erf}(x) = \frac{2}{\sqrt{\pi}}\int_x^\infty e^{-t^2}\mathrm{d}t$.

[11] Note, that there are other peak shape function like PEARSON VII [145] which are commonly used for fitting XRD or even RAMAN spectroscopy data.

[12] As visible in figure 2.16 the FWHM obtained from the LORENTZ fit function is always smaller than the one obtained from the VOIGT fit function.

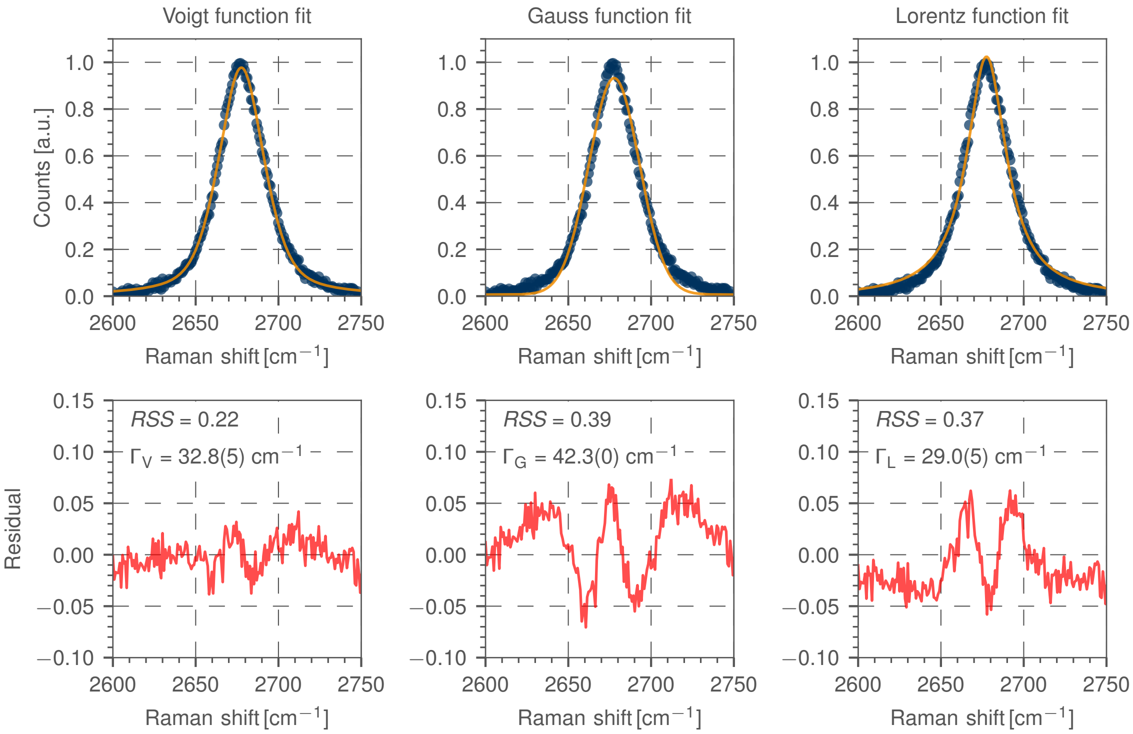

Fig. 2.16: Illustration of the different peak shape fitting models. The equations for fitting were (2.25), (2.28) and (2.29) for the VOIGT, GAUSS and LORENTZian shape, respectively. For comparison, the *RSS* values and the full widths at half maxima were calculated (see text).

The most important phonon modes are the iTO and iLO[13] (see figure 2.17a). In the vicinity of the zone centre (Γ-point), they correspond to the vibrations of the sublattice (🟧) against the sublattice (■) which leads to the G band at around 1580 cm^{-1} indicated in figure 2.17c. This band arises from a normal first order RAMAN scattering process (with $\vec{q} \approx 0$ near Γ) as shown in figure 2.17b. At the K-point the iTO and iLO modes are responsible for the D and 2D-band at around 2700 cm^{-1} and 1350 cm^{-1}, respectively [45]. These modes originates from a second order RAMAN scattering process, in which in case of the D (and D′) band, a defect must be present to scatter the electron back so that it recombines with the hole created in the same place in space (and therefore fulfils the conservation of momentum). Note, although the 2D band has nearly twice the energy of the D band, this second order RAMAN mode is also allowed in absence of any defects within the graphene lattice. The conservation of momentum is fulfilled for this scattering process due to the creation of two phonons [148]. The scattering process, e.g. for the 2D band double resonance, proceeds as follows: the photon creates an electron hole pair by exciting an electron from the valence band. The vertical transition of the electron is due to the small momentum of the photon which is only around 1/1000 of the width of the BRILLOUIN-zone. Therefore, the scattering process of the incoming photon with the electron occurs near the Γ-point (or even at the Γ-point itself if no phonon is created/annihilated). Due to electron-phonon scattering, a momentum $\vec{q}$ with $|\vec{q}| \approx |\vec{\mathrm{K}}|$ is exchanged and the first iTO phonon is created. The amount of momentum exchange is ≈ K, because the distance from K to K′ in the first BRILLOUIN zone is equal $|\vec{\mathrm{K}}|$ (see figure 1.2), so that the phonons are created at the K-point. The second phonon is created by another electron-phonon scattering process

---

[13] A and O stands for acoustic and optic phonon branches, i and o for in-plane and out-of-plane vibrations, respectively.

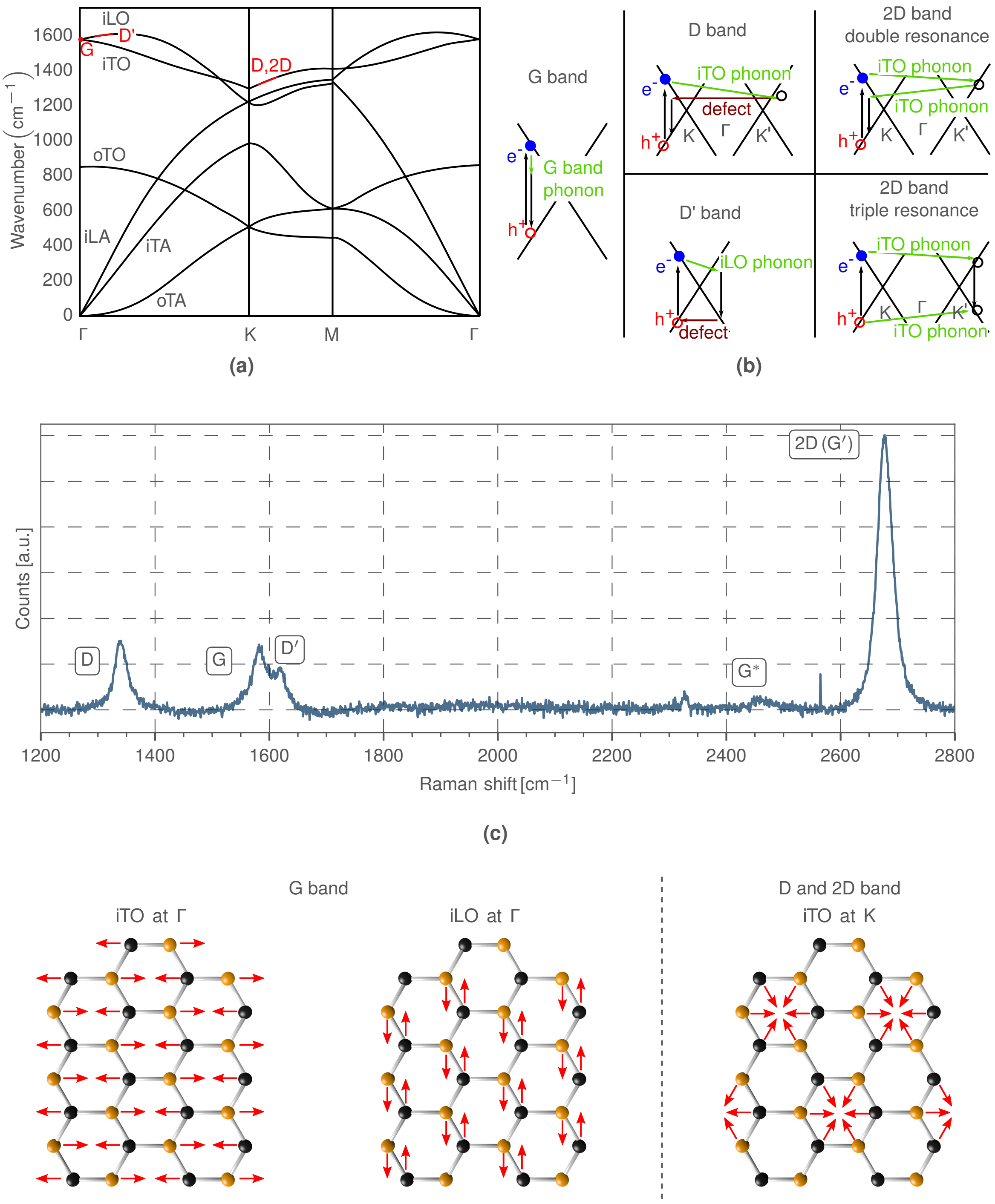

(a) (b) (c) (d)

Fig. 2.17: Overview of the RAMAN properties of graphene. (a) The phonon dispersion relation calculated ab initio with annotation of the phonon origins, (b) the DIRAC cones with annotation of the various scattering processes, (c) a RAMAN spectrum of single layer graphene showing the most prominent bands, (d) the corresponding vibrations of the sublattices (figure (a) and (b) modified after [45, 146], figure (d) modified after [147]).

with a momentum exchange of $-\vec{q}$ (for momentum conservation). Then, the electron and hole recombine and a photon with a smaller energy than the incident laser light is created. Similar processes lead to the other RAMAN bands. Note, there are other transitions within the DIRAC cones as well which give small contributions to the RAMAN spectrum of graphene beside those shown in figure 2.17b [148].

The D and 2D bands show a dispersive behaviour (due to the KOHN anomaly at the K-point [148]), i.e. their frequencies shifts with the laser energy. For an increasing laser photon energy the D band frequency upshifts linearly with a slope of around 50 cm^{-1}/eV. For the 2D band the upshift slope is around 100 cm^{-1}/eV [46, 149]. This is shown in figure 2.18. Note, the signal-to-noise ratio decreases with decreasing energy (increasing wavelength) as described in section 2.5.1.

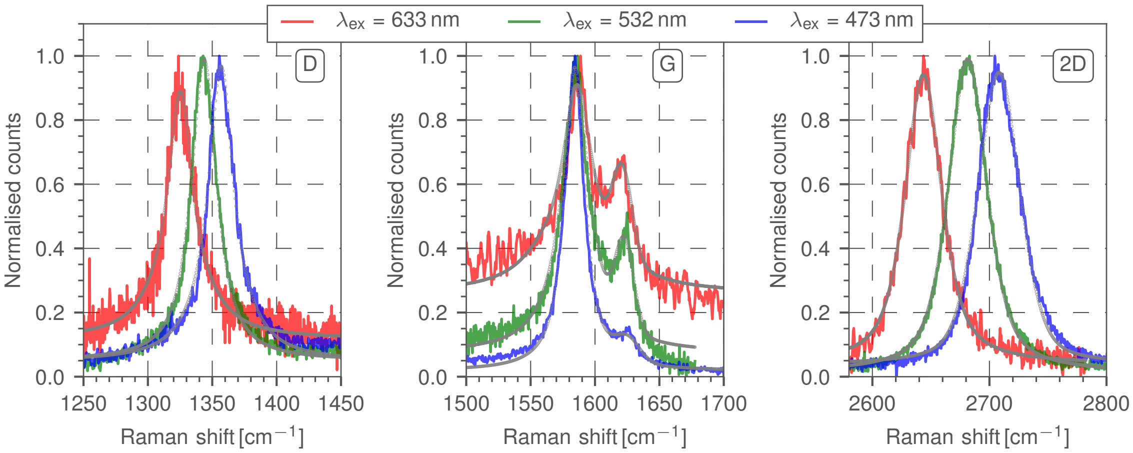

Fig. 2.18: Illustration of the dispersive behaviour of three main graphene RAMAN bands for the indicated photon wavelengths. The D band shifts from 1325.1(6) cm^{-1} over 1343.6(4) cm^{-1} to 1356.8(7) cm^{-1}. The G band stays nearly constant whereas the 2D band shifts again from 2643.6(1) cm^{-1} over 2681.4(7) cm^{-1} to 2708.1(0) cm^{-1}. The values were obtained from the fit curves (in grey).

The information about the spatial position of (sometimes) small graphene flakes is of great importance for the practical implementation of RAMAN spectroscopy measurements on graphene. If the graphene lies on a SiO_2/Si substrate it is easy to identify the graphene regions. It is also possible to differentiate graphene regions with different number of layers by the different contrast they show in the optical microscope (see also section 2.6.1 about layer number determination). A good contrast between graphene regions and the SiO_2/Si substrate is achieved with thicknesses of $d_{SiO_2} \sim 80, 280$ or 430 nm due to interference effects [150–152]. Graphene on copper (e.g. directly after the synthesis process) does not show such effects and is therefore not as easy to find as long as it is not several layers thick. One option is to wait until the copper is oxidised to copper oxide which is more red than orange. This oxidation takes place most in regions which are not covered by graphene. Therefore, the unoxidised regions can be identified as graphene regions. An approach to shorten the time for oxidation of the copper is to immerse it into warm water for several minutes. Note, this may lead to contamination of the graphene.

2.5.3 Further influences on the Raman bands

In this section the RAMAN bands already mentioned in section 2.5.2 are described in more detail. Moreover, the information on the graphene properties which can be extracted from the spectra will be presented.

For the following, the laser excitation wavelength is considered to be 532 nm. The influence of different laser wavelengths on the RAMAN spectra was already mentioned in 2.5.1 and 2.5.2. Also the position of the discussed RAMAN bands corresponds to ^{12}C graphene. For ^{13}C graphene, the spectrum is shifted to lower wavenumbers due to the increased mass of the carbon atoms.

Overview of the influences on the main Raman bands

The G band ($\sim 1580\,\mathrm{cm}^{-1}$) phonon is created near the Γ point with $\vec{q} \approx 0$. The RAMAN shift ω_G is blue-shifted for p-doped and red-shifted for n-doped graphene [153]. With increasing temperature T the band is also red-shifted. This is due to changes in the phonon-phonon coupling [154–156]. Furthermore, the linewidth (usually $\approx 10 - 15\,\mathrm{cm}^{-1}$) of the G band as well as the position is slightly influenced by the substrate underlying the graphene [157, 158]. The linewidth does also change with doping, temperature and strain [153, 159]. For bi-layer graphene an enhancement of the G band intensity occurs for certain rotational angles of the layers with respect to each other due to resonance with the excitation wavelength of 532 nm [160]. Due to interference effects the intensity of the G and 2D band depends on the substrate, e.g. the thickness of the $\mathrm{SiO_2}$ [151].

The 2D band ($\sim 2680\,\mathrm{cm}^{-1}$) shows a blue shift for p-doped and a red shift for n-doped graphene [153]. The line shape and position depend on the layer number and the stacking order [28, 45, 161–163] as well as the defect density [164] and the underlying substrate [165].

The D band ($\sim 1350\,\mathrm{cm}^{-1}$) can be used to quantify the disorder within the graphene layer [164, 166, 167]. The width of the band is also defect density related and can vary between $\approx 10\,\mathrm{cm}^{-1}$ up to $\approx 100\,\mathrm{cm}^{-1}$ for defect-rich graphene or even amorphised carbon. Due to the difficulty to measure absolute RAMAN intensities, the ratio $I_\mathrm{D}/I_\mathrm{G}$ is in general used to calculate the defect density in single layer graphene. It is important to know that this ratio does not only depend directly on the defect density, but also on the laser excitation wavelength since $I_\mathrm{G} \propto E_\mathrm{Laser}^4$, whereas I_D is independent from the laser energy [167, 168].

The position of all RAMAN bands depends also on the isotope of the carbon atoms. As already mentioned in section 2.5.1, the induced electrical dipole moment depends on the nuclei displacements from the equilibrium position. These displacements depend on the masses of the nuclei and therefore also on the isotope [135]. The shift of the peak wavenumbers for graphene can be calculated by[14]

$$\omega(x) = \omega_\mathrm{12C}\sqrt{\frac{m_\mathrm{12C}}{m_\mathrm{12C} + x\Delta m}}. \tag{2.30}$$

Here, x is the relative concentration of ^{13}C ($0 \leq x \leq 1$) in the enriched graphene sample, ω_12C represents the RAMAN frequency for the ^{12}C graphene sample, m_12C is the mass of the ^{12}C carbon isotope and Δm is the mass difference between the two carbon isotopes [169].

Note, most of the graphene synthesised by CVD or mechanical exfoliation contains carbon with the natural isotopic composition x in equation (2.30) becomes 0.011 for ^{13}C. The graphene synthesised in this thesis is composed out of ^{12}C only due to the mass selection within the ion implantation process (see section 2.2.3). The shift of the bands is only a few wavenumbers compared to natural carbon, depending on the purity of the precursor used for the graphene synthesis in the literature. The width of the bands are typically $> 10\,\mathrm{cm}^{-1}$. Therefore, the shift resulting from the natural carbon isotope ratio can be neglected. For pure ^{13}C graphene however, the G- and 2D- bands are downshifted by $\approx 60\,\mathrm{cm}^{-1}$ and $\approx 100\,\mathrm{cm}^{-1}$, respectively [170].

---

[14] By taking the ratio of the frequencies of the harmonic oscillator which is given by $f = \frac{1}{2\pi}\sqrt{\frac{k}{m}}$ with m as the mass of the atom and k as a constant.

Crystallite size and defect density

As already mentioned, Raman spectroscopy can be used to determine the defect density in graphene. This can be done by calculating the inter-defect length L_{D} by [166]

$$L_{\mathrm{D}}^2\left(\mathrm{nm}^2\right)=\frac{(4.3\pm1.3)\cdot10^3}{E_{\mathrm{Laser}}^4\left(\mathrm{eV}^4\right)}\left[\frac{I(\mathrm{D})}{I(\mathrm{G})}\right]^{-1} \tag{2.31}$$

for point defects separated $L_{\mathrm{D}}\geq 10\,\mathrm{nm}$ using laser light in the visible range. The defect density $n_{\mathrm{D}}\left(\mathrm{cm}^{-2}\right)=10^{14}/(\pi L_{\mathrm{D}}^2)$ can therefore be calculated by [166]

$$n_{\mathrm{D}}\left(\mathrm{cm}^{-2}\right)=(7.3\pm2.2)\cdot10^9E_{\mathrm{Laser}}^4\left(\mathrm{eV}^4\right)\left[\frac{I(\mathrm{D})}{I(\mathrm{G})}\right]. \tag{2.32}$$

These equations are only valid if the defects are Raman active. For example, there is no D band (called silent defects) for perfect zigzag edged graphene [171–173] or charged impurities within the lattice [153, 174].

The crystallite diameter size L_{a} can be calculated by [175]

$$L_{\mathrm{a}}\,(\mathrm{nm})=\frac{560}{E_{\mathrm{Laser}}^4\left(\mathrm{eV}^4\right)}\cdot\left[\frac{I(\mathrm{D})}{I(\mathrm{G})}\right]^{-1}. \tag{2.33}$$

2.5.4 Raman spectrometer for graphene characterisation and data acquisition

Raman spectrometer

The spectrometer used for the Raman spectroscopy measurements within this thesis was a LabRAM HR Evolution equipped with three different lasers, a Cobolt Blues$^{\mathrm{TM}}$ laser with 473.0 ± 0.3 nm wavelength and 50 mW power, a LaserQuantum torus Nd:YAG-laser with 532.0 ± 0.5 nm and 80 mW power as well as a MELLES GRIOT RED with 632.8 ± 0.2 nm with 17 mW power. Three different objectives are available, a Olympus MPlan N 100x/0.90, a Olympus MPlan N 10x/0.25 and a objective which can be directly used for the calibration of the spectrometer. The 100x objective which was used for all mapping measurements gives a spatial resolution of $\approx 0.2\,\mu$m. The scanning can be performed either via the Marzhauser stage or by moving a pair of galvano mirrors which are located above the objective while the sample is at a fixed position. The used spectrograph is equipped with two grids, one with $600\,\mathrm{l\,mm}^{-1}$ (lines per mm) and one with $1800\,\mathrm{l\,mm}^{-1}$ giving a spectral resolution of $1.9\,\mathrm{cm}^{-1}$ or $0.5\,\mathrm{cm}^{-1}$ for a laser wavelength of 532 nm (focal length of 80 cm, 50 μm spectrometer slit).

The optical path for the green laser is shown in figure 2.19[15]. The laser beam is coupled from outside into the laser path. The internal laser beam is directed by mirrors to a polariser and the neutral density (ND) filter with the optical density of 100 %, 50 %, 25 %, 10 %, 5 %, 3 %, 1 %, 0.1 % and 0.01 %. Afterwards, the beam is focused by the lens 1 on the pinhole which is used as a reference for alignment. Then, the beam is reflected by a mirror to the notch filter (for each wavelength there is a separate notch filter) with a certain angle so that the beam is reflected towards lens 2 in which it becomes parallised and enters the objective[16]. The Raman

---

[15] The other two laser beams travel the same path, only the notch filter is mechanically changed via software control.

[16] In this configuration the focus in the pinhole is conjugated with the laser spot focused on the sample

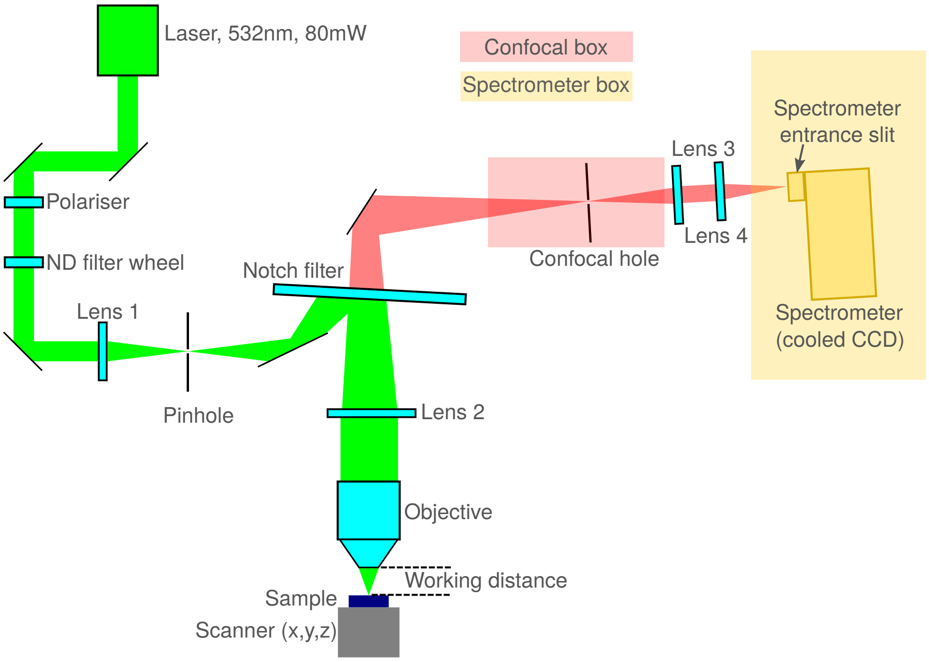

Fig. 2.19: Sketch of the LabRAM HR Evolution Raman spectrometer. The laser path goes through several optical elements and is focused by the objective onto the sample. The Raman spectroscopy light is collected by the objective and passes the same way back to the notch filter in which the laser light is filtered out. The remaining light passes the confocal hole which enables depth resolution and travels to the spectrometer.

light and the reflected laser light is collected and parallised by the objective and follows the same way back to the notch filter where the laser line is filtered out. Note, by use of this filter configuration, only Stokes-scattering can be measured (see section 2.5.1). The lens 2 reforms the image from the laser spot on the sample into the confocal hole[17]. The lenses 3 and 4 form a telescope which focuses the Raman light on the spectrometer entrance slit. After this slit, a shutter is applied to allow measuring a dark current spectrum and subtracting this from the measured spectra if necessary.

Raman measurement of graphene on copper substrates

The formation of graphene on the Cu surface has been confirmed by Raman spectroscopy in this thesis. However, Raman spectroscopy measurements of graphene on Cu, as shown on figure 2.20, are typically hampered by the huge fluorescence background from Cu as well as the relatively small 2D-peak intensity due to Cu/graphene interaction [44]. This can be reduced by using 473 nm laser excitation instead of 532 nm. Although, the signal intensity and the signal-to-noise ratio becomes better with lower wavelength excitation, the integration time has to be increased for measuring graphene on Cu (due to the not fully suppressed fluorescence) and therefore the duration for one mapping measurement (in order to obtain good statistics on the graphene quality) increases drastically. On average, the time increases by a factor of 3 in order to obtain the same signal-to-noise ratio, as reported in reference [176].

For graphene on Cu-foil, the mapping process becomes difficult due to the small working distance of 210 μm of the 100x objective and the ripple of the foils. In addition, the autofocus function could not be used for mapping. Intensive Raman spectroscopy mapping was therefore

---

[17] With this configuration the microscope becomes a confocal microscope with 2 focal points, one on the sample and one in the confocal hole by which light from deeper or lower regions is blocked.

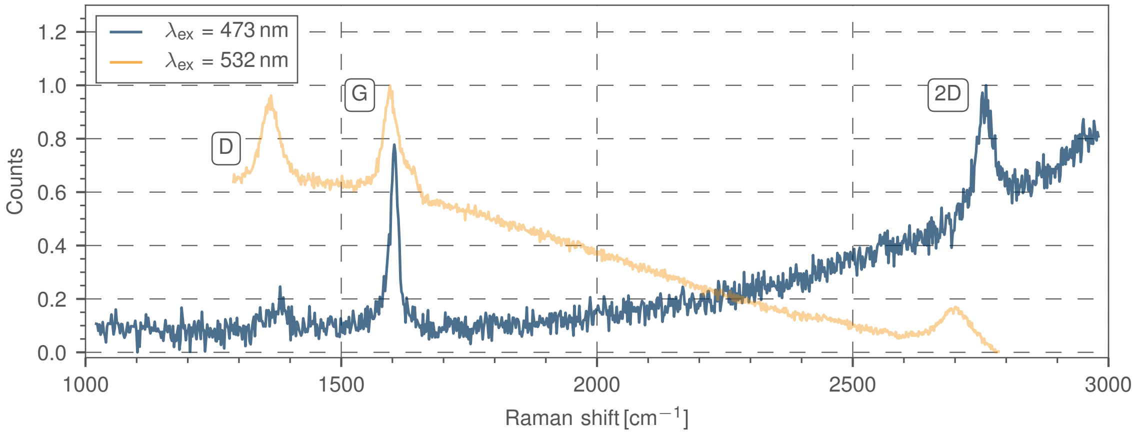

Fig. 2.20: RAMAN spectrum for graphene on Cu foil measured with 473 nm (blue) and 532 nm (orange) excitation wavelength and 2 minutes acquisition time. The laser power was 1 mW on the sample. No baseline correction was applied.

only performed on graphene that was transferred to silicon substrates.

Data acquisition and analysis

To obtain good statistics for the measurement of the graphene quality over a large area, RAMAN mapping has to be performed. This was typically done with the 600 l/mm grid, a laser power of 1 mW on the sample surface and the 100x objective. The integration time for measurements on Cu were 1 – 2 minutes per spectrum, depending on the number of measured points and the signal intensity. For measurements on silicon, the integration time was in the range of a few seconds only. The cosmic rays which may appear within the measurement were filtered out by measuring every spectrum twice.

For the evaluation of the RAMAN spectroscopy maps, a software called MINION[2] was programmed which is explained in appendix B. Note that the results for the fitting of the spectra are often shown as histograms (e.g. for the 2D-peak position or the FWHM). Together with the plot of these histograms, the implanted fluence, the mean value, the median (Med) and the standard deviation (Std), see e.g. figure 4.8e will be given. The most important values here are the median and the standard deviation as an estimate for the uncertainty for this value. The mean value is always given in order to show that most of the fitted parameters are in the plotted area of the histogram. For example, if the histogram for the 2D-peak position has x-axis limits of 2675 and 2695, values out of this range are not visible although they might exist due to bad fitting results or just due to a strongly inhomogeneous distribution of the respective values. This would be visible as a large difference between the mean and the median value.

2.6 Graphene layer number determination methods

2.6.1 Layer number determination by Raman-spectroscopy

Some of the physical properties of graphene, for example the behaviour as a conductor or a semiconductor, depend on the number of graphene layers [12, 13]. The determination of the layer number is therefore of interest.

There are several features available in the RAMAN spectra which can be used for the layer number determination. First, the 2D/G peak intensity ratio. If the 2D peak has more than twice the intensity of the G band, it can be an indicator for single layer graphene [151, 163].

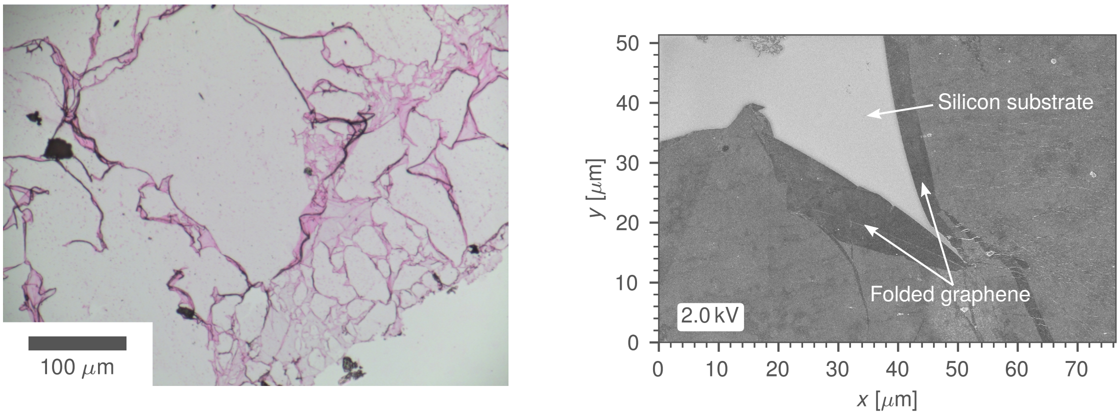

(a) (b)

Fig. 2.21: Example for the appearance of graphene with different layer numbers. (a) Optical image of graphene on SiO_2/Si (the darker, the more layers) and (b) SEM image (secondary electrons) of an edge of a graphene flake on SiO_2/Si with areas of folded graphene.

Note however, this ratio does not only depend on the layer number but also on the used laser excitation wavelength [149], the defect density [164], the delamination from the substrate [177] as well as the influence of the substrate itself [165, 178]. Another indicator for the layer number is the peak width and position of the 2D band. The width increases from $\approx 30\,\mathrm{cm}^{-1}$ for single layer graphene to $\approx 60\,\mathrm{cm}^{-1}$ for five layer graphene (it splits up in several bands when the layers are coupled to each other due to the overlapping of the π-orbitals). The position shifts from $\approx 2678\,\mathrm{cm}^{-1}$ for single layer over $\approx 2682\,\mathrm{cm}^{-1}$ for double layer to $\approx 2688\,\mathrm{cm}^{-1}$ for five layer graphene[18] [45, 161–163]. Another approach is to measure the C peak in the RAMAN spectrum which changes from $\approx 43\,\mathrm{cm}^{-1}$ for graphite to $\approx 31\,\mathrm{cm}^{-1}$ for bilayer graphene and disappears for single layer graphene [148, 179]. However, the position of this peak is close to the laser line itself. Thus, it was not possible to observe the C peak in this thesis. The position of the G peak is not a good indicator for the layer number because of its great dispersion [148].

2.6.2 Layer number determination by other methods

Besides RAMAN spectroscopy, there are several other methods for the layer number determination of graphene. Transmission electron microscopy (TEM) can be used to determine the number of layers if two or more are present. To confirm single layer graphene the sheet is folded and measured via TEM [28]. Another approach is to measure the transmission of light. The transmittance at a wavelength of 400 nm decreases from around 96% for single layer over 92% for bi-layer to 85% for five-layer graphene [161]. If the graphene lies on a silicon wafer, the intensity of the silicon band in the RAMAN spectrum can be used to determine the layer number [180]. Optical microscopy [150] or scanning electron microscopy (SEM) [181] can be used to distinguish between areas with different number of graphene layers (for graphene on silicon, see section 2.7.2 for details). This is shown in figure 2.21.

The determination of the layer number by atomic force microscopy (AFM) is not always accurate, for example, if the AFM is working in the tapping mode (see section 2.7.1 for details), the measured thickness strongly depends on the scan parameters like the strength of the tapping

---

[18] This holds for an excitation wavelength of 532 nm only (for dispersive behaviour of the 2D band see section 2.5.3).

of the AFM tip on the surface [182].

2.7 Thin film characterisation methods

In this section, an overview about the methods used for thin film characterisation is given. The details concerning the evaluation of the results are given in the respective section of part II. The used PYTHON scripts can be found in the appendix C.

2.7.1 Atomic force microscopy

Atomic force microscopy (AFM) is used to obtain information about the surface topography, in this thesis of the substrates which are used for the graphene synthesis, or of the graphene films themselves. The measurement principle is to move a tip with only a few atoms at the end over the surface of the sample. The tip-surface interaction is described by the LENNARD-JONES potential [118] which contains a superposition of the attractive VAN DER WAALS force and the PAULI repulsion and is given by

$$V(d) = 4\varepsilon\left[\left(\frac{\sigma}{d}\right)^{12} - \left(\frac{\sigma}{d}\right)^{6}\right], \tag{2.34}$$

where ε and σ are constant factors (ε is the depth of the potential well, σ is the equilibrium distance where the potential becomes zero).

In figure 2.22a the potential $V(d)$ is schematically shown as a function of the distance d between the tip and the sample. There are three modi in which the AFM can operate, contact mode, non-contact mode and an intermittent mode (tapping mode). In latter, the cantilever performs a driven oscillation with constant amplitude close the surface. This mode allows to obtain information about the surface of the sample on the microscopic scale. The cantilever vibrates and thus taps point after point of the sample which results in a surface topography image (x, y position value and the corresponding height z).

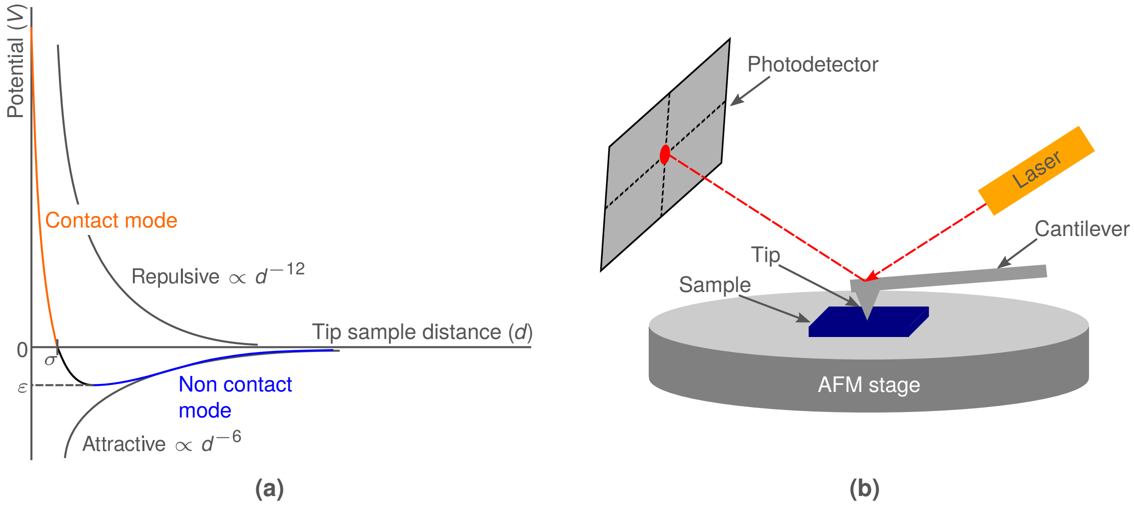

Fig. 2.22: (a) Sketch of the LENNARD-JONES potential and the different AFM operation modi. The potential is a sum of the repulsive potential which is proportional to d^{-12} and the attractive potential which is proportional to d^{-6}. (b) Schematic illustration of the AFM measurement setup. The laser is focused on the cantilever and reflected to the photodetector. During the scan this position is changing and yields information about the sample topography.((a) and (b) modified after [183]).

Figure 2.22b shows a sketch of the AFM setup. A laser which is focused on one end of the cantilever is reflected to a photodetector. For all three AFM modi, during the scan of the tip on the surface of a sample the cantilever is deflected and by that the position of the reflected laser beam on the photodetector depends on the z value at the scan position. This yields information of the surface topography of the sample. In tapping mode, the interaction between the surface and the tip changes the oscillation amplitude at a certain fixed resonance frequency. The information from an electrical control circuit which keeps this oscillation frequency nearly constant can now be used to extract a surface topography image of the scanned sample.

Figure 2.23 shows an AFM map of a graphene flake on a SiO_2/Si wafer after transfer from the Cu substrate and a 1D height distribution extracted from that map.

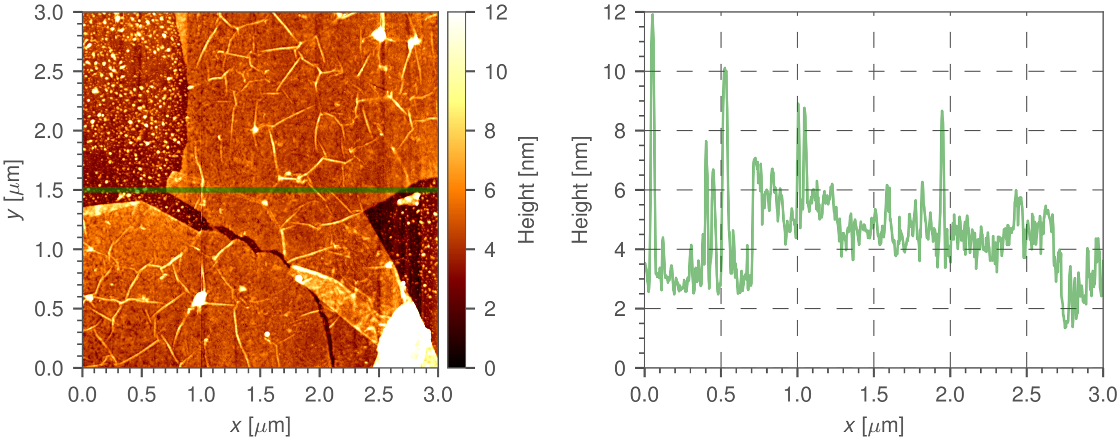

Fig. 2.23: An example showing a graphene flake after transfer from Cu to a SiO_2 substrate as an AFM map and a 1D line extracted from the values within the green bar.

The surface roughness is typically expressed as the root mean squared roughness (RMS). This can be calculated by

$$R_\mathrm{q} = \sqrt{\frac{1}{n}\sum_{i=1}^{n} |z_i - \bar{z}|^2}, \tag{2.35}$$

where n is the number of pixels, z_i the height value of the i-th pixel and $\bar{z} = \frac{1}{n}\sum_{i=1}^{n} z_i$ the arithmetical mean value of the surface height[19].

Almost all samples in this thesis were investigated with a large sample scanning atomic force microscope (Bruker Dimension ICON). Unless otherwise stated, all AFM measurements were performed in tapping mode.

2.7.2 Scanning electron microscope

In the scanning electron microscope (SEM) a focused beam of electrons with an energy between 0.1 and 50 keV is scanned over the sample which leads to interactions of the electrons with the. These interactions result in an emission of secondary electrons (SE), bremsstrahlung and characteristic X-ray radiation. Also some of the primary electrons will get backscattered (BSE). A schematic illustration of the SEM is shown in figure 2.24a.

---

[19] Note, the R_q value depends strongly on the size of the measured are. The roughness of a sample can be very small in a small area but high over a larger area and vise versa.

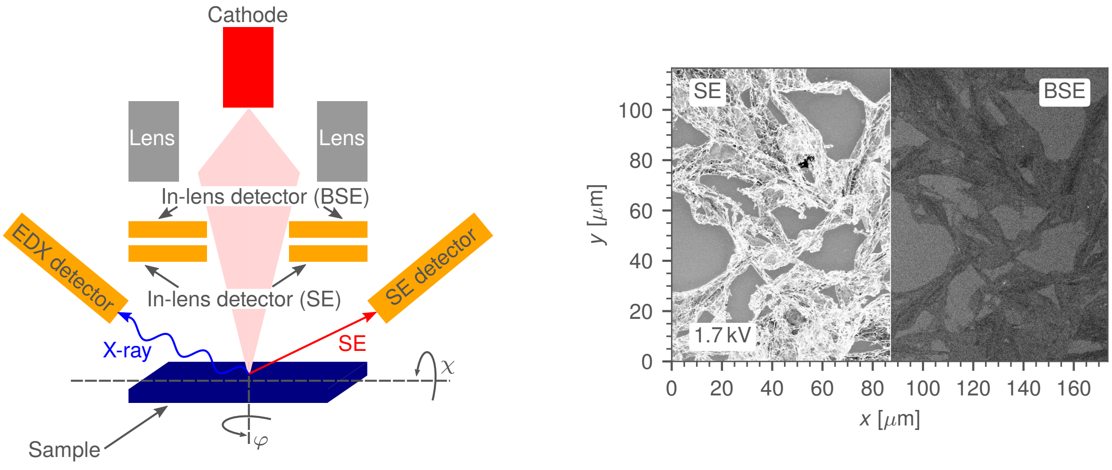

(a) **(b)**

Fig. 2.24: (a) Scheme of the SEM showing the position of the detectors. (b) Example showing an SEM image of rolled graphene on SiO_2/Si recorded with the SE detector (left) and the BSE detector (right). The dark regions are the graphene which has a lower electron backscatter yield than the SiO_2/Si. ((a) modified after [185]).

For imaging, typically the SEs are used. They have a comparable low energy in the range of 5 – 100 eV and therefore a limited escape depth out of the sample in the range of a few nm. Hence, they provide information about the surface topography. The SE are detected with a Everhart-Thornley detector [184] or an annular in-lens detector.

Moreover, the SEM can be used to distinguish regions covered with graphene from whose which are blank. This is done with a second annular in-lens detector which is sensitive to the BSE. To reduce the high yield from the SE, a negative voltage of a few hundred volts is applied to this detector. The backscatter yield of the electrons depends on the atomic number Z of the target atoms. Light atoms (low atomic number) have a lower backscatter yield than heavy atoms (high atomic number), thus they appear darker in an image obtained from backscattered electrons. This is demonstrated in figure 2.24b which shows a SEM image of a SiO_2/Si wafer with rolled graphene on top recorded with the SE detector (left) and the in-lens detector for the BSE (right). Because the carbon has a lower atomic number and therefore a lower backscatter yield than the SiO_2/Si, the graphene appears darker in this image. This imaging method can also be used to find graphene regions on Cu foils or Cu films which also appear darker compared to regions which are not covered with graphene. Note, that during SEM imaging carbon from the residual gas of the SEM chamber can lead to contamination of the graphene.

A detailed material analysis can be performed with energy dispersive X-ray spectroscopy (EDX). When electrons enter the sample they can scatter inelastically at atomic nuclei or electrons from the electron shell of the atoms which results in bremsstrahlung (continues X-ray spectrum). An incoming electron may knock out an electron from an inner shell of the target atom, leaving this atom in an excited state. This excitation relaxes very quickly by filling the hole in this inner electron shell by an outer electron, resulting in characteristic X-ray radiation (or Auger electrons). The energy of this radiation (or electron) is equal to the energy difference of the inner and the outer shell and therefore characteristic for each element.

In this thesis a Carl Zeiss Ultra 55 field emission SEM was used. The acceleration voltages used for the measurements are given in the respective SEM image.

2.7.3 X-ray diffraction

X-ray diffraction (XRD) was used to gain information about the crystal structure of the Cu-substrates used for the graphene synthesis. The measurement principle is based on the interference of the incident X-rays after they were scattered from the atoms in a crystal lattice. Constructive interference is given if the path distance for X-rays scattering from neighbouring atomic planes is $n\lambda$ with λ the wavelength of the X-rays and n as the diffraction order. In figure 2.25a it is shown that this path distance is $2d\sin(\theta)$ with d as the inter-planar spacing and θ the angle with respect to the sample surface. This can be summarised in the so called BRAGG equation

$$2d\sin(\theta) = n\lambda. \tag{2.36}$$

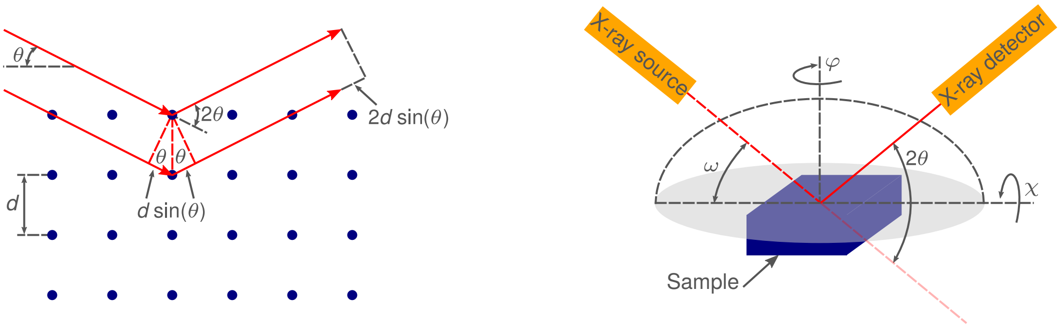

(a) (b)

Fig. 2.25: (a) Schematic illustration of the BRAGG equation in a crystal lattice. The inter-planar distance is d, the angle of the incident X-ray is θ. The path difference for the two different incident X-rays after scattering is $2d\sin(\theta)$, therefore, there will be a reflex of the order n if this path difference becomes $n\lambda$. (b) Goniometer geometry for XRD-measurements. ω is the angle between the incident X-ray and the sample surface, 2θ the angle between the incident X-ray and the detector. φ is the rotation angle around the sample normal. ((a) and (b) modified after [183, 186]).

Since $\sin(\theta)$ cannot exceed one, from equation (2.36) it follows

$$\lambda < 2d. \tag{2.37}$$

As the distance between crystal planes is normally of the order of 3 Å, λ cannot exceed about 6 Å for constructive interference to take place[20].

Equation (2.36) can be rewritten as

$$\lambda = 2\frac{d}{n}\sin(\theta). \tag{2.38}$$

With this equation, reflections of any order can be considered as reflections of first order from planes (real or fictious) spaced with distance $1/n$ of the previous spacing. This can be written as

$$2d_{hkl}\sin(\theta) = \lambda n \tag{2.39}$$

---

[20] Therefore, wavelengths in the X-ray regime are used for XRD.

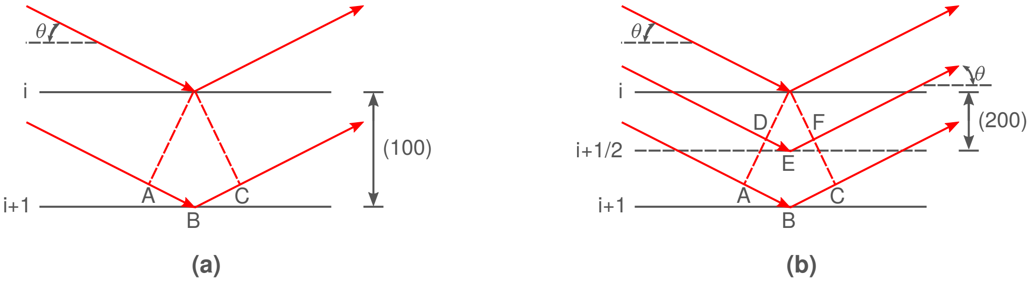

Fig. 2.26: Illustration of the equivalence of (a) a second order (100) reflection and (b) a first order (200) reflection (modified after [187]).

where d_{hkl} is the interplanar spacing and $h, k, l \in \mathbb{N}$ the Miller indices. The relation between the lattice parameter a of a cubic crystal and d_{hkl} is given by

$$d_{hkl} = \frac{a}{\sqrt{h^2 + k^2 + l^2}}, \tag{2.40}$$

whereas for a hexagonal crystal structure, the parameter a and c are related to d_{hkl} through

$$\frac{1}{d_{hkl}^2} = \frac{4}{3}\left(\frac{h^2 + hk + k^2}{a^2}\right) + \frac{l^2}{c^2}. \tag{2.41}$$

Figure 2.26 illustrates the usage of equation (2.39). In figure 2.26a, the second order reflection from the (100) plane is shown. Due to second order, the path difference (ABC) for the incident and reflected wave has to be 2λ for constructive interference. The two planes are labelled by i and $i + 1$. For a cubic lattice, due to equation (2.40), the lattice planes are separated by $d = a/\sqrt{(1^2 + 0^2 + 0^2)} = a$ (lines in figure 2.26a). If there were scatterers in the middle between the two planes (dotted line in figure 2.26b, this line would be occupied by atoms in the fcc and bcc lattice), the wavelength for the wave scattered at theses scatterers would be one wavelength out of phase with the scattered wave from the ith and $(i + 1)$th planes. Therefore, the ith, $(i + 1/2)$th and the $(i + 1)$th planes are positions which would satisfy equation (2.36) with $n = 2$. The lattice periodicity for the second order (100) reflection is $a/2$ and is indicated by d_{200}. Note that equation (2.40) yields $d_{200} = a/2$. Thus, the nth order diffraction from (hkl) with spacing $d = d_{hkl}/n$ can be considered as a first order diffraction from $(nh\,nk\,nl)$.

Figure 2.25b shows a sketch of the measuring geometry. Within this thesis, three measurement methods were used.

$2\theta - \omega$ scans were performed to determine the crystal structure of the substrate. Figure 2.27a shows an example. Within this type of measurement, the axes are moved so that the scattering angle of the X-rays is always 2θ. To determine the crystallite tilt distribution of the films, so called ω scans were performed (rocking curves). The FWHM of these curves gives information about the tilt of the crystallites. In this mode, the ω angle is scanned whereas 2θ is fixed corresponding to the selected Bragg reflection. To investigate the type of crystallinity (single crystal or poly-crystal) φ scans were performed by rotating the sample in plane at a fixed $2\theta - \omega$ position. For the case of Cu(111), in this measurement six peaks are observed for twinned Cu(111) crystals and only three peaks for a Cu(111) single crystal. Figure 2.27b shows an example of such measurement. A very detailed description of XRD measurements is given in reference [186].

Almost all samples in this thesis were investigated with an Ultima IV Type III (Rigaku Corp., Japan) diffractometer equipped with a Cu anode X-ray tube (Cu K_α radiation,

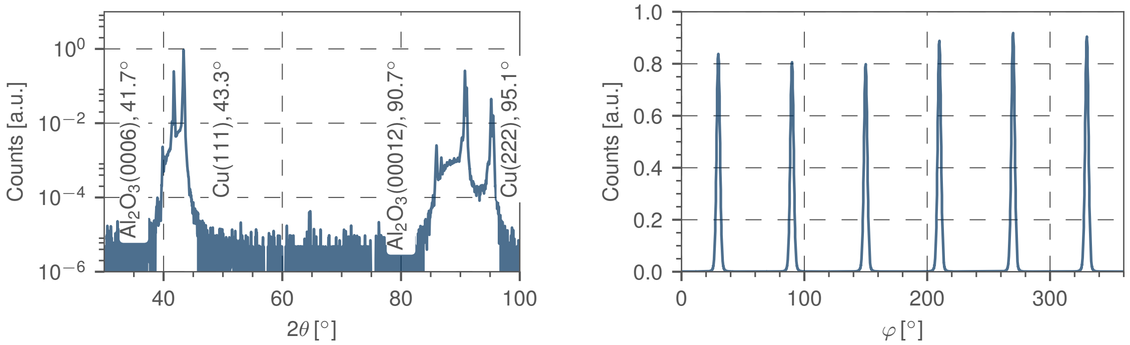

(a)

(b)

Fig. 2.27: (a)Example of a $2\theta-\omega$ scan of a Cu thin film showing Cu(111) orientation and reflexes from the Al_2O_3 substrate. (b) Example of a φ scan indicating twinning in the Cu film.

$\lambda = 0.15418\,\text{nm}$), a graded multilayer mirror to obtain a parallel beam, a theta-theta goniometer, a parallel slit analyser and a scintillation detector. With the used 0.05 mm slits the 2θ-resolution was 0.0084°. This diffractometer allows also a type of measurement called in-plane XRD (ipXRD) [188, 189].

2.7.4 X-ray photoelectron spectroscopy

The X-ray photoelectron spectroscopy (XPS) was used to obtain information about the chemical composition of the surface, e.g. etching residuals or other contaminations. The fundamental process is the photoelectric effect which describes the emission process of an electron from a surface due to photon absorption (X-rays in this case) with an energy $h \cdot f$. Due to the conservation of energy these emitted electrons have the kinetic energy

$$E_{\text{kin}} = h \cdot f - E_{\text{b}}^{\text{v}}(k). \tag{2.42}$$

Here, $E_{\text{b}}^{\text{v}}(k)$ is the binding energy (or ionisation potential) of an electron in the kth state with respect to the FERMI-level [190]. In practice, the specimen is electrically connected to the spectrometer in order to avoid charging effects and therefore a change of the potentials[21]. For metals, the FERMI energy is the energy of the highest occupied energy level [71, 72]. Starting from this assumption, the energy difference between the FERMI energy and the vacuum level is called the work function ϕ_{S}. A detailed energy diagram of a solid (metal in this case) connected to the spectrometer is given in figure 2.28a.

In general the vacuum level of the sample and the spectrometer are not equal which means that the released electron feels a retarding or accelerating potential $\phi_{\text{Spect}} - \phi_{\text{S}}$ where ϕ_{Spect} and ϕ_{S} are the work functions of the spectrometer and the sample. Consequently, the initial kinetic energy E'_{kin} of the electron released from the surface becomes E_{kin} in the spectrometer. Thus,

$$E_{\text{kin}} = E'_{\text{kin}} + \phi_{\text{S}} - \phi_{\text{Spect}}. \tag{2.43}$$

As shown in figure 2.28a for an identical FERMI energy of sample and spectrometer, it is

---

[21] Thus, the FERMI energy of the sample and the spectrometer are equal in thermodynamic equilibrium.

$$h \cdot f = E_{\mathrm{b}}^{\mathrm{F}}(k) + E_{\mathrm{kin}} + \phi_{\mathrm{Spect}}, \tag{2.44}$$

which gives the possibility to determine the element specific binding energy of an electron without knowing the work function of the sample. The ϕ_{Spect} is a term which can be obtained by calibration of the spectrometer.

Figure 2.28b shows a measurement example of a SiO_2/Si wafer. The background is due to inelastic scattering (electron-phonon or electron-electron scattering) within the sample. The exact composition (binding types) for each element within a chemical compound can be obtained by fitting the peaks with multiple (one for each element) VOIGT-functions [190].

With the used XPS system it is also possible to use argon ions to sputter the first layer of the specimen, in order to remove oxides or other contaminations before measuring the final XPS spectrum.

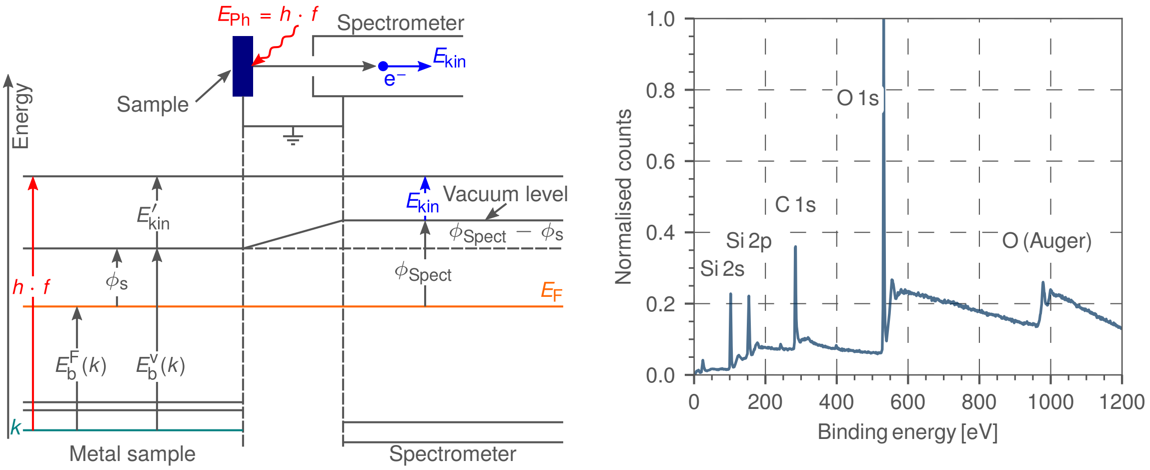

(a) **(b)**

Fig. 2.28: (a) Energy level diagram for a conductive sample (metal) in equilibrium with the spectrometer. For semiconductors or insulators the FERMI-energy would lie somewhere within the band gap of the material. (b) A measurement example of a SiO_2/Si wafer. ((a) modified after [190]).

Part II

Graphene synthesis by ion implantation and subsequent transfer

Chapter 3

Characterisation of Cu templates for graphene synthesis

In this part, the results of the characterisation of the Cu templates used for the synthesis of graphene will be presented. First, the properties of the Cu foils used is described, whereas in the second part, the results on fabricated Cu thin films are presented.

The pre-treatment of the templates covered in this chapter includes all steps before the ion implantation process, i.e. step (a) in figure 2.1 and (a) and (b) in figure 2.2.

3.1 Cu foil pre-treatment and characterisation

The used Cu foils with 50 μm thickness and a purity of 99.9999% were purchased from the company Alfa Aesar. At the beginning, foils with 25 μm thickness and 99.98% purity were also examined, but due to contamination (mainly carbon contamination) and handling issues, only the pure and thicker foils were used in the following.

3.1.1 SEM/AFM surface characterisation

In order to determine the surface roughness and grain sizes, SEM and AFM measurements were performed. Before annealing, the foils show a very rough surface containing scratches as shown in figure 3.1a and 3.1b. The observed scratches originate probably from the fabrication process. After an annealing step at 950 °C for 2 h in vacuum, a smoother surface with larger grains, as shown in figure 3.1c and 3.1d, was obtained. The largest grains are several hundred micrometre in diameter (see section 4.1.3) which is in agreement with results of annealed Cu foils in the literature [132]. The vacuum during the whole heating process was in the range of 10^{-7} mbar. For the pre-annealing steps, the oven described in section 2.4 was used.

As visible in figure 3.1d, the grain surfaces are not flat, but curved on a large scale forming a kind of 3D-surface. Therefore, the RMS roughness values were not determined over the whole AFM scan area, but on the grains themselves. The RMS values are $R_\mathrm{q} = 10.3(1)$ nm, $R_\mathrm{q} = 11.4(3)$ nm and $R_\mathrm{q} = 10.2(6)$ nm for the red, green and blue area in figure 3.1d, respectively.

Raman spectroscopy measurements were performed directly after the annealing step to check for residual carbon contamination. The excitation wavelength was 473 nm, the laser power was 1 mW on the sample. Within an area of $400 \times 400\,\mu\mathrm{m}^2$ 25 spectra were measured. The spectra are plotted in figure 3.2b showing no carbon on the surface after annealing. Note, this is in contrast to the literature in which Cu foils with a purity of only 99.98 % were used [39] which may contain residual carbon originating from the production process. The Cu foils used here

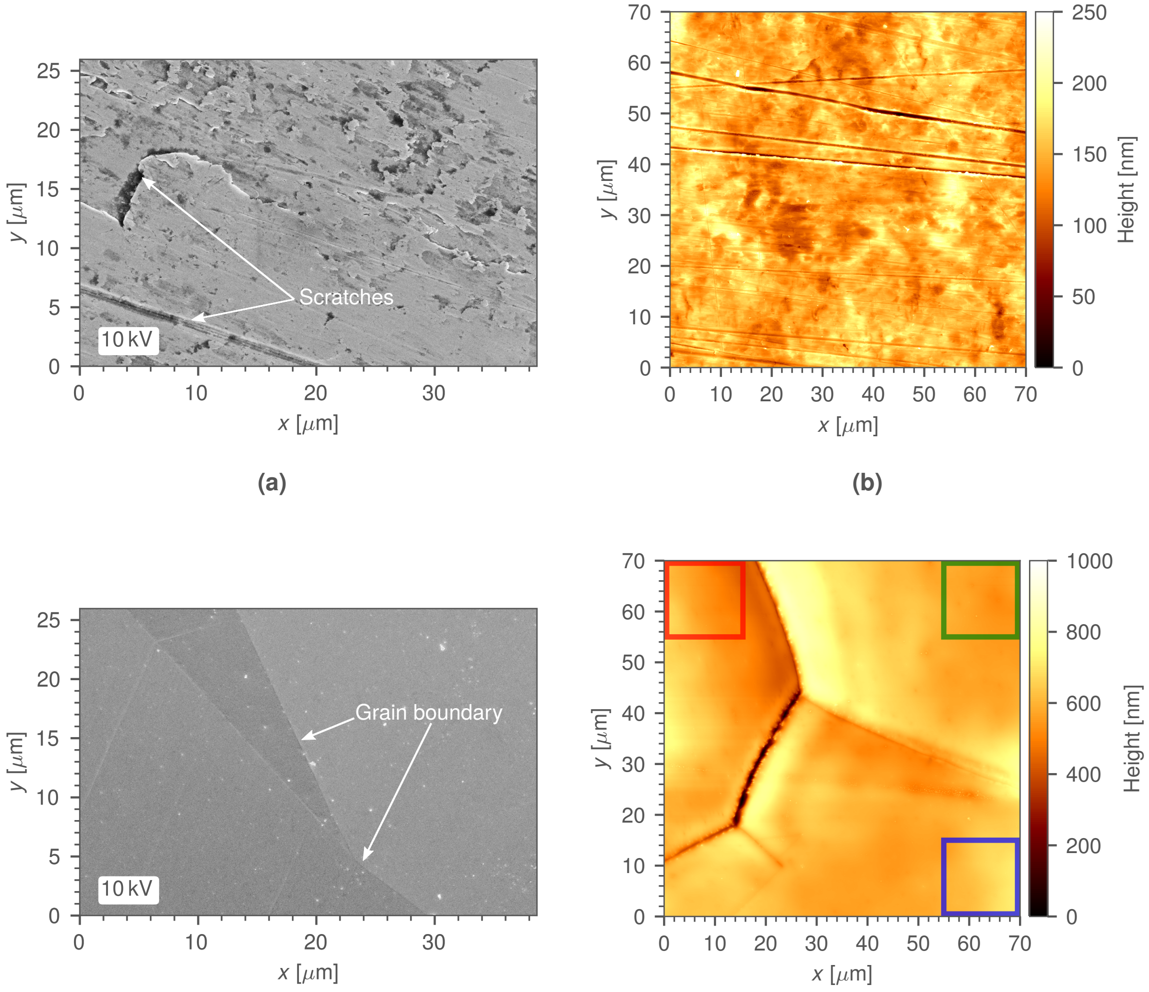

(a) (b) (c) (d)

Fig. 3.1: SEM and AFM images of (a,b) a Cu foil before annealing (as-received) and (c,d) after annealing at 950 °C for 2 h in vacuum. The RMS roughness values were determined on the Cu grains after annealing within the denoted areas in figure (d) [111].

are substantially cleaner. Moreover, no additional carbon contamination from the oven used for the heat treatment could be detected.

3.1.2 Crystalline properties of the Cu foils

In order to investigate the crystal structure of the Cu foils before and after annealing, XRD measurements were performed. The crystal orientation of the substrate which will be used for the synthesis of graphene is important due to the different lattice mismatches of the graphene and the underlying substrate which is, e.g. 19.9 % for Cu(200)/graphene and 3.8 % for Cu(111)/graphene [41–44, 111].

Figure 3.3 shows $2\theta/\omega$ scans for a Cu foil before and after annealing at 950 °C for 2 h in vacuum. The spectrum of the as received foil (figure 3.3a) shows four peaks at $2\theta = 43.3\,°$, $50.4\,°$, $74.2\,°$ and $90.1\,°$ which correspond to Cu(111), Cu(200), Cu(220) and Cu(311) orientations, respectively [111]. After annealing, the orientations Cu(111) and Cu(311) have vanished. The orientation Cu(220) is still observed, however the preferred orientation after annealing is Cu(200)

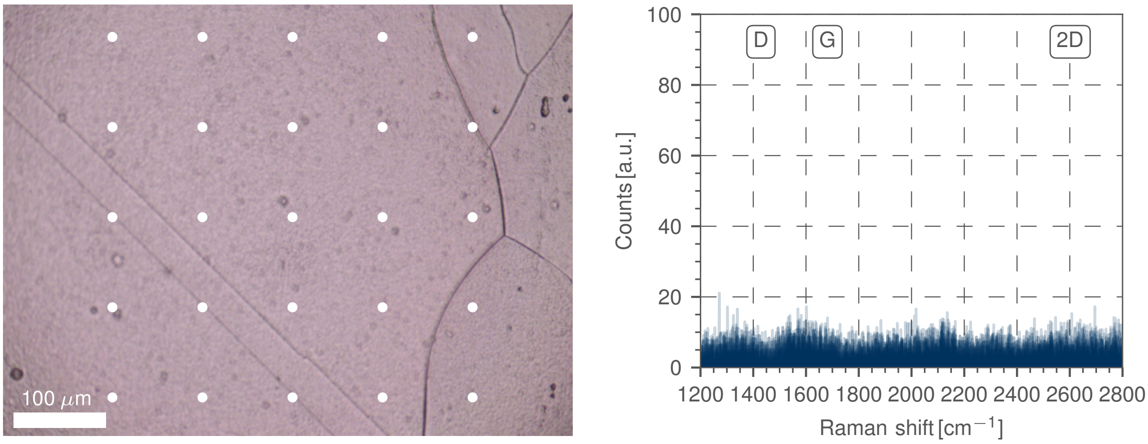

(a) (b)

Fig. 3.2: Surface characterisation by RAMAN spectroscopy on the Cu foil after annealing at 950 °C for 2 h in vacuum. (a) Optical microscope image of the foil. (b) Baseline corrected RAMAN spectra taken from the positions on the foil indicated in figure (a).

in agreement with the literature [191]. This change of the crystalline property originates from recrystallisation processes in the foil during the heat treatment. The FWHM of the Cu(200) peak decreases from 0.31(2) ° to 0.23(7) ° which indicates an increase in the crystalline quality due to the annealing step.

The peaks indicated by (▼) at $2\theta = 45.3\,°$ and (★) at $2\theta = 48.3\,°$ are due to the tungsten L_α X-ray radiation ($\lambda = 0.14764$ nm) and the W K_β X-ray radiation ($\lambda = 0.13926$ nm), respectively[1].

3.2 Cu(111) films deposited at room temperature, pretreatment and characterisation

In order to increase the quality of the graphene films by reducing the lattice mismatch, Cu(111) films were prepared. In order to obtain a Cu(111) crystal orientation, c-plane $Al_2O_3(0001)$ substrates were used [43, 44]. The size of the substrates was 1 cm × 1 cm, all depositions were performed at room temperature (depositions at high temperature are discussed in section 3.3). The substrate was cleaned prior deposition by ultrasonic cleaning with isopropanol followed by rinsing with with purified water.

Cu films with a thickness of 200 nm were prepared by magnetron sputtering using a DC-magnetron with a diameter of 6 inch and a Cu target with 99.999 % purity. The pressure during deposition was $\approx 8 \times 10^{-3}$ mbar (base pressure in the system $\approx 1 \times 10^{-6}$ mbar).

Cu films with a thickness of 450 nm were prepared by ion beam sputter deposition from a Cu target with 99.5 % purity. For this purpose, Ar^+ ions of 900 eV energy were employed with an angle of incidence of $\approx 60\,°$ with respect to the surface normal of the Cu target. The duration of the sputtering process was approximately 70 min. The pressure during deposition was $\approx 1.4 \times 10^{-4}$ mbar (base pressure in the system $\approx 1 \times 10^{-7}$ mbar).

The 200 nm films were annealed in vacuum ($\approx 5 \cdot 10^{-7}$ mbar) at 300 °C, 500 °C, 700 °C, 750 °C, 800 °C, 850 °C, 900 °C for 1 h, respectively, whereas the 450 nm films were annealed at 1020 °C for 20 min [192]. For these annealing steps, the oven described in section 2.4 was used.

---

[1] E.g. according to equation (2.39) and (2.40) the (200) reflex occurs at $2\theta = 45.37\,°$ for the CuK_β wavelength $\lambda = 0.13926$ nm and the lattice parameter for Cu $a = 0.361$ nm.

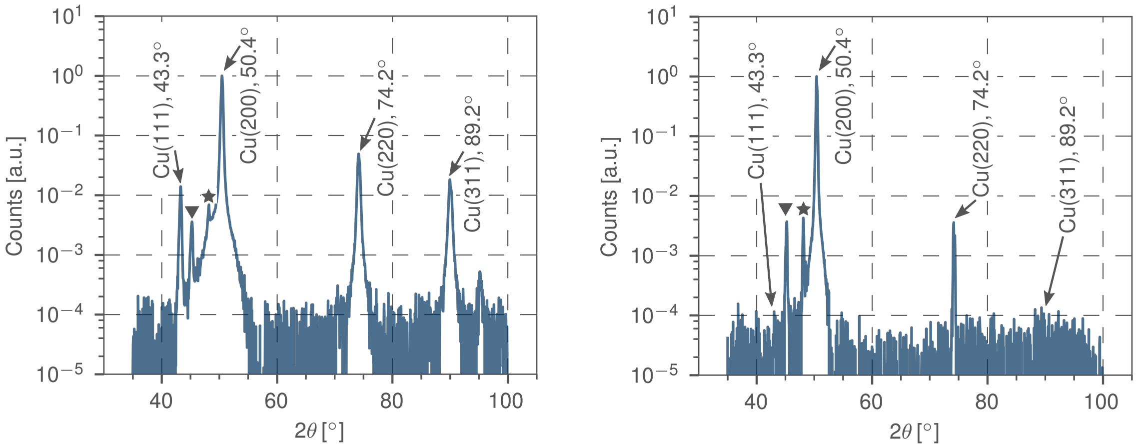

(a) (b)

Fig. 3.3: XRD spectra of (a) a Cu foil before annealing (as received) and (b) after annealing at 950 °C for 2 h in vacuum. The preferred crystal orientation after annealing is Cu(200) [111].

The main reason for the increased film thickness and the shorter annealing time at the highest temperature is that the Cu diffuses into the sapphire substrate (see section 3.2.2). In addition, a part of the Cu evaporates as 1020 °C is close to the melting point of 1083 °C of Cu. This evaporation can be reduced by formation of a carbon film on the surface during the annealing process due to segregation (see section 4.1.2).

3.2.1 SEM/AFM surface characterisation

Prior thermal treatment, the Cu films show small grain sizes as shown in figure 3.4a and 3.4b. To evaluate the grain size of the films, the height values from the AFM image were extracted from the area indicated by the green bar in figure 3.4b (40 lines), averaged and the resulting curve smoothed by a Savitzky-Golay-filter [193], in order to remove contributions from noise. The result is shown in figure 3.4c. The yellow crosses indicate the valleys determined automatically by the python-script given in appendix C.2. The difference between two neighbouring valleys corresponds to the size of the respective grain.

This procedure is repeated for the whole AFM image in vertical and horizontal direction. The size distribution is shown in figure 3.4d. The average grain size is around 38 nm. The difference in vertical and horizontal direction is due to the scanning direction of the AFM, which was horizontal in this case.

In figure 3.5a a SEM image is shown after an annealing at 300 °C for 1 h in vacuum. It can be seen that a few grains were removed from the surface due to the heat treatment. Figure 3.5b shows the surface after 700 °C for the same time showing an increase of the grain size. The grain boundaries are now more difficult to recognise due to the smoothed surface. In contrast to the Cu foils, here the grains are not forming a “3D-surface” which yields a lower contrast for the films in SEM imaging. Note that the Cu films are not single crystalline, which will be discussed in more detail in section 3.2.3. After an annealing at 800 °C for 1 h, etch holes appear on the surface as shown in figure 3.5c. These holes are of hexagonal shape due to the Cu(111) crystal orientation (see section 3.2.3). The size of these holes increases with annealing time and with increasing temperature. Below 800 °C no such holes were observed[2]. The depth of these etch

---

[2] Note that this temperature would not be high enough for the graphene growth as shown in section 4.2.1.

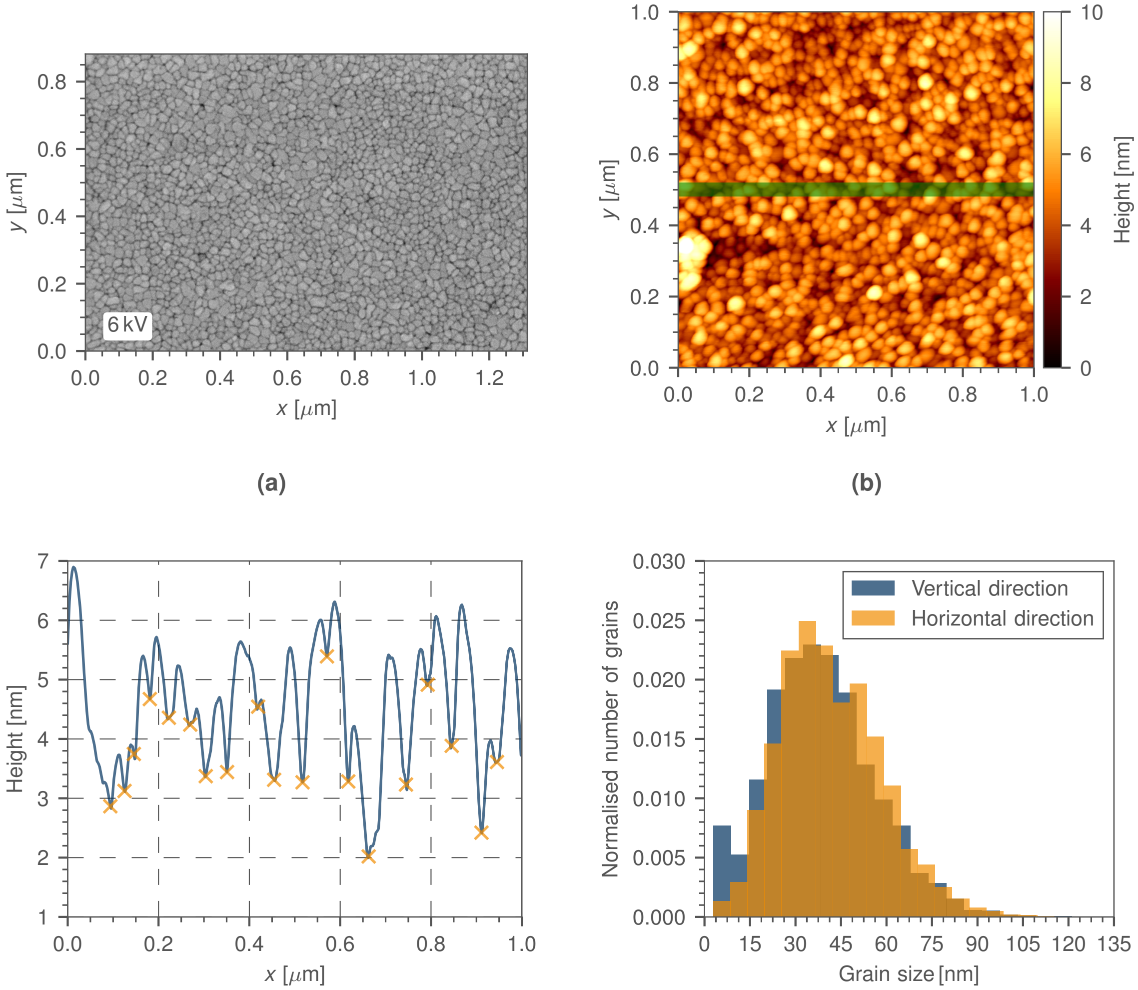

(a) (b)

(c) (d)

Fig. 3.4: Surface characterisation of the Cu(111) thin films before annealing. (a) SEM image and (b) AFM measurement showing a smooth surface with small grains. (c) Averaged line plot from the area indicated by the green bar in (b). (d) Grain size distribution of the whole image (b) determined by a peak find procedure (see text for details).

holes are given by the thickness of the Cu film. AFM measurements as shown in figure 3.5d which indicate a hole depth of 200 nm for a 200 nm thick Cu film confirm this observation also for the films with 450 nm thickness [192].

Figure 3.6 shows the RMS roughness values R_q of the Cu films after the different annealing steps. The large roughness values (within the area of $50 \times 50\,\mu\mathrm{m}^2$, blue curve) for temperatures above 800 °C originate from the presence of etch holes [192]. In order to compare the values with those of the Cu foils which were discussed in section 3.1.1, the R_q values were also determined in regions without etch holes, but of the same area as for the foils ($15 \times 15\,\mu\mathrm{m}^2$). As can be seen by the orange curve in figure 3.6, the values are increased for high temperature annealing, but compared to the foils, the Cu films are clearly smoother.

The typical temperature for graphene growth is around 1000 °C [84]. It turned out, however, that the Cu films annealed at temperatures above 800 °C were getting more and more transparent with increasing temperature and annealing time contrary to what is expected for a metallic film. Examples are shown in figure 3.7. To avoid this, the annealing at these high temperatures relevant for the synthesis of graphene was performed only for 20 min. Furthermore, the thickness

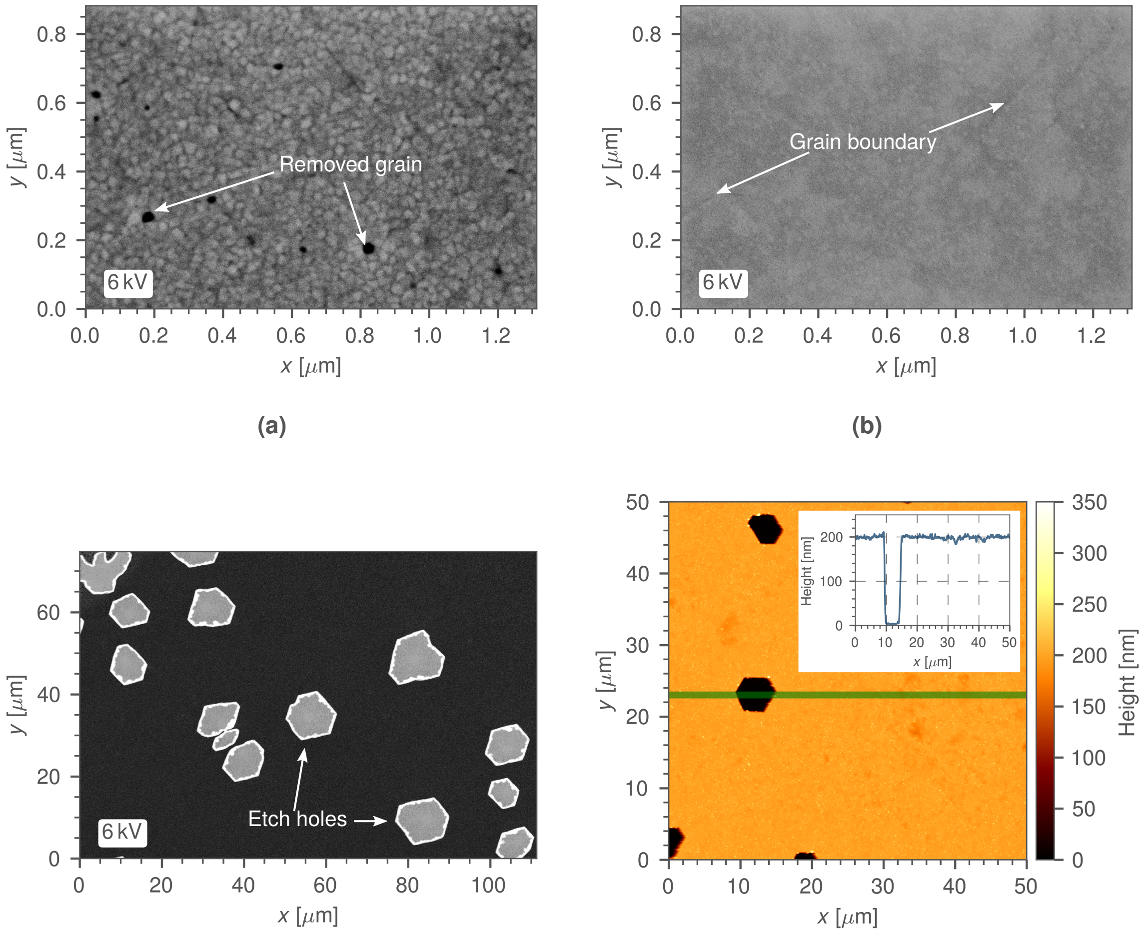

(a)

(b)

(c)

(d)

Fig. 3.5: SEM image of the Cu thin films after annealing at (a) 300 °C, (b) 700 °C and (c) 800 °C for 1 h in vacuum. At temperatures above 800 °C etch holes with hexagonal shape appear. The depth of these holes is given by the film thickness, as shown in (d) for a 200 nm thick Cu film [192].

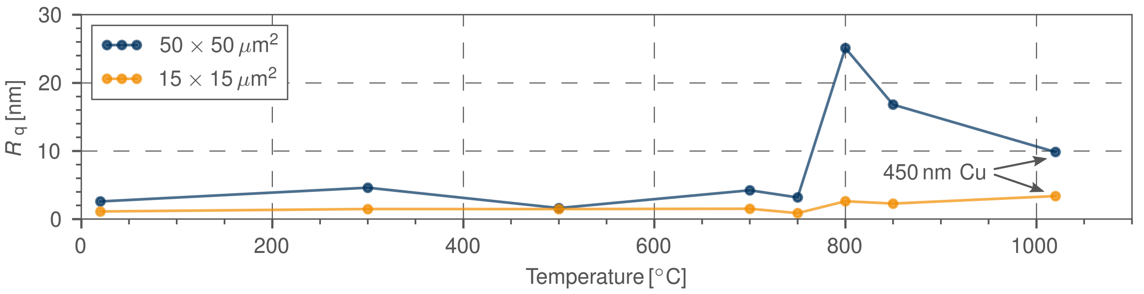

Fig. 3.6: RMS values of the Cu thin films after different annealing temperatures, 1 h in vacuum, respectively. The high values over the large area (blue curve) originates from the presence of etch holes. Within the smaller area (orange curve), the values are smaller compared to the Cu foils [192].

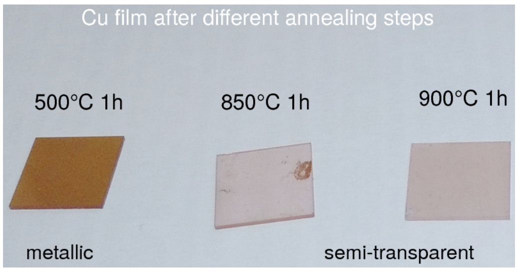

Fig. 3.7: Optical image of Cu thin films on sapphire after annealing at different temperatures. At temperatures above 800 °C the sample becomes transparent.

of the Cu film was increased from 200 nm to 450 nm. Note that films thicker than 450 nm were not sufficiently stable due to increased tensile stress.

To investigate what happens to the Cu films at these high temperatures RBS measurements were performed (see section 2.2.2) revealing diffusion of the Cu into the sapphire substrate. This will be discussed in the next section.

3.2.2 Diffusion of Cu into sapphire substrate

For the study of the composition of the Cu films and the interdiffusion of Cu film and Al_2O_3 substrate, RBS was employed using a 2.07 MeV He^+ ion beam with a diameter of ≈ 0.8 mm [3]. The film composition was determined from RBS data using the software XRUMP [129].

Figure 3.8a shows the measured spectra after different annealing steps up to 850 °C for an annealing time of 1 h (20 °C means not annealed). It can be seen that the thickness of the film slightly decreases (the area of the Cu film signal decreases, see section 2.2.2 equation (2.12)). Figure 3.8b shows a zoomed region between channel 200 and 700. For annealing temperatures below 750 °C, the RBS spectra show a pure Cu film and no interdiffusion of Cu film and sapphire substrate.

For the sample annealed at 750 °C a slight interdiffusion is noticably (magenta curve). A new phase between the Al_2O_3 substrate and the Cu film is created by interdiffusion. For temperatures up to 850 °C one still recognises a film of well-defined thickness on top of the sapphire substrate as schematically shown in figure 3.8c. This changes completely when the temperature is increased to 900 °C (see figure 3.8d). No separation between the original film and the substrate can be observed anymore [192].

The determined film composition after the different annealing steps is shown in table 3.1. Due to the low sensitivity of RBS for light elements like carbon, as explained in section 2.2.2, the carbon content could not be measured.

3.2.3 Crystalline properties

XRD measurements

In order to verify the Cu(111) crystal orientation and to determine the crystal quality, XRD measurements were performed for every annealing step.

Figure 3.9a shows an overview $2\theta - \omega$ scan directly after the sputtering of the Cu onto the Al_2O_3 substrate (200 nm Cu, no annealing). Only the Cu(111) crystal orientation was observed. The peaks indicated by (▼) at $2\theta = 38.9\,°$, (★) at $2\theta = 39.8\,°$ and (●) at $2\theta = 41.4\,°$ are originating from the Cu K_β X-ray radiation ($\lambda = 0.13926$ nm) for the Cu(111) orientation, the

---

[3] These experiments were performed at the LIPSION facility of the Group of Nuclear Solid State Physics at the University Leipzig.

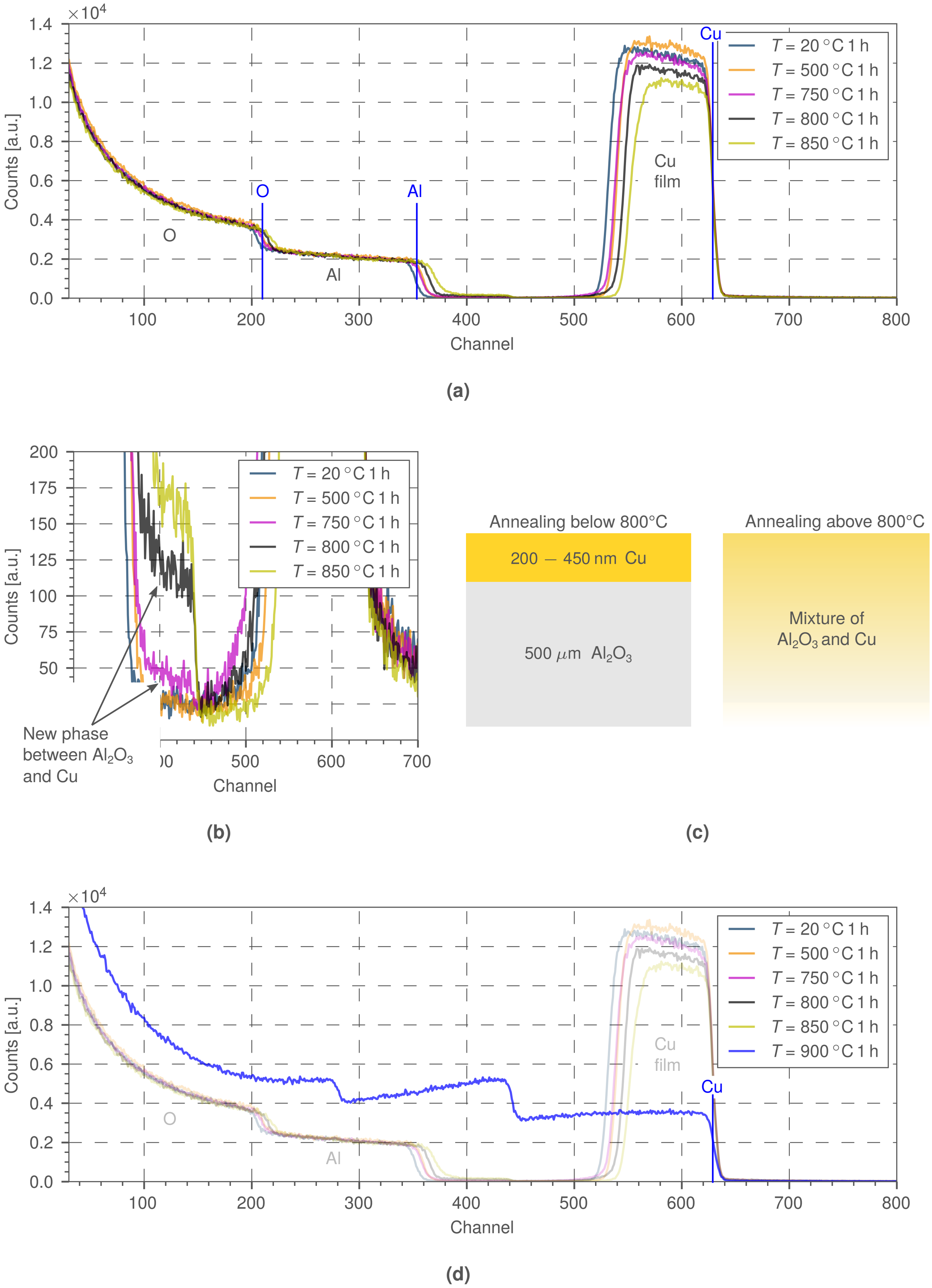

(a)

(b)

(c)

(d)

Fig. 3.8: RBS measurements for the investigation of the interdiffusion of Cu film and Al_2O_3 substrate. (a) RBS spectra for annealing temperatures up to 850 °C. The Cu film is separated from the substrate. (b) Zoom between channel 200 and 700 in (a) revealing a new phase between Cu film and substrate at temperatures above 750 °C. (c) showing schematically the diffusion process. (d) RBS spectrum after 900 °C annealing showing full diffusion of the Cu into the substrate [192].

Temp [°C]	Cu	Al	O
20	1	0	0
500	1	0	0
750	0.985	0.006	0.009
800	0.911	0.036	0.054
850	0.854	0.052	0.094
900	0.115	0.365	0.52

Table 3.1: Elemental composition in atomic fraction of the Cu film after thermal annealing for 1 h obtained from XRUMP analysis of the RBS spectra. The annealing temperatures are given in the left column [192].

W L_α X-ray radiation ($\lambda = 0.14764\,\text{nm}$) for the $Al_2O_3(0006)$ orientation and the W L_α X-ray radiation for the Cu(111) orientation, respectively. The peaks at angles above 80 ° are due to the reflection of second order.

Figure 3.9b and 3.9c show a high resolution $2\theta - \omega$ scan for the Cu(111) reflex after annealing at 300 °C and 800 °C for 1 h, respectively. The peaks each consist of two separate peaks due to the Cu K_{α_1} and K_{α_2} X-ray radiation. Therefore, the peaks were fitted by two VOIGT functions. For the sample, annealed at 300 °C the FWHM of the individual peaks is too large for a clear separation. This changes after annealing at temperatures above 800 °C. The shape of the peak now more clearly represents the shape of the substrate reflection.

For all annealing steps, the FWHM and the peak position for the Cu(111) reflection due to the Cu K_{α_1} wavelength are shown in figure 3.9d. The FWHM decreases with increasing annealing temperature which indicates an improvement of the crystal quality [187]. The position stays nearly constant for annealing steps below 850 °C. After annealing at 900 °C it shifts to $2\theta = 43.31\,°$ which is closer to the theoretical value of 43.32 °[4]. Note that it was still possible to obtain Cu(111) XRD reflexes although the sample appeared transparent after annealing.

The XRD spectrum of the sample with 450 nm Cu film thickness annealed at 1020 °C for 20 min is shown in figure 3.10. The position of $2\theta = 43.37\,°$ is not shifted as much as for the annealing step at 900 °C, mainly because of the shorter annealing time. The FWHM is comparable with the one observed for the samples annealed at 850 °C for 1 h.

In order to study fact whether the films are single crystalline after a certain annealing step XRD-ϕ scans were performed (see section 2.7.3). The azimuthal XRD scans of the Cu $\{111\}$ planes shown exemplarily for three samples in figure 3.11a, reveal a peak separation of 60 ° which indicates twinning of the Cu(111) crystals [44, 194]. For all annealing treatments studied here, six peaks were observed in these scans demonstrating that no single-crystalline Cu(111) crystal was obtained. Note that in the literature, a route for the production of single-crystalline Cu(111) films is discussed [44, 194], however the results could not be verified in our study.

To investigate the tilt of the grains with respect to each other, XRD-rocking curves were recorded. They were fitted and the FWHM, a measure for the amount of tilt was determined. The results are shown in figure 3.11b. The FWHM decreases with increasing temperature up to 700 °C. Then it remains nearly constant up to 850 °C and decreases further for the temperature of 900 °C. The value for the 450 nm film is a little higher after 1020 °C anneal for 20 min, which might again be due to the shorter annealing time. Note that the error bars for the fit parameter of the FWHM are smaller than the plot symbols.

---

[4] Which can be calculated by equation (2.40) with lattice parameter $a = 0.361\,\text{nm}$ and a K_{α_1} wavelength of 1.540562 nm.

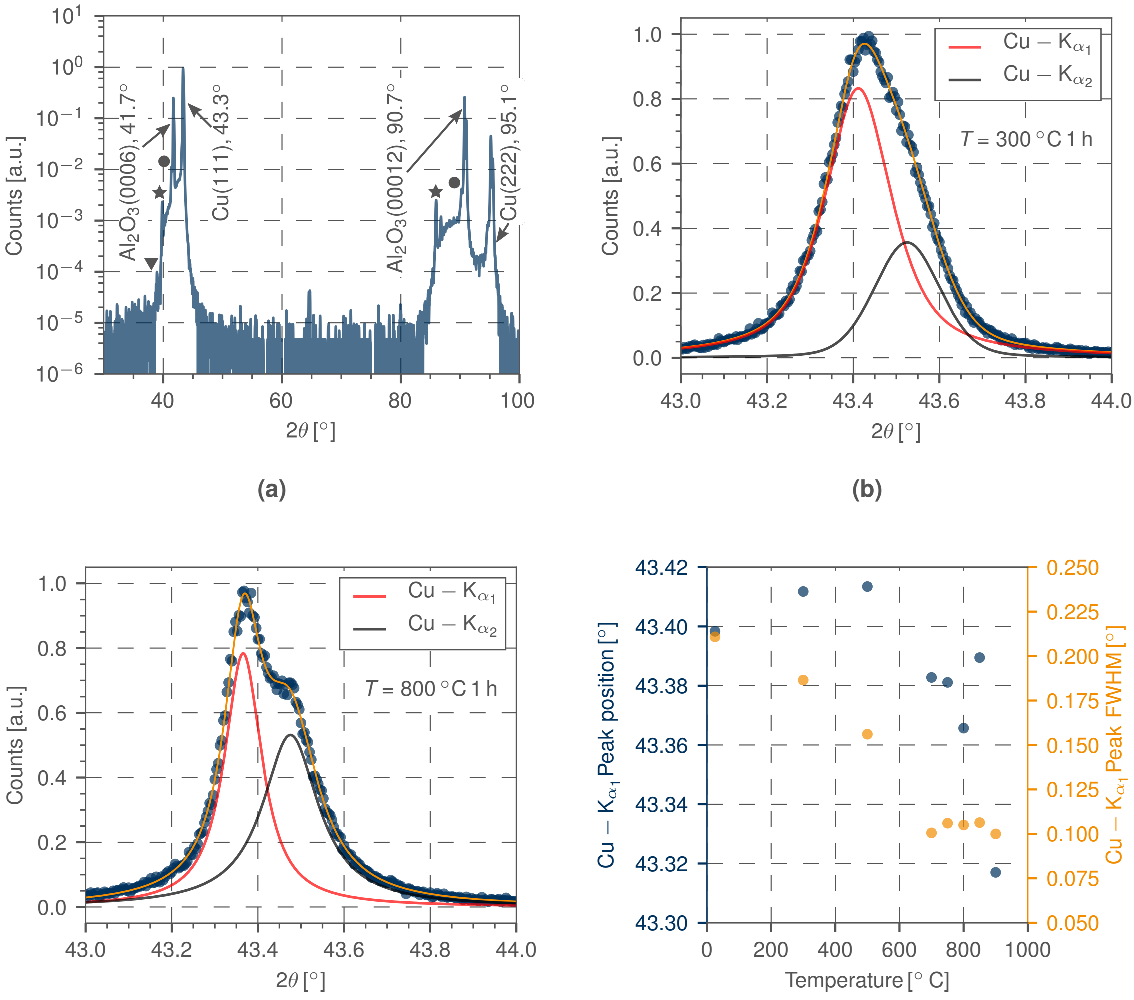

(a) **(b)**

(c) **(d)**

Fig. 3.9: XRD measurements for the different annealing steps of the 200 nm Cu films. (a) An overview $2\theta-\omega$ scan showing only Cu(111) reflexes (and reflexes from the substrate). (b) A high resolution scan of the Cu(111) reflex after annealing at 300 °C and (c) at 800 °C for 1 h, respectively. (d) Scatter plot for the peak position and FWHM after the different annealing steps [192].

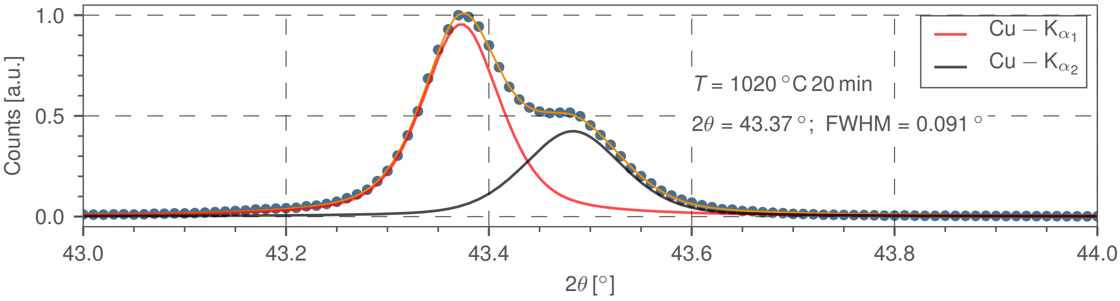

Fig. 3.10: High resolution scan of the Cu(111) reflex of the 450 nm Cu film after annealing at 1020 °C for 20 min.

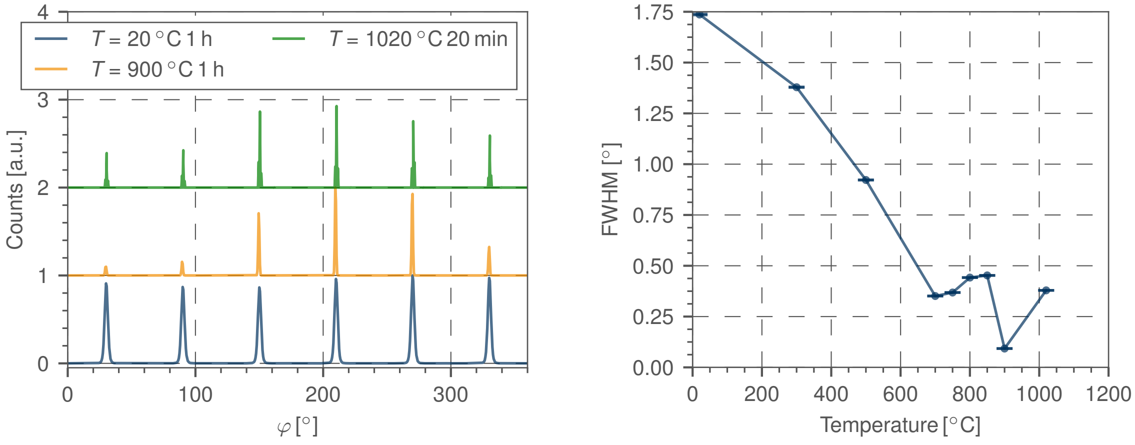

(a) **(b)**

Fig. 3.11: (a) Azimuthal XRD scans of the {111} planes showing twinning of the Cu(111) crystals and (b) FWHM of the rocking curves for the Cu(111) peak, the error bars for the fit parameter of the FWHM are smaller than the plot symbols [192].

RBS-channeling

For further investigation of the crystalline properties of the Cu films, RBS-channeling measurements on a sample annealed at 700 °C for one hour were performed. Figure 3.12 shows the two RBS spectra collected for random ion incidence and for ion incidence into the ⟨111⟩ axis of the Cu (aligned orientation), respectively, as well as the ratio of aligned to random yield from which a normalised minimum yield $\chi_{\text{min}} = 0.33$ was calculated. The fact that ion channeling could be observed everywhere on the sample demonstrates that the whole film has the same Cu(111) orientation. The comparably high χ_{min} values can be assigned to the twinned Cu(111) crystals in the film and the presence of point defects in the Cu lattice [192].

3.2.4 Residual carbon removal and purification of Cu films

Raman spectroscopy

The surface of the Cu films was investigated by Raman spectroscopy in order to obtain information about the carbon contamination. The excitation wavelength was 473 nm in order to reduce the fluorescence of the Cu film. In contrast to the Cu foils used, the films show high carbon contamination. The carbon may originate mainly from the residual gas present in the sputtering process. The carbon segregates on the surface of the Cu film due to the low solubility of carbon in copper [195]. The detailed process will be described in section 4.1.2.

Figure 3.13 shows the results of the Raman spectroscopy measurements. In order to extract meaningful information about the carbon material formed on the surface, 625 spectra were recorded within an area of $50 \times 50\,\mu\text{m}^2$ on each Cu film. Due to fluorescence of the Cu film, every single spectrum was baseline corrected in order to obtain the correct intensity and intensity ratios of the peaks. After that, the intensities of the D- (1200–1400 cm^{-1}), G- (1500–1750 cm^{-1}) and 2D- (2600–2800 cm^{-1}) bands were integrated and averaged. The error bars are the standard deviation of the 625 individual intensities used for averaging. The result is shown in figure 3.13a [192].

The non-annealed sample shows no detectable carbon formation on the surface. After annealing within the 300 °C to 700 °C temperature range, Raman spectra were obtained which indicate the presence of amorphous carbon at the surface as shown exemplarily in figure 3.13b.

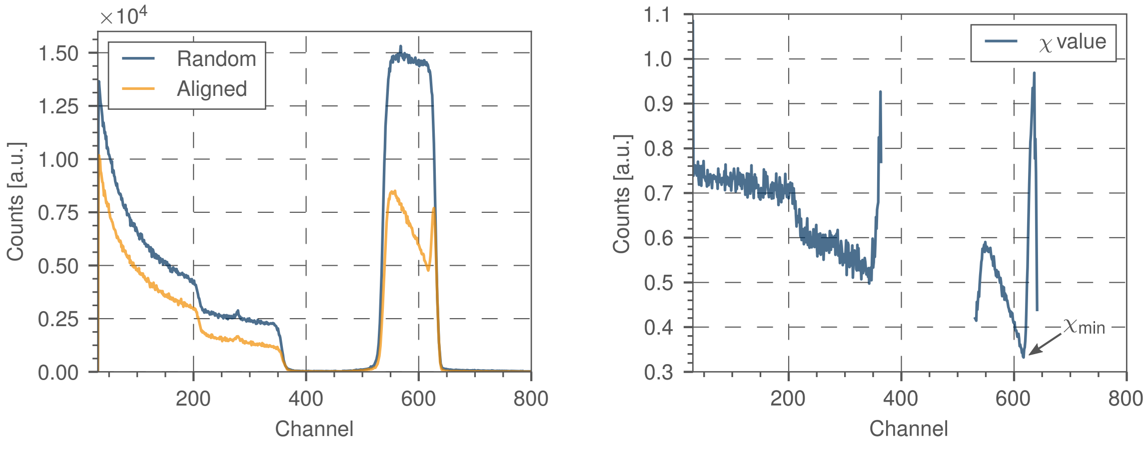

(a) (b)

Fig. 3.12: (a) RBS-channelling spectra for random and aligned ion incidence from a sample annealed at 700 °C for one hour and (b) ratio of the two spectra to obtain $\chi_{\mathrm{min}} = 0.33$. The surface peak arises from ion backscattering in the first monolayers of the Cu film where ion channeling is not yet established [192].

This carbon formation is probably a result of chemical reduction of surface adsorbates [192]. After the annealing step at 750 °C, no carbon is found at the surface (via RAMAN spectroscopy). It seems that the surface adsorbates are removed at this temperature leaving a clean surface. At the same time, carbon diffusion in the bulk of the Cu film has not yet started. This diffusion starts to become noticable at 800 °C allowing the carbon atoms from the bulk to move to the surface. Also at this temperature, a formation of graphite/graphene layers occurs which can be seen from the appearance of the 2D-peak, shown in figure 3.13c. For 1020 °C annealing temperature, the RAMAN spectrum resembles that of graphene of very low defect density, as shown in figure 3.13d [164, 166, 167]. Note, that no implantation of additional carbon was performed.

X-ray photoelectron spectroscopy

The surface was also characterised by XPS where an increase of the carbon content at the surface from 30 at.-% after the 300 °C anneal to 67 at.-% after the 700 °C anneal has been observed. In contrast to the RAMAN spectroscopy measurements, a carbon content of 56 at.-% was observed after the annealing step at 750 °C. Via XPS it was possible to determine the sp^2-content of the carbon for the high temperature annealing step at 1020 °C to 72.5%. For the lower temperatures, the sp^2-content could not be unambiguously determined.

Carbon removal by UV-ozone cleaning

In order to allow adjusting the layer number of graphene by the ion fluence, the template for the graphene synthesis should be carbon-free. Therefore, the residual carbon which is formed on the surface after the pre-annealing steps[5] has to be removed. For this purpose, UV-ozone cleaning was used.

In this process, a Xe_2^* excimer 172/630 Z lamp system was used [196], applying a VUV power of up to 30 mW cm^{-2} at a distance from the sample of 2 cm. The excimer lamp has a continuous emission in the VUV wavelength range from $\lambda = 160$ to 195 nm (photon energy

---

[5] Pre-annealing means prior the implantation process.

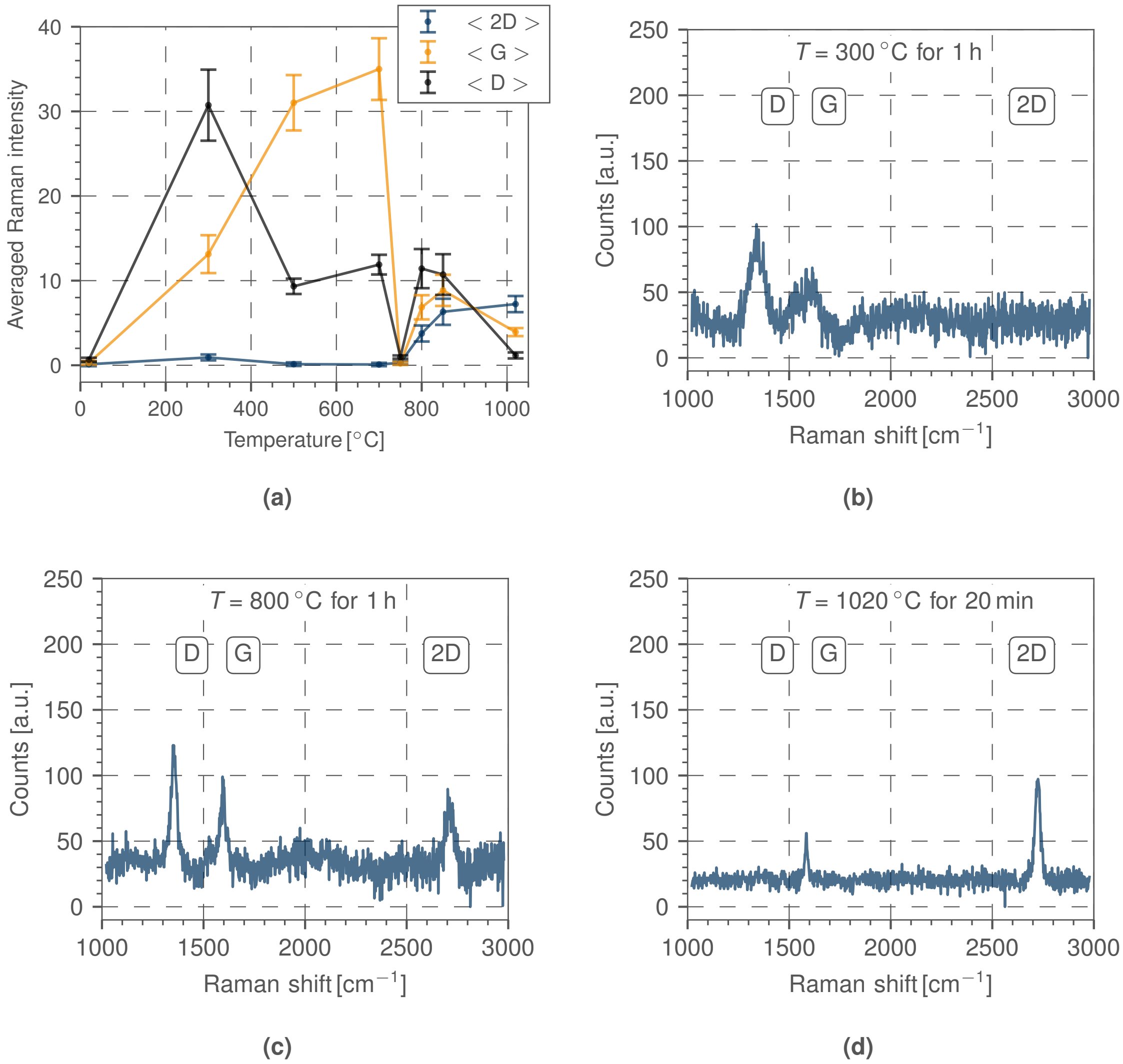

(a) (b) (c) (d)

Fig. 3.13: RAMAN spectroscopy on the surface of the Cu films after annealing at different temperatures. (a) RAMAN spectroscopy intensities for the D-, G-, and 2D-bands calculated from 625 spectra within an area of $50 \times 50\,\mu\mathrm{m}^2$ and (b) typical spectrum after annealing at 300 °C, (c) 800 °C and (d) 1020 °C [192].

$7.75\,\mathrm{eV} > E_{\mathrm{Ph}} > 6.36\,\mathrm{eV}$; $614\,\mathrm{kJ\,mol^{-1}} < \Delta E < 748\,\mathrm{kJ\,mol^{-1}}$)[6] with the maximum at 172 nm ($E_{\mathrm{Ph}} = 7.21\,\mathrm{eV}$; $696\,\mathrm{kJ\,mol^{-1}}$). The normalised emission spectrum of the used lamp is shown in figure 3.14a. Table 3.2 gives an overview on the chemical bond energies for different surface contaminations [197].

The irradiation was carried out in a chamber flushed with nitrogen containing 0.25 vol.-% oxygen to minimize VUV absorption by molecular oxygen and ozone formation on one hand [198] and maintain oxidative conditions on the other, as published for the conversion of perhydropolysilazane to silica [201].

A simplified schematic representation of the UV-ozone cleaning process is shown in figure 3.14b. Due to the irradiation, the oxygen molecules are dissociated and form oxygen radicals which themselves react with the surface of the sample. The oxygen molecules can also react with the radicals and form ozone which itself can be dissociated by the UV light forming again oxygen

---

[6] The energy E per mol of an electromagnetic wave with wavelength λ can be calculated by $E = Nhc/\lambda \cdot 10^5\,\mathrm{kJmol^{-1}}$ with N as the AVOGADRO constant, c the velocity of light and h the PLANCK constant.

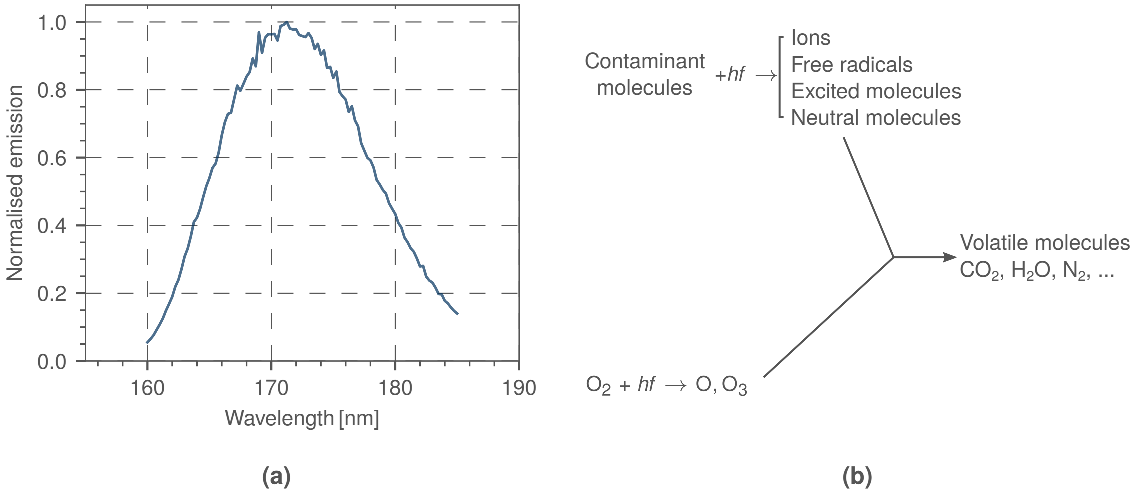

Fig. 3.14: (a) Normalised emission spectrum for the used Xe_2^* excimer lamp. (b) simplified schematic representation of the UV/ozone cleaning process. Data for (a) provided by L. Prager [198, 199], (b) modified after [200].

Bond	Bond energy (kJ/mol)	Bond	Bond energy (kJ/mol)
$O-O$	138.9	$C=C$	607
$O=O$	490.4	$C\equiv C$	828
$C-O$	351.5	$C=O$	724
$C-C$	347.7	$C-Cl$	328.4
$C-H$	413.4	$C-N$	291.6
$C-F$	441	$C\equiv N$	791

Table 3.2: Overview of the chemical bond energies [197].

radicals. The organic contaminants on the surface of the sample are also affected by the UV light (see table 3.2). Finally, due to chemical reactions, carbon dioxide and other volatile molecules are formed. A detailed study about the physical and chemical mechanisms of hydrocarbon removal by UV-ozone treatment can be found in reference [202].

The duration of the UV-treatment was 30 min for all samples which represents a radiant exposure of $33\,\mathrm{J\,cm^{-2}}$ at the sample height. During this process, the temperature of the sample increased to approximately 50 °C. After this UV ozone cleaning and an additional shorter annealing step at 1020 °C no carbon signal was observed on the surface of the 450 nm Cu film demonstrating the successful purification of the Cu film with regard to carbon contamination. Note that the Cu film seems to be protected from evaporation by the formation of this carbon layer on top. Therefore, the annealing steps after UV-cleaning and prior ion implantation were only carried out for several minutes in order to prevent the evaporation of the Cu film.

In summary, to obtain the possibility to adjust the number of layers (thickness) of the graphene films via the implanted carbon fluence, it is essential to remove the residual carbon. Therefore, the pre-annealing step and the UV-ozone cleaning prior ion implantation are necessary to purify the film. Furthermore, the crystal quality increases due to the annealing process, as described in section 3.2.3.

3.3 Cu(111) films deposited at high temperatures, pre-treatment and characterisation

For the Cu deposition at elevated temperatures, the heater stage described in section 2.3.1, was used. The working pressure during magnetron sputtering was the same as for the samples deposited at room temperature. The Al_2O_3 (c-plane) substrate was heated to the desired temperature with a slope of 50 °C per minute. Five minutes after the desired temperature was achieved, the sputter process was started. The film thickness has been set to 450 nm. Note that the measurement for the thickness is performed by a quartz crystal oscillator which is calibrated for measurements at room temperature.

3.3.1 Cu deposition at 450 °C

The first sample was deposited at a substrate temperature of 450 °C. The result is shown in figure 3.15. AFM measurement itself showed an incompletely covered surface (fig. 3.15a). The roughness on the grains is very small as shown in figure 3.15b. It was determined within the green surrounded area (the black areas are the substrate which appear black due to the small height range covered by the color bar) to $R_\mathrm{q} = 0.1(4)$ nm. XRD measurements revealed Cu(111) crystal orientation as shown in figure 3.15c. The FWHM of the Cu-K_{α_1} reflex was determined to 0.053 ° which is smaller than the values obtained for the annealed samples (see section 3.2.3). These values for the FWHM and the roughness R_q are much smaller than values in the literature reporting roughness values around 10 nm or more [194]. Figure 3.15d shows Raman spectra which do not show any carbon on the surface of the Cu grains. As described in section 3.2.4, this temperature is not sufficient in order to mobilise the carbon to move to the surface.

In order to mobilise the residual carbon during the sputtering process and therefore be able to remove this carbon without an additional annealing step (which is usually performed before the ion implantation), the temperature has to be increased. Note that Cu films deposited at temperatures below 650 °C do not show carbon on top of the surface (not shown here).

3.3.2 Cu deposition at 650 °C

The Cu deposition at a substrate temperature of 650 °C was done similar to the one at 450 °C. The results of optical microscopy and Raman spectroscopy are shown in figure 3.16.

As it can clearly be recognised from figure 3.16a, the amount of Cu which forms the film on the Al_2O_3 substrate is drastically decreased compared to the sample sputtered at 450 °C. Furthermore, the measured 2D-peak intensity map shown in figure 3.16b clearly indicates carbon on the surface of the small Cu grains. Figure 3.16c shows Raman spectra exported from the map. On the Cu grains, residual carbon forms a mixture of graphene/graphite. This carbon can be removed by UV ozoning as described in section 3.2.4, but it is obvious that with these Cu template, no large graphene domains can be produced.

3.4 Summary

In this chapter, the preparation of the templates for the graphene synthesis was described. The Cu foils were annealed at 950 °C for 2 h in vacuum. No residual carbon was found after the pre-annealing process. The crystal orientation was Cu(200) for all foils after annealing. The roughness on the grains was around 10 nm as determined by AFM. This pre-implantation procedure was applied to all foils used for the graphene synthesis.

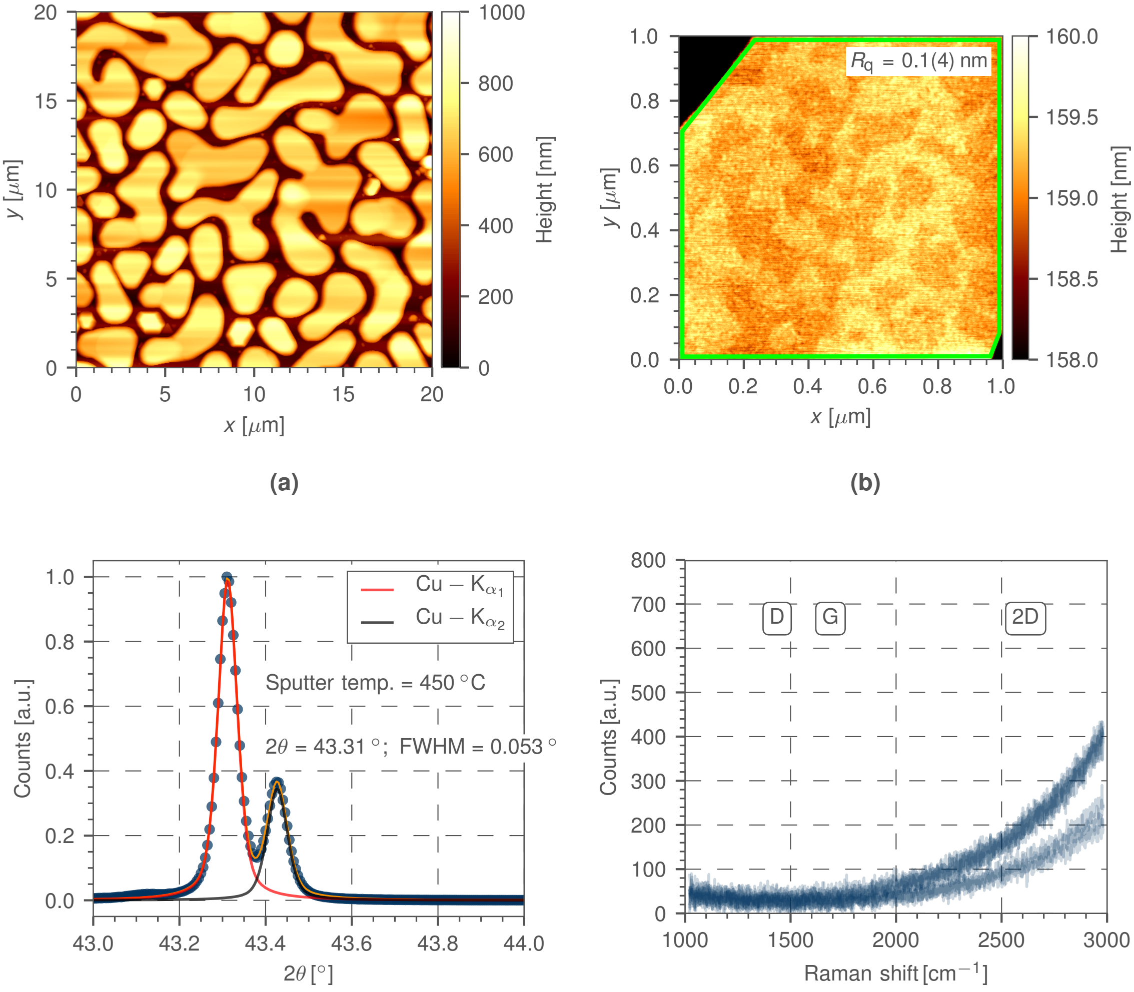

(a) (b)

(c) (d)

Fig. 3.15: Characterisation of Cu film, deposited by magnetron sputtering at 450 °C. (a) AFM image showing the incompletely coverage with Cu, (b) a zoomed scan area showing very smooth surface on the Cu grains, (c) XRD measurement which indicates Cu(111) orientation with high crystal quality and (d) RAMAN spectra indicating no carbon formation on the surface of the Cu grains.

The Cu thin films deposited at room temperature were annealed at different temperatures between 300 °C and 900 °C for 1 h each, and 1020 °C for 20 min in order to study the crystalline quality and the surface roughness. The Cu crystal orientation was found to be (111) for all Cu films. The surface roughness values were below 4 nm. At temperatures higher than 750 °C, diffusion of the Cu film into the sapphire substrate was observed and characterised via RBS. In addition, etch holes with hexagonal shape start to appear at this temperature. Because of the diffusion, the annealing time for the high temperatures was reduced to 20 min, and the thickness of the Cu film was increased to 450 nm. At annealing temperatures above 800 °C, the residual carbon inside the Cu film starts to segregate on the surface and forms graphite/graphene at the surface which can be removed by UV ozone treatment.

The Cu thin films deposited at temperatures between 450 °C and 600 °C show improved crystal quality and roughness compared to Cu films deposited at room temperature. They are even superior to the samples annealed at high temperature after Cu deposition at room temperature. Carbon segregation on the surface during the deposition procedure could only be

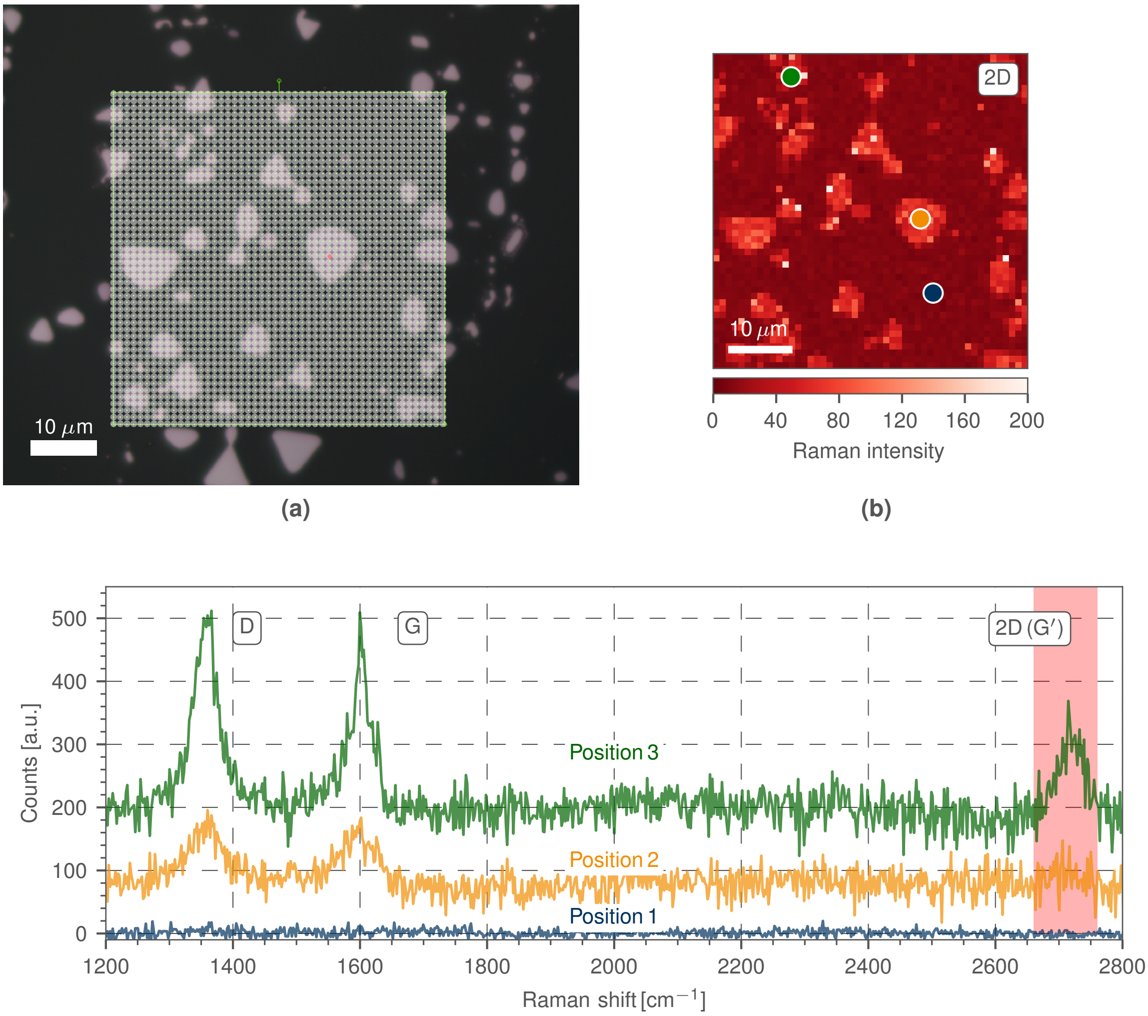

(a) **(b)**

(c)

Fig. 3.16: Characterisation of Cu film, deposited by magnetron sputtering at 650 °C. (a) Optical image showing only small Cu grains on the surface of the Al_2O_3 substrate. (b) RAMAN map of the 2D-peak intensity and (c) exported RAMAN spectra from the positions indicated in (b).

achieved at temperatures above 600 °C during sputtering. At these temperatures, the Cu does not form a closed film anymore, but grains with sizes of several micrometers. Therefore, they could not be used for large area graphene synthesis.

Therefore, for the graphene synthesis, the foils were pre-annealed at 950 °C for 2 h. The thin films were deposited at room temperature then pre-annealed at 1020 °C for 20 min and cleaned via UV ozone treatment.

Chapter 4

Graphene synthesis on Cu foils and Cu(111) films by ion implantation and transfer

In this chapter, the graphene synthesis on Cu foils on Cu(111) thin films as well as the characterisation of the graphene will be discussed. Furthermore, the different transfer processes used will be described. Consequently, these sections deal with the steps (b)-(f) in figure 2.1 and (c)-(g) in figure 2.2.

4.1 Graphene synthesis on Cu foils

4.1.1 Carbon ion implantation

For the ion implantation process, an energy of 35 keV (15 kV extraction voltage, 20 kV accelerator voltage, see section 2.2.3) for the ^{12}C ions was used. Lower ion energies were not possible due to the decrease of the ion beam current density for smaller extraction voltages and due to an inhomogeneous beam shape present at lower accelerator voltage. Higher energies are not beneficial as this results in more damage of the sample surface due to sputtering. Figure 4.1a shows the depth distribution of the ions for a fluence of $1 \cdot 10^{16}\,\mathrm{cm}^{-2}$ (2 ML graphene) and an energy of 35 keV and 100 keV, respectively. For bulk Cu samples the projected range R_P of ions is negligible compared to the thickness of the Cu sample. This situation is changed in case of Cu films (see section 4.2). Figure 4.1b shows the number of displacements produced by ions with 35 keV and with 100 keV as a comparison. The total number of displacements is smaller for lower ion energies. Nevertheless, the large number of $10^{24}\,\mathrm{cm}^{-3}$ displacements means that every Cu atom is replaced several times.

For the implantation process the accelerator described in section 2.2.3 was used. It is shown in figure 4.2a. The Cu foils were mounted on a 4-inch Si wafer (figure 4.2b) which was attached to the aluminium sample holder. After the implantation process, the foils were removed from the wafer and the parts covered by the tape were cut off in order to avoid contamination. Fluences in the range of $5 \cdot 10^{15}\,\mathrm{cm}^{-2}$ (1 ML) to $2.5 \cdot 10^{16}\,\mathrm{cm}^{-2}$ (5 ML) were implanted. The implantation process was performed at room temperature.

The beam current density is in the range of $5\,\frac{\mu\mathrm{A}}{\mathrm{cm}^2}$ which corresponds to approximately $5 \cdot 10^{12}\,\frac{\mathrm{ions}}{\mathrm{cm}^2\mathrm{s}}$. The implantation process for a fluence of $5 \cdot 10^{15}\,\frac{\mathrm{ions}}{\mathrm{cm}^2}$ (1 ML graphene) takes therefore around 10 minutes. The temperature of the sample reached 50 °C at maximum during implantation. Note that the implanted carbon consists out of ^{12}C due to the mass selection within the magnet. The case of ^{13}C is similar.

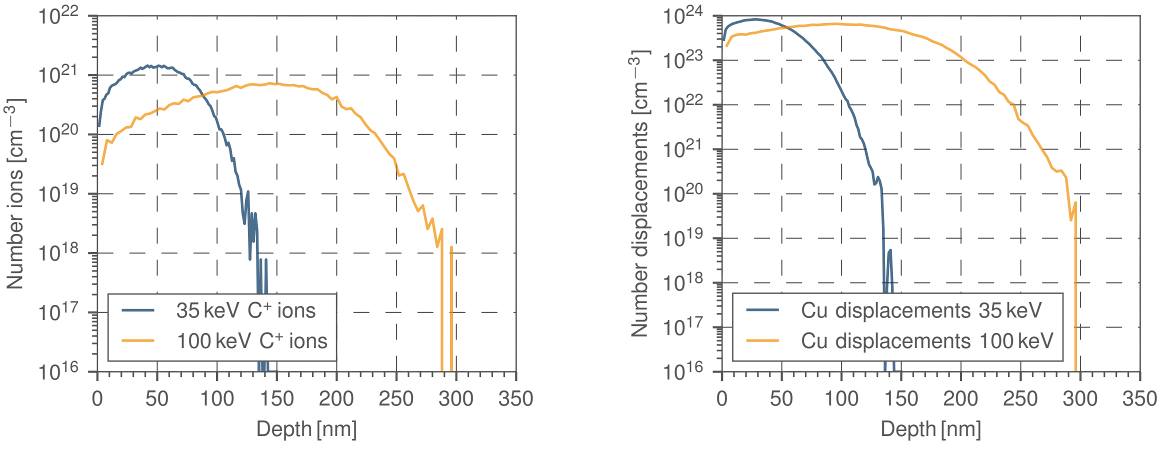

(a) **(b)**

Fig. 4.1: SRIM simulation of the carbon implantation process with 35 keV and 100 keV ion energy and $1 \cdot 10^{16}$ cm^{-2} fluence. (a) Number of ions over sample depth and (b) number of the produced displacements.

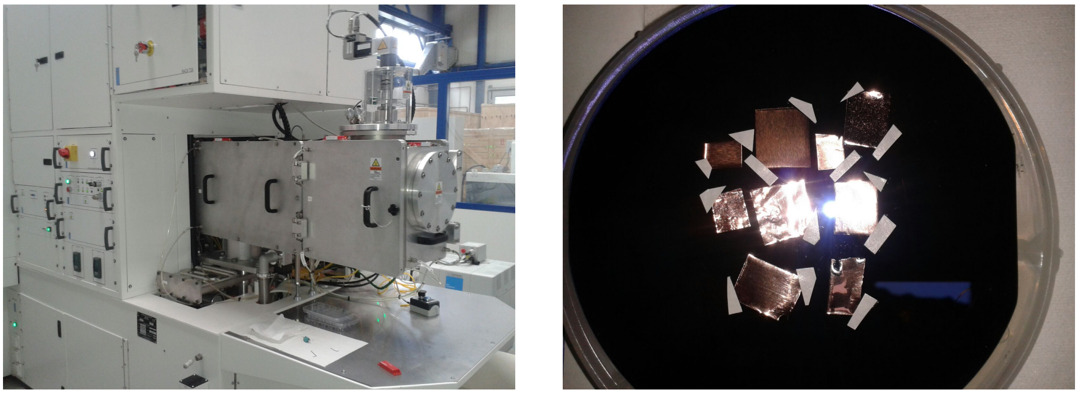

(a) **(b)**

Fig. 4.2: Image of the ion implanter (a) and the samples mounted on a 4-inch Si wafer (b).

4.1.2 Activation annealing of implanted Cu foils

For the activation annealing step, the oven described in section 2.4 was used. The temperature in case of the Cu foils was 850 °C, the duration 2 h. The heating rate was 50 K min^{-1}, the cooling rate $1-2$ K min^{-1}. The cooling down process occurred in vacuum, no process gas was used.

The process of activation annealing is schematically shown in figure 4.3. After ion implantation, the carbon is distributed at the very top of the Cu foil (penetration depth of the ions ≈ 100 nm, thickness of the foil 50 μm). Due to the thermal energy in the annealing, the carbon starts to diffuse until it is redistributed homogeneously.

The diffusion at the beginning is driven by the gradient of the carbon concentration as described by the diffusion equation [203]

$$\frac{\partial c}{\partial t} = D\frac{\partial^2 c}{\partial x^2}, \tag{4.1}$$

with c as the concentration, t the time, D the diffusion constant and x the position is space. The diffusion constant of carbon atoms in Cu of $D = 3 \cdot 10^{-11}$ m^2/s at 1143 K (870 °C) is

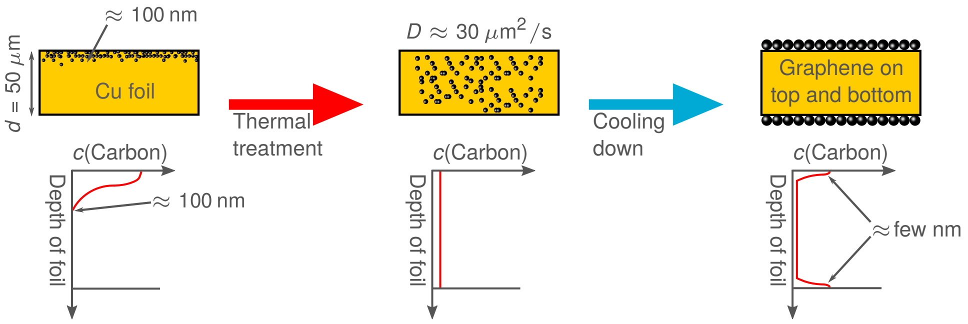

Fig. 4.3: Schematic illustration of the annealing process of implanted Cu foils. At the beginning the Cu is only close to the implanted surface of the foils. Due to thermal activation and concentration gradient, it becomes redistributed within the foil and segregates on the surface due to the low solubility of the C in Cu. The carbon concentration as function of the depth is also schematically shown. Note that within the foil the carbon concentration may not be zero due to segregation at the grain boundaries.

predicted to be of similar order of magnitude as the volume diffusion coefficient of carbon in Ni [195, 204, 205] at the same homologous temperature $T/T_\mathrm{m} = 0.84$ with T_m as the melting temperature. For Ni, at 1450 K (1177 °C, $T/T_\mathrm{m} = 0.84$), the volume diffusion coefficient of carbon equals $D = 1 \cdot 10^{-10}\,\mathrm{m}^2/\mathrm{s}$ [206].

By means of the diffusion length $L = 2\sqrt{Dt}$ [35, 203] which provides a measure of how far the concentration has propagated in a direction by diffusion within the time t and which can be calculated to 10.9 μm for an annealing time of 1 second, it can be assumed that the carbon atoms are redistributed homogeneously within the entire foil after an annealing time of 1 h. Note that also during the second annealing step, although the temperature is lower than the temperature for the pre-annealing step, recrystallisation processes within the Cu foil can occur, which may affect the carbon diffusion [191, 207]. The generated defects due to the ion implantation process may also influence the diffusion of the carbon. Due to the annealing at temperatures near the melting point of Cu, the foil is able to recrystallise despite the ion damage from the implantation. This has been confirmed by XRD measurements.

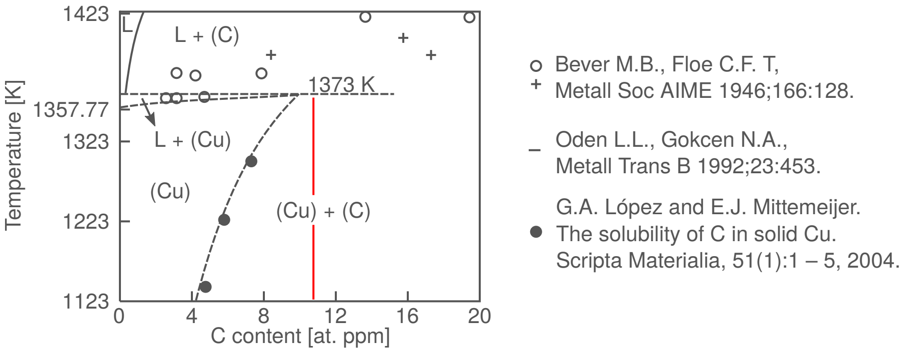

Fig. 4.4: Equilibrium phase diagram of peritectic type of the Cu-C system at the Cu-rich side (modified after [195]). The sources for the measured points are given within the figure.

Another important parameter is the solubility of C in Cu which is less than 0.001 at% at 1000 °C [195, 208]. Figure 4.4 shows a phase diagram of C-Cu system (on the Cu-rich side) [195]. The number of atoms in a Cu foil with volume 1 cm · 1 cm · 50 μm can be calculated by

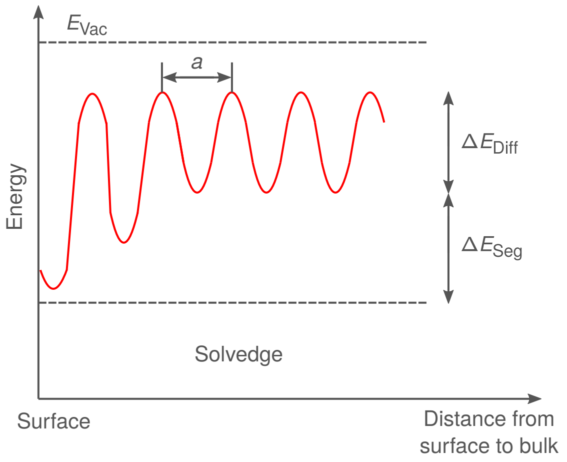

Fig. 4.5: Sketch of the energy relations for the surface segregation. *a* is the lattice parameter of Cu (modified after [210]).

$$N(\mathrm{Atoms_{Cu}}) = \frac{\rho_{\mathrm{Cu}} \cdot 1\,\mathrm{cm} \cdot 1\,\mathrm{cm} \cdot 50\,\mu\mathrm{m}}{m_{\mathrm{Cu}}} \tag{4.2}$$

with $\rho_{\mathrm{Cu}} = 8920 \cdot 10^{-6}\,\mathrm{kg\,cm^{-3}}$ the mass density of Cu and $m_{\mathrm{Cu}} = 63.55 \cdot 1.660 \cdot 10^{-27}\,\mathrm{kg}$ as the molecular weight. Therefore, a foil of this dimension contains $4.23 \cdot 10^{20}$ Cu atoms. The number of carbon atoms implanted is $5 \cdot 10^{15}$ (if the fluence was $5 \cdot 10^{15}\,\mathrm{cm^{-2}}$). For fluences between $5 \cdot 10^{15}\,\mathrm{cm^{-2}}$ (1ML) and $1.5 \cdot 10^{16}\,\mathrm{cm^{-2}}$ (3ML), the C content ranges 11.8 ppm (red line in figure 4.4) and 23.7 ppm.

By use of the phase diagram in figure 4.4 this means that even at high temperatures of 1020 °C, most of the implanted carbon will not be solved in the Cu and will therefore start to segregate at the surface of the foil. Note that surface in this case can also be the backside which was not implanted or even the grain boundaries inside the foil. Within the cooling down process, the solubility decreases further and the carbon which may have been solved will move to the surface and segregate there forming graphene/graphite [35,39,195]. There are also values for the solubility of carbon in copper which are reported to be in the range of 250 – 300 ppm at 1000 °C [209]. In this case, the carbon would be fully solved in the Cu at 1020 °C and would segregate at the surface below a certain temperature during the cooling down process because the solubility decreases with decreasing temperature [35,195].

Surface segregation is the enrichment at the surface or near surface region of one component (here C) as a result of diffusion of that element from the bulk to the surface region. The driving force for segregation is the difference in the chemical potential between the surface and the bulk for this component. When the equilibrium is reached, minimisation of the local free energy at given temperature may result in surface segregation so that thermodynamic equilibrium is achieved. The amount of the segregation enrichment will depend on the equilibrium temperature and the concentration of the component in the bulk.

The simplest model for the calculation of the amount of segregation was prepared by McLean [210]. If the amount of segregation at the surface (only the topmost layer) is θ, denoted in fractions of a monolayer, then

$$\frac{\theta}{1-\theta} = \chi \exp\left(-\frac{\Delta E_{\mathrm{Seg}}}{k_{\mathrm{B}} T}\right), \tag{4.3}$$

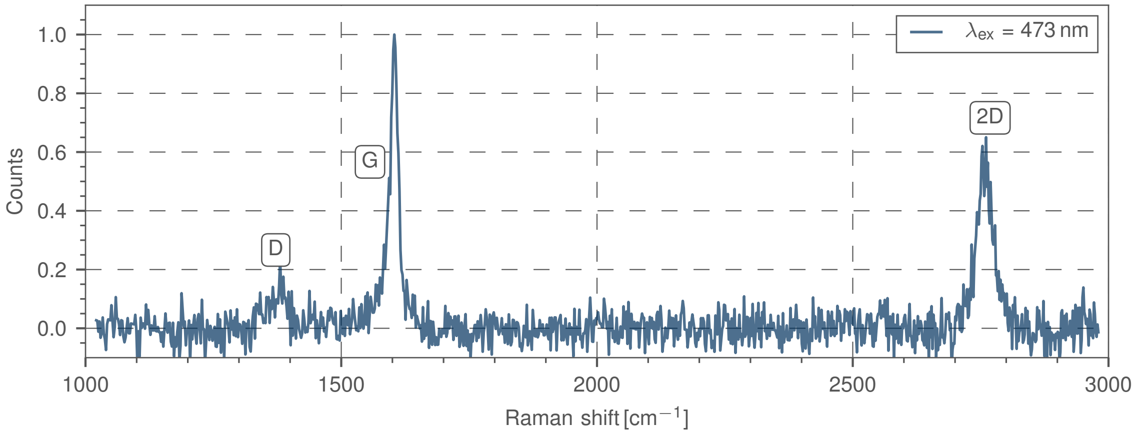

Fig. 4.6: RAMAN spectrum for graphene on Cu foil measured with 473 nm excitation wavelength and 2 minutes acquisition time. The laser power was 1 mW on the sample.

where $\chi = \chi_b/(1-\chi_b)$ is the concentration in the bulk.

The heat of segregation, ΔE_{Seg}, is the system energy change when an atom originally in the bulk exchanges position with an atom originally at the surface, as indicated in figure 4.5. Positive values of ΔE_{Seg} correspond to enrichment at the surface[1]. The segregation enthalpy ΔH_{Seg} and the entropy ΔS_{Seg} are related to ΔE_{Seg} by

$$\Delta E_{\mathrm{Seg}} = \Delta H_{\mathrm{Seg}} - T\Delta S_{\mathrm{Seg}}. \tag{4.4}$$

A determination of ΔE_{Seg} is difficult because highly resolved depth profiles of C in Cu would need to be measured.

Segregation may also take place at the grain boundaries within the foil so that the carbon concentration may not be zero within the foil [210].

The formation of graphene on the Cu surface has been confirmed by RAMAN spectroscopy before the graphene transfer[2], as shown in figure 4.6. Afterwards, the graphene was transferred to a SiO_2/Si wafer. Note that every parameter was kept constant if the transfer process was changed and vice versa in order to reduce the influence of the transfer step on the final results.

For the transfer of graphene from Cu foils to SiO_2, the PMMA-free process described in section 2.1.2 was used with the parameters as described in the following.

First transfer method

For the first transfer method, 100 ml etchant was prepared by dissolving $(NH_4)_2S_2O_8$ in millipure water in a molar ratio of 0.1 : 125. The dissolution of the Cu foil took approximately 2 h.

Figure 4.7 shows the results of the transfer process for a foil implanted with a fluence of $5 \cdot 10^{15}\,\mathrm{cm}^{-2}$ (1ML). Figure 4.7a shows an optical image of the transferred graphene on the SiO_2/Si wafer. Together with figure 4.7b, which shows a 2D peak intensity RAMAN map (within the bright square in figure 4.7a), it can be seen that the graphene is rolled/shrinked. Figure 4.7c shows RAMAN spectra from the different positions indicated by numbers in figure 4.7a and 4.7b. The red rectangle shows the region of interest from which the maximum value was extracted and used for the 2D-peak intensity RAMAN map of figure 4.7b.

---

[1] A negative value for ΔE_{Seg}, which can also be expressed as the GIBBS energy ΔG would mean that the carbon and the copper form a compound.

[2] Note, no graphene was detected on unimplanted Cu foils after identical heat treatment.

At position 1, no graphene could be detected. The spectra taken at positions 2-5 show a 2D peak, which indicates the presence of graphite/graphene at these positions. In general, if the graphene is rolled up after the transfer process, the Raman spectra still show a typical graphene spectrum, but with a stronger intensity, because the signal arises from multiple but uncoupled (single layer or multilayer) graphene layers [148, 163]. This is the case at position 3. If the graphene is heavily damaged or destroyed due to the shrinking, the Raman spectrum looks like graphene/graphite like at the positions 2, 4 and 5. The G-peak becomes much broader and a broad D-peak appears, both showing the presence of graphite [163].

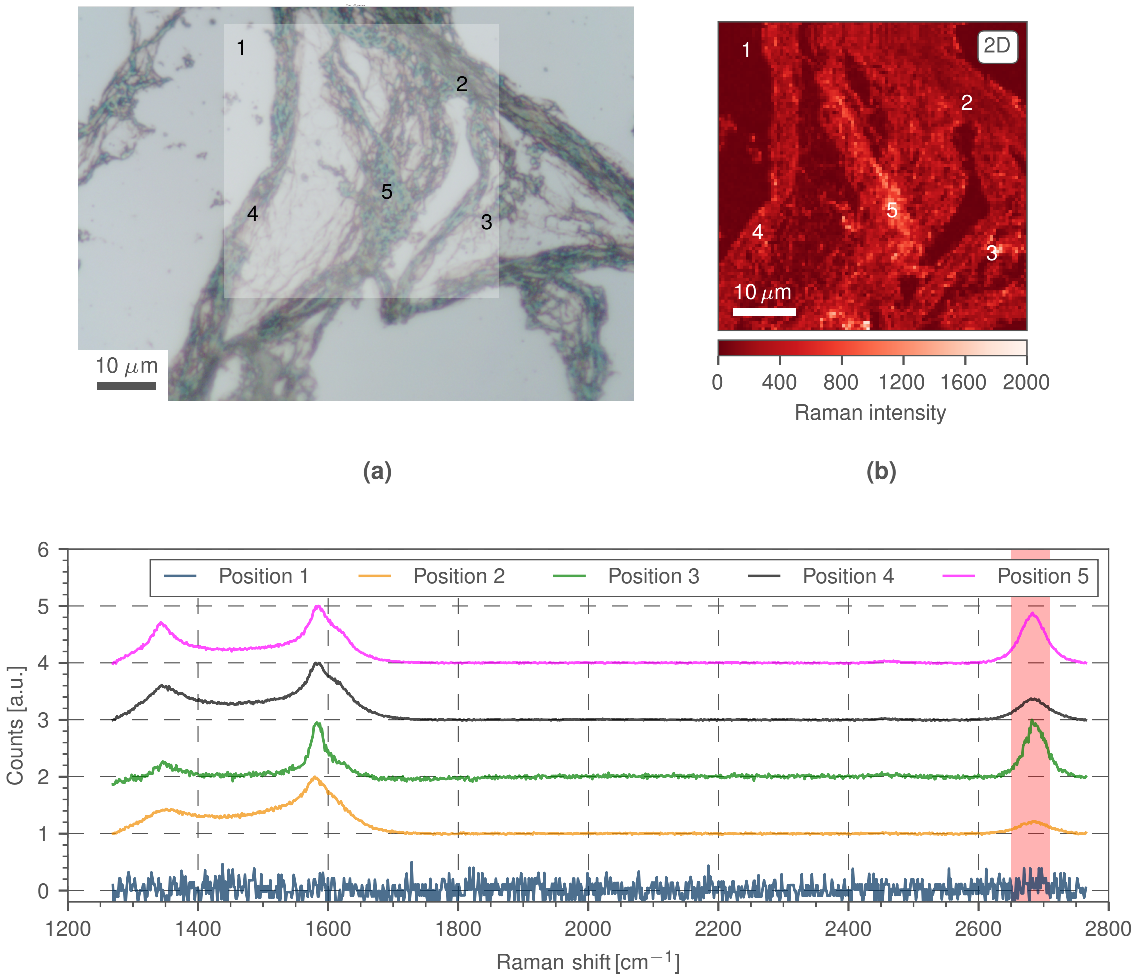

(a) (b)

(c)

Fig. 4.7: Graphene/graphite after transfer from the Cu foil to a SiO_2 wafer (first transfer method). The optical image (a) shows graphene wrinkles. The numbers are the positions where the spectra were taken, the bright rectangle shows the area of the Raman map (b). (c) The Raman spectra. The implanted fluence was $5 \cdot 10^{15}$ cm^{-2} (1ML), excitation wavelength 532 nm, laser power 1 mW.

Second transfer method

The shrinking and rolling of the graphene was obtained for all samples transferred with the first method. Also it seems that the shrinking is a result of the etching/washing process. In order to avoid this shrinking and to obtain flat graphene on the silicon substrate, the transfer method was slightly changed. The etching solution was kept unchanged, but the water for washing the graphene after the etching of the Cu foil was heated up to around 90 °C in order to reduce the surface tension [211].

Figure 4.8 shows the results for this transfer method. The implanted fluence was again $5 \cdot 10^{15}\,\mathrm{cm}^{-2}$ (1ML). Figure 4.8a shows the optical image with indication of the area used for the $10 \times 10\,\mu\mathrm{m}^2$ RAMAN mapping (bright rectangle). A representative spectrum with the fit function is shown in figure 4.8b. Due to the strong D-peak intensity, the intensity of the D′ peak increases. Therefore, not a 3-peak VOIGT function but a 4-peak VOIGT function was used to fit the spectra[3] to allow for the separation of G and D′ peak.

Figure 4.8c shows the distribution of intensity ratios of the D- and G-peak, extracted from the fitted RAMAN spectra. The mean value for the distribution of the D- and G-peak ratio intensity is 3.35 ± 0.44, i.e. the D-peak has a 3 times higher intensity than the G-peak on average as it is visible in figure 4.8b. According to equation (2.31), with $I(\mathrm{D})/I(\mathrm{G}) = 3.35$, the inter-defect length can be calculated to $L_\mathrm{D} = 6.6\,\mathrm{nm}$ which is a very small value compared to literature values which usually are in the range of a few tenth of nm if the D-peak intensity is nearly zero [162, 166]. The crystallite size can be calculated according to equation (2.33) to $L_\mathrm{a} = 5.8\,\mathrm{nm}$.

Figure 4.8d shows the distribution for the intensity ratios of the 2D- and G-peak, extracted from the fitted RAMAN spectra. The value was detmined to be 1.1 ± 0.24. The 2D peak position was determined to $2679.89\,\mathrm{cm}^{-1} \pm 1.2\,\mathrm{cm}^{-1}$, as shown in figure 4.8e clearly reveals single layer graphene [28, 45, 161–163]. The low value (lower than 2) for the 2D-G peak intensity ratio could originate from the high defect density (see section 2.6.1). The 2D-peak FWHM of $38.90\,\mathrm{cm}^{-1} \pm 2.14\,\mathrm{cm}^{-1}$ shown in figure 4.8f also indicates low quality graphene.

In order to investigate the origin of the high D-peak intensity, an AFM measurement was performed within the $10 \times 10\,\mu\mathrm{m}^2$ area. The result is shown in figure 4.9. Within this area, numerous holes in the graphene layer can be seen. Small wrinkles which contribute to the D-peak intensity are visible. The strong intensity of the D-peak is due to the existence of edges or wrinkles which is investigated with RAMAN spectroscopy. comes because in almost every spot which is measured an edge or wrinkle exists. Especially at graphene edges, the D-peak becomes very strong [46, 163].

In summary, by washing the graphene with hot instead of cold water, it was possible to obtain flat graphene on the $\mathrm{SiO_2/Si}$ substrate after the transfer.

Third transfer method

In order to improve the quality of the graphene after the transfer, a second etch solution was tested. This time, 100 ml etchant was prepared by mixing $\mathrm{FeCl_3}$, HCl, and $\mathrm{H_2O}$ in a molar ratio of 1.2 : 1 : 174, respectively. After approximately 40 min, the dissolution of the Cu foil was complete and the etchant was removed by flowing 10 l of 90 °C millipore water at a flow rate of 2 l/h.

Figure 4.10 shows the results of the graphene transfer with this etch solution. Figure 4.10a shows the optical figure of the graphene lying on the substrate. The bright areas are single layer graphene, the darker areas are multiple layers or wrinkles which may originate from the transfer process. Another assumption could be that these wrinkles originate due to the grain boundaries of the Cu foil. This will be discussed in section 4.1.3. The small rectangle (marked with the white arrow) indicates again the $10 \times 10\,\mu\mathrm{m}^2$ area which was used for the RAMAN measurement. Note that this time the $\mathrm{SiO_2}$ layer was 800 nm thick and therefore appears brighter and more

---

[3] 4-peak VOIGT function means Fit-Function = VOIGT1 + VOIGT2 + VOIGT3 + VOIGT4 by use of equation (2.27) for the 10000 spectra.

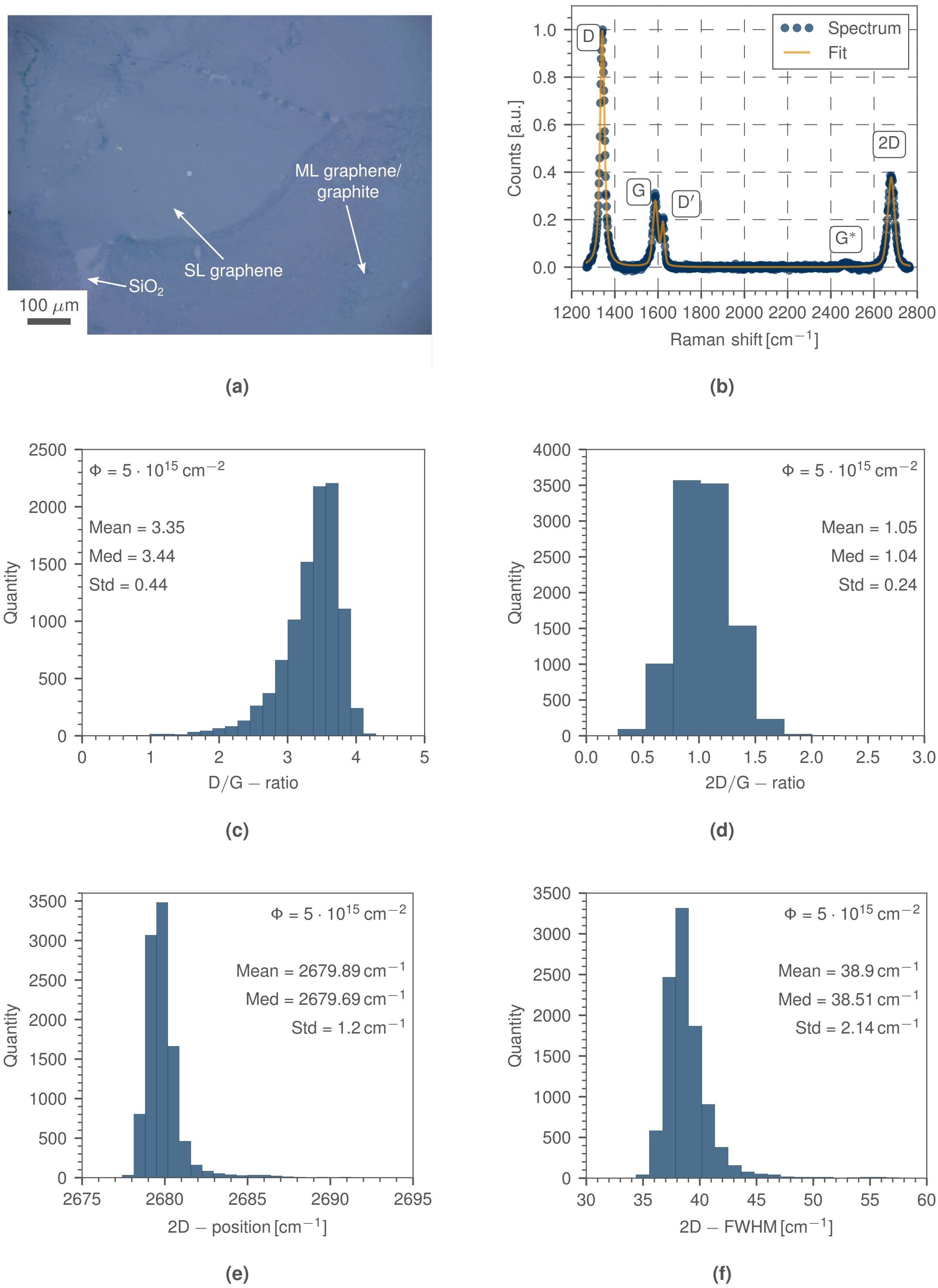

(a) **(b)**

(c) **(d)**

(e) **(f)**

Fig. 4.8: Graphene after transfer from the Cu foil to a SiO_2 wafer after washing with hot water (second transfer method). The optical image (a) shows the graphene lying flat on the SiO_2 substrate. (b) Shows a representative spectrum exported from the RAMAN map and fitted by a 4-VOIGT function (the G* peak is not fitted). (c)-(f) Shows the D/G and 2D/G peak intensity ratios as well as the 2D-peak position and 2D-peak FWHM, extracted from the RAMAN map over $10 \times 10\,\mu m^2$ (10000 spectra). The implanted fluence was $5 \cdot 10^{15}\,cm^{-2}$ (1ML), excitation wavelength 532 nm, laser power 1 mW.

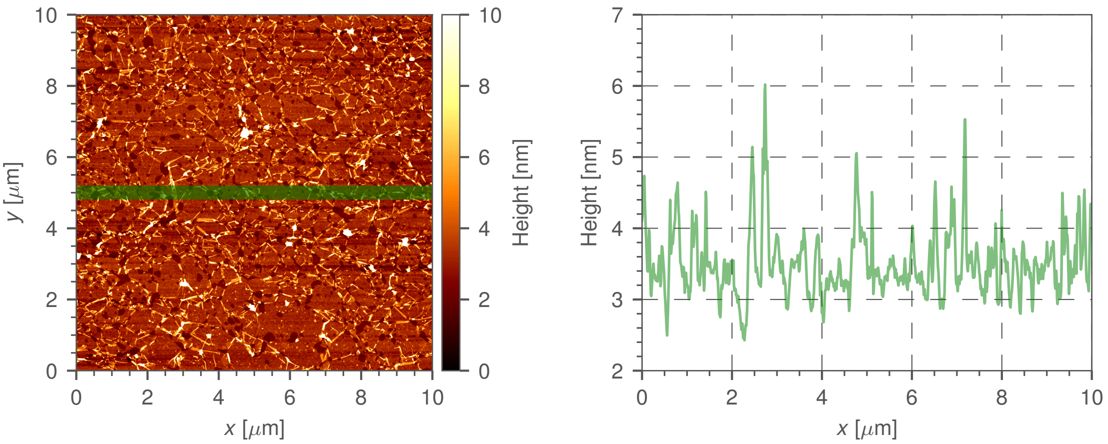

Fig. 4.9: AFM measurment of graphene transferred to SiO_2 substrate (second transfer method). The green bar shows the area from which the height distribution was extracted over 40 lines. The graphene lies flat on the surface. Wrinkles and edges are visible which contribute to the high D-peak in the RAMAN spectra.

pink than the other substrates used before.

Figure 4.10b shows an exported spectrum from the map, fitted with a 4-peak VOIGT function. The D-peak intensity is much lower compared to the spectra of the sample transferred with the $(NH_4)_2S_2O_8$ etch solution. With this 4-peak VOIGT fit function, all spectra were fitted.

Figure 4.10c shows the D/G-peak intensity peak ratio. The mean value was determined to 0.82 ± 0.22. This value is drastically lower than for the second transfer method, thus the graphene quality is improved. According to equation (2.31), with $I(\mathrm{D})/I(\mathrm{G}) = 0.82$, the inter-defect length can be calculated to $L_\mathrm{D} = 13.5\,\mathrm{nm}$. These values are comparable to literature values for the graphene synthesis via ion implantation [33,39]. The crystallite size also increases to $L_\mathrm{a} = 23.5\,\mathrm{nm}$, according to equation (2.33).

Figure 4.10d shows the distribution of the intensity ratios of the 2D- and G-peak. The mean value was determined to 2.16 ± 0.78 which is typically used in literature to assert that it is single layer graphene [46]. The 2D-peak position at $2678.10 \pm 1.36\,\mathrm{cm}^{-1}$ and the 2D-peak FWHM of $31.24 \pm 2.28\,\mathrm{cm}^{-1}$, shown in figure 4.10e and 4.10f also reveal single layer graphene [28,45,161–163].

AFM measurements were performed within the single layer graphene area. The result is shown in figure 4.11. The holes in the graphene are smaller than for the second transfer method, thus there is a smaller fraction of edges contributing to RAMAN spectroscopy mapping. Consequently, the D-peak intensity is decreased. The small high spots within the AFM image (for example at $(x, y) = 0.5, 1)$, also visible in the optical image as small pink spots within the single layer graphene region, are residuals from the etching process. XPS measurements (figure 4.12) revealed that these residuals consist mostly of iron which may originate from the $FeCl_3$ etching solution. Also F was found as contamination from an unidentified source. However, there is no Cu visible in the region of the sensitive Cu 2p doublet (932 and 952 eV).

In order to study the homogeneity of the graphene, RAMAN mapping was performed in a $1000\,\mu\mathrm{m} \times 400\,\mu\mathrm{m}$ area. Figure 4.13a shows the optical image with the rectangle in which the RAMAN measurement was performed. Etching residuals and wrinkles are indicated. The SEM image in figure 4.13b, taken within the indicated area after RAMAN mapping, also shows homogeneous graphene flat on the substrate. Figure 4.13c, 4.13d and 4.13e shows the RAMAN peak intensity for the 2D-, G- and D-peak, respectively. They were obtained by summation over a region of interest window of $1320 - 1440\,\mathrm{cm}^{-1}$ for the D-peak, $1520 - 1620\,\mathrm{cm}^{-1}$ for the G-peak and $2600 - 2750\,\mathrm{cm}^{-1}$ for the 2D-peak. 2D-peak intensity increases at the wrinkles, because there

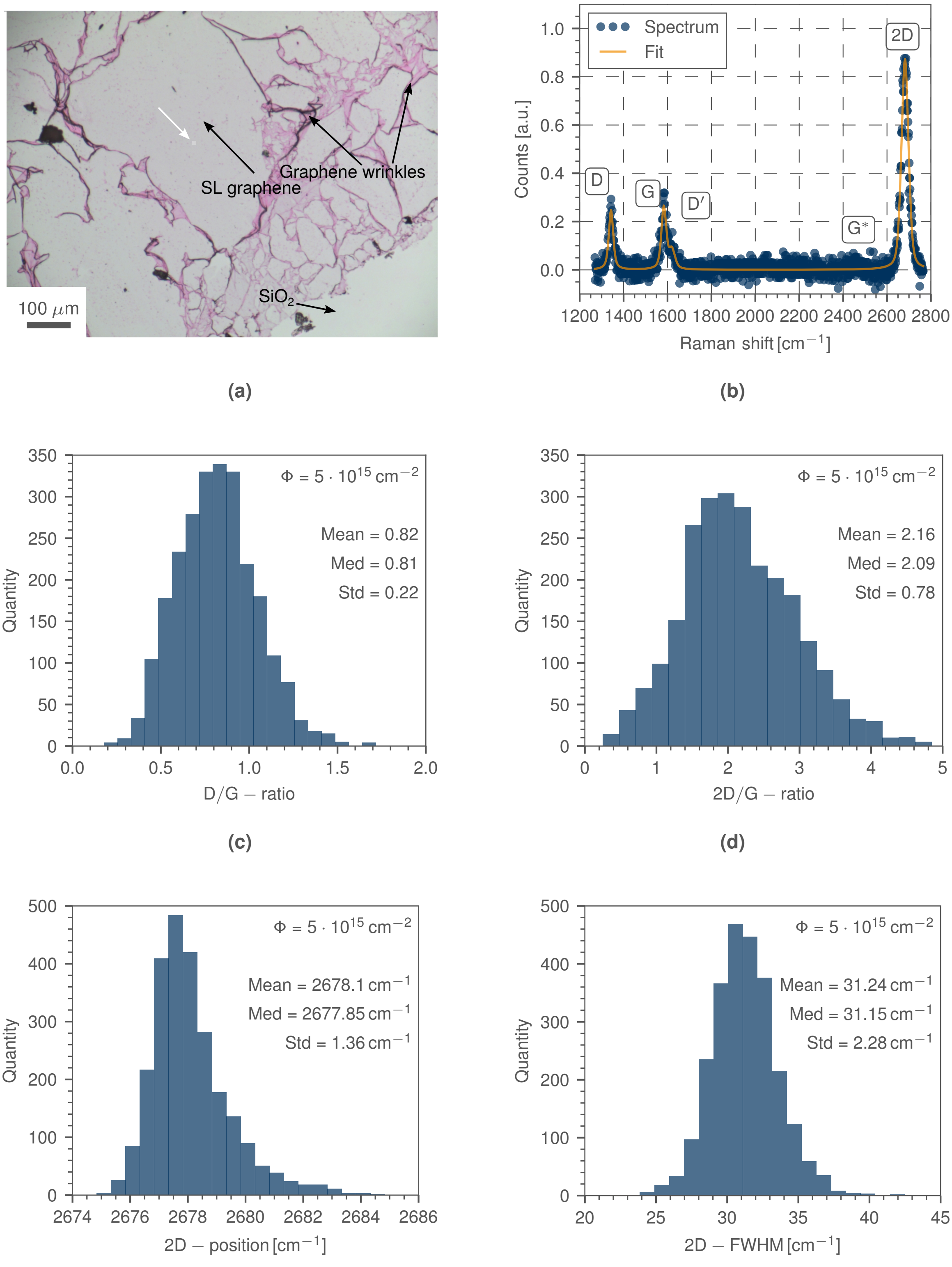

(a) **(b)**

(c) **(d)**

(e) **(f)**

Fig. 4.10: Graphene after transfer from the Cu foil to a SiO$_2$ wafer employing washing with hot water and the second etch solution (third transfer method). The optical image (a) shows the graphene lying again flat on the SiO$_2$ substrate. (b) Shows a representative spectrum exported from the RAMAN map and fitted by a 4-VOIGT function (the G* peak is not fitted). (c)-(f) Shows the D/G and 2D/G peak intensity ratios as well as the 2D-peak position and 2D-peak FWHM, extracted from the RAMAN map over 10 × 10 µm^2 (2500 spectra). The implanted fluence was $5 \cdot 10^{15}$ cm^{-2} (1ML), excitation wavelength 532 nm, laser power 1 mW.

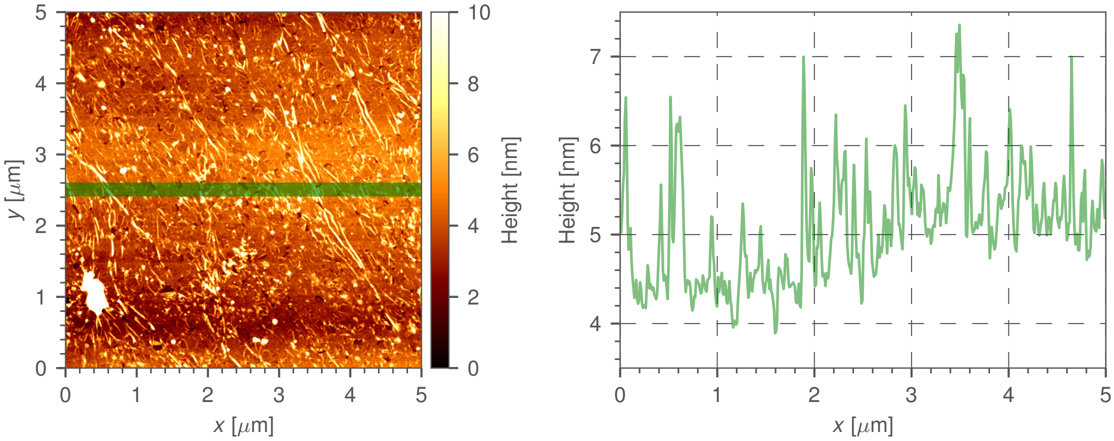

Fig. 4.11: AFM measurment of graphene transferred to SiO_2 substrate (third transfer method). The green bar shows the area from which the height distribution was extracted over 25 lines. The graphene lies flat on the surface.

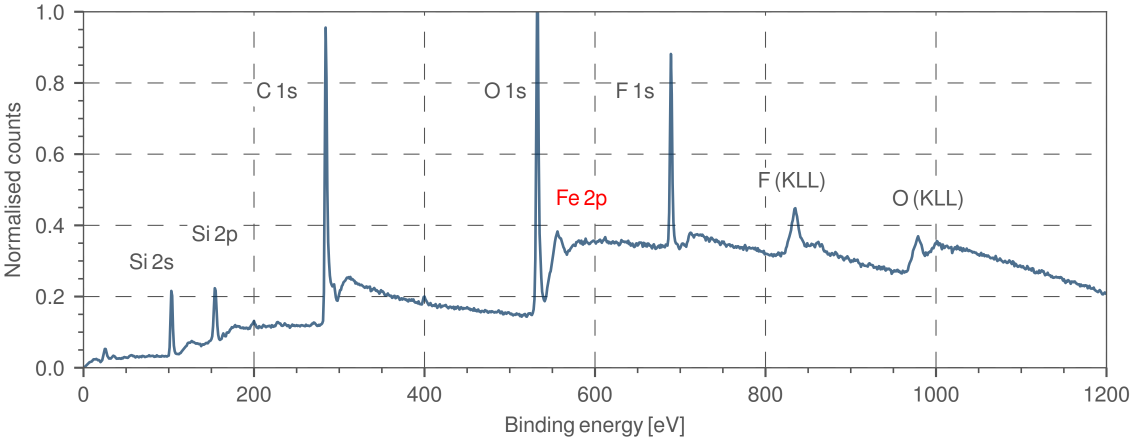

Fig. 4.12: Survey XPS spectrum of graphene on SiO_2/Si wafer that shows Fe and F as contamination [111].

is more graphene, but the G-peak intensity increases even more. The D-peak is also strongest at the wrinkles. This behaviour is the same for rolled/shrinked graphene after the first transfer process. Figure 4.13f shows the 2D/G intensity ratio. The values are > 2.1 which indicates monolayer graphene within the complete area, excluding the regions of the wrinkles. The origin of these wrinkles is discussed in the next section.

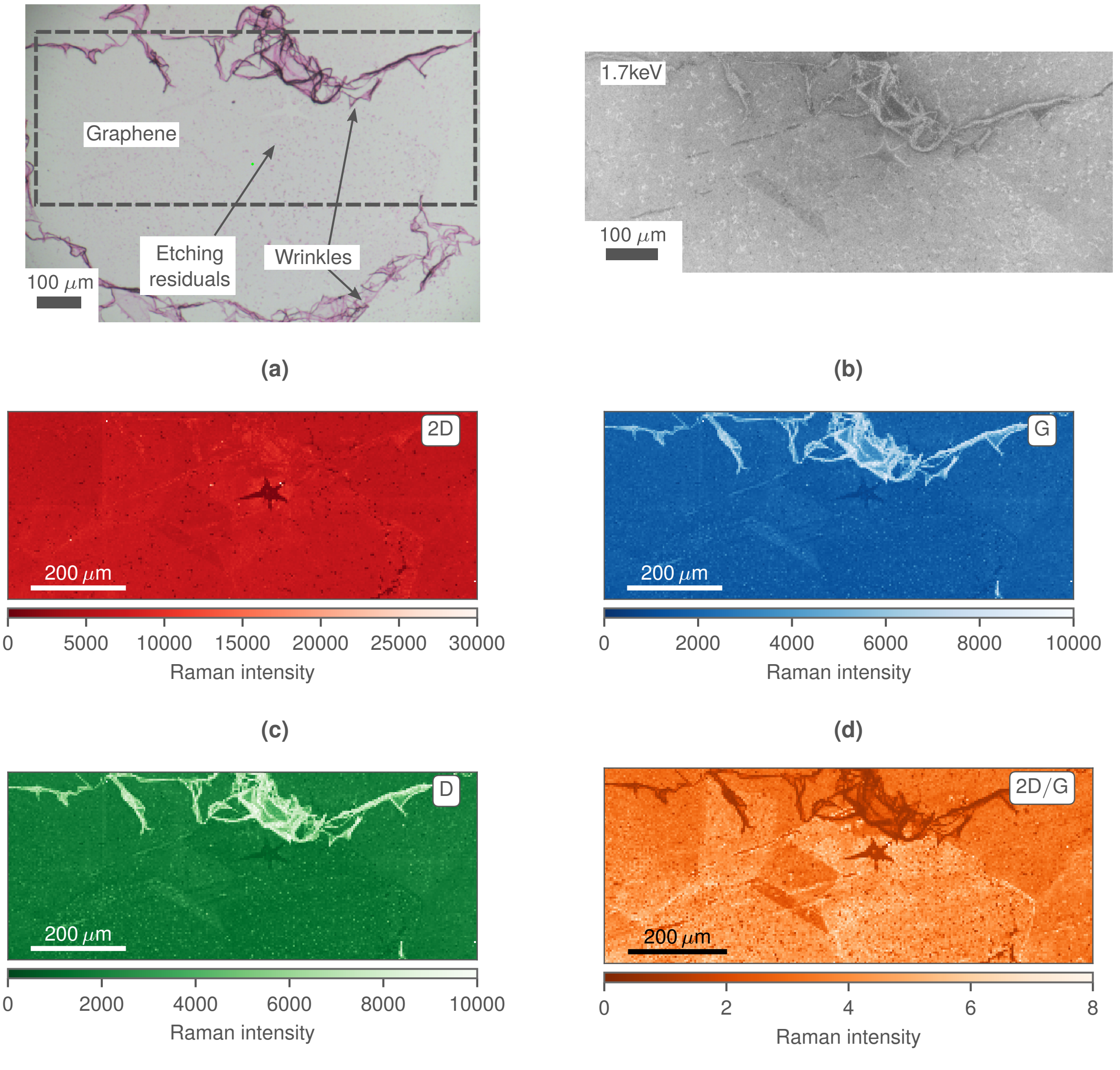

(a) (b)

(c) (d)

(e) (f)

Fig. 4.13: Graphene characterisation on a large area (third transfer method). (a) Optical image of a domain of monolayer graphene on SiO_2/Si with wrinkles at the boundaries and residuals from the etching process. Dashed lines indicate the SEM and RAMAN scanning area. (b) SEM image taken with 1.7 keV electron energy. (c) RAMAN maps of the 2D-peak, (d) the G-peak, (e) the D-peak intensities and (f) the 2D/G peak ratio within the 1000 μm × 400 μm scan area indicated in (a) [111].

4.1.3 Correlation between grain sizes of graphene and Cu foil

In order to compare the grain sizes of the Cu foils (after pre-annealing) and the transferred graphene, SEM images taken from both, were coloured (by etch detection) so that every grain has its specific color. Figure 4.14a and 4.14b shows the SEM images of the Cu foil after pre-

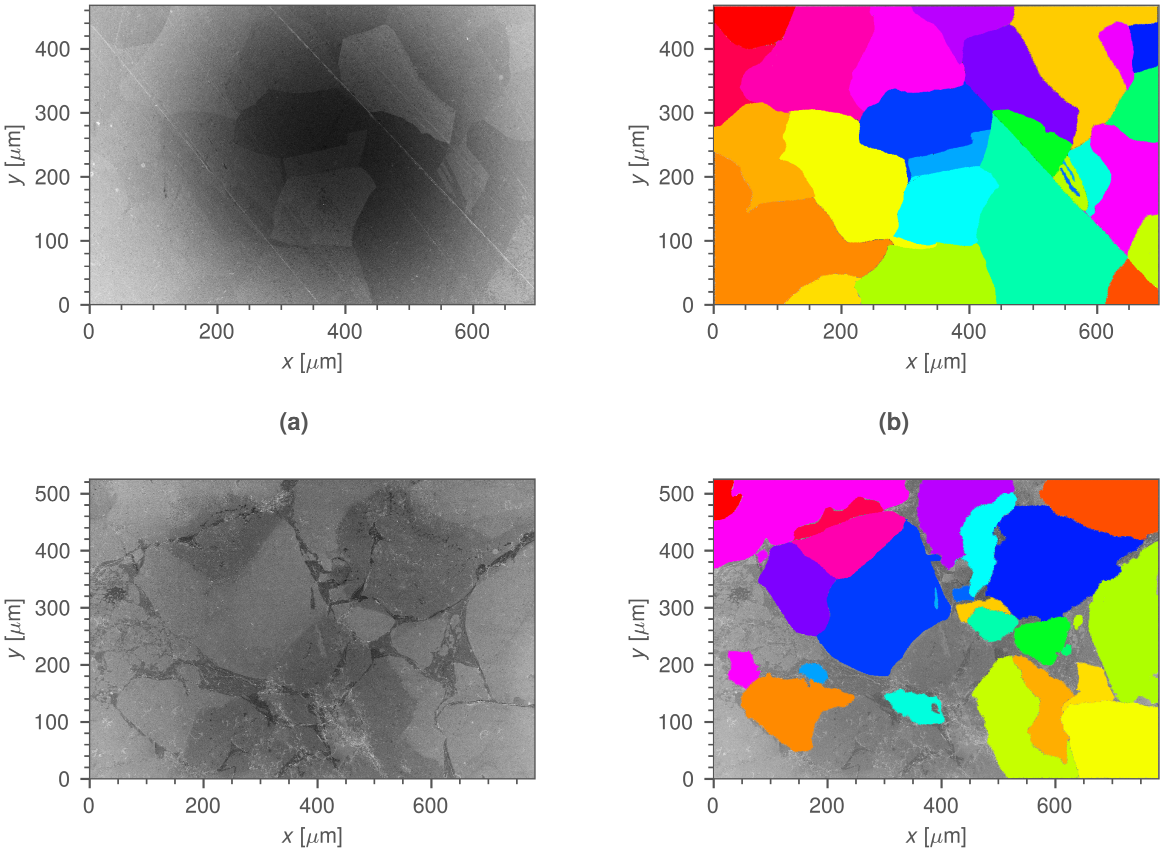

(a) (b)

(c) (d)

Fig. 4.14: SEM image for obtaining the grain size distribution of a Cu foil annealed at 950 °C for 2 h in vacuum and graphene which was transferred to a SiO_2 substrate. (a) and (c) shows the raw SEM images, (b) and (d) the coloured coded grains, respectively.

annealing at 950 °C for 2 h in vacuum in greyscale and after colour coding. Note that the position of the two SEM images in figure 4.14a and 4.14c are not the same. Figures 4.14c and 4.14d shows the same for the transferred graphene on the SiO_2 wafer. The transfer was done via the third transfer method. In order to determine the area of the grains, the size of a pixel was determined by dividing the number of pixels by the size of the measured area. For this purpose, a PYTHON script was written which is given and described in appendix C.3. The number of pixels of a certain colour was counted. With the size of the pixel in μm^2 and the number of pixels, the area of the grains was determined.

The grain size distribution for the Cu foil after annealing and the grain size distribution of the transferred graphene film on the SiO_2 substrate is shown in figure 4.15.

The total number of evaluated grains is 27. Within an area of up to 10.000 μm^2 there are 15 grains of the Cu foil and 16 of the graphene, between 10.000 μm^2 and 20.000 μm^2 there are 7 grains of the Cu foil and 6 of graphene, between 20.000 μm^2 and 30.000 μm^2 there are 3 grains for both and between 30.000 μm^2 and 40.000 μm^2 there are 2 grains for both as well. Although the statistics is limited, this shows that there is a correlation between the grain size of the Cu foil and the final grain size of the transferred graphene. At least, the sizes for both are in the same order of magnitude. The presence of hints that the graphene starts to grow at the grain boundaries of the Cu foil. A correlation between the graphene domains and the grain size of the metal template was also found in reference [212].

Note, the Cu-foil used for the grain size determination was not the same from which the graphene was transferred due to the dissolution of the foil required for the transfer. However, the Cu-foil used for the graphene synthesis came from the same batch and all Cu foils showed similar grain sizes after identical heat treatment, so that this procedure is justified.

The next section deals with the correlation between the implanted fluence and the thickness (layer number) of the synthesised graphene.

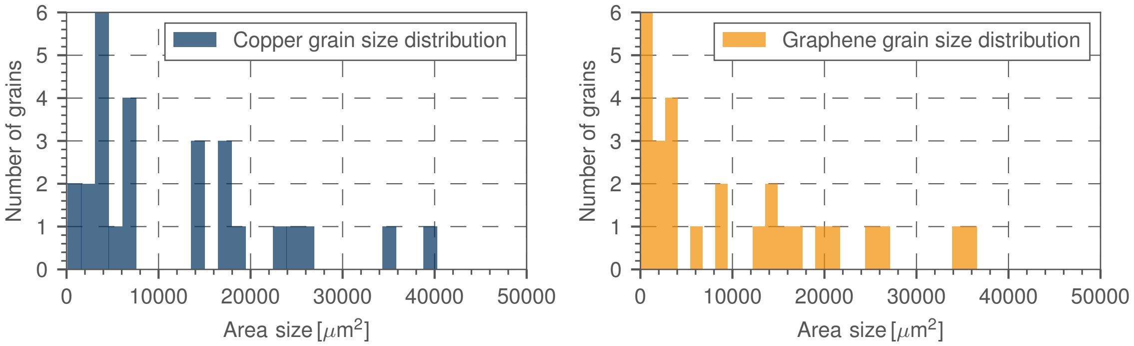

Fig. 4.15: Histogram for the calculated grain size distribution for the Cu foil and the transferred graphene.

4.1.4 Synthesis of multilayer graphene on Cu foils

One of the main goals was to investigate the possibility of adjusting the thickness of the graphene by the ion fluence. The adjustment of the thickness is important for, e.g. filter applications [213, 214] or batteries [215, 216] where no single layer graphene is needed.

Figure 4.16 shows optical images taken on three samples which were implanted with a fluence of $5 \cdot 10^{15}\,\mathrm{cm}^{-2}$ (1ML), $1 \cdot 10^{16}\,\mathrm{cm}^{-2}$ (2ML) and $2.5 \cdot 10^{16}\,\mathrm{cm}^{-2}$ (5ML), respectively. All the samples were pre-annealed at 950 °C in vacuum for 2 h, implanted and again annealed at 850 °C in vacuum for 2 h. For transfer of the graphene from the Cu foil, the third approach as described in section 4.1.2 was used. With increasing fluence, the thickness of the graphene (or the amount of graphene on the SiO_2 substrate) increases.

In order to study this correlation between the fluence and the amount of graphene in more detail, Raman spectroscopy measurements were performed on each sample. Figure 4.17a shows

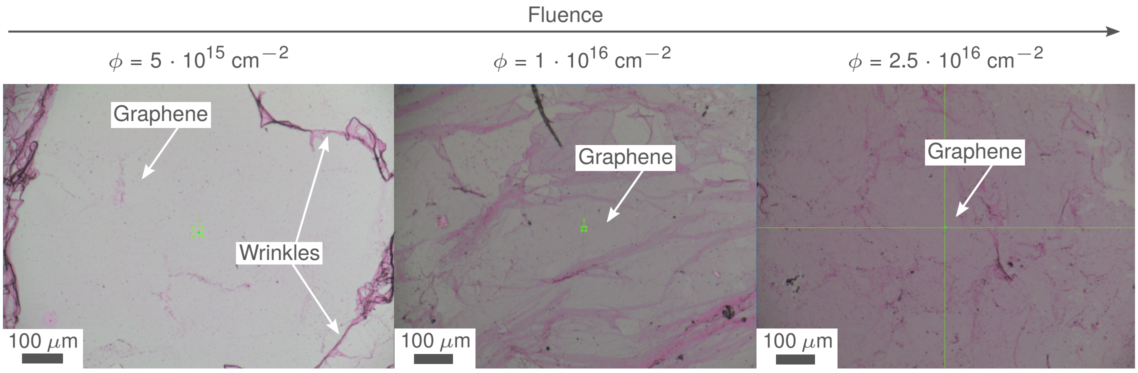

Fig. 4.16: Optical figure of three samples, implanted with fluences between $5 \cdot 10^{15}\,\mathrm{cm}^{-2}$ (1ML) and $2.5 \cdot 10^{16}\,\mathrm{cm}^{-2}$ (5ML). With increasing fluence, the thickness of the graphene increases.

the Raman spectra for the three implantation fluences. For the three implantation fluences, the average FWHM and position of the 2D-peak were obtained by fitting 1, 4 or 6 Voigt functions, respectively, to the 625 spectra recorded (and baseline corrected) within a graphene domain of each sample (see figure 4.17c, 4.17d and 4.17e). As shown in figure 4.17b, the values for the FWHM increases from ≈ 31 $\mathrm{cm^{-1}}$ over ≈ 41 $\mathrm{cm^{-1}}$ to ≈ 59 $\mathrm{cm^{-1}}$, whereas the 2D-peak position shifts from ≈ 2678 $\mathrm{cm^{-1}}$ over ≈ 2681 $\mathrm{cm^{-1}}$ to ≈ 2688 $\mathrm{cm^{-1}}$ with increasing ion fluence. These values correspond to the ones reported for 1 ML, 2 ML and 5 ML graphene layers [28,45,161–163]. The nearly linear shift of the 2D-peak position with layer thickness shown in figure 4.17b is in line with these findings as well [111]. The number of Voigt functions required to properly fit the 2D-peak is a further indication that the layer numbers assigned above to the ion fluences are correct. The error bars determined as the standard deviation within the 625 spectra recorded for each fluence indicate that the 1 ML graphene is more homogeneous than the 2 ML and 5 ML graphene. This might be attributed to the large lattice mismatch between graphene and Cu(200) which does impede an A-B stacking of the individual graphene layers (see section 1.1.1 and 3.1.2). Note that no domains with an enhancement in the G-peak intensity due to resonances with the Raman laser line were found [160]. The large error bar of the FWHM for the $2.5 \times 10^{16}\,\mathrm{cm^{-2}}$ fluence is due to the relatively poor signal-to-noise ratio of the 2D-peak in some of the recorded spectra which leads to difficulties in the peak fitting process [111].

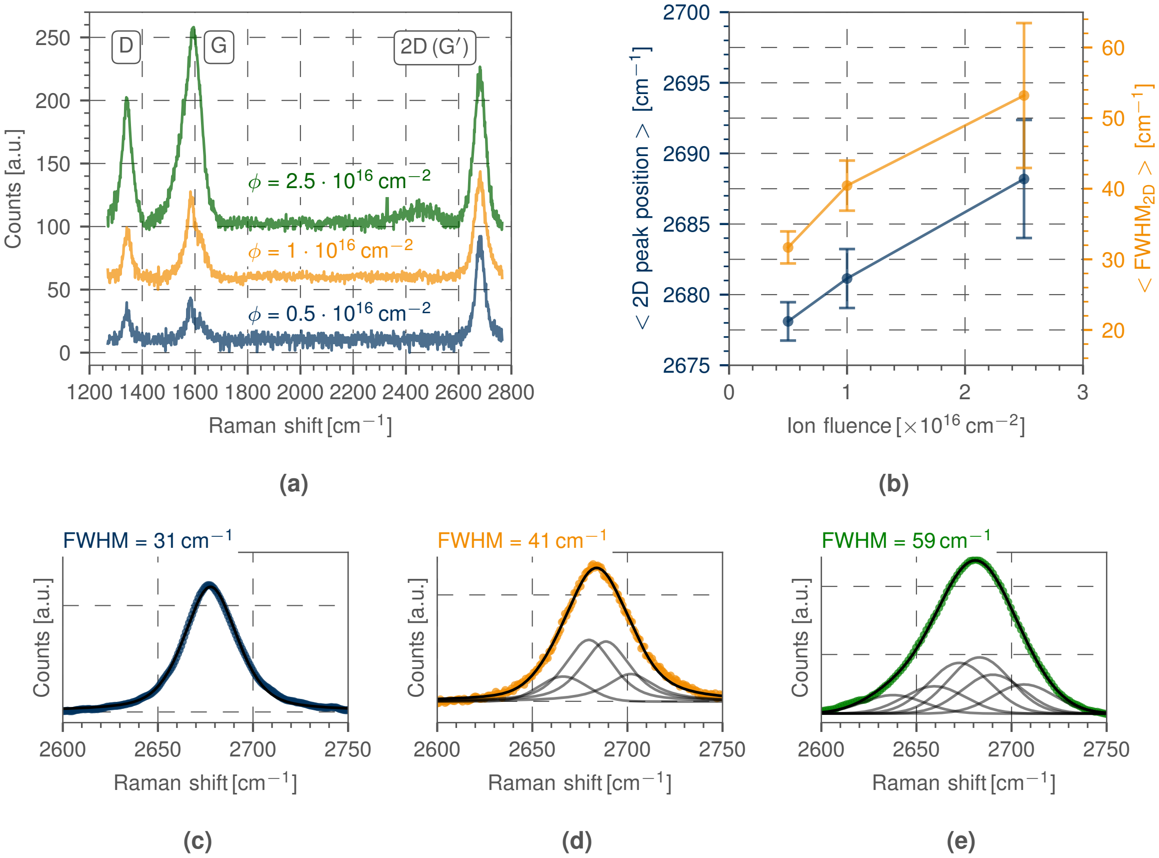

Fig. 4.17: Raman characterisation of graphene with different layer number, synthesised by implantation of different fluences of ions. (a) Raman spectra of graphene transferred to SiO_2/Si for different implantation fluences. (b) Average of 2D-peak position and FWHM as a function of the implanted fluence. Error bars represent the standard deviation within the 625 spectra recorded for each fluence. (c), (d) and (e) Typical 2D-peak fitted with 1, 4 and 6 Voigt functions for ion fluences of $5 \cdot 10^{15}\,\mathrm{cm^{-2}}$ (1ML), $1 \cdot 10^{16}\,\mathrm{cm^{-2}}$ (2ML) and $2.5 \cdot 10^{16}\,\mathrm{cm^{-2}}$ (5ML), respectively [111].

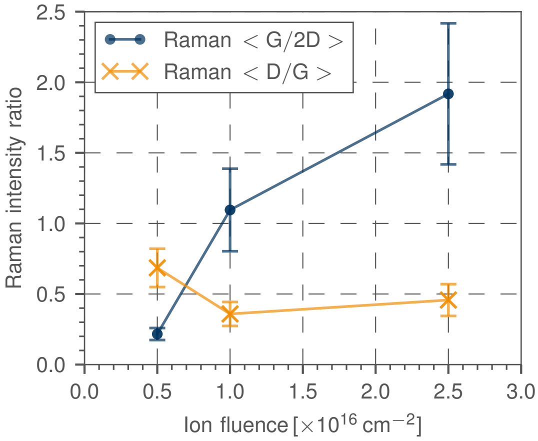

Fig. 4.18: Average of G/2D and D/G peak ratio of graphene on SiO_2/Si as a function of the implanted ion fluence. Error bars were determined by combining the uncertainties for the D-, G- and 2D-peak intensities for all 625 spectra of each fluence, respectively [111].

As already mentioned, the RAMAN spectrum allows to estimate the layer number from the G/2D-band ratio [163][4]. For this purpose, the G/2D-peak intensity ratio averaged over the 625 recorded spectra was obtained by summation over a region of interest window of 1320–1440 cm^{-1} for the D-peak, 1520 – 1620 cm^{-1} for the G-peak and 2600 – 2750 cm^{-1} for the 2D-peak for each implanted fluence, respectively, with the result shown in figure 4.18. The G/2D values increase with increasing fluence from 0.22 ± 0.04 over 1.09 ± 0.29 to 1.91 ± 0.5 which reflects the increase in layer number with the amount of implanted ions. The small ratio of G/2D ≈ 0.22 compared to 0.4 – 0.5 found in the literature for ML graphene [46] and compared to the value of 0.46 obtained for the transferred graphene layers in section 4.1.2 (third transfer), might be due to the graphene layer being delaminated in some areas of the scanned region as a result of the transfer process to SiO_2/Si [177] or due to the influence of the substrate itself [111, 165, 178].

The D/G ratios which are also shown in figure 4.18 have no strong variation upon ion fluence and therefore layer number, in contrast to reference [40]. This indicates that the surface damage in the Cu foil accumulated in the ion implantation process is not the main reason for the presence of the D-peak, i.e. the defects in the synthesised graphene. It seems that the thermal treatment during the graphene synthesis anneals out the implantation damage in the Cu foil even for the highest implanted fluence.

4.1.5 ^{13}C graphene synthesis on Cu foils

The mass selection employed in the ion implantation process gives the possibility to implant not only ^{12}C, but also to choose the isotope ^{13}C of mass 13u [5]. With the analyser magnet (see section 2.2.3) a separation of ^{12}CH and ^{13}C is not possible. Thus, at this mass, ^{13}C or the molecule ^{12}CH are implanted. Due the low content of ^{13}C in natural CO_2 gas used to produce the ions in the ion source (natural isotope ratio of ^{12}C:^{13}C is 0.989 : 0.011), the current density was too low to reach a fluence of e.g. $5 \cdot 10^{15}$ cm^{-2} (1ML) in a reasonable time. Therefore, a CO_2 gas bottle with enriched ^{13}C was used. The composition of ^{12}C:^{13}C in this bottle was 0.5 : 0.5.

The Cu foils used were pre-annealed at 950 °C for 2 h, implanted with a fluence of $5 \cdot 10^{15}$ cm^{-2}

---

[4] Note that for illustration reasons, here the G/2D ratio is used in contrast to section 4.1.2 where the 2D/G ratio was used.

[5] Note that if an atomic mass of 12u is chosen for the implantation process, pure ^{12}C is implanted and therefore, the graphene consists only of ^{12}C atoms.

of ions with mass 13 amu (expected to correspond to ^{13}C, but also ^{12}CH). The energy of the ions was 35 keV. The post-annealing was performed at 850 °C for 1 h. For the transfer of the graphene to the SiO_2 wafer, the third transfer method as described in section 4.1.2 was used.

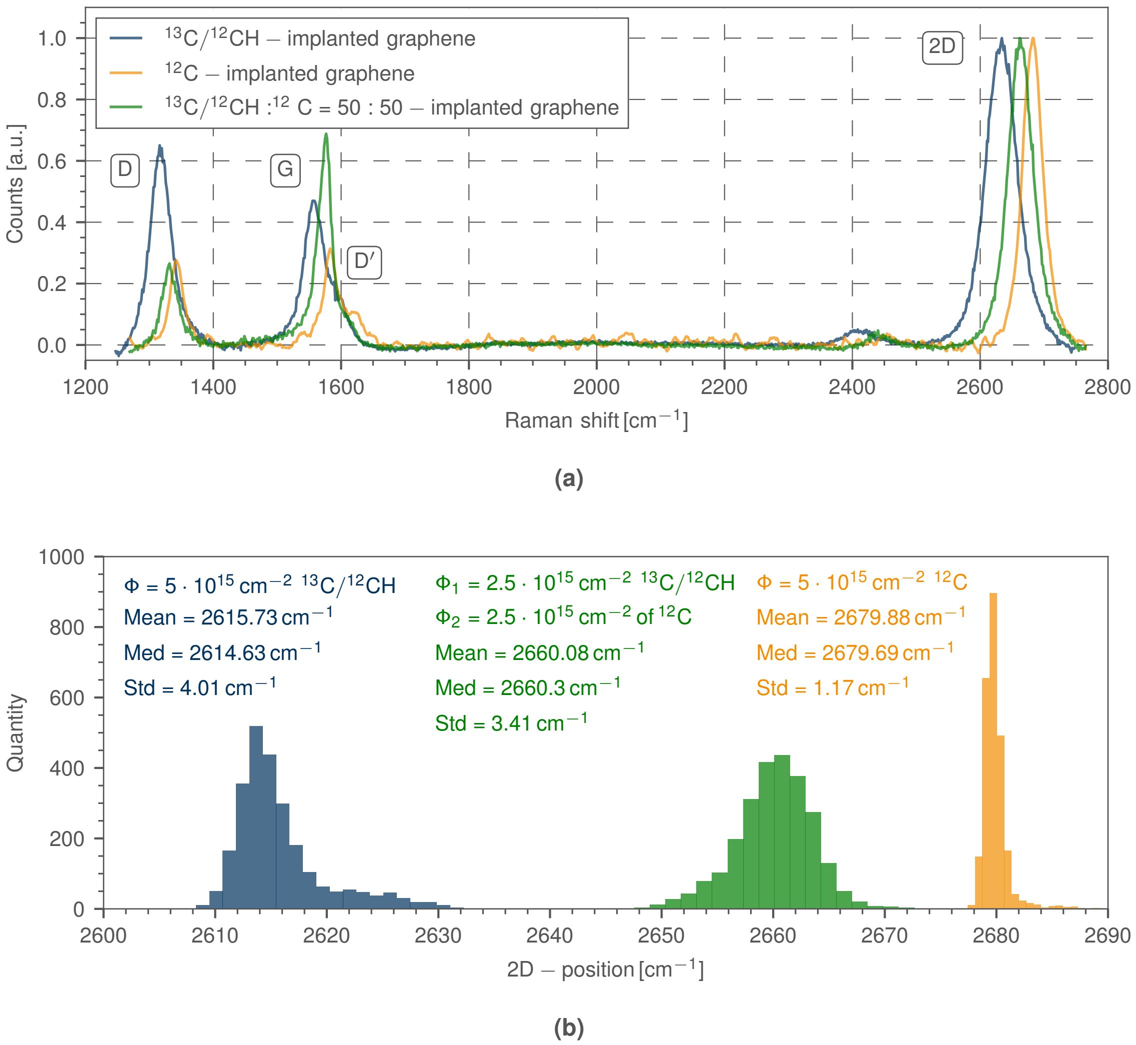

(a)

(b)

Fig. 4.19: Comparison of a sample implanted with $5 \cdot 10^{15}\,\mathrm{cm}^{-2}$ ions/molecules with the respective ratio of ^{13}C or ^{12}CH and pure ^{12}C. (a) RAMAN spectra of graphene synthesised by implantation of the two different carbon isotopes with different ratios. (b) Histogram of the 2D-peak positions for the three samples implanted with different isotopes.

Figure 4.19a shows three RAMAN spectra, one of graphene synthesised by implantation of ^{12}C (orange), one synthesised by implantation of mass 13 amu which gives in principle ^{13}C or ^{12}CH (blue) and one synthesised by implantation of a mix of ^{13}C/^{12}CH and pure ^{12}C with a ratio of 50/50 (green). All graphene samples were transferred to a respective SiO_2 wafer and measured with a laser excitation of 532 nm. Due to the different masses of the atoms, the spectra are shifted relatively to each other as described in section 2.5.3. For the determination of the 2D-peak position, the spectra were baseline corrected and fitted by a 4-VOIGT function.

To obtain a better comparison between the samples which were implanted with ^{12}C and with ions of mass 13 amu, the 2D-peak positions are plotted as histograms, as shown in figure 4.19b. The mean value for the mass 13 amu sample was determined to $(2615.73 \pm 4.01)\,\mathrm{cm}^{-1}$ whereas for the ^{12}C sample, a mean value of $(2679.88 \pm 1.17)\,\mathrm{cm}^{-1}$ was obtained. With equation (2.30), the ^{13}C content of the graphene can be calculated which gives a ratio of 0.59/0.41 for

$^{13}C/^{12}C$. The residual ^{12}C originates from the implantation of ^{12}CH or from other carbon contamination source. Due to this mixture of ^{12}C and ^{13}C within the volume measured with Raman spectroscopy, the variation for the 2D-peak position is higher than for the pure ^{12}C graphene for which the 2D-peak is only shifted due to thickness, doping or stress [46]. The results for a mixed implantation of ^{12}C and mass 13 amu with a ratio of 50/50 ($2.5 \cdot 10^{15}\,\mathrm{cm}^{-2}$ ions of ^{12}C and $2.5 \cdot 10^{15}\,\mathrm{cm}^{-2}$ ions with mass 13 amu) is also shown in figure 4.19a and 4.19b. These values give a ratio of 0.17/0.83 for $^{13}C/^{12}C$, but a ratio of 0.295/0.705 for $^{13}C/^{12}C$ is expected[6] which hints that there must be another carbon source.

These results from ^{13}C graphene show that the graphene synthesised on the foils is indeed made from the carbon which was implanted before.

4.1.6 Summary

In summary, the synthesis of low-defect large-area graphene on Cu foils with a purity of 99.9999 % is possible using carbon ion implantation with the ability to control the number of layers of graphene by the amount of implanted ions. The graphene was transferred to a SiO_2/Si wafer with a PMMA-free wet etching method. The Raman spectra show a small D-peak and a D/G ratio which does not vary strongly with the implanted fluence. The highest graphene quality was obtained for a monolayer. This is due to lattice strain of the first monolayer impeding ideal A-B stacking for the subsequent layers [43] [111]. For monolayer graphene, the size of the obtained graphene domains correlates with the grains size of the Cu foils. Also, the synthesis of isotopically labelled graphene was possible which shows that the graphene synthesised on the foils is made from the implanted carbon. The synthesis of pure ^{13}C graphene was not possible with the gas mixture used due to the contributions from ^{12}CH molecules to the ion implantation.

4.2 Graphene on Cu(111) films deposited at room temperature

This part presents the results for the graphene synthesis on 450 nm Cu(111) films. The pre-implantation annealing (1020 °C for 20 min) and cleaning procedure was already described in the sections 3.2 and 3.2.4. For the graphene transfer, the procedure described in section 2.1.2 was used.

4.2.1 Carbon ion implantation and activation annealing

Carbon ion implantation

The ion implantation parameters were the same for the Cu(111) films as for the Cu foils, i.e. the energy for the ^{12}C ions was 35 keV. Now, this energy is an essential parameter. Apart from the fact that higher energies would produce more defects in the film, at some point the penetration depth of the ions would exceed the thickness of the Cu film, thus they would stop in the Al_2O_3 substrate. These carbon ions would not be available for the synthesis of graphene. For the 35 keV, the maximal penetration depth of the ions is around 150 nm (see figure 4.1a). Note that one reason to use 450 nm and not only 200 nm thick Cu films was the diffusion of the Cu into the Al_2O_3 substrate. This might be the reason for the unsuccessful synthesis of graphene after ion implantation of all 200 nm films as they were probably to thin.

---

[6] With the obtained values for the implantation of ions with mass 13 amu and the assumption that the contamination is only due to ^{12}CH implantation, the ^{12}C content should be $0.5 + 0.5 \cdot 0.41 = 0.705$.

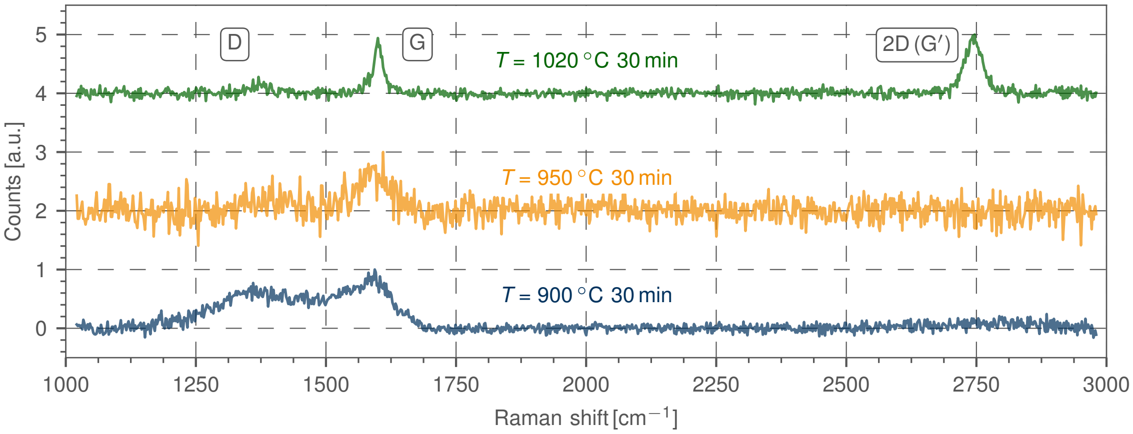

Fig. 4.20: Raman spectra for three Cu films implanted with a fluence of $1 \cdot 10^{16}\,\mathrm{cm}^{-2}$ each and annealed at different temperatures after implantation. The characteristic 2D peak for graphene appears only after high temperature annealing. Excitation wavelength was 473 nm, the laser power was 1 mW on the sample (100x objective).

Activation annealing

Also for the Cu films, the synthesis of graphene is based on the low solubility of carbon in the copper, as already explained in section 4.1.2.

The main difference between the Cu foils and the Cu films was the temperature necessary to synthesise graphene and not graphite on the surface of the substrate. This was investigated by Raman spectroscopy. Figure 4.20 shows the result for three different samples, implanted with a fluence of $1 \cdot 10^{16}\,\mathrm{cm}^{-2}$ and annealed at 900 °C, 950 °C and 1020 °C for 30 min, respectively. The 2D peak characteristic for graphene appears only for temperatures above 950 °C. These temperatures are around 50 °C higher than reported in literature [217].

4.2.2 Synthesis of multilayer graphene on Cu(111) films

At the beginning a fluence of $5 \cdot 10^{15}\,\mathrm{cm}^{-2}$ was chosen for the synthesis of single layer graphene, as for the Cu foils, was chosen. However, after the activation annealing and transfer of the graphene, no single layer graphene but multilayer graphene was detected. The reason for the shift of the fluence to lower values for single layer graphene might be that the Cu film is much thinner than the Cu foils. Within these foils, the carbon might segregate at the grain boundaries as well, which also act as surfaces as mentioned in section 4.1.2 [210]. Here, the films are only 450 nm thick so that the depth dimension of the grain boundaries is decreased too. Therefore, less carbon can segregate on these grain boundaries. This might also be the reason why the transferred graphene synthesised on Cu films does not show such pronounced wrinkles as the graphene synthesised on the Cu foils.

Single layer graphene

Due to the lower amount of carbon which segregates at the grain boundaries within the Cu films, the implanted fluence to obtain single layer graphene was decreased to $2 \cdot 10^{15}\,\mathrm{cm}^{-2}$ [7]. The activation annealing after the implantation was performed at 1020 °C for a duration of 30 min for each sample.

---

[7] This fluence correspond to approximately 0.5ML graphene. This leads to graphene sheet sizes smaller than the dimension of 1 cm × 1 cm for the used Cu thin film substrate.

Figure 4.21 shows the results. In figure 4.21a an optical image of the graphene on the SiO_2 substrate is shown. In contrast to the graphene, transferred from Cu foils, the amount of wrinkles is greatly reduced. The small rectangle indicates again the $10 \times 10\,\mu m^2$ area where Raman spectroscopy mapping was performed.

Figure 4.21b shows an exported spectrum from the map, fitted with a 4-peak Voigt function. The D-peak is even smaller than for the graphene synthesised on the Cu foils. With this 4-peak Voigt fit function, all spectra were fitted.

Figure 4.21c shows the D/G intensity ratio. The obtained value of 0.51 ± 0.18 is less than the value obtained for the graphene from the Cu foils, which basically means that the quality is improved. The inter-defect length (equation (2.31)) and the crystallite size (equation (2.33)) also increase to $L_D = 16.9\,\mathrm{nm}$ and $L_a = 37.3\,\mathrm{nm}$, respectively. These values are superior to the literature values from the graphene synthesis via ion implantation [33, 39].

Figure 4.21d shows the distribution for the intensity ratios of the 2D- and G-peak. The mean value was determined to 3.08 ± 0.57 which indicates the presence of single layer graphene [28, 45, 161–163]. The 2D-peak position is slightly shifted (compared to the graphene from the foils) to $2685.65 \pm 0.65\,\mathrm{cm^{-1}}$ and the 2D-peak FWHM is slighly increased to $34.45 \pm 0.77\,\mathrm{cm^{-1}}$ as shown in figure 4.21e and 4.21f. The standard deviation are smaller compared to the graphene from the Cu foils which also indicates a better quality. The red-shift of the 2D peak may be due to the PMMA transfer method.

The results of an AFM measurement performed in the area used for the Raman mapping is shown in figure 4.22. The graphene shows small wrinkles which may originate from the transfer process. Similar results were obtained for CVD graphene transferred to SiO_2 substrates in reference [218]. In contrast to the literature, these wrinkles could not be reduced by vacuum annealing [218] and no change in the Raman spectra was observed. Note, in contrast to the graphene synthesised on the Cu foils, here, the SiO_2 surface is nearly completely covered by the graphene (inside the scanned area[8]).

In order to study the homogeneity of the graphene on a larger scale, Raman mapping was performed in a $50\,\mu m \times 50\,\mu m$ area. Figure 4.23a shows the optical image with the rectangle in which the Raman measurement was performed. The AFM image in figure 4.23b, taken in the indicated area, shows holes in the graphene.

Figure 4.23c, 4.23d and 4.23e shows the Raman peak intensity for the 2D-, G- and D-peak, respectively. They were obtained by summation over a region of interest window of $1320 - 1440\,\mathrm{cm^{-1}}$ for the D-peak, $1520 - 1620\,\mathrm{cm^{-1}}$ for the G-peak and $2600 - 2750\,\mathrm{cm^{-1}}$ for the 2D-peak. Figure 4.23f and 4.23g shows the 2D/G and D/G intensity ratio. Within the holes, the Raman intensities are nearly zero indicating no graphene. The 2D/G intensity values are > 2.3 (excluding the holes) which indicates monolayer graphene within the complete area. The D/G intensity values are nearly constant.

The holes in the graphene have a diameter of about $3 - 5\,\mu m$ and thus about the same dimension as the etch holes in the Cu film after the thermal treatment (see figure 3.5d in section 3.2).

Multilayer graphene

For the Cu thin films, the possibility of adjusting the thickness of the graphene by an increased ion fluence was investigated as well. The Cu films were pre-annealed as usual (1020 °C for 20 min) and UV cleaned (see section 3.2.4). The implanted fluences were $2 \cdot 10^{15}\,\mathrm{cm^{-2}}$ (0.5ML), $5 \cdot 10^{15}\,\mathrm{cm^{-2}}$ (1ML), $1 \cdot 10^{16}\,\mathrm{cm^{-2}}$ (2ML) and $2.5 \cdot 10^{16}\,\mathrm{cm^{-2}}$ (5ML).

---

[8] That does not mean that the whole SiO_2 wafer surface to which the graphene was transferred is fully covered with graphene.

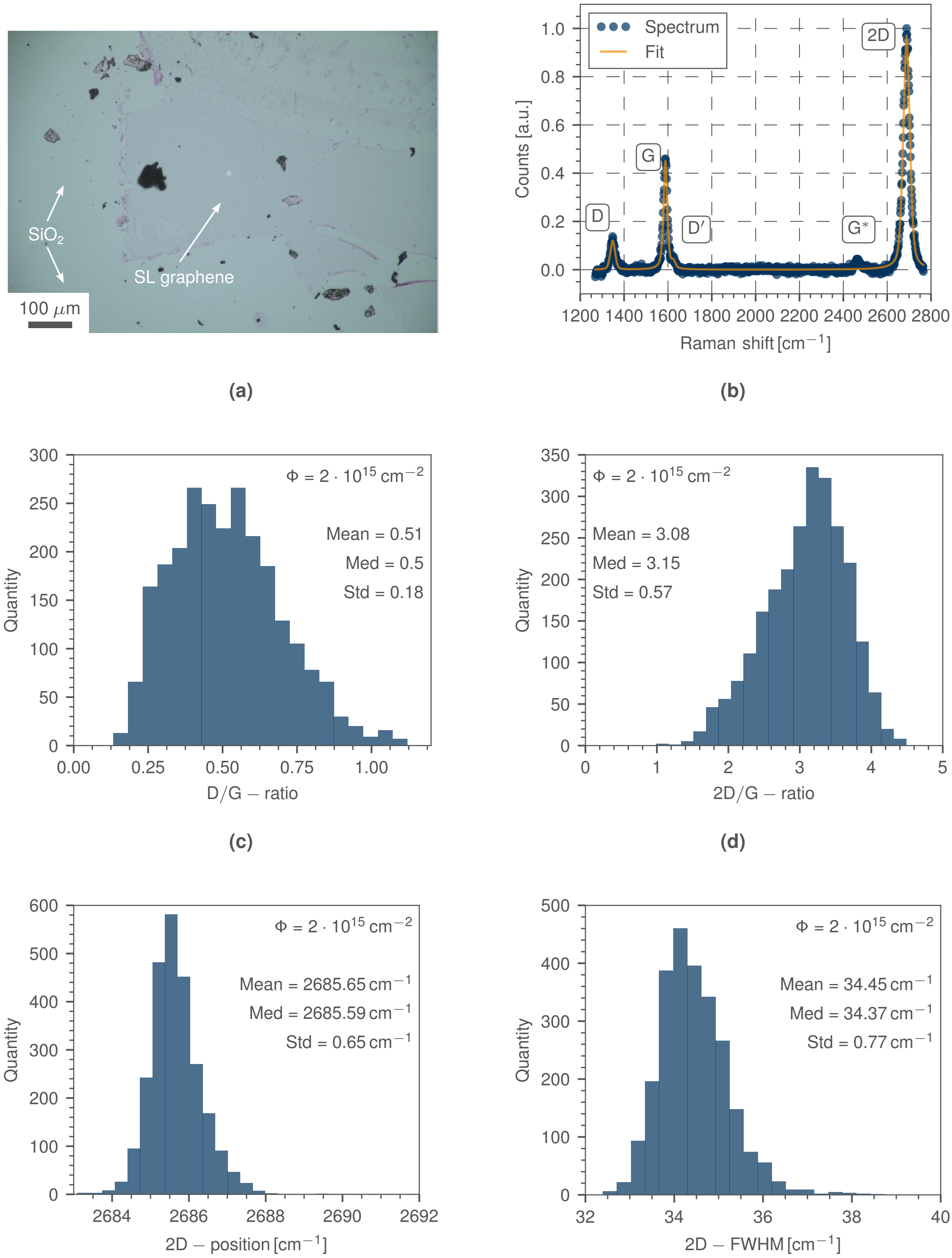

(a) (b)

(c) (d)

(e) (f)

Fig. 4.21: Graphene after transfer from a 450 nm Cu film to a SiO$_2$ wafer. The optical image (a) shows the graphene lying flat on the SiO$_2$ substrate. (b) Shows a representative spectrum exported from the RAMAN map and fitted by a 4-VOIGT function (the G* peak is not fitted). (c)-(f) Shows the D/G and 2D/G peak intensity ratios as well as the 2D-peak position and 2D-peak FWHM, extracted from the RAMAN map over 10 × 10 μm^2 (2500 spectra). The implanted fluence was $2 \cdot 10^{15}$ cm^{-2} (0.5ML), excitation wavelength 532 nm, laser power 1 mW.

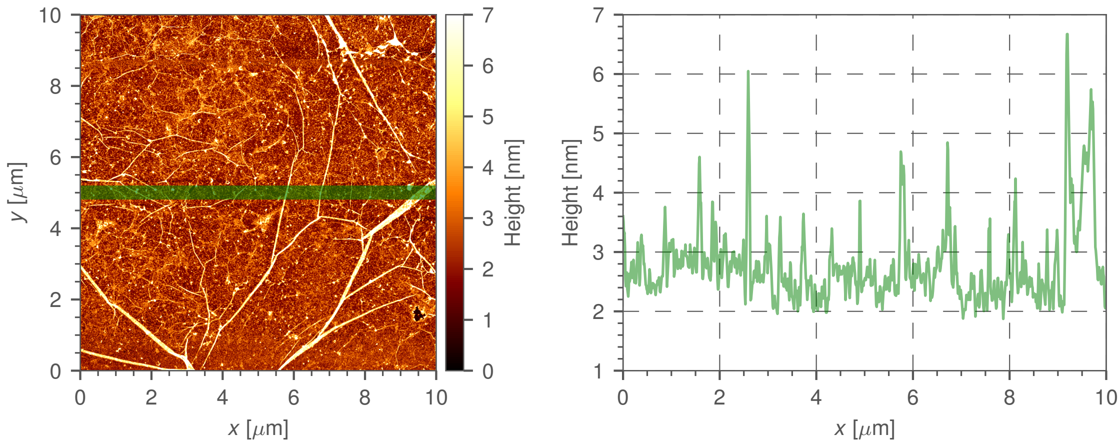

Fig. 4.22: AFM measurement of graphene transferred to SiO_2 substrate. The green bar shows the area from which the height distribution was extracted over 40 lines. The surface of the SiO_2 substrate is nearly fully covered with graphene (inside the scanned area). The few strong wrinkles may originate from the transfer process or the synthesis process due to the different thermal expansion coefficients of the Cu film and the graphene on the surface.

Figure 4.24 shows the results for the position and FWHM of the Raman 2D-peak for the different fluences as well as the peak intensity ratios, recorded within an area of $50 \times 50\,\mu\mathrm{m}^2$ [9].

As shown in figure 4.24a, the values for the FWHM increase from $\approx 34\,\mathrm{cm}^{-1}$ over $\approx 36\,\mathrm{cm}^{-1}$ and $\approx 38\,\mathrm{cm}^{-1}$ to $\approx 55\,\mathrm{cm}^{-1}$, whereas the 2D-peak position increases from $\approx 2685\,\mathrm{cm}^{-1}$ over $\approx 2686\,\mathrm{cm}^{-1}$ to $\approx 2690\,\mathrm{cm}^{-1}$ with increasing ion fluence. The 2D-peak position for the highest implanted fluence could not be determined accurately due to the very low signal of the 2D peak. This fact is reflected in the very large error bar. The determined values show again the possibility to adjust the graphene thickness by the amount of implanted carbon. Although the Cu lattice of the films had Cu(111) orientation, no stacked graphene was obtained. Again, no domains with an enhancement in the G-peak intensity due to resonances with the Raman laser line were found [160] as for the graphene synthesised on Cu foils.

The G/2D-peak intensity ratio averaged over the 2500 recorded spectra was obtained by summation over a region of interest window of $1320-1440\,\mathrm{cm}^{-1}$ for the D-peak, $1520-1620\,\mathrm{cm}^{-1}$ for the G-peak and $2600-2750\,\mathrm{cm}^{-1}$ for the 2D-peak for each implanted fluence, respectively, with the result shown in figure 4.24b. The G/2D values increase with increasing fluence from 0.34 ± 0.08 over 0.65 ± 0.10 and 0.80 ± 0.22 to 5.45 ± 3.1 which reflects the increase in layer number with the amount of implanted ions, the same way as found for the graphene from the Cu foils. The large value for the highest fluence is due to the very low intensity of the 2D peak. The error bars, determined by combining the uncertainties of the G- and 2D-peak intensities, reflect the homogeneity of the graphene within the scanned area in terms of the thickness.

The D/G ratios shown in figure 4.24b have no strong variation upon ion fluence. This was also the case for the graphene synthesised on the Cu foils. This indicates that the surface damage in the Cu films accumulated in the ion implantation process is, like in case of the Cu foils, not the main reason for the presence of the D-peak. Here, the D-peak may also appear due to PMMA residuals originating from the transfer process. The small error bars reflect a homogeneous distribution of defects within the scanned area for all fluences. They were determined by combining the uncertainties of the D- and G-peak intensities.

---

[9] Note that again for illustration reasons, the G/2D ratio is used in contrast to section 4.1.2 where the 2D/G ratio was used.

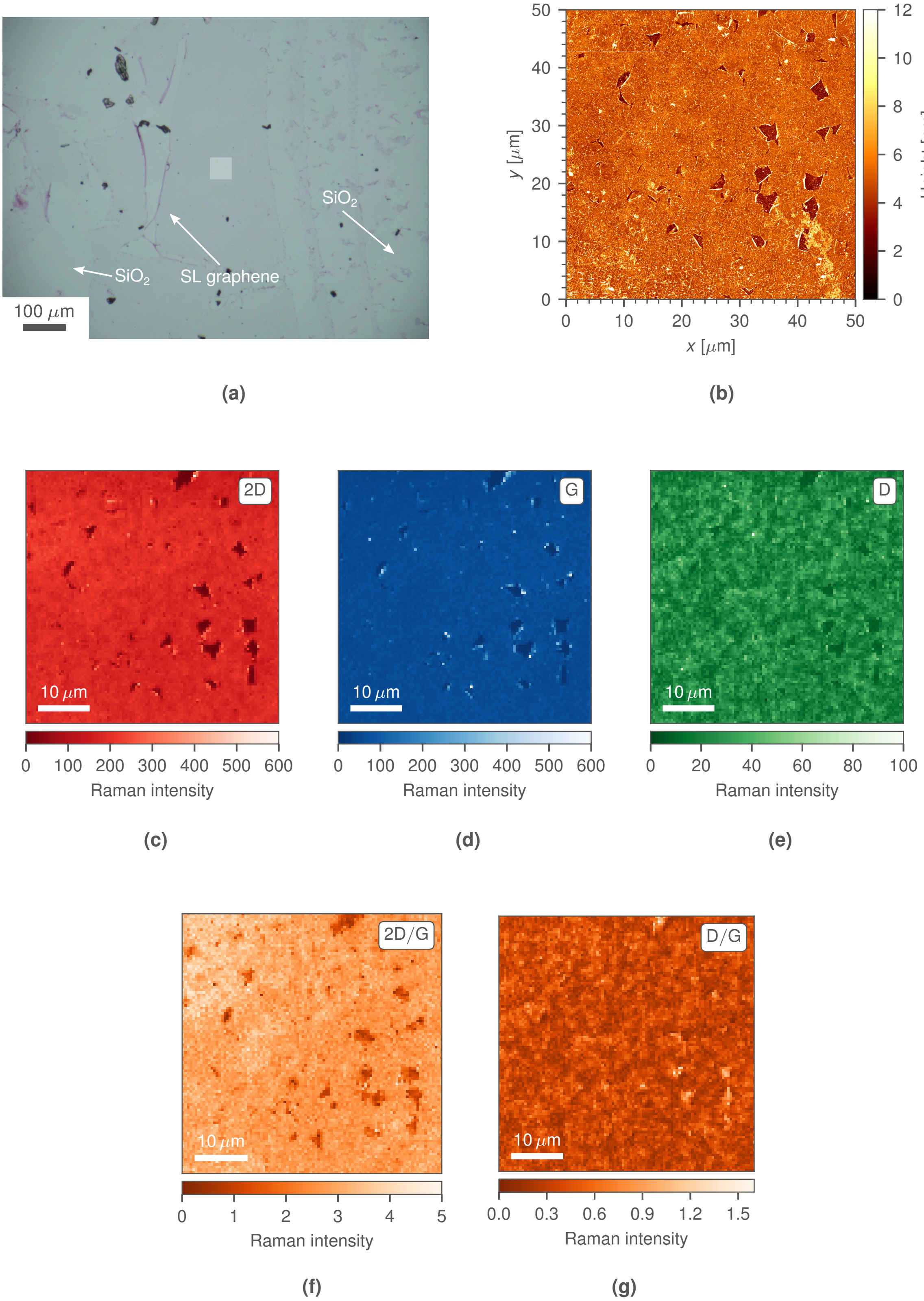

Fig. 4.23: Graphene characterisation on an area of 50 × 50 μm^2. (a) Optical image with indication of the area in which Raman and AFM measurements were performed. (b) AFM measurement which shows holes in the graphene. (c)-(g) Raman maps of the 2D-peak, the G-peak, the D-peak intensities and the 2D/G and D/G peak intensity ratios extracted from the spectra measured within the indicated region in (a).

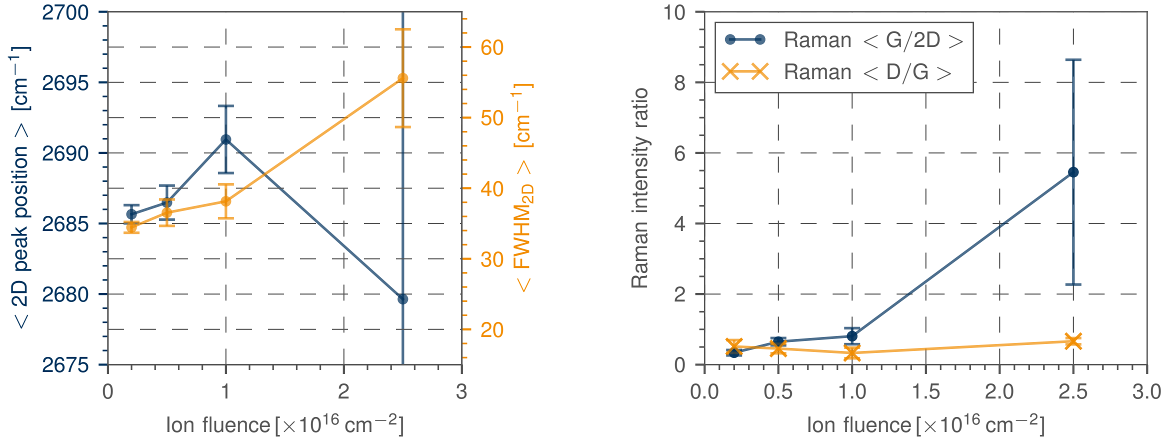

(a) **(b)**

Fig. 4.24: (a) Average of 2D-peak position and FWHM as a function of the implanted fluence. Error bars represent the standard deviation within the 2500 spectra recorded for each fluence. (b) Average of G/2D and D/G peak ratio of graphene on SiO_2/Si as a function of the implanted ion fluence. Error bars were determined by combining the uncertainties of the D-, G- and 2D-peak intensities for all 2500 spectra of each fluence, respectively.

4.2.3 Summary

In summary, the low-defect graphene synthesis by ion implantation into cleaned Cu(111) thin film templates and subsequent annealing is possible. Furthermore the thickness of the graphene could be controlled by the amount of implanted ions. The graphene was transferred to a SiO_2/Si wafer by a PMMA wet etching method. The D-peak intensity varies only slightly with the implanted fluence. The highest graphene quality was obtained for monolayer graphene. The coverage of the SiO_2 wafer with graphene is limited by holes in the graphene which may arise from the etch holes in the Cu thin film after the pre-annealing step. Small wrinkles are present after the transfer process with may originate from the transfer process itself [212].

4.3 Comparison of graphene synthesised on Cu foils and Cu films

Graphene was synthesised both on Cu foils (transferred with the third transfer method) and Cu thin films. The mean values for the different parameter determined by RAMAN spectroscopy are shown in table 4.1 and 4.2. Note that the values correspond to the implantation of ^{12}C.

For the synthesis of monolayer graphene, the fluence was reduced from $5 \cdot 10^{15}\,\mathrm{cm}^{-2}$ in case

Fluence [$\times 10^{16}\,\mathrm{cm}^{-2}$]	2D pos [cm^{-1}]		2D FWHM [cm^{-1}]	
	Foil	Film	Foil	Film
0.2	-	2685.6 ± 0.6	-	34.4 ± 0.7
0.5	2678.1 ± 1.3	2686.4 ± 1.2	31.2 ± 2.3	36.5 ± 1.8
1.0	2681.1 ± 2.1	2690.9 ± 2.4	40.4 ± 3.5	38.1 ± 2.4
2.5	2688.2 ± 4.2	2679.6 ± 24.2	53.2 ± 10.3	55.5 ± 6.9

Table 4.1: Overview of the RAMAN peak position and FWHM of the 2D peak of graphene for the Cu foils and Cu films implanted with different fluences.

of the Cu foils to $2 \cdot 10^{15}\,\mathrm{cm}^{-2}$ for the Cu thin films. The reason for the reduced need of carbon lies in the decreased amount of carbon which segregates at the grain boundaries within the Cu template (see section 4.2.2). In general, for the graphene synthesis on the Cu films, less carbon is needed for the same graphene thickness compared to the Cu foils, which is visible, e.g. from the G/2D ratio values.

The 2D-peak position is shifted to higher wave numbers in case of the graphene synthesised on the Cu films and transferred via PMMA method. This shift indicates a doping of the graphene which may originate from the PMMA residuals. The 2D-peak position for the fluence of $2.5 \cdot 10^{16}\,\mathrm{cm}^{-2}$ in case of the Cu films could not be determined accurately due to the very low Raman intensity. Thus, with this high fluence, graphitic material was synthesised. The FWHM of the 2D-peak is slightly increased in case of the graphene synthesised on the Cu films. This could be again due to the doping resulting from PMMA residuals. In general, the values for the 2D-peak position and the FWHM increase with increasing ion fluence which shows the dependence of the graphene thickness on this parameter.

Fluence $[\times 10^{16}\,\mathrm{cm}^{-2}]$	G/2D		D/G	
	Foil	Film	Foil	Film
0.2	-	0.34 ± 0.08	-	0.51 ± 0.18
0.5	0.22 ± 0.04	0.65 ± 0.10	0.82 ± 0.22	0.45 ± 0.138
1.0	1.09 ± 0.29	0.80 ± 0.22	0.36 ± 0.08	0.33 ± 0.15
2.5	1.91 ± 0.50	5.4 ± 3.1	0.45 ± 0.11	0.66 ± 0.09

Table 4.2: Overview of the Raman intensity for the G/2D and D/G peak ratios of graphene for the Cu foils and Cu films implanted with different fluences, measured in an area of $10\,\mu\mathrm{m} \times 10\,\mu\mathrm{m}$.

The G/2D values also show a dependence on the implanted amount of ions which indicates a dependence of the thickness on the ion fluence. Graphene synthesised on Cu films show a smaller D-peak intensity. The homogeneity of the defects within the graphene is similar for graphene from the Cu foils and graphene from the Cu thin films. The strong wrinkles observed for the graphene from the foils due to the PMMA-free transfer process and the non flat Cu foil were not observed for graphene transferred from the Cu films. Here, only small wrinkles were observed which originate from the transfer process as well. Also, the dimensions of the grain boundaries were much smaller in case of the Cu films compared to them in the Cu foils which might also have an influence on the dimension of the graphene wrinkles.

The domain size for graphene from the Cu foils is limited by the grain size of the Cu foils itself and can be close to 1 mm. In case of the Cu films, it seems that the size of graphene domains without any holes is only limited by the number and size of the etch holes which appear in the Cu film after pre-annealing. On average, for monolayer graphene synthesised on Cu films, the maximal domain size without holes was around $10 \times 10\,\mu\mathrm{m}^2$.

Chapter 5

Electrical characterisation of graphene on SiO_2

In this chapter, the electrical properties of the synthesised graphene are presented. First, the results of the sheet resistance measurements are discussed and second the transport measurements which were performed on structured graphene are presented. An overview over the techniques used for the structuring of the graphene will be given as well.

5.1 Sheet resistance measurement

Electrical characterisation was done by VAN DER PAUW measurements [219] without any lithography, performed on the graphene.

The sheet resistance ρ/d with ρ as the specific resistance and d as the thickness of the graphene film was measured in a home built $I-V$ measurement system. This is equipped with 4 tips ($15\,\mu$m thick at the end), micromanipulators S-725 from SIGNATONE, a LEICA stereo microscope and a KEITHLEY 2602A System SourceMeter. The setup is shown in figure 5.1a, a sample contacted by the 4 tips in figure 5.1b. Prior graphene characterisation, the proper function the setup was verified by measuring a known resistor and different diodes.

In order to measure the sheet resistance without the influence from the contacts themselves, the VAN DER PAUW geometry was used [219]. Several assumptions have to be made for the validity of this method [220, 221]. The sample has to have a uniform thickness, it should not contain any isolated holes, the contacts have to be applied at the edges of the sample and they have to be small compared to the dimension of the sample.

The sheet resistance can then be calculated by [219]

$$e^{-\pi\frac{d}{\rho}R_{\mathrm{AB,CD}}} + e^{-\pi\frac{d}{\rho}R_{\mathrm{BC,DA}}} = 1. \tag{5.1}$$

The resistance $R_{\mathrm{AB,CD}}$ is measured by applying a current between the contacts A and B and measuring the voltage between C and D. This type of measurement is shown in figure 5.1b. The $I-V$ curve can be fitted and the slope gives the ohmic resistance. After this, the contact assignment is changed to measure the resistance $R_{\mathrm{BC,DA}}$. With these two resistance values, equation (5.1) can be solved and the sheet resistance ρ/d can be determined. The solution was found by use of the NEWTON-method [222]. For this, a PYTHON script was written which is given in appendix C.4.

To measure a current and voltage over the whole sample (dimension of $1\,\mathrm{cm}^2$), the graphene has to be without any large holes that would disconnect any of the four contact areas from each

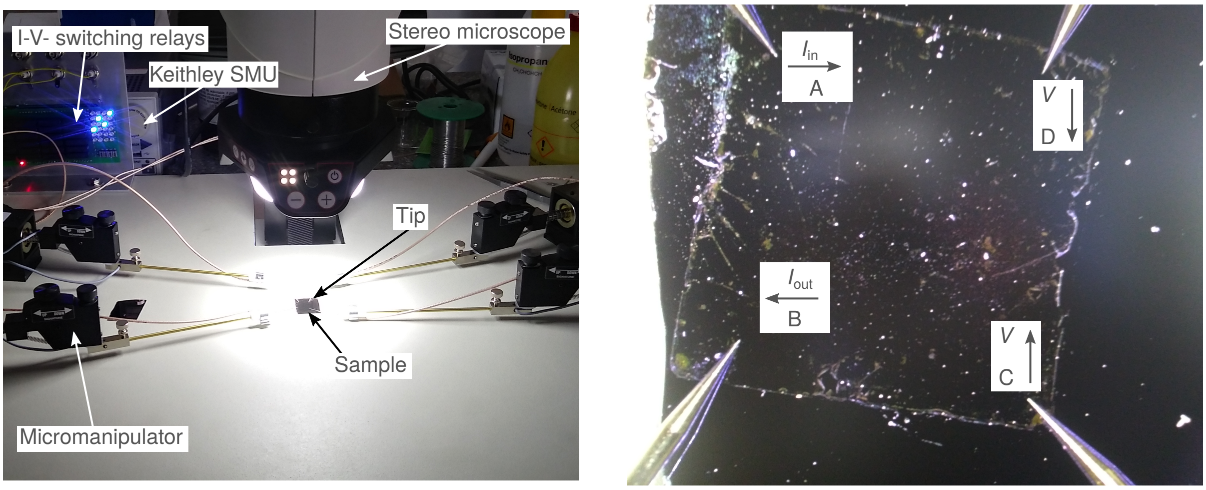

(a) (b)

Fig. 5.1: Home built *I-V* measurement system. (a) The individual parts of the measurement system and (b) a sample contacted by the 4 tips.

other. Figure 5.2 shows the result of a $I-V$ measurement for samples synthesised with a fluence of $2 \cdot 10^{15}\,\mathrm{cm}^{-2}$ (figure 5.2a) and $5 \cdot 10^{15}\,\mathrm{cm}^{-2}$ (figure 5.2b).

The first sample shows a very high resistance of $\approx 171\,\mathrm{M\Omega}$ and $\approx 245\,\mathrm{M\Omega}$ for $R_{\mathrm{AB,CD}}$ and $R_{\mathrm{BC,DA}}$, respectively. The sheet resistance was calculated to $\rho/d \approx 933.7\,\mathrm{M\Omega}/\square$. In order to exclude conduction problems between the needles and the sample, Ti contacts were fabricated on the edges of the sample by ion beam sputtering (see section 2.3). For this, the sample was covered with an aluminium mask leaving the edges uncovered. The repeated measurements showed the same results. The high resistance may be due to the graphene being not fully closed over this large area.

To solve this and to obtain an at least fully closed film (but maybe not of homogeneous thickness over the $1 \times 1\,\mathrm{cm}^2$), the fluence was increased as described above. This sample shows a resistance between A and B of $R_{\mathrm{AB,CD}} = (572.6 \pm 0.42)\,\Omega$ and between B and C of $R_{\mathrm{BC,DA}} = (541.17 \pm 0.67)\,\Omega$. The uncertainties are the errors of the linear fits of the $I-V$ curves. These values give a sheet resistance of $\rho/d = 2525.547\,\Omega/\square$ which is comparable to values from the literature [223–227] which may be due to the wrinkles within the graphene sheet which may act as resistors.

5.2 Electrical characterisation and transport measurements

5.2.1 Structuring of graphene

In order to measure further the electrical properties of the synthesised graphene, the graphene had to be structured. Two different approaches were tested, first the structuring with a He$^+$-ion beam of a He-microscope (ORION NanoFab) [228] from ZEISS at the UFZ in Leipzig[1] that would allow a direct removal without the need of PMMA masks. The second approach was done by help of e-beam lithography at the SUM group of the University of Leipzig[2].

---

[1] UFZ - Helmholtz-Zentrum für Umweltforschung Leipzig, together with Dr. Matthias Schmidt.

[2] Together with Dr. José Luis Barzola-Quiquia, Division of Superconductivity and Magnetism, Faculty of Physics and Earth Sciences of the University of Leipzig.

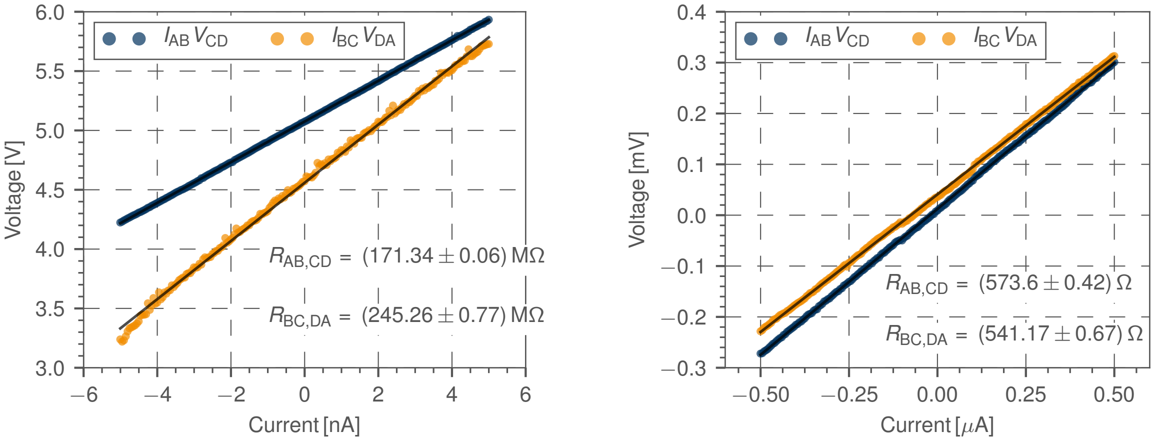

(a) **(b)**

Fig. 5.2: *I-V* curve measurement for a sample implanted with a fluence of $2 \cdot 10^{15}\,\mathrm{cm}^{-2}$ (a) and with a fluence of $5 \cdot 10^{15}\,\mathrm{cm}^{-2}$ (b). The high resistance of the sample with lower fluence may originate from a not fully closed graphene film. The black line shows the respective linear fit of the measured curve. Note that the dimensions for the current and the voltages in (a) and (b) are different.

Structuring with He-microscope

For the structuring by use of the He microscope, a purchased sample (GRAPHENEA) was used in order to establish the He^+ fluences required for graphene removal. For this purpose it was tested whether it is possible to derive by characterisation of the sample (position and quality of the graphene) where structures have been introduced into the graphene. Once it became clear that the graphene is not immediately destroyed by scanning over it with the He^+ beam, 3 lines were drawn within the scanning software. These lines have the same area A but different widths (and thus different lengths) in order to investigate the smallest possible structure which can be written. The energy of the ions was 25 keV, the beam current 1 pA and the applied fluence $1 \cdot 10^{15}\,\mathrm{cm}^{-2}$. The results are shown in figure 5.3.

As shown in figure 5.3a, the areas which were scanned by the He^+ ion beam show a higher RAMAN D/G peak intensity ratio indicating defects which were created in these areas. In figure 5.3b, RAMAN spectra for the respective positions are given. Outside of the lines, the graphene has no significant defects whereas within the lines, the spectra show a strong defect peak. Nevertheless, also within the lines, a 2D peak is still present. Thus, a total removal of the graphene from the surface within the scanned areas was not successful for a fluence of $1 \cdot 10^{15}\,\mathrm{cm}^{-2}$. To remove the graphene completely (or the residual carbon after the graphene is converted to amorphous carbon due to the through the ion beam induced damage), the fluence has to be increased to an amount for which the irradiation time for an ion current of a few pico amperes would increase to a non-practical value.

Note, however, that with this technique, local defect engineering would be possible in order to change the electronic properties of the graphene [229–231].

Structuring with e-beam lithography and fabrication of electric contacts

For the e-beam lithography a sample was prepared with a fluence of $2 \cdot 10^{15}\,\mathrm{cm}^{-2}$ (450 nm Cu, pre-annealed at 1020 °C, 20 min, post implantation annealing at 1020 °C, 30 min).

As already mentioned in the previous section, structuring of graphene on a large scale is not easily possible by ion beams (at least not in the micrometre or millimetre regime). Therefore,

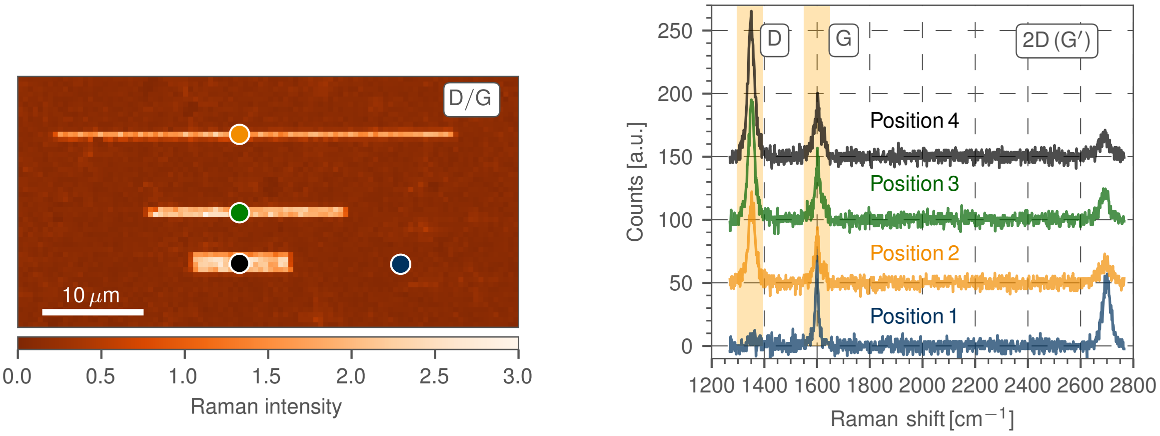

(a) (b)

Fig. 5.3: RAMAN characterisation of graphene, irradiated with 25 keV He^+ ions. (a) Shows a RAMAN map of the D/G peak intensity ratio. The highest intensities are in the irradiated area. (b) Shows RAMAN spectra, exported from the coloured positions within the map in (a) with indication of the ROI which was used for the map in (b).

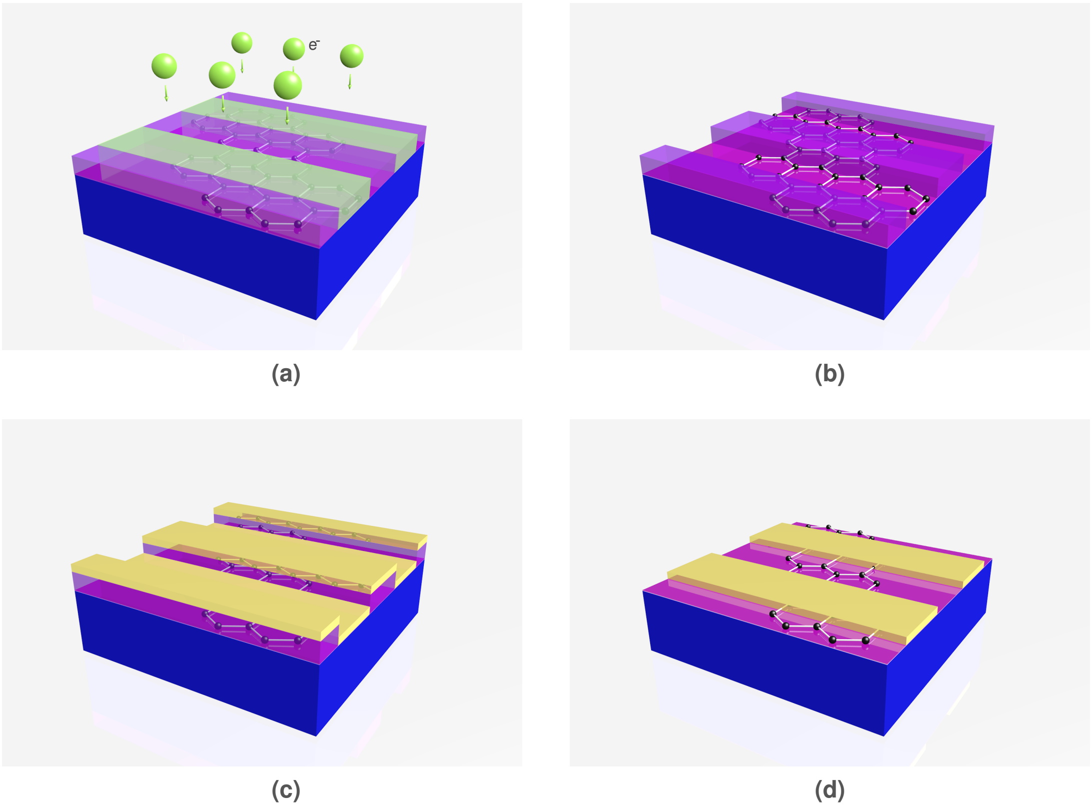

Fig. 5.4: Individual steps for the preparation of the contacts by e-beam lithography. (a) Shows the spin coated sample under e-beam exposure. (b) Shows the sample after chemical development and (c) after metal deposition. (d) The final sample with metallic contacts after PMMA removal (lift-off of the metal).

e-beam lithography was used in order to structure the graphene on a larger scale. Also large scale contacts were built on the graphene by use of this technique.

An overview of the different steps required for the structuring of the graphene and the fabrication of contacts is shown in figure 5.4. First, the sample is coated with a positive photoresist (PMMA) using a spin coater. The sample was coated for 10 seconds with 6000 rpm. Afterwards, the whole stack was baked in an oven at 180 °C for 20 minutes, resulting in a homogeneous PMMA layer with a thickness of approximately 300 – 400 nm. The coated sample is exposed with a 10 keV electron beam with a current of 0.58 nA by help of a FEI NovaLab SEM controlled by an ELPHY PLUS pattern generator from Raith GmbH (figure 5.4a). With this pattern generator, it is possible to scan the electron beam in a defined was over the sample. During the exposure, the electrons penetrate into the PMMA and cause modification of the PMMA molecular structure due to elastic collisions between the electrons and the atoms of the resists. This modification allows the removal of the irradiated areas (they become more soluble in the developer solution). For this, the sample was dipped in the developer AR 600-551 for a total time of approximately 20 seconds. Immediately after that, the sample was put in AR 600-602 for one minute to neutralise the solvent. The written structure can now be seen in the resist (figure 5.4b).

To remove the graphene in the uncovered areas, oxygen plasma was used. For this purpose, the graphene was dry-etched in a reactive-ion etching (RIE) chamber. The sample was exposed to a Ar/O plasma (90%; 10%) at a pressure of 26.7 mbar (20 mTorr), the inductively coupled plasma power were 50 W.

An example for structured graphene is shown in figure 5.5. Figure 5.5a shows an optical image of the graphene. The structured (appear brighter) areas are indicated. A Raman map was performed within the structured areas in order to investigate the amount of removal of the graphene. The 2D-peak intensity map is shown in figure 5.5b. The coloured dots indicate the positions from which Raman spectra were exported, they are shown in figure 5.5c. In the plasma etched areas, almost no graphene is present anymore.

Influence of the PMMA coating

The influence of the PMMA coating and removal was investigated by Raman spectroscopy. The results are shown in figure 5.6. In figure 5.6a and 5.6b, the D/G Raman intensity ratios are shown before and after the structuring process, respectively. The mean value before the PMMA coating procedure was 0.57 ± 0.19. No strong change was observed after structuring. The D/G ratio became 0.47 ± 0.27. The reason why the value has even decrease indicating lower defect denisty may lie in the fact that the position of the Raman measurement was not the same. The 2D-peak position seems slightly red-shifted from $2684.53\,\mathrm{cm}^{-1} \pm 2.12\,\mathrm{cm}^{-1}$ before the structuring process to $2687.21\,\mathrm{cm}^{-1} \pm 3.09\,\mathrm{cm}^{-1}$ after the process. This shift may originate from PMMA residuals [232]. The large variance for the 2D-peak position after the structuring process also shows that the graphene has become more inhomogeneous.

Fabrication of contacts

In order to fabricate contacts on the graphene, the first two steps in figure 5.4 were repeated. Now as a third step, ohmic contacts were prepared on the graphene. For this, chrome and gold were thermally evaporated in high vacuum conditions and then deposited on the substrate, as shown in figure 5.4c. A bilayer film consisting of 5 nm chrome and 30 nm gold were used to form the electrodes. The chrome layer is used in order to improve adhesion of the contacts on the sample surface. The pressure in the sputtering chamber was 10^{-6} mbar and the working pressure of the Ar gas was 10^{-3} mbar. As final step, the remaining PMMA is removed by acetone leaving a contacted sample as shown in figure 5.4d.

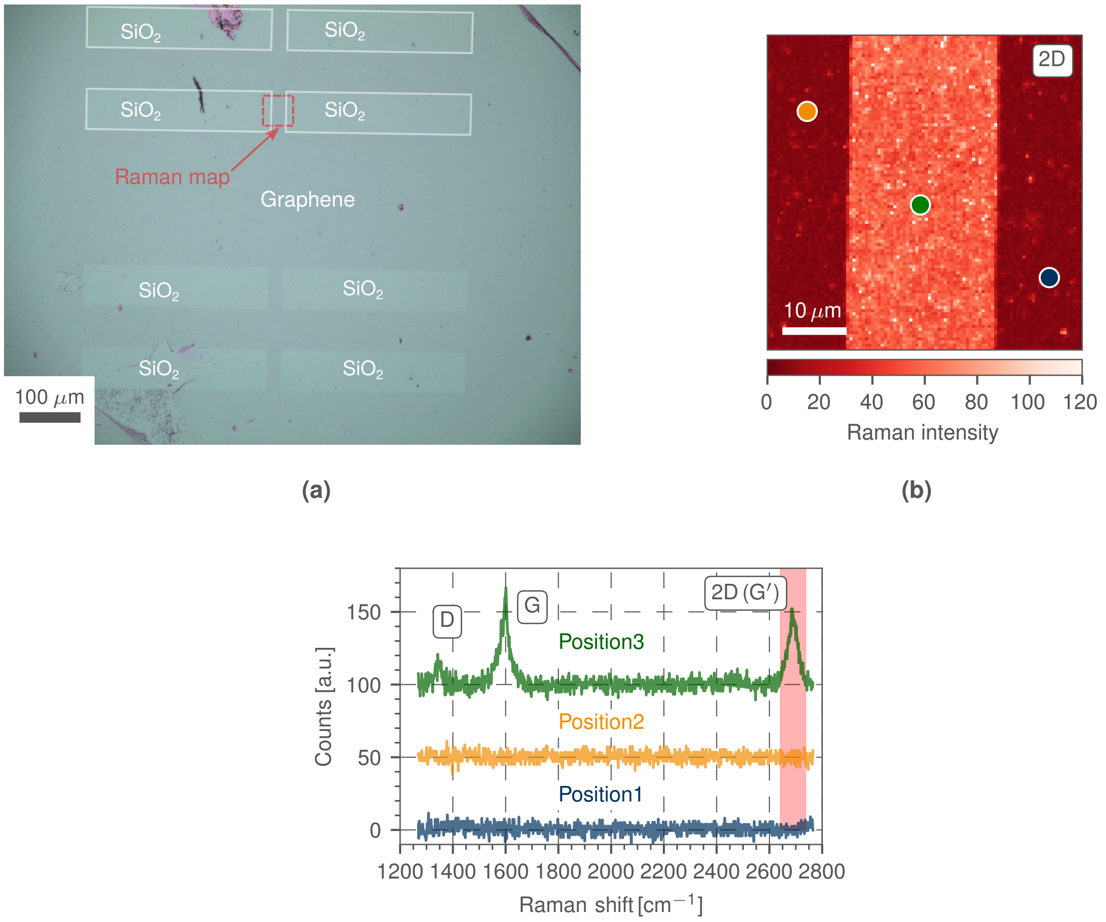

(a)

(b)

(c)

Fig. 5.5: Structured graphene sample. (a) Optical image with indication of the removed area. (b) RAMAN 2D-peak intensity within the area indicated by the red square in (a). (c) Exported spectra from the 2D-RAMAN map.

5.2.2 Resistance - Temperature dependency and transport measurement

Due to the better conductivity, the sample implanted with $5 \cdot 10^{15}$ cm^{-2} was used for the transport measurements. To prepare the sample for transport properties measurements, it was contacted with gold wires of 25 μm diameter. The gold wires were fixed on the substrate with G3303A silver paste. The sample was then left to dry for about 20 minutes. Afterwards, the sample was mounted on a sample holder using varnish. The 4-point probe method was employed for transport measurements [233]. Figure 5.7 shows the graphene with electric contacts made with the method described in section 5.2.1. Via contact A and D a current is inserted and the voltage is measured between contact B and C. The distance between neighbouring contacts was approximately 400 μm.

With this setup, the temperature dependence of the electrical resistance and transport properties were measured which are described in the next two sections.

Temperature dependence of the resistance

Figure 5.8 shows the conductance as a function of temperature. The measured curve was fitted by a sum of two contributions, the variable range hopping (VRH) mechanism and the conductance

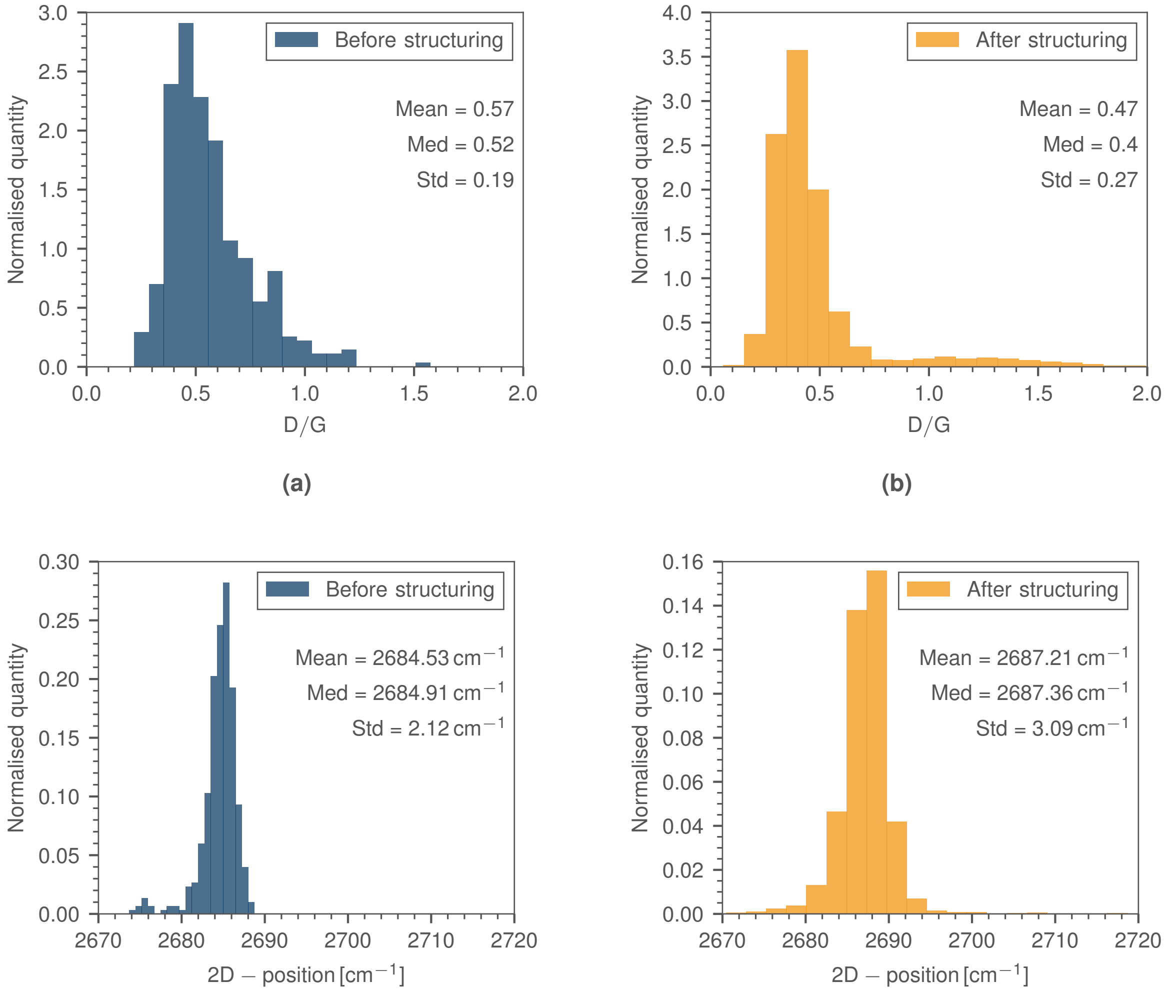

(a) **(b)**

(c) **(d)**

Fig. 5.6: RAMAN characterisation of graphene before and after the structuring process. (a) and (b) shows the D/G RAMAN peak intensity ratio which is nearly the same before and after the process. (c) and (d) shows the 2D-peak position, which is slightly red-shifted after the structuring process.

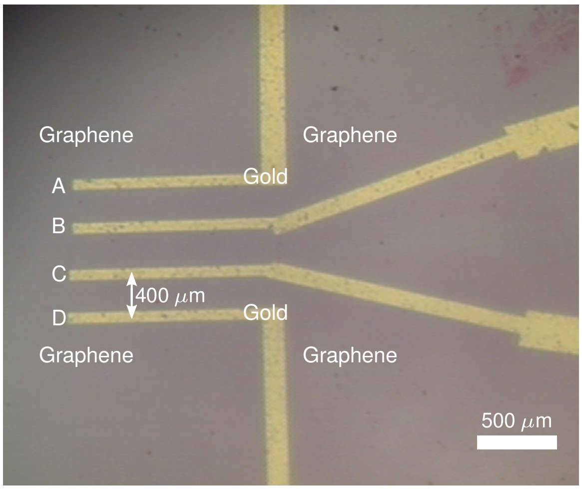

Fig. 5.7: Graphene on SiO_2 with Cr/Au contacts for measurement of resistivity and transport properties.

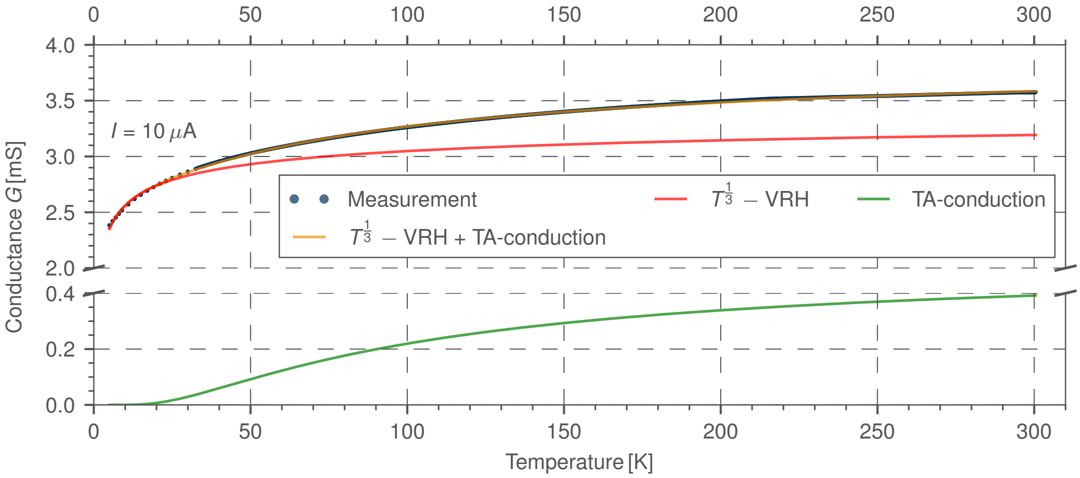

Fig. 5.8: Conductance as a function of temperature. The VRH dominates the conduction mechanism. However, at temperatures above 20 K thermally activated charge carries also contribute to the conduction. The orange curve is the sum of the two different conduction mechanisms. Note that the y-axis is separated into two parts.

via thermally activated charge carriers. The VRH shows a $T^{\frac{1}{3}}$ behaviour [234] via

$$\sigma_{\mathrm{VRH}} = \sigma_{0,\mathrm{VRH}} \exp\left(-T_0/T^{1/(1+d)}\right), \tag{5.2}$$

with $\sigma_{0,\mathrm{VRH}}$ as a free pre-factor, T_0 a characteristic temperature coefficient and d as the dimensionality, here 2 [233]. For the thermally activated band conduction in a semiconductor film, the conductance can be expressed by

$$\sigma_{\mathrm{th}} = \sigma_{0,\mathrm{th}} \exp\left(-\frac{E_\mathrm{a}}{k_\mathrm{B}\,T}\right), \tag{5.3}$$

where $\sigma_{0,\mathrm{th}}$ is a constant pre-factor, E_a is the activation energy, and k_B is BOLTZMANNs constant [235].

The sum of both conduction mechanisms

$$G = \sigma_{\mathrm{VRH}} + \sigma_{\mathrm{th}} \tag{5.4}$$

fits the measured data well as can be seen by the orange curve in figure 5.8.

The conduction at temperatures below 20 K is dominated by the VRH. For higher temperatures, a part of the conduction that increases with temperature is due to thermally activated charge carriers. The same behaviour for graphene is reported in the literature [236]. The values for the parameters are $\sigma_{0,\mathrm{VRH}} = 0.003500 \pm 4 \cdot 10^{-6}$, $\sigma_{0,\mathrm{th}} = 0.000520 \pm 2.4 \cdot 10^{-6}$, $T_0 = 0.340 \pm 4 \cdot 10^{-3}$ and $E_\mathrm{a} = (0.0150 \pm 1 \cdot 10^{-4})\,\mathrm{eV}$. The activation energy of around 15 meV which is reasonable compared to other results reported for thin films [235, 237].

EFROS-SHKLOVSKII proposed to fit the measured data with $d = 1$ in equation (5.2) in case that a bandgap is present at the FERMI level [238], together with a fluctuation-induced tunnelling model [239, 240] relevant for low temperatures [233]. This approach was not successful for the data presented in figure 5.8.

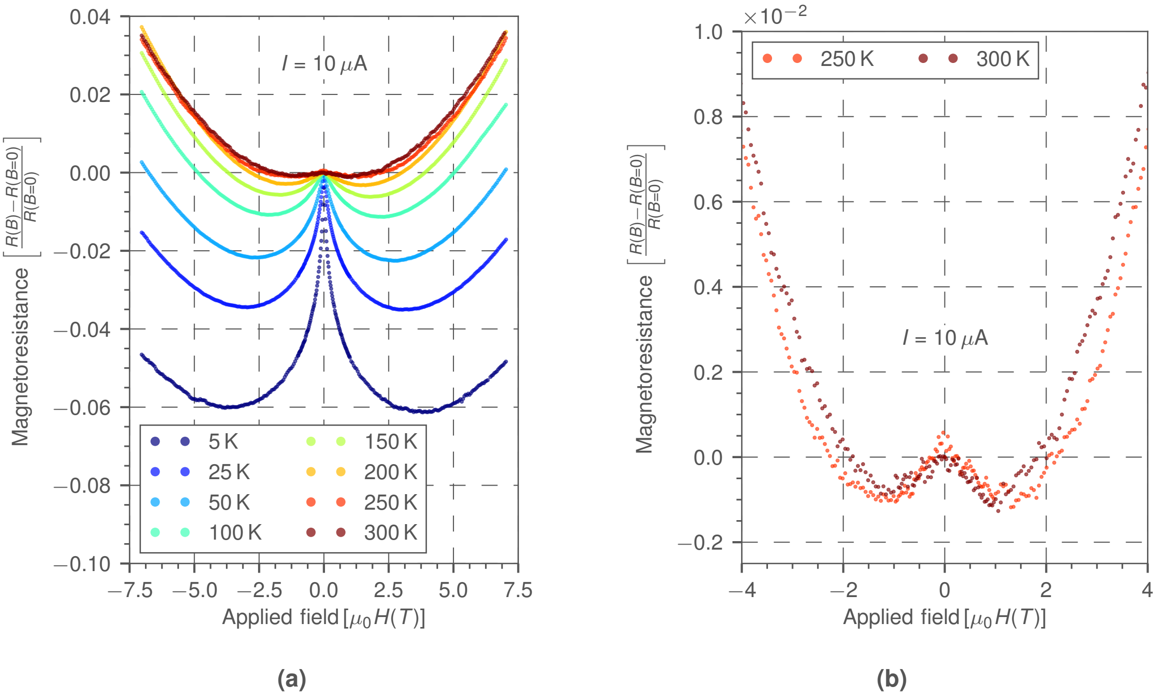

Fig. 5.9: Magnetoresistance measurements at (a) different temperatures and (b) for $T = 250\,\mathrm{K}$ and $T = 300\,\mathrm{K}$. Also for these temperatures a negative magnetoresistance was measured at lower magnetic fields.

Weak localisation and negative magnetoresistance

As described in section 1.1.3, a change of the resistance is expected if an external magnetic field is applied to the sample. Figure 5.9a shows the normalised magnetoresistance measurements as a function of the magnetic field applied perpendicular to the sample. The current through the sample was chosen to be $10\,\mu$A. The measurements were performed for a temperature range between 5 K and 300 K. The measurement geometry was the same as explained in figure 5.7.

The magnetoresistance is negative[3] for all measured temperatures, even at room temperature for lower magnetic fields. This is in contrast to the literature where the negative magnetoresistance was only reported for temperatures of a few K [70] or the magnetoresistance was positive at all [69]. The negative magnetoresistance at low temperatures can be well understood by weak localisation, as explained in 1.1.3. However, for room temperature this effect cannot be explain the negative magnetoresistance. One explanation could be that due to the defects in the graphene, a certain disorder is present that leads to ANDERSON localisation [241, 242]. This could be checked, e.g. by creating a higher amount of disorder by irradiation of the graphene with ions and measuring the transport properties afterwards again [243]. This however, is not part of this thesis.

5.2.3 Summary

A maskless structuring of the graphene films with a He$^+$ ion beam from a He ion microscope was not possible because the removal of the graphene takes too long to be feasible. Therefore, the graphene was structured by e-beam lithography. The electrical characterisation was performed on graphene sheets with $\approx 1\,\mathrm{cm}^2$ in size by use of the VAN DER PAUW geometry and reveals sheet resistances of the order of M$\Omega/\square$ to k$\Omega/\square$, depending on the implanted ion fluence.

---

[3] That means the change of the resistance is negative, i.e. it becomes smaller.

The temperature dependence of the resistance showed a semiconductor-like behaviour. For temperatures below 20 K, $T^{1/3}$-VRH dominates. For higher temperatures, VRH still dominates but also thermal activation of the charge carries contributes. Negative magneto-resistance was found for all temperatures between 5 K and 300 K. For low temperatures, this may originate from weak localisation. The reason for the negative magneto-resistance at high temperatures could not be clearly identified.

Chapter 6

Summary and outlook

The aim of this work was explore the potential of carbon ion implantation in copper for the synthesis of graphene. As template for the graphene synthesis, commercially available copper foils as well as Cu thin films fabricated via physical vapour deposition were used. These templates were investigated by AFM, SEM, XRD, XPS and RAMAN-spectroscopy before and after heat treatment in order to characterise the roughness, surface texture, grain sizes, crystal orientation and the content of carbon residuals. Afterwards, they were implanted with carbon ions with a specific fluence. An additional anealing step allowed the carbon to move to the surface, segregate there and form graphene.

The used copper foils with a purity of 99.9999% and a thickness of 50 μm showed large scratches before annealing, which originate from the fabrication process. After pre-annealing at 950 °C for 2 h in vacuum, the foils exhibited a Cu(200) crystal orientation. Grain sizes up to 900 μm in diameter were found. The RMS surface roughness on the grains was determined to 10 nm. No carbon was found on the surface of the foils by RAMAN spectroscopy after the pre-annealing step.

The Cu thin films (thickness 200 nm - 450 nm) prepared by Cu sputter deposition on c-plane $Al_2O_3(0001)$ substrates (1 cm × 1 cm in size) showed Cu(111) crystal orientation directly after deposition, but no single crystallinity. The deposition was performed at room temperature. The grain sizes were $\sim$ 40 nm in diameter. A carbon contamination on the surface was detected which may originate from the residual gas in the sputter chamber. The films were annealed under vacuum conditions at different temperatures between 300 °C and 900 °C for 1 h each, and 1020 °C for 20 min. It could be shown that temperatures above 850 °C are required for a sufficient mobility of the carbon atoms in the Cu film to allow for purification from carbon contamination. Etch holes of hexagonal shape appeared after heat treatment above 800 °C. The surface roughness values were below 4 nm after treatment at 1020 °C. The residual carbon on the surface was removed by an UV-ozone cleaning procedure. RBS measurements revealed that a diffusion of the Cu film in to the Al_2O_3 substrate occurs at temperatures above 750 °C. Because of this diffusion, the annealing time for Cu films was reduced from 1 h to 20 min for the high temperature annealing process. In addition, the thickness of the Cu was increased from 200 nm to 450 nm.

Cu films were also prepared at temperatures between 450 °C and 600 °C by magnetron sputtering. A heater stage was specially built and used for this purpose. The films exhibited improved properties in terms of crystal quality and roughness compared to Cu films deposited at room temperature. The values were also better compared to samples sputtered at room temperature and annealed afterwards at high temperature. A carbon segregation on the surface during the sputter deposition procedure could only be achieved at sputter temperatures above 600 °C. However, at these temperatures, no complete Cu film on the sapphire substrate was formed. The grain sizes were found to be only 10 μm in diameter. Thus, these templates were not used for the synthesis of graphene.

First, the graphene was synthesised on the Cu foils. For this, they were implanted with C^+ ions with a fluence of $5 \cdot 10^{15}\,\mathrm{cm}^{-2}$ and an energy of 35 keV. The post-annealing was performed at 850 °C for 1 h in vacuum. The graphene was transferred from the Cu foils by a novel PMMA-free wet chemical etching process. The etchant was prepared by dissolving $(NH_4)_2S_2O_8$ in millipure water in a molar ratio of 0.1 : 125. The dissolution of the Cu foil took approximately 2 h. With this method, no flat but only rolled/curved graphene could be achieved after transfer to SiO_2/Si. To avoid this shrinking of the graphene the process was modified by heating the water used to wash the graphene after etching the Cu foil up to 90 °C in order to reduce the surface tension. With this approach, flat graphene on SiO_2/Si was obtained. Raman mapping was performed and showed a 2D-peak position of $2679.89\,\mathrm{cm}^{-1} \pm 1.20\,\mathrm{cm}^{-1}$ which indicates single layer graphene. A D- and G-peak intensity ratio of $I(\mathrm{D})/I(\mathrm{G}) = 3.35 \pm 0.44$ was observed which gives an inter-defect length of $L_\mathrm{D} \approx 6.6$ nm and a crystallite size of $L_\mathrm{a} \approx 5.8$ nm. Compatible with this high defect density, the FWHM of the 2D-peak was determined to $38.9\,\mathrm{cm}^{-1} \pm 4.58\,\mathrm{cm}^{-1}$. Another transfer method using a different etch solution was used. The etchant was prepared by mixing $FeCl_3$, HCl, and H_2O in a molar ratio of 1.2 : 1 : 174, respectively. After approximately 40 min, the dissolution of the Cu foil was complete and the etchant was removed by flowing 10 l of 90 °C millipore water at a flow rate of 2 l/h. With these transfer process parameters, single layer graphene with a 2D-peak position at $2678.10\,\mathrm{cm}^{-1} \pm 1.36\,\mathrm{cm}^{-1}$ and a 2D-peak FWHM of $31.24\,\mathrm{cm}^{-1} \pm 2.19\,\mathrm{cm}^{-1}$ was achieved. The D- and G-peak intensity ratio was $I(\mathrm{D})/I(\mathrm{G}) = 0.82 \pm 0.22$ which gives an inter-defect length of $L_\mathrm{D} \approx 13.5$ nm and a crystallite size $L_\mathrm{a} \approx 23.5$ nm. The domain size of the produced graphene was up to 900 μm in diameter. It was found that the sizes of the transferred graphene correspond to the grain sizes of the Cu foil. The influence of the ion fluence on graphene formation was investigated. For this purpose, C^+ ions with fluences between $5 \cdot 10^{15}\,\mathrm{cm}^{-2}$ and $2.5 \cdot 10^{16}\,\mathrm{cm}^{-2}$ and an energy of 35 keV were implanted. It was found that an increase of the ion fluence yields in a decrease of the amount of single layer graphene and therefore an influence on the number of graphene layers. The values for the 2D-peak FWHM increased from $\approx 31\,\mathrm{cm}^{-1}$ over $\approx 41\,\mathrm{cm}^{-1}$ to $\approx 59\,\mathrm{cm}^{-1}$, whereas the 2D-peak position increased from $\approx 2678\,\mathrm{cm}^{-1}$ over $\approx 2681\,\mathrm{cm}^{-1}$ to $\approx 2688\,\mathrm{cm}^{-1}$ with increasing ion fluence. The G/2D values increased with increasing fluence from 0.22 ± 0.04 over 1.09 ± 0.29 to 1.91 ± 0.50 as well. This demonstrates the possibility of changing the amount of graphene layers by changing the amount of implanted ions. It could be shown that the increased fluence has no strong influence on the D/G Raman intensity ratio and therefore the defect density of the graphene.

Isotopically labelled ^{13}C graphene was produced in order to prove that the synthesised graphene is made from the implanted carbon. By use of CO_2 gas enriched with ^{13}C (the composition of ^{12}C and ^{13}C was 0.5 : 0.5), graphene with a ratio of 0.59 : 0.41 for $^{13}\mathrm{C} :^{12}\mathrm{C}$ was synthesised, as determined by Raman-spectroscopy. The contamination with ^{12}C originates from the implantation of ^{12}CH which could not be separated from ^{13}C with the mass analyser magnet of the ion implanter.

Second, graphene was synthesised on Cu(111) thin films. The pre-annealed and via UV-ozoning cleaned substrates were implanted with 35 keV C^+ ions and post-annealed at 1020 °C for 30 min under vacuum conditions. The transfer of the graphene to the SiO_2/Si wafer was done by a standard PMMA based wet chemical etching process using concentrated nitric acid (millipore, 65%) to remove the Cu. For the synthesis of single layer graphene, the fluence had to be decreased from $5 \cdot 10^{15}\,\mathrm{cm}^{-2}$ to $2 \cdot 10^{15}\,\mathrm{cm}^{-2}$. The reason probably is that the grain boundary area within the films is smaller than the grain boundary area within the foils, because the films are much thinner. Therefore, less carbon can segregate in the film at these boundaries. Thus, more carbon can segregate on the surface and form graphene. The transferred single layer graphene with a D/G Raman intensity ratio of $I(\mathrm{D})/I(\mathrm{G}) = 0.51 \pm 0.18$ showed a better quality compared to the graphene synthesised on Cu foils. With this value, an inter-defect length of $L_\mathrm{D} \approx 16.9\,\mathrm{nm}$ and a crystallite size $L_\mathrm{a} \approx 37.3\,\mathrm{nm}$ were calculated. The 2D-peak position of $2685.65\,\mathrm{cm}^{-1} \pm 0.65\,\mathrm{cm}^{-1}$ is slightly shifted to higher wavenumbers. This shift probably originates from the PMMA residuals. Increasing the fluence from $2 \cdot 10^{15}\,\mathrm{cm}^{-2}$ over $5 \cdot 10^{15}\,\mathrm{cm}^{-2}$, $1 \cdot 10^{16}\,\mathrm{cm}^{-2}$ to $2.5 \cdot 10^{16}\,\mathrm{cm}^{-2}$ yields in multilayer graphene. The D/G Raman intensity ratio showed no strong dependence on the implanted fluence, similar to the graphene from Cu foils. The values for the 2D-peak FWHM increased from $\approx 34\,\mathrm{cm}^{-1}$ over $\approx 36\,\mathrm{cm}^{-1}$ and $\approx 38\,\mathrm{cm}^{-1}$ to $\approx 55\,\mathrm{cm}^{-1}$. The 2D-peak position increases from $\approx 2685\,\mathrm{cm}^{-1}$ over $\approx 2686\,\mathrm{cm}^{-1}$ to $\approx 2690\,\mathrm{cm}^{-1}$. The 2D-peak position for the fluence of $2.5 \cdot 10^{16}\,\mathrm{cm}^{-2}$ could not be determined accurately, because of the very low intensity. Also, the G/2D values increased with increasing fluence from 0.34 ± 0.08 over 0.65 ± 0.10 and 0.80 ± 0.22 to 5.45 ± 3.10.

The single layer graphene on $\mathrm{SiO_2}$ which was produced on the Cu(111) templates, was used for electrical characterisation. For this purpose, a home-built Van der Pauw measurement setup was used. The measured area was $1 \times 1\,\mathrm{cm}^2$. By this, a sheet resistance of $\rho/d = 2525.5\,\Omega/\square$ for a sample implanted with $5 \cdot 10^{15}\,\mathrm{cm}^{-2}$ carbon ions was obtained.

The transport mechanisms in the graphene were investigated by temperature dependent resistivity measurements. It was found that the conduction between 5 K and 20 K is dominated by the $T^{1/3}$-VRH[1]. Above 20 K, thermally activated charge carriers contribute to the conduction. The activation energy for these charge carriers was determined to $E_\mathrm{a} = (0.01500 \pm 8 \cdot 10^{-5})\,\mathrm{eV}$. Magnetoresistance measurements were performed between 5 K and 300 K. A negative magneto resistance was observed up to 300 K which can be explained by weak localisation in the low temperature regime and by Anderson localisation in the high temperature regime.

For the evaluation of the different Raman-spectroscopy measurements (single spectra and maps), a software was developed which is based on python code. It has a GUI[2] in order to ensure better user-friendliness. It consists of several modules. The first is the baseline correction. This is performed by determining the baseline points and fitting them with the best polynom (based on least square). The baseline points can be set manually as well. The second module allows to fitting the baseline corrected spectra with Voigt functions. Thus, the parameter for the different peaks in the spectrum are obtained.

This work explores several pathways for the graphene synthesis by ion implantation in copper and its subsequent transfer to silicon dioxide substrates. The results demonstrate that graphene synthesis was successful by use of the ion implantation technique combined with specific thermal treatments. Furthermore the impact of the used templates as well as the transfer method on the properties of graphene was shown.

Regarding the purity of the Cu templates there seems to be further potential for optimisation which could be studied in more detail e.g. a detailed analysis of the influence of the temperature used for the pre-implantation treatment. Also, the influence of the annealing duration could be investigated in more detail. A doping of the graphene during the synthesis process by co-implantation of other ion species beside carbon might be a promising approach for manipulating the electrical properties of the graphene without creating additional defects by doping after graphene synthesis and may be a topic of future research.

---

[1] variable range hopping

[2] graphic user interface

Appendix A

Derivation of important formulas

A.1 Raman lineshape and linewidth

The phonon excitation within the RAMAN scattering process can be expressed by a harmonic oscillator damped by the surrounding excitations in a medium but excited from an external force. Therefore, it yields the differential equation

$$m\ddot{x} + b\dot{x} + Dx = F_0 \cos(\omega t) \tag{A.1}$$

which becomes with $\omega_0^2 = D/m$, $\gamma = b/2m$ and $K = F_0/m$

$$\ddot{x} + 2\gamma\dot{x} + \omega_0^2 x = K \cdot \cos(\omega t). \tag{A.2}$$

This equation has the general solution [245]

$$x(t) = A_1 e^{-\gamma t} \cdot \cos(\omega_1 t + \varphi_1) + A_2 \cdot \cos(\omega t + \varphi) \tag{A.3}$$

with $\omega_1 = \sqrt{\omega_0^2 - \gamma^2}$ as the frequency of the unforced damped oscillation. For $t \gg 1/\gamma$ (after long time) the first term becomes negligible small. The steady state can therefore be described by

$$x(t) = A_2 \cdot \cos(\omega t + \varphi) \tag{A.4}$$

Insertion of (A.4) in (A.2) gives by help of trigonometric identities

$$\Big[(\omega_0^2 - \omega)A_2 \cos(\varphi) - 2\gamma A_2 \omega \sin(\varphi) - K\Big] \cos(\omega t) \tag{A.5}$$

$$- \Big[(\omega_0^2 - \omega)A_2 \sin(\varphi) + 2\gamma A_2 \omega \cos(\varphi)\Big] \sin(\omega t) = 0. \tag{A.6}$$

This should be valid for all times t, thus

$$(\omega_0^2 - \omega)A_2 \cos(\varphi) - 2\gamma A_2 \omega \sin(\varphi) - K = 0 \tag{A.7}$$

and

$$(\omega_0^2 - \omega) A_2 \sin(\varphi) + 2\gamma A_2 \omega \cos(\varphi) = 0. \tag{A.8}$$

Solving (A.7) for $A_2 \cdot \sin(\varphi)$ or $A_2 \cdot \cos(\varphi)$ becomes with (A.8)

$$A_2 \cdot \sin(\varphi) = \frac{2\gamma\omega K}{(\omega_0^2 - \omega^2)^2 + (2\gamma\omega)^2} \tag{A.9}$$

or

$$A_2 \cdot \cos(\varphi) = \frac{(\omega_0^2 - \omega^2) K}{(\omega_0^2 - \omega^2)^2 + (2\gamma\omega)^2}. \tag{A.10}$$

Summation of (A.9) and (A.10) and taking the square gives with $K = F_0/m$

$$A_2(\omega) = \frac{F_0/m}{\sqrt{(\omega_0^2 - \omega^2)^2 + (2\gamma\omega)^2}} \tag{A.11}$$

The energy balance for the oscillation can be obtained by multiplying equation (A.1) with $\dot{x}$ which gives

$$m\ddot{x}\dot{x} + Dx\dot{x} = -b\dot{x}^2 + F(t)\dot{x} \tag{A.12}$$

which is equal

$$\frac{\mathrm{d}}{\mathrm{d}t}\left(\frac{m}{2}\dot{x}^2 + \frac{D}{2}x^2\right) = \frac{\mathrm{d}E}{\mathrm{d}t} = -b\dot{x}^2 + F(t)\dot{x}. \tag{A.13}$$

The left side describes the change in time of the kinetic and potential energy. This is decreased by the power dissipated due to the damping and increased by the power plugged in via the external force. The energy absorbed by the system within one period of oscillation T is

$$W = \int_t^{t+T} b\dot{x}^2 \mathrm{d}t = b\omega^2 A_2^2 \int_t^{t+T} \sin^2(\omega t + \varphi)\mathrm{d}t = \frac{b}{2}\omega^2 A_2^2 T. \tag{A.14}$$

With $b = 2\gamma m$, the power absorbed by the system is

$$I(\omega) = \frac{W(\omega)}{T} = m\gamma\omega^2 A_2^2 = \frac{F_0^2 \gamma\omega^2}{m} \frac{1}{(\omega_0^2 - \omega^2)^2 + (2\gamma\omega)^2}. \tag{A.15}$$

For $\gamma \ll \omega_0$ the linewidth becomes due to the small damping factor very small. Thus, the function $I(\omega)$ has only non zero values near ω_0. In other words, the full width at half maximum of $I(\omega)$ is small compared to the frequency ω_0[1]. Therefore it yields $\omega_0 \approx \omega$ and in equation (A.15) ω can be replaced by ω_0 except in the term $(\omega_0^2 - \omega^2)^2$. This gives

---

[1] This is only true for high wavenumbers for example the 2D peak of graphene with $\omega_0 \approx 2680\,\mathrm{cm}^{-1}$ and a full width at half maximum of $\sim 30\,\mathrm{cm}^{-1}$.

$$I(\omega) = \frac{F_0^2\gamma\omega^2}{m}\frac{1}{(\omega_0-\omega)^2(\omega_0+\omega)^2+(2\gamma\omega)^2} \tag{A.16}$$

$$\approx \frac{F_0^2\gamma\omega_0^2}{m}\frac{1}{(\omega_0-\omega)^2(\omega_0+\omega_0)^2+(2\gamma\omega_0)^2} \tag{A.17}$$

$$= \frac{F_0^2}{m}\frac{\gamma\omega_0^2}{(\omega_0-\omega)^2\cdot 4\omega_0^2+4\omega_0^2\gamma^2} \tag{A.18}$$

$$= \frac{F_0^2}{m\gamma}\frac{\gamma^2\omega_0^2}{4\omega_0^2((\omega_0-\omega)^2+\gamma^2)}, \tag{A.19}$$

and thus

$$I(\omega) = I_0\left[\frac{\gamma^2}{(\omega-\omega_0)^2+\gamma^2}\right] = I_0\left[\frac{1}{1+\left(\frac{\omega-\omega_0}{\gamma}\right)^2}\right] \tag{A.20}$$

This is a LORENTZ shape for the dissipated power of the oscillator which is in the end proportional to the signal measured with the spectrometer CCD. In this case, I_0 is the peak height[2] and the full width at half maximum is given by 2γ.

---

[2] Normally the LORENTZ function is a probability density function only if it is normalised by $\int_{-\infty}^{\infty}\frac{\gamma}{(\omega_0-\omega)^2+\gamma^2}\mathrm{d}\omega = \pi$.

A.2 Weak localisation

In figure 1.4a a sketch of the different paths which can be taken by an electron in order to move from an initial position x_0 (at t_0) to the final position x_2 (at t_2) is shown. The time evolution of the state vector $|\psi(t)\rangle$ is determined by the SCHRÖDINGER equation

$$i\hbar\frac{\partial}{\partial t}\,|\psi(t)\rangle = H\,|\psi(t)\rangle\,, \tag{A.21}$$

which has the formal solution

$$|\psi(t_2)\rangle = U(t_2,t_0)\,|\psi(t_0)\rangle\,, \tag{A.22}$$

with $U(t_2,t_0) = \exp\left[-\frac{iH}{\hbar}(t_2-t_0)\right]$ as an unitary operator [143]. The position representation can be obtained by multiplication with an eigenstate $\langle x_2|$ in which the electron is at time t_2. This gives

$$\begin{aligned}\langle x_2|\psi(t_2)\rangle &= \langle x_2|U(t_2,t_0)|\psi(t_0)\rangle \qquad &\text{(A.23)}\\ &= \int \mathrm{d}x_0\,\langle x_2|U(t_2,t_0)|x_0\rangle\,\langle x_0|\psi(t_0)\rangle\,. \qquad &\text{(A.24)}\end{aligned}$$

Here, the operator $\int \mathrm{d}x_0\,|x_0\rangle\,\langle x_0| = 1$ was inserted. The probability amplitude for the electron to move from the position x_0 to the position x_2 is given by [246]

$$\psi(x_2,t_2) = \langle x_2|\psi(t_2)\rangle = \int \mathrm{d}x_0\,\langle x_2|U(t_2,t_0)|x_0\rangle\,\langle x_0|\psi(t_0)\rangle\,, \tag{A.25}$$

thus that it is the sum over all initial positions x_0 weighted with the position representation of the time evolution operator. This can be written as

$$\langle x_2|U(t_2,t_0)|x_0\rangle\,. \tag{A.26}$$

In short notation it is

$$\psi(x_2,t_2) = \int \mathrm{d}x_0 K(x_2,t_2,x_0,t_0)\psi(x_0,t_0), \tag{A.27}$$

with $K(x_2,t_2,x_0,t_0) \equiv \langle x_2|U(t_2,t_0)|x_0\rangle$ as the so called propagator of the wave function [143, 246].

If an intermediate time t_1 is introduced ($t_0 < t_1 < t_2$), the state vector from equation (A.22) can be expressed by

$$|\psi(t_2)\rangle = U(t_2,t_1)\,U(t_1,t_0)\,|\psi(t_0)\rangle \tag{A.28}$$

and in position representation it follows

$$\langle x_2|\psi(t_2)\rangle = \langle x_2|U(t_2,t_1)U(t_1,t_0)\psi(t_0)\rangle \tag{A.29}$$

$$= \int \mathrm{d}x_1\mathrm{d}x_0 \, \langle x_2|U(t_2,t_1)|x_1\rangle \, \langle x_1|U(t_1,t_0)|x_0\rangle \, \langle x_0|\psi(t_0)\rangle \, . \tag{A.30}$$

By use of analogue expression like equation (A.26) that can be written as

$$\psi(x_2,t_2) = \int \mathrm{d}x_1\mathrm{d}x_0 K(x_2,t_2,x_1,t_1)K(x_1,t_1,x_1,t_0). \tag{A.31}$$

It yields with equation (A.25) and (A.31)

$$K(x_2,t_2,x_0,t_0) = \int \mathrm{d}x_1 K(x_2,t_2,x_1,t_1)K(x_1,t_1,x_1,t_0). \tag{A.32}$$

Now, the summation is over all possible paths which can be taken by the electrons in order to reach x_2 (instead a summation over all initial positions).

In non-relativistic quantum mechanics, the propagator gives the probability amplitude for a particle to travel from one spatial point to another. Therefore, with equation (A.26), it yields for the probability for the electron to move from position x_0 to x_2 [143, 246]

$$P(x_0 \to x_2) = |\, \langle x_2|U(t_2,t_0)|x_0\rangle \,|^2 = |K(x_2,t_2,x_0,t_0|^2, \tag{A.33}$$

and by equation (A.32) this is the sum over all paths $x_{j,1}$ (at time $t_{j,1}$) which the electron could take. For discrete indices (here $j = 1, 2, 3$) the integral in equation (A.32) becomes a sum and for the probability amplitude it yields[3]

$$K(x_2,t_2,x_0,t_0) = \sum_j K(x_2,t_2,x_{1,j},t_{1,j})K(x_{1,j},t_{1,j},x_0,t_0). \tag{A.34}$$

An illustration of this propagator is shown in figure 1.4a for the electron moving from (x_0, t_0) to (x_2, t_2) with possible intermediate states $(x_{1,j}, t_{1,j})$.

For the probability for the motion of the electron from (x_0, t_0) to (x_2, t_2), equation (A.33) gives

$$P(x_0 \to x_2) = |\sum_j K(x_2,t_2,x_{1,j},t_{1,j})K(x_{1,j},t_{1,j},x_0,t_0)|^2. \tag{A.35}$$

With a short hand notation $A_j = K(x_2,t_2,x_{1,j},t_{1,j})K(x_{1,j},t_{1,j},x_0,t_0)$ that gives

$$P(x_0 \to x_2) = \left|\sum_j A_j\right|^2 = \sum_j |A_j|^2 + \sum_{j\neq k} A_j A_k^*. \tag{A.36}$$

The first term of the right side in equation (A.36) is the sum of the squared amplitudes of each path and corresponds to the probability for a classical particle. The second term is an

---

[3] Note the probability to move from x_0 to x_2 via $x_{1,j}$ is the product of the probability to move from x_0 to $x_{1,j}$ and from $x_{1,j}$ to x_2.

interference term which gives the quantum correction. That only applies for non losing phase coherence on the way from x_0 to x_2. The phase coherence may break due to inelastic scattering (e.g. at phonons which are thermally activated if $T > 0\,\mathrm{K}$) and is only conserved if the phase coherence length $l_\phi \sim v_\mathrm{F}\tau_\phi$ is much larger than the mean free path of the electron $l_\mathrm{el} = v_\mathrm{F}\tau_\mathrm{el}$[4].

Thus, the probability $P(x_0 \to x_2)$ that an electron is reflected from x_0 to x_2 is obtained by squaring the sum of the amplitudes for all paths connecting the initial state x_0 and the final state x_2, so it can be written as

$$P(x_0 \to x_2) = |A_1(x_0 \to x_2) + A_2(x_0 \to x_2) + ...|^2. \tag{A.37}$$

In most cases, the paths have a different length (see figure 1.4a, the lengths of $x_{1,j}$ are different). Therefore, the electrons acquire random distributed phases which vanish on the average [74]. Thus, the square of sum is equal to the sum of squares, the phases can be neglected and the probability can be obtained by adding probabilities instead of probability amplitudes.

The situation changes if the initial and final states are the same. If the path starts and ends at x_0, the electron can take a way like

$$x_0 \to x_{0,1} \to x_{0,2} \to x_{0,3} \cdots \to x_{0,N-1} \to x_{0,N} \to x_0,$$

as indicated in figure 1.4b. For each path like this, there is a time reversed path (red arrows in 1.4b)

$$x_0 \leftarrow x_{0,1} \leftarrow x_{0,2} \leftarrow x_{0,3} \cdots \leftarrow x_{0,N-1} \leftarrow x_{0,N} \leftarrow x_0,$$

which has to be added as well. The probability $P(x_0 \to x_0)$ becomes therefore

$$P(x_0 \to x_0) = |(A_1(x_0 \to x_0) + A_2(x_0 \to x_0) + ...) \tag{A.38}$$

$$+(A_{1\mathrm{R}}(x_0 \to x_0) + A_{2\mathrm{R}}(x_0 \to x_0) + ...)|^2 \tag{A.39}$$

$$\equiv |A + A_\mathrm{R}|^2. \tag{A.40}$$

Here, A is the sum of the amplitudes of all the paths of the first set and A_R is the sum of the amplitudes of all the paths of the time reversed set. For a isotropic space and no magnetic field, the amplitudes are equal so that $A = A_\mathrm{R}$ [74]. Hence, the probability becomes

$$P(x_0 \to x_0) = |A + A|^2 = |2A|^2 = 4|A|^2. \tag{A.41}$$

This is called enhanced (or coherent) backscattering which leads to so called *weak-localisation* [75]. Due to the increase of the probability for the electron to end up at the same point where it starts from the probability to reach the point x_2 has to decrease due to the conservation of the net probability. This leads to a lower measurable current (at the same voltage) and therefore to an increase of electrical resistance.

If now a magnetic field is present, the amplitude along the time reversed paths do not accumulate identical phases anymore. The amplitude A_j associated with any path j acquires an

---

[4] $v_\mathrm{F} = p_\mathrm{F}/m$ is the FERMI velocity and τ_ϕ and τ_el the mean free times between two scatter events.

additional phase proportional to the line integral of the vector potential $\vec{A}$ along this path [74]. Therefore[5]

$$A_j \to A_j \exp\left[\frac{ie}{\hbar}\int_{\mathrm{path}\,j}\vec{A}\cdot\mathrm{d}\vec{r}\right]. \tag{A.42}$$

For a closed loop, as indicated in figure 1.4b, the phase factor is proportional to the magnetic flux passing through the area S_j, enclosed by the path, so it can be expressed by

$$A_j \to A_j \exp\left[\frac{ie}{\hbar}\oint_{\mathrm{path}\,j}\vec{A}\cdot\mathrm{d}\vec{r}\right] = A_j \exp\left[\frac{ie}{\hbar}BS_j\right]. \tag{A.43}$$

The amplitude as an function of the field B can therefore be written as

$$A_j(B) = A_j(0)\exp\left[\frac{ie}{\hbar}BS_j\right]. \tag{A.44}$$

The phase acquired by the time reversed path $j\mathrm{R}$ (red arrows in figure 1.4b) is the negative value of the phase acquired on the path j [74], so

$$A_{j\mathrm{R}}(B) = A_{j\mathrm{R}}(0)\exp\left[-\frac{ie}{\hbar}BS_j\right]. \tag{A.45}$$

The total amplitude for path j in case of an external magnetic field becomes

$$A_j(B) + A_{j\mathrm{R}}(B) = 2A_j(0)\cos(eBS_j/\hbar) \equiv A'_j. \tag{A.46}$$

With equation (A.36) the probability for the electron to become backscattered in case of an external magnetic field becomes now

$$\begin{aligned}
\left|\sum_j A'_j\right|^2 &= \left|\sum_j 2A_j(0)\cos(eBS_j/\hbar)\right|^2 && \text{(A.47)}\\
&= |2A_1(0)\cos(eBS_1/\hbar) + 2A_2(0)\cos(eBS_2/\hbar) + ...|^2 && \text{(A.48)}\\
&= 4|A_1(0)\cos(eBS_1/\hbar) + A_2(0)\cos(eBS_2/\hbar)|^2 && \text{(A.49)}\\
&= 4\sum_j |A_j(0)|^2\cos^2(eBS_j/\hbar) + 4\sum_{j\neq k} A_j(0)A_k^*(0)\cos(eBS_j/\hbar)\cos(eBS_k/\hbar). && \text{(A.50)}
\end{aligned}$$

For randomly distributed and independent path lengths and therefore for randomly distributed and independent areas S_j, it yields[6] [74]

---

[5] This can be obtained by solving the SCHRÖDINGER equation for a charged particle within a vector potential and leads to the magnetic AHARONOV-BOHM effect [76].

[6] To make this approximation, the magnetic field has to be large enough in order to ensure the cosine goes at least a full period [74].

$$\left|\sum_j A'_j\right|^2 \approx \sum_j |A_j(0)|^2 \underbrace{\langle\cos^2(eBS_j/\hbar)\rangle}_{1/2} + 4\sum_{j\neq k} A_j(0)A_k(0)^* \underbrace{\cos(eBS_j/\hbar)\cos(eBS_k/\hbar)}_{0} \quad (A.51)$$

$$= 2\sum_j |A_j(0)|^2. \quad (A.52)$$

The probability that the electron moves from a point x_0 on a certain way back again to x_0 is only half as large as without the magnetic field. Therefore, the probability to move to x_2 has to increase, which yields in a decrease of electrical resistant.

In conclusion, the probability for an electron to become backscattered to a certain position (here x_0) is enhanced by a factor of two due to quantum mechanical corrections. This reduces the conductivity. However, an external magnetic field breaks the reversal symmetry, induces a phase difference between the two paths which starts and ends at x_0, reduces therefore the probability for returning at this point x_0, and enhances the conductivity.

Appendix B

Documentation for the software package MINION^2

The software MINION^2 is a software for evaluation single or multiple spectra, here single RAMAN spectra or RAMAN maps, with a graphic user interface (GUI). It consists of several modules.

The first module is the plotting and correcting module. The user can load single spectra or maps (in ASCII format) and plot them. A baseline correction procedure is applied which is described in appendix C.1. For this procedure the maximum as well as minimum degree of the fitted polynomial function can be chosen. Also the indexes which should be used for the baseline can be effected by a slider value for value of bg_idx (see C.1 source code line 5). Maps (including scale bar) can be plotted for three different regions of interests (ROI). The plotted maps can either be the area within the ROI or the maximum value of the spectra in this region. Two maps containing the ratios of these maps can also be plotted. The baseline correction procedure is parallelised and runs on up to four CPUs by dividing the array into 4 pieces beforehand. These produced arrays are treated in different processes by use of the *multiprocessing* module.

The second module is the fitting module. Here, the corrected spectra can be fitted with VOIGT functions. Up to four functions (for 4 peaks) can be fitted by setting the position, FWHM and intensity as the starting values for the fitting process. Several plots like 2D-scatter plots or histograms for the FWHM, peak position or ratio of peak intensities can be obtained. Together with the plot of these histograms, the implanted fluence, the mean value, the median (Med) and the standard deviation (Std) will be given (see e.g. figure 4.8e). The most important value here is the median and the standard deviation as the error for this value. The mean value is always given in order to show that most of the fitted parameters are in the plotted area of the histogram. For example, if the histogram for the 2D-peak position has for the x-axis limits of 2675 and 2695, values out of this range are not visible although they might exist due to bad fitting results or just due to a inhomogeneous distribution of the respective values. This would be visible as a large difference between the mean and the median value.

The export module gives the opportunity to export a certain spectrum from a RAMAN map by clicking on the respective point in the map. The corresponding spectrum to this x-y position is shown and can be exported as ASCII. If the map has a high resolution, a zoom into the map via the mousewheel can be performed.

The complete evaluation e.g. of a RAMAN map can be exported by one click to ASCII files for every parameter of the VOIGT functions, the corrected spectra, the original spectra, the corresponding baseline and several pdf and png files for the different plots.

The import of single RAMAN spectra is also possible, in order to perform a baseline correction which can be done automatically as described above or by choosing the baseline points by hand.

The whole program requires PYTHON 3.x to run. Furthermore, the program was converted to a .exe file via PYINSTALLER. To run this program, windows x64 is required.

Appendix C

Python software scripts

C.1 Raman baseline correction

In order to compare for example the Raman intensities of the several characteristic graphene peaks in a recorded spectrum a background correction procedure is required. Within this procedure it is essential to exclude the Raman peak regions from the baseline correction process.

Figure C.1a shows an spectrum of multilayer graphene measured on copper film by a 473 nm laser excitation. The challenge is now to find all points which are belonging to the baseline but not to the peaks themselves to prevent a change in the peak shape within the baseline subtraction. This should be done automatically in order to be able to correct many spectra within a Raman-map in short time.

In line number 1, the spectrum is smoothed by applying a Savitzky-Golay-filter [193]. In line number 2 and 3 a filter is applied which calculates at every position of the spectrum the median and maximum value which yields in two (one for the median, one for the maximum values) new spectra showed in figure C.1b. In line number 5, the vector *bg_idx* is obtained by looking at which position the value $\frac{\text{ymax}}{\text{ymed}}$ is smaller than a certain limit, in this case 1.05. In general, this value should lie in between 1.01 and 1.1. Figure C.1c show the plot of the filter ratio values. The red line indicates the threshold whether the points should be attended to the baseline fit or not. The original spectrum and the points which were found for the baseline fit are shown in figure C.1d. Line number 7-9 gives the possibility to exclude some values which are higher than a certain limit (here 350). This can be useful for instance to exclude regions between the D and G-peak of the graphene/graphite spectrum. In this example, the points at around 1500 cm^{-1} would also lie within the baseline region, but they should correspond to the spectrum. Line number 11 and 12 gives the possibility to append certain points from the start and the end of the spectrum which makes the fit procedure much easier. To avoid double entries within the vector, in line number 13 these will be deleted. To do this, in line number 12 the whole array is converted into integer values.

```
1  y2 = scipy.signal.savgol_filter(y, 11, 2)
2  ymed = filters.median_filter(y2, size=int(len(y2)/5), mode='nearest')
3  ymax = filters.maximum_filter(y2, size=int(len(y2)/40), mode='nearest')
4  
5  bg_idx = np.where(ymax/ymed <= 1.05)
6  
7  too_big = np.where(y>350)
8  bg_idx_neu = [i for i in bg_idx[0] if not i in too_big[0]]
9  bg_idx = bg_idx_neu
10 
11 bg_idx = np.append(bg_idx, np.arange(0,20))
12 bg_idx = np.append(bg_idx, np.arange(len(x)-20, len(x)))
13 bg_idx = bg_idx.astype(int)
14 bg_idx = np.unique(bg_idx)
```

The next step is to fit the determined baseline points by a polynomial function. Line number 15-17 defines the start values for this procedure. *poly_max* is the highest possible order and *polynum* defines the order for the first used polynom. Within line number 19-30 the polynom is fitted. The result is showing in figure C.1e. After every fitting process (line 20, 21) a χ^2 test is applied to evaluate the quality of the fitted polynom with respect to the points (line 22, 24). This continues until either the χ^2 value is lower than a certain given value or it getting worst again (line 24). In the last case, the condition in line number 24 is always true (because the left side is going to be negative) and the procedure stops. Note, there is the possibility that this procedure stops e.g. at a order of 5 but a polynomial function of a much higher order would lead to a smaller χ^2 value[1]. Line number 33 prints the used polynomial order to the user, line number 33 and 34 fits the baseline points with the evaluated order. In line number 36, the original data is subtracted by that polynom in order to receive the corrected spectrum as shown in figure C.1f.

Note that all theses values can be set by sliders in the GUI.

```
15 chi_best = 10000
16 poly_max = 20
17 polynum = 2
18
19 while polynum <= poly_max:
20     p = np.polyfit(x[bg_idx][::1], y[bg_idx][::1], polynum)
21     bg = np.polyval(p, x)
22     chi,_ = stat.chisquare(y[bg_idx], bg[bg_idx])
23     print(chi)
24     if chi_best - chi < chi/1000:
25         polynum -= 1
26         break
27     else:
28         chi_best = chi
29         polynum += 1
30 chi_list.append(chi_best)
31
32 print('best results with:', polynum, chi_best)
33 p = np.polyfit(x[bg_idx][::1], y[bg_idx][::1], polynum)
34 bg = np.polyval(p, x)
35
36 y = y-bg
```

---

[1] In general it would be possible to change the code and look for the polynomial function with the smallest χ^2 value, but this leads sometimes to an “over-fitting” of the baseline points with oscillations at the edges of the spectrum. Also the time would increase if this is applied to a huge number of spectra e.g. within a Raman-map

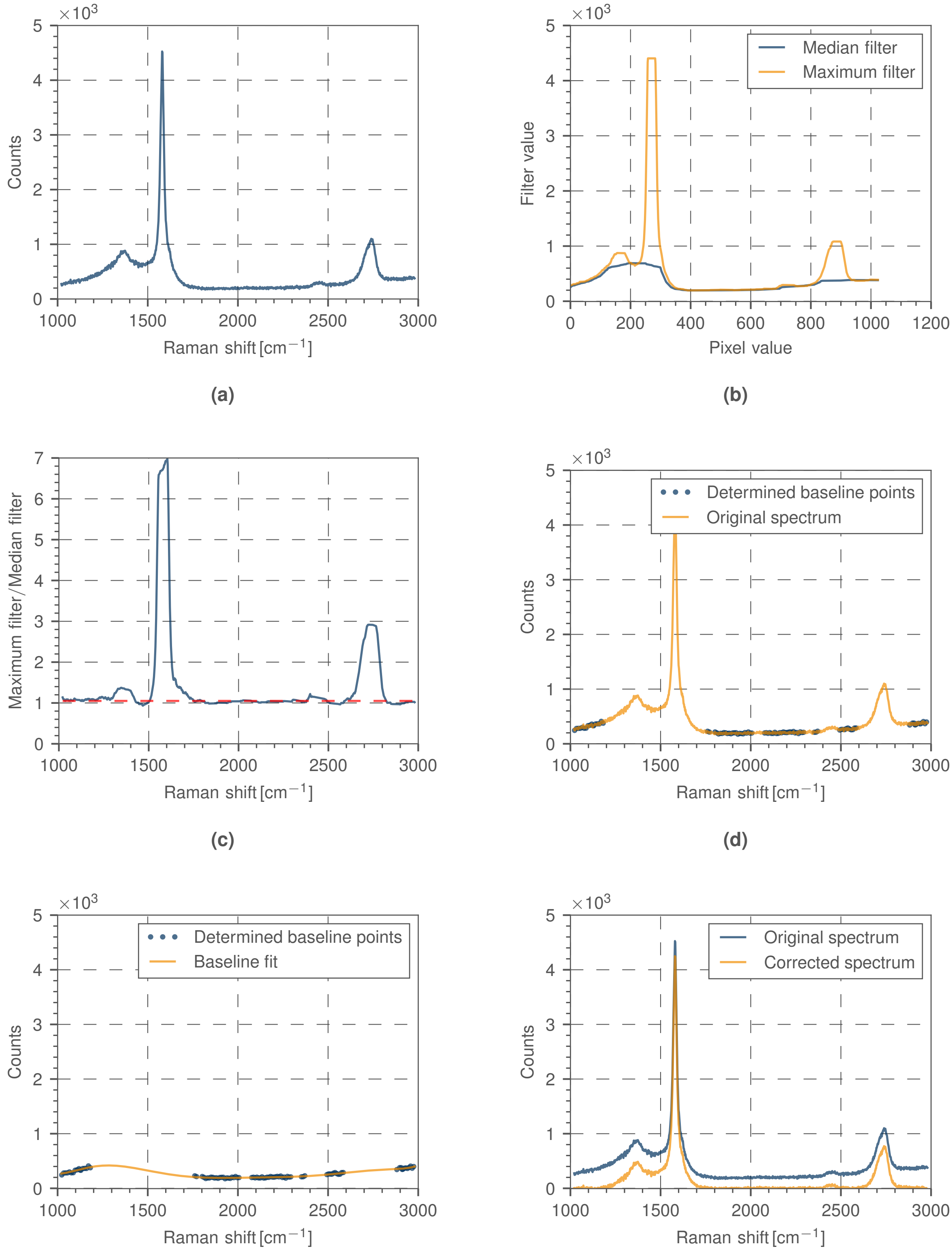

(a) (b)

(c) (d)

(e) (f)

Fig. C.1: Baseline correction of a multilayer graphene spectrum on Cu film measured with a 473 nm laser excitation. Figure (a) shows the original spectrum, (b) the values for the applied median and maximum filter, (c) the ratio of these two filters and in red the threshold for the values within the vector *bg_idx* (see text for explanation), (d) the original RAMAN spectrum and the automatically determined baseline points, (e) the fit of these points by a polynomial function and (f) the original as well as the baseline corrected spectrum.

C.2 Peak find algorithm for AFM image grain size determination

In order to find the peak positions and the number of peaks in a certain area a perk find algorithm was used. In general it is based on the difference between neighbouring points $dx = x[1:] - x[:-1]$ if x is the list or the array of the data. The minimum distance between two peeks can be set. Also if the ’peak’ is a minimum or a maximum can be selected. In general it is advisable to perform some smoothing of the data by use a Savitzky-Golay-filter [193] before the algorithm is applied. Note that this kind of algorithm can be used for every set of data, not only AFM height distributions.

```
import numpy as np

def detect_peaks(x, mph=None, mpd=1, threshold=0, edge=’rising’,
                 kpsh=False, valley=False, show=False, ax=None):


    x = np.atleast_1d(x).astype(’float64’)
    if x.size < 3:
        return np.array([], dtype=int)
    if valley:
        x = -x
    # find indices of all peaks
    dx = x[1:] - x[:-1]
    # handle NaN’s
    indnan = np.where(np.isnan(x))[0]
    if indnan.size:
        x[indnan] = np.inf
        dx[np.where(np.isnan(dx))[0]] = np.inf
    ine, ire, ife = np.array([[], [], []], dtype=int)
    if not edge:
        ine = np.where((np.hstack((dx, 0)) < 0) & (np.hstack((0, dx)) > 0))[0]
    else:
        if edge.lower() in [’rising’, ’both’]:
            ire = np.where((np.hstack((dx, 0)) <= 0) & (np.hstack((0, dx)) > 0))[0]
        if edge.lower() in [’falling’, ’both’]:
            ife = np.where((np.hstack((dx, 0)) < 0) & (np.hstack((0, dx)) >= 0))[0]
    ind = np.unique(np.hstack((ine, ire, ife)))
    # handle NaN’s
    if ind.size and indnan.size:
        # NaN’s and values close to NaN’s cannot be peaks
        ind = ind[np.in1d(ind, np.unique(np.hstack((indnan, indnan-1, indnan+1))), invert=True)]
    # first and last values of x cannot be peaks
    if ind.size and ind[0] == 0:
        ind = ind[1:]
    if ind.size and ind[-1] == x.size-1:
        ind = ind[:-1]
    # remove peaks < minimum peak height
    if ind.size and mph is not None:
        ind = ind[x[ind] >= mph]
    # remove peaks - neighbors < threshold
    if ind.size and threshold > 0:
        dx = np.min(np.vstack([x[ind]-x[ind-1], x[ind]-x[ind+1]]), axis=0)
        ind = np.delete(ind, np.where(dx < threshold)[0])
    # detect small peaks closer than minimum peak distance
    if ind.size and mpd > 1:
        ind = ind[np.argsort(x[ind])][::-1] # sort ind by peak height
        idel = np.zeros(ind.size, dtype=bool)
        for i in range(ind.size):
            if not idel[i]:
                # keep peaks with the same height if kpsh is True
                idel = idel | (ind >= ind[i] - mpd) & (ind <= ind[i] + mpd) \
                    & (x[ind[i]] > x[ind] if kpsh else True)
                idel[i] = 0 # Keep current peak
        # remove the small peaks and sort back the indices by their occurrence
        ind = np.sort(ind[~idel])

```

```
    if show:
        if indnan.size:
            x[indnan] = np.nan
        if valley:
            x = -x
        _plot(x, mph, mpd, threshold, edge, valley, ax, ind)

    return ind
```

C.3 Grain size determination from SEM images

In order to determine the grain sizes of the graphene grains and the grains of the Cu foils, a script was written which uses an Otsu threshold filter [247]. First, the region of the SEM image which contains the scale bar overlay is extracted (line 65). This cropped images called *info1* is usually a greyscale image with values from 0 to 255. By use of the Otsu threshold filter (line 71) it is converted to a binary image (line 72). In line 73, an array is created in which all connected regions are assigned the same integer value [248]. This array is now used to determine the number of objects (which were labelled). This is done in line 74. Here, a list of tuples, with each tuple containing N slices (N as the dimension of the input array) is created. The slices correspond to the minimal parallelepiped that contains the object. The shape of this list of tuples is equal the number of labelled objects (which is basically the same number as the maximum integer value within the array). In line 81-83, an iteration within these slices is performed which gives the width of the objects. In general this extracted image contains of the scale bar and the scale number. The scale bar is the largest (broadest in this case) object. In line 88-93, the size of the pixel is determined by help of the *scalewidth* and the *var* value which is the scale number from the SEM image.

To measure the size of the grains, they were colour coded with a certain color for each grain, respectively. At the end, these pixels are counted and multiplied with the size of a pixel which gives the size of the grains (line 99).

```
1   import matplotlib.pyplot as plt
2   import PIL as pil
3   import numpy as np
4   from matplotlib import rc
5   from matplotlib import rcParams
6   from skimage import measure, filters, morphology, exposure
7   import scipy.ndimage as ndi
8
9   number_color = np.zeros(27)
10  number_color_graphene = np.zeros(27)
11
12  color1 = (255,0,0)
13  color2 = (255,0,80)
14  color3 = (255,0,174)
15  color4 = (255,0,246)
16  color5 = (186,0,255)
17  color6 = (126,0,255)
18  color7 = (0,60,255)
19  color8 = (0,168,255)
20  color9 = (0,255,252)
21  color10 = (0,255,174)
22  color11 = (0,255,36)
23  color12 = (174,255,0)
24  color13 = (246,255,0)
25  color14 = (255,222,0)
26  color15 = (255,174,0)
27  color16 = (255,138,0)
28  color17 = (255,78,0)
29  color18 = (198,255,0)
30  color19 = (252,0,255)
31  color20 = (0,255,222)
32  color21 = (0,162,255)
33  color22 = (0,102,255)
34  color23 = (186,255,0)
35  color24 = (0,255,108)
36  color25 = (0,30,255)
37  color26 = (240,0,255)
38  color27 = (255,204,0)
39
40  colors = [color1, color2, color3, color4, color5, color6, color7, color8, color9, color10, color11, color12
         , color13, color14, color15, color16, color17, color18, color19, color20, color21, color22, color23,
         color24, color25, color26, color27] ###list with all colors
```

```python

im = pil.Image.open('UPCU3_geheizt_01_colored.png')

pixels = list(im.getdata())

for pixel in pixels:
    for i in range(0,len(number_color)):
    # print(colors[i])
        #print(i)
        if pixel == colors[i]:
            number_color[i] = number_color[i] + 1

print(number_color) #number pixels with certain color

#dimension_pixel_cu_grains

im_cu_grains = pil.Image.open('UPCU3_geheizt_01.tif')

imarray_cu_grains = np.array(im_cu_grains)

n, m = np.shape(imarray_cu_grains)

imarray_cu_grains = np.flipud(imarray_cu_grains)

info1 = imarray_cu_grains[20:60,:180]

var=100
imarray_cu_grains = imarray_cu_grains[80:,:]


threshold_global_otsu = filters.threshold_otsu(info1)
info1 = info1 >= threshold_global_otsu+1
labels = measure.label(info1)
objects = ndi.measurements.find_objects(labels)
numobjects, _ = np.shape(objects)
print('objects found in info:', numobjects)


objectwidth = np.zeros(numobjects)
i = 0
for y, x in objects:
    objectwidth[i] = x.stop-x.start
    i += 1

scalewidth = objectwidth.max()
print('scalewidth:', scalewidth)

ylen, xlen = np.shape(imarray_cu_grains)
print(ylen, xlen)

xmax = xlen*var/scalewidth
ymax = ylen*var/scalewidth
pixelwidth = var/scalewidth

print("pixelwidth = ", pixelwidth)

pixel_area = pixelwidth*pixelwidth ###area of one pixel in the sem image in micro squared

area_grains_cu = [i * pixel_area for i in number_color] ###here, the list which is used for the histogram is produced

print(area_grains_cu)

im_graphene = pil.Image.open('UPCu9_22_colored.png')

pixels_graphene = list(im_graphene.getdata())

for pixel in pixels_graphene:
    for i in range(0,len(number_color_graphene)):
    # print(colors[i])
```

```
        #print(i)
        if pixel == colors[i]:
            number_color_graphene[i] = number_color_graphene[i] + 1

print(number_color_graphene) #number pixels with certain color



#dimension_pixel_graphene_grains

im_graphene_grains = pil.Image.open('UPCu9_22.tif')

imarray_graphene_grains = np.array(im_graphene_grains)

n, m = np.shape(imarray_graphene_grains)
print(n, m)

imarray_graphene_grains = np.flipud(imarray_graphene_grains)

info1 = imarray_graphene_grains[20:60,:180]


#var = float(input('Please enter length of scale in microns:'))
var=100
imarray_graphene_grains = imarray_graphene_grains[80:,:]


threshold_global_otsu = filters.threshold_otsu(info1)
info1 = info1 >= threshold_global_otsu+1
labels = measure.label(info1)
objects = ndi.measurements.find_objects(labels)
numobjects, _ = np.shape(objects)
print('objects found in info:', numobjects)


objectwidth = np.zeros(numobjects)
i = 0
for y, x in objects:
    objectwidth[i] = x.stop-x.start
    i += 1

scalewidth = objectwidth.max()
print('scalewidth:', scalewidth)



ylen, xlen = np.shape(imarray_graphene_grains)
print(ylen, xlen)

xmax = xlen*var/scalewidth
ymax = ylen*var/scalewidth
pixelwidth_graphene = var/scalewidth

print("pixelwidth = ", pixelwidth_graphene)


pixel_area_graphene = pixelwidth_graphene*pixelwidth_graphene ###area of one pixel in the sem image in micro squared

area_grains_graphene = [i * pixel_area_graphene for i in number_color_graphene] ###here, the list which is used for the histogram is produced
```

C.4 Newtons method script

```

######calculate sheet resistance######


def derivative(f): # here, the derivation of the function (f(x) below) is derived
    def compute(x, dx):
        return (f(x+dx) - f(x))/dx
    return compute

def newtons_method(f, x, dx=0.000001, tolerance=0.000001): # here, newtons method is applied, with step dx for the derivation of the function and a specific tolerance
    '''f is the function f(x)'''
    df = derivative(f)
    while True:
        x1 = x - f(x)/df(x, dx)
        t = abs(x1 - x)
        if t < tolerance:
            break
        x = x1
    return x

def f(x):
    return exp(-np.pi*(1/x)*abs(popt[0])) + exp(-np.pi*(1/x)*abs(popt1[0])) - 1 # this is the Van-Der-Pauw equation, popt[0] and popt1[0] are the resistors calculated by a linear fit of the respective I-V-curve

x_approx = 1000 # rough guess here ca. 4*R12,R34
# f refers to the function f(x)
x = newtons_method(f, x_approx)
print("x = %0.3f" % x) # the result is printed
```

Bibliography

[1] A. K. Geim and K. S. Novoselov. The rise of graphene. *Nature Materials*, 6:183–191, 2007.

[2] A. K. Geim. Graphene: Status and Prospects. *Science*, 324(5934):1530–1534, 2009.

[3] J. Scott Bunch, Arend M. van der Zande, Scott S. Verbridge, Ian W. Frank, David M. Tanenbaum, Jeevak M. Parpia, Harold G. Craighead, and Paul L. McEuen. Electromechanical Resonators from Graphene Sheets. *Science*, 315(5811):490–493, 2007.

[4] J. Scott Bunch, Scott S. Verbridge, Jonathan S. Alden, Arend M. van der Zande, Jeevak M. Parpia, Harold G. Craighead, and Paul L. McEuen. Impermeable Atomic Membranes from Graphene Sheets. *Nano Letters*, 8(8):2458–2462, 2008.

[5] Y. Shao, J. Wang, H. Wu, J. Liu, I. A. Aksay, and Y. Lin. Graphene Based Electrochemical Sensors and Biosensors: A Review. *Electroanalysis*, 22(10):1027–1036, 2010.

[6] Xuan Wang, Linjie Zhi, and Klaus Müllen. Transparent, Conductive Graphene Electrodes for Dye-Sensitized Solar Cells. *Nano Letters*, 8(1):323–327, 2008.

[7] Simone Schuler, Daniel Schall, Daniel Neumaier, Lukas Dobusch, Ole Bethge, Benedikt Schwarz, Michael Krall, and Thomas Mueller. Controlled Generation of a p-n Junction in a Waveguide Integrated Graphene Photodetector. *Nano Letters*, 16(11):7107–7112, 2016.

[8] Andrea C. Ferrari, Francesco Bonaccorso, Vladimir Falko, Konstantin S. Novoselov, Stephan Roche, Peter Boggild, Stefano Borini, Frank H. L. Koppens, Vincenzo Palermo, Nicola Pugno, Jose A. Garrido, Roman Sordan, Alberto Bianco, Laura Ballerini, Maurizio Prato, Elefterios Lidorikis, Jani Kivioja, Claudio Marinelli, Tapani Ryhänen, Alberto Morpurgo, Jonathan N. Coleman, Valeria Nicolosi, Luigi Colombo, Albert Fert, Mar Garcia-Hernandez, Adrian Bachtold, Gregory F. Schneider, Francisco Guinea, Cees Dekker, Matteo Barbone, Zhipei Sun, Costas Galiotis, Alexander N. Grigorenko, Gerasimos Konstantatos, Andras Kis, Mikhail Katsnelson, Lieven Vandersypen, Annick Loiseau, Vittorio Morandi, Daniel Neumaier, Emanuele Treossi, Vittorio Pellegrini, Marco Polini, Alessandro Tredicucci, Gareth M. Williams, Byung Hee Hong, Jong-Hyun Ahn, Jong Min Kim, Herbert Zirath, Bart J. van Wees, Herre van der Zant, Luigi Occhipinti, Andrea Di Matteo, Ian A. Kinloch, Thomas Seyller, Etienne Quesnel, Xinliang Feng, Ken Teo, Nalin Rupesinghe, Pertti Hakonen, Simon R. T. Neil, Quentin Tannock, Tomas Löfwander, and Jari Kinaret. Science and technology roadmap for graphene, related two-dimensional crystals, and hybrid systems. *Nanoscale*, 7:4598–4810, 2015.

[9] Dong Wook Chang and Jong-Beom Baek. Covalently functionalized graphene with organic semiconductors for energy and optoelectronic applications. *Materials Research Express*, 3(4):044001, 2016.

[10] N. Kheirabadi, A. Shafiekhani, and M. Fathipour. Review on graphene spintronic, new land for discovery. *Superlattices and Microstructures*, 74:123–145, 2014.

[11] Drew Higgins, Pouyan Zamani, Aiping Yu, and Zhongwei Chen. The application of graphene and its composites in oxygen reduction electrocatalysis: a perspectiveand review of recent progress. *Energy and EnvironmentalScience*, 9:357–390, 2016.

[12] Jeroen B. Oostinga, Hubert B. Heersche, Xinglan Liu, Alberto F. Morpurgo, and Lieven M. K. Vandersypen. Gate-induced insulating state in bilayer graphene devices. *Nature Materials*, 7:151–157, 2007.

[13] Eduardo V. Castro, K. S. Novoselov, S. V. Morozov, N. M. R. Peres, J. M. B. Lopes dos Santos, Johan Nilsson, F. Guinea, A. K. Geim, and A. H. Castro Neto. Biased Bilayer Graphene: Semiconductor with a Gap Tunable by the Electric Field Effect. *Phys. Rev. Lett.*, 99:216802, Nov 2007.

[14] S. Saqib Shams, Ruoyu Zhang, and Jin Zhu. Graphene synthesis: a Review. *Materials Science-Poland*, 33(3):566–578, 2015.

[15] Peter Boggld. The war on fake graphene. *Nature*, 562:502–503, 2018.

[16] K. S. Novoselov, A. K. Geim, S. V. Morozov, D. Jiang, Y. Zhang, S. V. Dubonos, I. V. Grigorieva, and A. A. Firsov. Electric Field Effect in Atomically Thin Carbon Films. *Science*, 306(5696):666–669, 2004.

[17] Goki Eda, Giovanni Fanchini, and Manish Chhowalla. Large-area ultrathin films of reduced graphene oxide as a transparent and flexible electronic material. *Nature Nanotechnology*, 3:270–274, 2008.

[18] Yenny Hernandez, Valeria Nicolosi, Mustafa Lotya, Fiona M. Blighe, Zhenyu Sun, Sukanta De, I. T. McGovern, Brendan Holland, Michele Byrne, Yurii K. Gun'Ko, John J. Boland, Peter Niraj, Georg Duesberg, Satheesh Krishnamurthy, Robbie Goodhue, John Hutchison, Vittorio Scardaci, Andrea C. Ferrari, and Jonathan N. Coleman. High-yield production of graphene by liquid-phase exfoliation of graphite. *Nature Nanotechnology*, 3:563–568, 2008.

[19] C. Berger, Z. Song, X. Li, X. Wu, N. Brown, C. Naud, D. Mayou, T. Li, J. Hass, A. N. Marchenkov, E. H. Conrad, P. N. First, and W. A. de Heer. Electronic Confinement and Coherence in Patterned Epitaxial Graphene. *Science*, 312:1191–1196, 2006.

[20] K. V. Emtsev, A. Bostwick, K. Horn, J. Jobst, G. L. Kellogg, L. Ley, J. L. McChesney, T. Ohta, S. A. Reshanov, J. Roehrl, E. Rotenberg, A. K. Schmid, D Waldmann, H. B. Weber, and T. Seyller. Towards wafer-size graphene layers by atmospheric pressure graphitization of silicon carbide. *Nature Materials*, 8:203–207, 2009.

[21] Phaedon Avouris and Christos Dimitrakopoulos. Graphene: Synthesis and Applications. *Materials Today*, 15(3):86 – 97, 2012.

[22] Yi Zhang, Luyao Zhang, and Chongwu Zhou. Review of Chemical Vapor Deposition of Graphene and Related Applications. *Accounts of Chemical Research*, 46(10):2329–2339, 2013.

[23] H. J. Park, J. Meyer, S. Roth, and V. Skákalová. Growth and properties of few-layer graphene prepared by chemical vapor deposition. *Carbon*, 48, 2010.

[24] Xianping Chen, Lili Zhang, and Shanshan Chen. Large area CVD growth of graphene. *Synthetic Metals*, 210:95–108, 2015.

[25] Maria Losurdo, Maria Michela Giangregorio, Pio Capezzuto, and Giovanni Bruno. Graphene CVD growth on copper and nickel: role of hydrogen in kinetics and structure. *Phys. Chem. Chem. Phys.*, 13:20836–20843, 2011.

[26] W. Liu, C.-H. Chung, C.-Q. Miao, Y.-J. Wang, B.-Y. Li, L.-Y. Ruan, K. Patel, Y.-J. Park, J. Woo, and Y.-H. Xie. Chemical vapor deposition of large area few layer graphene on Si catalyzed with nickel films. *Thin Solid Films*, 518, 2010.

[27] Z. Chen, W. Ren, B. Liu, L. Gao, S. Pei, Z. . S. Wu, J. Zhao, and H. . M. Cheng. Bulk growth of mono- to few-layer graphene on nickel particles by chemical vapor deposition from methane. *Carbon*, 48, 2010.

[28] Xuesong Li, Weiwei Cai, Jinho An, Seyoung Kim, Junghyo Nah, Dongxing Yang, Richard Piner, Aruna Velamakanni, Inhwa Jung, Emanuel Tutuc, Sanjay K. Banerjee, Luigi Colombo, and Rodney S. Ruoff. Large-Area Synthesis of High-Quality and Uniform Graphene Films on Copper Foils. *Science*, 324(5932):1312–1314, 2009.

[29] Cecilia Mattevi, Hokwon Kim, and Manish Chhowalla. A review of chemical vapour deposition of graphene on copper. *J. Mater. Chem.*, 21:3324–3334, 2011.

[30] Wei Liu, Hong Li, Chuan Xu, Yasin Khatami, and Kaustav Banerjee. Synthesis of high-quality monolayer and bilayer graphene on copper using chemical vapor deposition. *Carbon*, 49(13):4122 – 4130, 2011.

[31] Chi Vo-Van, Amina Kimouche, Antoine Reserbat-Plantey, Olivier Fruchart, Pascale Bayle-Guillemaud, Nedjma Bendiab, and Johann Coraux. Epitaxial graphene prepared by chemical vapor deposition on single crystal thin iridium films on sapphire. *Applied Physics Letters*, 98(18):181903, 2011.

[32] Saman Choubak, Pierre L. Levesque andEtienne Gaufres andMaxime Biron, Patrick Desjardins, and Richard Martel. Graphene CVD: Interplay Between Growth and Etching on Morphology and Stacking by Hydrogen and Oxidizing Impurities. *Journal of Physical Chemistry C*, 118:21532–21540, 2014.

[33] Slaven Garaj, William Hubbard, and J. A. Golovchenko. Graphene synthesis by ion implantation. *Applied Physics Letters*, 97, 2010.

[34] Janghyuk Kim, Geonyeop Lee, and Jihyun Kim. Wafer-scale synthesis of multi-layer graphene by high-temperature carbon ion implantation. *Applied Physics Letters*, 107:033104, 2015.

[35] L. Baraton, Z. B. He, C. S. Lee, C. S. Cojocaru, M. Chatelet, J.-L. Maurice, Y. H. Lee, and D. Pribat. On the mechanisms of precipitation of graphene on nickel thin films. *EPL (Europhysics Letters)*, 96(4):46003, 2011.

[36] Gang Wang, Guqiao Ding, Yun Zhu, Da Chen, Lin Ye, Li Zheng, Miao Zhang, Zengfeng Di, and Su Liu. Growth of controlled thickness graphene by ion implantation for field-effect transistor. *Materials Letters*, 107:170 – 173, 2013.

[37] J.J. Ying, X.H. Xiao, Z.G. Dai, W. Wu, W.Q. Li, F. Mei, G.X. Cai, F. Ren, and C.Z. Jiang. Synthesis of graphene by MEVVA source ion implantation. *Nuclear Instruments*

and Methods in Physics Research Section B: Beam Interactions with Materials and Atoms, 305:29 – 32, 2013.

[38] R. Zhang, Z. S. Wang, Z. D. Zhang, Z. G. Dai, L. L. Wang, H. Li, L. Zhou, Y. X. Shang, J. He, D. J. Fu, and J. R. Liu. Direct graphene synthesis on SiO_2/Si substrate by ion implantation. *Applied Physics Letters*, 102(19):193102, 2013.

[39] Jae Sung Lee, Chan Wook Jang, Jong Min Kim, Dong Hee Shin, Sung Kim, Suk-Ho Choi, K. Belay, and R.G. Elliman. Graphene synthesis by C implantation into Cu foils. *Carbon*, 66:267 – 271, 2014.

[40] Li Hui, Shang Yan-Xia, Zhang Zao-Di, Wang Ze-Song, Zhang Rui, and Fu De-Jun. Preparation of graphene on Cu foils by ion implantation with negative carbon clusters. *Chinese Physics B*, 24(1):018502, 2015.

[41] Hyeon-Jin Shin, Seon-Mi Yoon, Won Mook Choi, Seongjun Park, Dongwook Lee, In Yong Song, Yun Sung Woo, and Jae-Young Choi. Influence of Cu crystallographic orientation on electron transport in graphene. *Applied Physics Letters*, 102(16):163102, 2013.

[42] Dae Woo Kim, Seon Joon Kim, Jae Sung Kim, Minju Shin, Gyu-Tae Kim, and Hee-Tae Jung. The Influence of Cu Lattices on the Structure and Electrical Properties of Graphene Domains during Low-Pressure Chemical Vapor Deposition. *ChemPhysChem*, 16(6):1165–1171, 2015.

[43] Li Gao, Jeffrey R. Guest, and Nathan P. Guisinger. Epitaxial Graphene on Cu(111). *Nano Letters*, 10(9):3512–3516, 2010.

[44] Ken Verguts, Bart Vermeulen, Nandi Vrancken, Koen Schouteden, Chris Van Haesendonck, Cedric Huyghebaert, Marc Heyns, Stefan De Gendt, and Steven Brems. Epitaxial Al2O3(0001)/Cu(111) Template Development for CVD Graphene Growth. *The Journal of Physical Chemistry C*, 120(1):297–304, 2016.

[45] L.M. Malard, M.A. Pimenta, G. Dresselhaus, and M.S. Dresselhaus. Raman spectroscopy in graphene. *Physics Reports*, 473(5):51 – 87, 2009.

[46] Ado Jorio, Riichiro Saito, Gene Dresselhaus, and Mildred S. Dresselhaus. *Raman Spectroscopy in Graphene Related Systems*. Wiley-VCH Velag GmbH, 2011.

[47] S. Reich, J. Maultzsch, C. Thomsen, and P. Ordejón. Tight-binding description of graphene. *Phys. Rev. B*, 66:035412, 2002.

[48] Vitor M. Pereira, A. H. Castro Neto, and N. M. R. Peres. Tight-binding approach to uniaxial strain in graphene. *Phys. Rev. B*, 80:045401, 2009.

[49] P. R. Wallace. The Band Theory of Graphite. *Phys. Rev.*, 71:622–634, 1947.

[50] A. H. Castro Neto, F. Guinea, N. M. R. Peres, K. S. Novoselov, and A. K. Geim. The electronic properties of graphene. *Rev. Mod. Phys.*, 81:109–162, 2009.

[51] Zhenhua Ni, Yingying Wang, Ting Yu, Yumeng You, and Zexiang Shen. Reduction of Fermi velocity in folded graphene observed by resonance Raman spectroscopy. *Phys. Rev. B*, 77:235403, 2008.

[52] Giovanni Borghi, Marco Polini, Reza Asgari, and A.H. MacDonald. Fermi velocity enhancement in monolayer and bilayer graphene. *Solid State Communications*, 149(27):1117 – 1122, 2009.

[53] S. Das Sarma, Shaffique Adam, E. H. Hwang, and Enrico Rossi. Electronic transport in two-dimensional graphene. *Rev. Mod. Phys.*, 83:407–470, 2011.

[54] Chun Hung Lui, Zhiqiang Li, Zheyuan Chen, Paul V. Klimov, Louis E. Brus, and Tony F. Heinz. Imaging Stacking Order in Few-Layer Graphene. *Nano Letters*, 11(1):164–169, 2011. PMID: 21121668.

[55] Jinglei Ping and Michael S. Fuhrer. Layer Number and Stacking Sequence Imaging of Few-Layer Graphene by Transmission Electron Microscopy. *Nano Letters*, 12(9):4635–4641, 2012.

[56] Ahti Niilisk, Jekaterina Kozlova, Harry Alles, Jaan Aarik, and Vaino Sammelselg. Raman characterization of stacking in multi-layer graphene grownÂ onÂ Ni. *Carbon*, 98:658 – 665, 2016.

[57] Yufeng Hao, Yingying Wang, Lei Wang, Zhenhua Ni, Ziqian Wang, Rui Wang, Chee Keong Koo, Zexiang Shen, and John T. L. Thong. Probing Layer Number and Stacking Order of Few-Layer Graphene by Raman Spectroscopy. *Small*, 6(2):195–200, 2010.

[58] Qiang Wang, Li Wei, Michael Sullivan, Shuo-Wang Yang, and Yuan Chen. Graphene layers on Cu and Ni(111) surfaces in layer controlled graphene growth. *RSC Adv.*, 3:3046–3053, 2013.

[59] Victor Carozo, Clara M. Almeida, Erlon H. M. Ferreira, Luiz Gustavo Cancado, Carlos Alberto Achete, and Ado Jorio. Raman Signature of Graphene Superlattices. *Nano Letters*, 11(11):4527–4534, 2011.

[60] Junto Tsurumi, Yuika Saito, and Prabhat Verma. Evaluation of the interlayer interactions of few layers of graphene. *Chemical Physics Letters*, 557:114 – 117, 2013.

[61] K.I. Bolotin, K.J. Sikes, Z. Jiang, M. Klima, G. Fudenberg, J. Hone, P. Kim, and H.L. Stormer. Ultrahigh electron mobility in suspended graphene. *Solid State Communications*, 146(9):351 – 355, 2008.

[62] K. I. Bolotin, K. J. Sikes, J. Hone, H. L. Stormer, and P. Kim. Temperature-Dependent Transport in Suspended Graphene. *Phys. Rev. Lett.*, 101:096802, 2008.

[63] P. Neugebauer, M. Orlita, C. Faugeras, A.-L. Barra, and M. Potemski. How perfect can graphene be? *Phys. Rev. Lett.*, 103:136403, 2009.

[64] Marlene Bonmann, Andrei Vorobiev, Michael A. Andersson, and Jan Stake. Charge carrier velocity in graphene field-effect transistors. *Applied Physics Letters*, 111(23):233505, 2017.

[65] C. Canali, C. Jacoboni, F. Nava, G. Ottaviani, and A. Alberigi-Quaranta. Electron drift velocity in silicon. *Phys. Rev. B*, 12:2265–2284, 1975.

[66] Kin Fai Mak, Matthew Y. Sfeir, Yang Wu, Chun Hung Lui, James A. Misewich, and Tony F. Heinz. Measurement of the Optical Conductivity of Graphene. *Phys. Rev. Lett.*, 101:196405, 2008.

[67] R. R. Nair, P. Blake, A. N. Grigorenko, K. S. Novoselov, T. J. Booth, T. Stauber, N. M. R. Peres, and A. K. Geim. Fine Structure Constant Defines Visual Transparency of Graphene. *Science*, 320(5881):1308–1308, 2008.

[68] T. Stauber, N. M. R. Peres, and A. K. Geim. Optical conductivity of graphene in the visible region of the spectrum. *Phys. Rev. B*, 78:085432, 2008.

[69] Gopinadhan Kalon, Shin Young Jun, Jalil Rashid, Venkatesan Thirumalai, Geim Andre K., Neto Antonio H. Castro, and Yang Hyunsoo. Extremely large magnetoresistance in few-layer graphene/boron-nitride heterostructures. *Nature Communications*, 6, 2015.

[70] Kalon Gopinadhan, Young Jun Shin, Indra Yudhistira, Jing Niu, and Hyunsoo Yang. Giant magnetoresistance in single-layer graphene flakes with a gate-voltage-tunable weak antilocalization. *Phys. Rev. B*, 88:195429, 2013.

[71] Siegfried Hunklinger. *Festkörperphysik*. Oldenbourg Verlag, 2007.

[72] N. W. Ashcroft and D. N. Mermin. *Festkörperphysik*. Oldenbourg Wissenschaftsverlag, 2001.

[73] R. Gross and A. Marx. *Festkörperphysik*. Oldenbourg Wissenschaftsverlag, 2012.

[74] S. Datta. *Electronic Transport in Mesoscopic Systems*. Cambridge Studies in Semiconductor Physics and Microelectronic Engineering. Cambridge University Press, 1997.

[75] B. L. Altshuler, D. Khmel'nitzkii, A. I. Larkin, and P. A. Lee. Magnetoresistance and Hall effect in a disordered two-dimensional electron gas. *Phys. Rev. B*, 22:5142–5153, 1980.

[76] Y. Aharonov and D. Bohm. Significance of Electromagnetic Potentials in the Quantum Theory. *Phys. Rev.*, 115:485–491, 1959.

[77] D. Feng and G. Jin. *Introduction to Condensed Matter Physics*. Number Bd. 1 in Introduction to Condensed Matter Physics. World Scientific, 2005.

[78] J. L. Olsen. *Electron Transport in Metals*. Interscience tracts on physics and astronomy. Interscience, 1962.

[79] A.B. Pippard. *Magnetoresistance in Metals*. Cambridge Studies in Low Temperature Physics. Cambridge University Press, 1989.

[80] J. D. Burton, A. Kashyap, M. Ye. Zhuravlev, R. Skomski, E. Y. Tsymbal, S. S. Jaswal, O. N. Mryasov, and R. W. Chantrell. Field-controlled domain-wall resistance in magnetic nanojunctions. *Applied Physics Letters*, 85(2):251–253, 2004.

[81] R. V. Coleman and A. Isin. Magnetoresistance in Iron Single Crystals. *Journal of Applied Physics*, 37(3):1028–1029, 1966.

[82] M. N. Baibich, J. M. Broto, A. Fert, F. Nguyen Van Dau, F. Petroff, P. Etienne, G. Creuzet, A. Friederich, and J. Chazelas. Giant Magnetoresistance of (001)Fe/(001)Cr Magnetic Superlattices. *Phys. Rev. Lett.*, 61:2472–2475, 1988.

[83] A. Yu. Kuntsevich, L. A. Morgun, and V. M. Pudalov. Electron-electron interaction correction and magnetoresistance in tilted fields in Si-based two-dimensional systems. *Phys. Rev. B*, 87:205406, 2013.

[84] S.A. Bhuyan, N. Uddin, M. Islam, F.A. Bipasha, and S.S. Hossain. Synthesis of graphene. *Int Nano Lett*, 6:65–83, 2016.

[85] Na Liu, Fang Luo, Haoxi Wu, Yinghui Liu, Chao Zhang, and Ji Chen. One-Step Ionic-Liquid-Assisted Electrochemical Synthesis of Ionic-Liquid-Functionalized Graphene Sheets Directly from Graphite. *Advanced Functional Materials*, 18(10):1518–1525, 2008.

[86] Athanasios B. Bourlinos, Vasilios Georgakilas, Radek Zboril, Theodore A. Steriotis, and Athanasios K. Stubos. Liquid-Phase Exfoliation of Graphite Towards Solubilized Graphenes. *Small*, 5(16):1841–1845, 2009.

[87] Chang-Duk Kim, Bong-Ki Min, and Woo-Sik Jung. Preparation of graphene sheets by the reduction of carbon monoxide. *Carbon*, 47(6):1610 – 1612, 2009.

[88] Andreas Hirsch. Unzipping Carbon Nanotubes: A Peeling Method for the Formation of Graphene Nanoribbons. *Angewandte Chemie International Edition*, 48(36):6594–6596, 2009.

[89] L. Jiao, L. Zhang, X. Wang, G. Diankov, and H. Dai. Narrow graphene nanoribbons from carbon nanotubes. *Nature*, 458, 2009.

[90] E. Rollings, G.-H. Gweon, S.Y. Zhou, B.S. Mun, J.L. McChesney, B.S. Hussain, A.V. Fedorov, P.N. First, W.A. de Heer, and A. Lanzara. Synthesis and characterization of atomically thin graphite films on a silicon carbide substrate. *Journal of Physics and Chemistry of Solids*, 67(9):2172 – 2177, 2006.

[91] Walt A. de Heer, Claire Berger, Xiaosong Wu, Phillip N. First, Edward H. Conrad, Xuebin Li, Tianbo Li, Michael Sprinkle, Joanna Hass, Marcin L. Sadowski, Marek Potemski, and Gerard Martinez. Epitaxial graphene. *Solid State Communications*, 143(1):92 – 100, 2007.

[92] Alexander Mattausch and Oleg Pankratov. Density functional study of graphene overlayers on SiC. *physica status solidi (b)*, 245(7):1425–1435, 2008.

[93] Z. H. Ni, W. Chen, X. F. Fan, J. L. Kuo, T. Yu, A. T. S. Wee, and Z. X. Shen. Raman spectroscopy of epitaxial graphene on a SiC substrate. *Phys. Rev. B*, 77:115416, 2008.

[94] Th. Seyller, A. Bostwick, K. V. Emtsev, K. Horn, L. Ley, J. L. McChesney, T. Ohta, J. D. Riley, E. Rotenberg, and F. Speck. Epitaxial graphene: a new material. *physica status solidi (b)*, 245(7):1436–1446, 2008.

[95] M. Sprinkle, P. Soukiassian, W. A. de Heer, C. Berger, and E. H. Conrad. Epitaxial graphene: the material for graphene electronics. *physica status solidi (RRL) - Rapid Research Letters*, 3(6):A91–A94, 2009.

[96] Xianbao Wang, Haijun You, Fangming Liu, Mingjian Li, Li Wan, Shaoqing Li, Qin Li, Yang Xu, Rong Tian, Ziyong Yu, Dong Xiang, and Jing Cheng. Large-Scale Synthesis of Few-Layered Graphene using CVD. *Chemical Vapor Deposition*, 15(1-3):53–56, 2009.

[97] Enkeleda Dervishi, Zhongrui Li, Fumiya Watanabe, Abhijit Biswas, Yang Xu, Alexandru R. Biris, Viney Saini, and Alexandru S. Biris. Large-scale graphene production by RF-cCVD method. *Chem. Commun.*, pages 4061–4063, 2009.

[98] Michael Nastasi and James W. Mayer. *Ion Implantation and Synthesis of Materials*. Springer, 2006.

[99] Mingguang Chen, Robert C. Haddon, Ruoxue Yan, and Elena Bekyarova. Advances in transferring chemical vapour deposition graphene: a review. *Mater. Horiz.*, 4:1054–1063, 2017.

[100] Robust graphene wet transfer process through low molecular weight polymethylmethacrylate. *Carbon*, 98:352 – 357, 2016.

[101] Sandeep Gorantla, Alicja Bachmatiuk, Jeonghyun Hwang, Hussain A. Alsalman, Joon Young Kwak, Thomas Seyller, Jürgen Eckert, Michael G. Spencer, and Mark H. Rümmeli. A universal transfer route for graphene. *Nanoscale*, 6:889–896, 2014.

[102] Gao Libo, Ren Wencai, Xu Huilong, Jin Li, Wang Zhenxing, Ma Teng, Ma Lai-Peng, Zhang Zhiyong, Fu Qiang, Peng Lian-Mao, Bao Xinhe, and Cheng Hui-Ming. Repeated growth and bubbling transfer of graphene with millimetre-size single-crystal grains using platinum. *Nature Communications*, 3(699), 2012.

[103] Kamrul Islam, Ahmed Suhail, and Genhua Pan. A Label-Free and Ultrasensitive Immunosensor for Detection of Human Chorionic Gonadotrophin Based on Graphene FETs. *Biosensors*, 7(3), 2017.

[104] Bae Sukang, Kim Hyeongkeun, Lee Youngbin, Xu Xiangfan, Park Jae-Sung, Zheng Yi, Balakrishnan Jayakumar, Lei Tian, Ri Kim, Hye Song, Young Il, Kim Young-Jin, Kim Kwang S., Özyilmaz Barbaros, Ahn Jong-Hyun, Hong Byung Hee, and Iijima Sumio. Roll-to-roll production of 30-inch graphene films for transparent electrodes. *Nature Nanotechnology*, 5(574), 2010.

[105] Junmo Kang, Soonhwi Hwang, Jae Hwan Kim, Min Hyeok Kim, Jaechul Ryu, Sang Jae Seo, Byung Hee Hong, Moon Ki Kim, and Jae-Boong Choi. Efficient Transfer of Large-Area Graphene Films onto Rigid Substrates by Hot Pressing. *ACS Nano*, 6(6):5360–5365, 2012.

[106] Ahn Se Hyun and Guo L. Jay. High-Speed Roll-to-Roll Nanoimprint Lithography on Flexible Plastic Substrates. *Advanced Materials*, 20(11):2044–2049.

[107] Sondergaard Roar R., Hösel Markus, and Krebs Frederik C. Roll-to-Roll fabrication of large area functional organic materials. *Journal of Polymer Science Part B: Polymer Physics*, 51(1):16–34.

[108] Xuesong Li, Yanwu Zhu, Weiwei Cai, Mark Borysiak, Boyang Han, David Chen, Richard D. Piner, Luigi Colombo, and Rodney S. Ruoff. Transfer of Large-Area Graphene Films for High-Performance Transparent Conductive Electrodes. *Nano Letters*, 9(12):4359–4363, 2009.

[109] Xuelei Liang, Brent A. Sperling, Irene Calizo, Guangjun Cheng, Christina Ann Hacker, Qin Zhang, Yaw Obeng, Kai Yan, Hailin Peng, Qiliang Li, Xiaoxiao Zhu, Hui Yuan, Angela R. Hight Walker, Zhongfan Liu, Lian-mao Peng, and Curt A. Richter. Toward Clean and Crackless Transfer of Graphene. *ACS Nano*, 5(11):9144–9153, 2011.

[110] Mingguang Chen, Dejan Stekovic, Wangxiang Li, Bassim Arkook, Robert C Haddon, and Elena Bekyarova. Sublimation-assisted graphene transfer technique based on small polyaromatic hydrocarbons. *Nanotechnology*, 28(25):255701, 2017.

[111] Jan Lehnert, Daniel Spemann, M. Hamza Hatahet, Stephan Mändl, Michael Mensing, Annemarie Finzel, Aron Varga, and Bernd Rauschenbach. Graphene on silicon dioxide via carbon ion implantation in copper with PMMA-free transfer. *Applied Physics Letters*, 110(23):233114, 2017.

[112] Jinglei Ping and Michael S. Fuhrer. Carbon impurities on graphene synthesized by chemical vapor deposition on platinum. *Journal of Applied Physics*, 116(4):044303, 2014.

[113] J.F. Ziegler, J.P. Biersack, and M.D. Ziegler. *SRIM, the Stopping and Range of Ions in Matter.* SRIM Company, 2008.

[114] Simulationssoftware SRIM J. Ziegler. URL: `http://www.srim.org/`.

[115] Krishna Seshan. *Handbook of Thin Film Deposition Processes and Technologies.* Noyes Publication, 2 edition, 2002.

[116] L.B. Freund and S. Suresh. *Thin Film Materials Stress, Defect Formation and Surface Evolution.* Cambridge University Press, 2003.

[117] Daniel Spemann. *Anwendung hochenergetischer Ionenstrahlen in den Materialwissenschaften.* PhD thesis, Universität Leipzig, 2007.

[118] On the determination of molecular fields. —ii. from the equation of state of a gas. *Proceedings of the Royal Society of London A: Mathematical, Physical and Engineering Sciences*, 106(738):463–477, 1924.

[119] James F. Ziegler and Jochen P. Biersack. *The Stopping and Range of Ions in Matter*, pages 93–129. Springer US, 1985.

[120] J.F. Ziegler. *The Stopping and Ranges of Ions in Matter*, volume 1. 1977.

[121] C. Varelas and J. Biersack. Reflection of energetic particles from atomic or ionic chains in single crystals. *Nuclear Instruments and Methods*, 79(2):213–218, 1970.

[122] J.F. Ziegler and W.K. Chu. Stopping cross sections and backscattering factors for 4he ions in matter Z = 1-92, E(4He) = 400-4000 kev. *Atomic Data and Nuclear Data Tables*, 13(5):463–489, 1974.

[123] H. Bethe. Zur Theorie des Durchgangs schneller Korpuskularstrahlen durch Materie. *Annalen der Physik*, 397(3):325–400, 1930.

[124] G. Götz and K. Gärtner. *High Energy Ion Beam Analysis of Solids.* Akademie-Verlag, Berlin, 1988.

[125] O.B. Firsov. A qualitative treatment of the average energy of electron excitation in atomic collisions. *Zh. Eksp. Teor. Fiz*, 36:1517–1523, 1959.

[126] J. Lindhard, M. Scharff, and H.E. Schiott. Range concepts and heavy ion ranges. *Mat. Fys. Medd. K. Dan. Vidensk. Selsk*, 33(14), 1963.

[127] Wei-Kan Chu, J.W. Mayer, and M.A. Nicolet. *Backscattering spectrometry.* New York: Academic Press, 1978.

[128] W. Assmann, H. Huber, Ch. Steinhausen, M. Dobler, H. Glückler, and A. Weidinger. Elastic recoil detection analysis with heavy ions. *Nuclear Instruments and Methods in Physics Research Section B: Beam Interactions with Materials and Atoms*, 89(1):131–139, 1994.

[129] Lawrence R. Doolittle. Algorithms for the rapid simulation of Rutherford backscattering spectra. *Nuclear Instruments and Methods in Physics Research Section B: Beam Interactions with Materials and Atoms*, 9(3):344 – 351, 1985.

[130] *TRAINING WORKBOOK MODEL IMC SERIES ION IMPLANTER*, 2008.

[131] Christian Patzig. *Glancing Angle Deposition of Silicon Nanostructures by Ion Beam Sputtering.* PhD thesis, Universität Leipzig, 2009.

[132] J.S. Huang, J. Zhang, A. Cuevas, and K.N. Tu. Recrystallization and grain growth in bulk Cu and Cu(Sn) alloy. *Materials Chemistry and Physics*, 49(1):33 – 41, 1997.

[133] S Simoes, R Calinas, M T Vieira, M F Vieira, and P J Ferreira. In situ TEM study of grain growth in nanocrystalline copper thin films. *Nanotechnology*, 21(14):145701, 2010.

[134] David L. Miller, Mark W. Keller, Justin M. Shaw, Katherine P. Rice, Robert R. Keller, and Kyle M. Diederichsen. Giant secondary grain growth in Cu films on sapphire. *AIP Advances*, 3(8):082105, 2013.

[135] W. Demtröder. *Laserspektroskopie, Grundlagen und Techniken.* Springer, 2004.

[136] Derek A. Long. *The Raman Effect: A Unified Treatment of the Theory of Raman Scattering by Molecules.* John Wiley and Sons Ltd, 2002.

[137] M. Cardona, R.K. Chang, G. Güntherodt, M.B. Long, and H. Vogt. *Light Scattering in Solids II.* Springer.

[138] D.J. Gardiner and P.R. Grawes. *Practical Raman Spectroscopy.* Springer Berlin, 1989.

[139] Achintya K. Ganguly and Joseph L. Birman. Theory of Lattice Raman Scattering in Insulators. *Phys. Rev.*, 162:806–816, Oct 1967.

[140] R. Loudon. The raman effect in crystals. *Advances in Physics*, 50(7):813–864, 2001.

[141] P. Klar, E. Lidorikis, A. Eckmann, I. A. Verzhbitskiy, A. C. Ferrari, and C. Casiraghi. Raman scattering efficiency of graphene. *Phys. Rev. B*, 87:205435, 2013.

[142] Hans-Jörg Kull. *Laserphysik.* Oldenbourg Verlag, 2010.

[143] David Griffiths. *Introduction of Quantum Mechanics.* Prentice Hall, Inc., 1995.

[144] J.J. Olivero and R.L. Longbothum. Empirical fits to the Voigt line width: A brief review. *Journal of Quantitative Spectroscopy and Radiative Transfer*, 17(2):233 – 236, 1977.

[145] Karl Pearson. III. Contributions to the mathematical theory of evolution. *Proceedings of the Royal Society of London*, 54(326-330):329–333, 1894.

[146] Michele Lazzeri, Claudio Attaccalite, Ludger Wirtz, and Francesco Mauri. Impact of the electron-electron correlation on phonon dispersion: Failure of LDA and GGA DFT functionals in graphene and graphite. *Phys. Rev. B*, 78:081406, Aug 2008.

[147] Ryan Beams, Luiz Gustavo Cancado, and Lukas Novotny. Raman characterization of defects and dopants in graphene. *Journal of Physics: Condensed Matter*, 27(8):083002, 2015.

[148] Andrea C. Ferrari and Denis M. Basko. Raman spectroscopy as a versatile tool for studying the properties of graphene. *Nature Nanotechnology*, 8:235–246, 2013.

[149] D. L. Mafra, G. Samsonidze, L. M. Malard, D. C. Elias, J. C. Brant, F. Plentz, E. S. Alves, and M. A. Pimenta. Determination of LA and TO phonon dispersion relations of graphene near the Dirac point by double resonance Raman scattering. *Phys. Rev. B*, 76:233407, 2007.

[150] P. Blake, E. W. Hill, A. H. Castro Neto, K. S. Novoselov, D. Jiang, R. Yang, T. J. Booth, and A. K. Geim. Making graphene visible. *Applied Physics Letters*, 91(6):063124, 2007.

[151] Duhee Yoon, Hyerim Moon, Young-Woo Son, Jin Sik Choi, Bae Ho Park, Young Hun Cha, Young Dong Kim, and Hyeonsik Cheong. Interference effect on Raman spectrum of graphene on SiO_2/Si. *Phys. Rev. B*, 80:125422, 2009.

[152] S. Roddaro, P. Pingue, V. Piazza, V. Pellegrini, and F. Beltram. The Optical Visibility of Graphene: Interference Colors of Ultrathin Graphite on SiO_2. *Nano Letters*, 7(9):2707–2710, 2007.

[153] A. Das, S. Pisana, B. Chakraborty, S. Piscanec, S.K. Saha, U.V. Waghmare, K.S. Novoselov, H.R. Krishnamurthy, A.K. Geim, A.C. Ferrari, and A.K. Sood. Monitoring dopants by Raman scattering in an electrochemically top-gated graphene transistor. *Nature Nanotechnology*, 3:210–215, 2008.

[154] I. Calizo, A. A. Balandin, W. Bao, F. Miao, and C. N. Lau. Temperature Dependence of the Raman Spectra of Graphene and Graphene Multilayers. *Nano Letters*, 7(9):2645–2649, 2007.

[155] D. L. Nika, S. Ghosh, E. P. Pokatilov, and A. A. Balandin. Lattice thermal conductivity of graphene flakes: Comparison with bulk graphite. *Applied Physics Letters*, 94(20):203103.

[156] Nachiket R. Raravikar, Pawel Keblinski, Apparao M. Rao, Mildred S. Dresselhaus, Linda S. Schadler, and Pulickel M. Ajayan. Temperature dependence of radial breathing mode Raman frequency of single-walled carbon nanotubes. *Phys. Rev. B*, 66:235424, 2002.

[157] Irene Calizo, Wenzhong Bao, Feng Miao, Chun Ning Lau, and Alexander A. Balandin. The effect of substrates on the Raman spectrum of graphene: Graphene-on-sapphire and graphene-on-glass. *Applied Physics Letters*, 91(20):201904, 2007.

[158] Anindya Das, Biswanath Chakraborty, and A. K. Sood. Raman spectroscopy of graphene on different substrates and influence of defects. *Bulletin of Materials Science*, 31(3):579–584, 2008.

[159] Jun Yan, Erik A. Henriksen, Philip Kim, and Aron Pinczuk. Observation of Anomalous Phonon Softening in Bilayer Graphene. *Phys. Rev. Lett.*, 101:136804, 2008.

[160] Scott W. Schmucker, Cory D. Cress, James C. Culbertson, Jeffrey W. Beeman, Oscar D. Dubon, and Jeremy T. Robinson. Raman signature of defected twisted bilayer graphene. *Carbon*, 93:250 – 257, 2015.

[161] Zhe Lin, Xiaohui Ye, Jinpeng Han, Qiao Chen, Peixun Fan, Hongjun Zhang, Dan Xie, Hongwei Zhu, and Minlin Zhong. Precise Control of the Number of Layers of Graphene by Picosecond Laser Thinning. *Scientific Reports*, 5, 2015.

[162] Andrea C. Ferrari. Raman spectroscopy of graphene and graphite: Disorder, electron-phonon coupling, doping and nonadiabatic effects. *Solid State Communications*, 143(1-2):47–57, 2007.

[163] A. C. Ferrari, J. C. Meyer, V. Scardaci, C. Casiraghi, M. Lazzeri, F. Mauri, S. Piscanec, D. Jiang, K. S. Novoselov, S. Roth, and A. K. Geim. Raman Spectrum of Graphene and Graphene Layers. *Phys. Rev. Lett.*, 97:187401, Oct 2006.

[164] E. H. Martins Ferreira, Marcus V. O. Moutinho, F. Stavale, M. M. Lucchese, Rodrigo B. Capaz, C. A. Achete, and A. Jorio. Evolution of the Raman spectra from single-, few-, and many-layer graphene with increasing disorder. *Phys. Rev. B*, 82:125429, 2010.

[165] Qing Hua Wang, Zhong Jin, Ki Kang Kim, Andrew J. Hilmer, Geraldine L. C. Paulus, Chih-Jen Shih, Moon-Ho Ham, Javier D. Sanchez-Yamagishi, Kenji Watanabe, Takashi Taniguchi, Jing Kong, Pablo Jarillo-Herrero, and Michael S. Strano. Understanding and controlling the substrate effect on graphene electron-transfer chemistry via reactivity imprint lithography. *Nature Chemistry*, 4:724–732, 2012.

[166] L.G. Cancado, A. Jorio, E.H. Martins Ferreira, F. Stavale, C.A. Achete, R.B. Capaz, M.V.O. Moutinho, A. Lombardo, T.S. Kulmala, and A.C. Ferrari. Quantifying Defects in Graphene via Raman Spectroscopy at Different Excitation Energies. *Nano Letters*, 11(8), 2011.

[167] M. A. Pimenta, G. Dresselhaus, M. S. Dresselhaus, L. G. Cancado, A. Jorio, and R. Saito. Studying disorder in graphite-based systems by Raman spectroscopy. *Phys. Chem. Chem. Phys.*, 9:1276–1290, 2007.

[168] K. Sato, R. Saito, Y. Oyama, J. Jiang, L.G. CanÃ§ado, M.A. Pimenta, A. Jorio, Ge.G. Samsonidze, G. Dresselhaus, and M.S. Dresselhaus. D-band Raman intensity of graphitic materials as a function of laser energy and crystallite size. *Chemical Physics Letters*, 427(1):117 – 121, 2006.

[169] Bruno R. Carvalho, Yufeng Hao, Ariete Righi, Joaquin F. Rodriguez-Nieva, Luigi Colombo, Rodney S. Ruoff, Marcos A. Pimenta, and Cristiano Fantini. Probing carbon isotope effects on the Raman spectra of graphene with different ^{13}C concentrations. *Phys. Rev. B*, 92:125406, 2015.

[170] O. Frank, L. Kavan, and M. Kalbac. Carbon isotope labelling in graphene research. *Nanoscale*, 6:6363–6370, 2014.

[171] L.G. Cancado, M. A. Pimenta, B. R. A. Neves, M. S. S. Dantas, and A. Jorio. Influence of the Atomic Structure on the Raman Spectra of Graphite Edges. *Phys. Rev. Lett.*, 93:247401, 2004.

[172] C. Casiraghi, A. Hartschuh, H. Qian, S. Piscanec, C. Georgi, A. Fasoli, K. Novoselov, D. Basko, and A. Ferrari. Raman spectroscopy of graphene edges. *Nano Letters*, 9(4), 2009.

[173] B. Krauss, P. Nemes-Incze, V. Skakalova, P. Biro, K. Klitzing, and J. H. Smet. Raman Scattering at Pure Graphene Zigzag Edges. *Nano Letters*, 10, 2010.

[174] C. Casiraghi, S. Pisana, K. S. Novoselov, A. K. Geim, and A. C. Ferrari. Raman fingerprint of charged impurities in graphene. *Applied Physics Letters*, 91(23):233108, 2007.

[175] L. G. Cancado, K. Takai, T. Enoki, M. Endo, Y. A. Kim, H. Mizusaki, A. Jorio, L. N. Coelho, R. Magalhaes-Paniago, and M. A. Pimenta. General equation for the determination of the crystallite size L_{a} of nanographite by Raman spectroscopy. *Applied Physics Letters*, 88(16):163106, 2006.

[176] Resonant Raman spectroscopy of graphene grown on copper substrates. *Solid State Communications*, 152(15):1317 – 1320, 2012.

[177] Zhen Hua Ni, Ting Yu, Zhi Qiang Luo, Ying Ying Wang, Lei Liu, Choun Pei Wong, Jianmin Miao, Wei Huang, and Ze Xiang Shen. Probing Charged Impurities in Suspended Graphene Using Raman Spectroscopy. *ACS Nano*, 3:569–574, 2009.

[178] Ying ying Wang, Zhen hua Ni, Ting Yu, Ze Xiang Shen, Hao min Wang, Yi hong Wu, Wei Chen, and Andrew Thye Shen Wee. Raman Studies of Monolayer Graphene: The Substrate Effect. *The Journal of Physical Chemistry C*, 112(29):10637–10640, 2008.

[179] P. H. Tan, W. P. Han, W. J. Zhao, Z. H. Wu, K. Chang, H. Wang, Y. F. Wang, N. Bonini, N. Marzari, N. Pugno, G. Savini, A. Lombardo, and A. C. Ferrari. The shear mode of multilayer graphene. *Nature Materials*, 11:294–300, 2012.

[180] N. You-Shin, C. Hong Kyw, K. Jin-Soo, K. Hakseong, Y. Young-Jun, C. Choon-Gi, and C. Jin Sik. Layer number identification of CVD-grown multilayer graphene using Si peak analysis. *Scientific Reports*, 8(571), 2018.

[181] Hidefumi Hiura, Hisao Miyazaki, and Kazuhito Tsukagoshi. Determination of the Number of Graphene Layers: Discrete Distribution of the Secondary Electron Intensity Stemming from Individual Graphene Layers. *Applied Physics Express*, 3(9):095101, 2010.

[182] P. Nemes-Incze, Z. Osvath, K. Kamaras, and L.P. Biro. Anomalies in thickness measurements of graphene and few layer graphite crystals by tapping mode atomic force microscopy. *Carbon*, 46(11):1435–1442, 2008.

[183] Xinxing Sun. *Phase Transformation and Switching of Chalcogenide Phase-change Material Films Prepared by Pulsed Laser Deposition.* PhD thesis.

[184] T E Everhart and R F M Thornley. Wide-band detector for micro-microampere low-energy electron currents. *Journal of Scientific Instruments*, 37(7):246, 1960.

[185] Annemarie Finzel. *Ionenstrahlgestützte Molekularstrahlepitaxie von Galliumnitrid-Schichten auf Silizium.* PhD thesis, Universität Leipzig, 2015.

[186] L. Spiess, G. Teichert, R. Schwarzer, H. Behnken, and C. Genzel. *Moderne Röntgenbeugung: Röntgendiffraktometrie für Materialwissenschaftler, Physiker und Chemiker.* Vieweg/Teubner, 2009.

[187] B.D. Cullity and S.R. Stock. *Elements of X-RAY Diffraction.* Prentice Hall, Inc., 3 edition, 2001.

[188] W. C. Marra, P. Eisenberger, and A. Y. Cho. X-ray total-external-reflection-Bragg diffraction: A structural study of the GaAs-Al interface. *Journal of Applied Physics*, 50(11):6927–6933, 1979.

[189] Erik Thelander. *Epitaxial Ge-Te-Sb Thin Films by Pulsed Laser Deposition.* PhD thesis, Universität Leipzig, 2014.

[190] C.R. Brundle and A.D. Baker. *Electron Spectroscopy: Theory, Techniques and Applications*, volume 2. Academic Press, 1978.

[191] Pragya Tiwari, Himanshu Srivastava, Sanjay Rai, and S. K. Deb. Recrystallization, Grain Growth in Copper Foil at High Temperature Studied By Electron Back Scatter Diffraction. *AIP Conference Proceedings*, 1349(1):705–706, 2011.

[192] J. Lehnert, D. Spemann, S. Surjuse, M. Mensing, C. Grüner, P. With, P. Schumacher, A. Finzel, D. Hirsch, and B. Rauschenbach. Preparation and characterisation of carbon-free Cu(111) films on sapphire for graphene synthesis. *Journal of Physics: Conference Series*, 992(1):012024, 2018.

[193] Abraham. Savitzky and M. J. E. Golay. Smoothing and Differentiation of Data by Simplified Least Squares Procedures. *Analytical Chemistry*, 36(8):1627–1639, 1964.

[194] Tao Ma, Hiroko Ariga, Satoru Takakusagi, and Kiyotaka Asakura. Smooth epitaxial copper film on sapphire surface suitable for high quality graphene growth. *Thin Solid Films*, 646:12–16, 2018.

[195] G.A. López and E.J. Mittemeijer. The solubility of C in solid Cu. *Scripta Materialia*, 51(1):1 – 5, 2004.

[196] B. Eliasson and U. Kogelschatz. UV excimer radiation from dielectric-barrier discharges. *Applied Physics B*, 46(4):299–303.

[197] *Handbook of Chemistry*, volume 2. Chemical Society of Japan.

[198] Lutz Prager, Andreas Dierdorf, Hubert Liebe, Sergej Naumov, Sandra Stojanovic, Roswitha Heller, Luise Wennrich, and Michael Buchmeiser. Conversion of Perhydropolysilazane into a SiO_x Network Triggered by Vacuum Ultraviolet Irradiation: Access to Flexible, Transparent Barrier Coatings. *Chemistry - A European Journal*, 13(30):8522–8529, 2007.

[199] *Personal conversation with Dr. Lutz Prager (IOM-Leipzig).*

[200] Research and Development Technical Report. Ultraviolet-Ozone Cleaning of Semiconductor Surfaces. 1992.

[201] Zs Laszlo, G. Ilisz Peintler, and A. Dombi. VUV Intensity Measurement of a 172nm Xe Excimer Lamp by means of Oxygen Actinometry. *Ozone: Science & Engineering*, 20(5):421–432, 1998.

[202] Srinandan R. Kasi and M. Liehr. Vapor phase hydrocarbon removal for Si processing. *Applied Physics Letters*, 57(20):2095–2097, 1990.

[203] R. Byron Bird, Warren E. Stewart, and Edwin N. Lightfoot. *Transport Phenomena.* John Wiley & Sons, Inc., second edition edition, 2002.

[204] Zhou Hong-Bo and Jin Shuo. Towards understanding the carbon trapping mechanism in copper by investigating the carbon-vacancy interaction. *Chinese Physics B*, 22(7):076104, 2013.

[205] Zhijuan Zhao, Zhifa Shan, Cankun Zhang, Qiongyu Li, Bo Tian, Zhiyi Huang, Weiyi Lin, Xiangping Chen, Hengxing Ji, Weifeng Zhang, and Weiwei Cai. Study on the Diffusion Mechanism of Graphene Grown on Copper Pockets. *Small*, 11(12):1418–1422.

[206] Landolt-Bornstein. *Numerical Data and Functional Relationships in Science and Technology, New Series, Group III: Crystal and Solid State Physics, Diffusion in Metals and Alloys*, volume Vol. 26. Springer-Verlag, Berlin, 1990.

[207] Stefan Thiele, Alfonso Reina, Paul Healey, Jakub Kedzierski, Peter Wyatt, Pei-Lan Hsu, Craig Keast, Juergen Schaefer, and Jing Kong. Engineering polycrystalline Ni films to improve thickness uniformity of the chemical-vapor-deposition-grown graphene films. *Nanotechnology*, 21(1):015601, 2010.

[208] Eunho Kim, Yong Seung Kim, Jaehyun Park, Sajjad Hussain, Seung-Hyun Chun, Seong Jun Kim, Ki-Seok An, Won-Jun Lee, Wan-Gyu Lee, and Jongwan Jung. Graphene film growth on sputtered thin Cu-Ni alloy film by inductively coupled plasma chemical vapor deposition. *RSC Adv.*, 4:63349–63353, 2014.

[209] Subramanian P.R and Laughlin D.E. *Phase diagrams of binary copper alloys. Monograph series on alloy phase diagrams*, volume 10. Materials Park, OH: ASM International, 1994. page 109.

[210] Donals McLean. *Grain boundaries in metals.* Oxford, Clarendon Press, 1957.

[211] N. B. Vargaftik, B. N. Volkov, and L. D. Voljak. International Tables of the Surface Tension of Water. *Journal of Physical and Chemical Reference Data*, 12(3):817–820, 1983.

[212] Nan Liu, Zhonghuai Pan, Lei Fu, Chaohua Zhang, Boya Dai, and Zhongfan Liu. The origin of wrinkles on transferred graphene. *Nano Research*, 4(10):996, Jun 2011.

[213] Shahin Homaeigohar and Mady Elbahri. Graphene membranes for water desalination. *Npg Asia Materials*, 9, 2017.

[214] Graphene sieve turns seawater into drinking water. *Filtration + Separation*, 54(3):30 – 32, 2017.

[215] Khan M.F. Shahil and Alexander A. Balandin. Thermal properties of graphene and multilayer graphene: Applications in thermal interface materials. *Solid State Communications*, 152(15):1331 – 1340, 2012.

[216] Sanghyun Cho, Insub Jung, Hee-Jeong Jang, Lichun Liu, and Sungho Park. Bimetallic junction mediated synthesis of multilayer graphene edges towards ultrahigh capacity for lithium ion batteries. *Nanoscale*, 10:5214–5220, 2018.

[217] Janghyuk Kim, Hong-Yeol Kim, Jeong Heum Jeon, Sungjoo An, Jongwon Hong, and Jihyun Kim. Study on the formation of graphene by ion implantation on Cu, Ni and CuNi alloy. *Applied Surface Science*, 451:162 – 168, 2018.

[218] A. Pirkle, J. Chan, A. Venugopal, D. Hinojos, C. W. Magnuson, S. McDonnell, L. Colombo, E. M. Vogel, R. S. Ruoff, and R. M. Wallace. The effect of chemical residues on the physical and electrical properties of chemical vapor deposited graphene transferred to SiO_2. *Applied Physics Letters*, 99(12):122108, 2011.

[219] L.J. Van der Pauw. A method of measuring specific resistivity and Hall effect of discs of arbitrary shape. *Philips Research Reports*, 13, 1958.

[220] Simon M. Sze and Kwok K. Ng. *Physics of Semiconductor Devices*, volume 3. John Wiley & Sons, 2006.

[221] Sune Thorsteinsson, Fei Wang, Dirch H. Petersen, Torben Mikael Hansen, Daniel Kjaer, Rong Lin, Jang-Yong Kim, Peter F. Nielsen, and Ole Hansen. Accurate microfour-point probe sheet resistance measurements on small samples. *Review of Scientific Instruments*, 80(5):053902, 2009.

[222] K. Königsberger. *Analysis 1*. Springer-Lehrbuch. Springer Berlin Heidelberg, 2003.

[223] G. Deokar, J. Avila, I. Razado-Colambo, J.-L. Codron, C. Boyaval, E. Galopin, M.-C. Asensio, and D. Vignaud. Towards high quality CVD graphene growth and transfer. *Carbon*, 89:82 – 92, 2015.

[224] Alfonso Reina, Xiaoting Jia, John Ho, Daniel Nezich, Hyungbin Son, Vladimir Bulovic, Mildred S. Dresselhaus, and Jing Kong. Large Area, Few-Layer Graphene Films on Arbitrary Substrates by Chemical Vapor Deposition. *Nano Letters*, 9(1):30–35, 2009.

[225] Gunho Jo, Minhyeok Choe, Chu-Young Cho, Jin Ho Kim, Woojin Park, Sangchul Lee, Woong-Ki Hong, Tae-Wook Kim, Seong-Ju Park, Byung Hee Hong, Yung Ho Kahng, and Takhee Lee. Large-scale patterned multi-layer graphene films as transparent conducting electrodes for GaN light-emitting diodes. *Nanotechnology*, 21(17):175201, 2010.

[226] Gunho Jo, Minhyeok Choe, Sangchul Lee, Woojin Park, Yung Ho Kahng, and Takhee Lee. The application of graphene as electrodes in electrical and optical devices. *Nanotechnology*, 23(11):112001, 2012.

[227] Keun Soo Kim, Yue Zhao, Houk Jang, Sang Yoon Lee, Jong Min Kim, Kwang S. Kim, Jong-Hyun Ahn, Philip Kim, Jae-Young Choi, and Byung Hee Hong. Large-scale pattern growth of graphene films for stretchable transparent electrodes. *Nature*, 457:706–710, 2009.

[228] B. W. Ward, John A. Notte, and N. P. Economou. Helium ion microscope: A new tool for nanoscale microscopy and metrology. *Journal of Vacuum Science & Technology B: Microelectronics and Nanometer Structures Processing, Measurement, and Phenomena*, 24(6):2871–2874, 2006.

[229] Lili Liu, Miaoqing Qing, Yibo Wang, and Shimou Chen. Defects in Graphene: Generation, Healing, and Their Effects on the Properties of Graphene: A Review. *Journal of Materials Science & Technology*, 31(6):599 – 606, 2015.

[230] Adriano Ambrosi and Martin Pumera. The CVD graphene transfer procedure introduces metallic impurities which alter the graphene electrochemical properties. *Nanoscale*, 6:472–476, 2014.

[231] P. Ahlberg, F. O. L. Johansson, Z.-B. Zhang, U. Jansson, S.-L. Zhang, A. Lindblad, and T. Nyberg. Defect formation in graphene during low-energy ion bombardment. *APL Materials*, 4(4):046104, 2016.

[232] Eunhye Koo and Sang-Yong Ju. Role of residual polymer on chemical vapor grown graphene by Raman spectroscopy. *Carbon*, 86:318 – 324, 2015.

[233] J. Barzola-Quiquia, P. Esquinazi, M. Lindel, D. Spemann, M. Muallem, and G.D. Nessim. Magnetic order and superconductivity observed in bundles of double-wall carbon nanotubes. *Carbon*, 88:16 – 25, 2015.

[234] N. F. Mott. Conduction in non-crystalline materials. *The Philosophical Magazine: A Journal of Theoretical Experimental and Applied Physics*, 19(160):835–852, 1969.

[235] Mohd Zubair Ansari and Neeraj Khare. Thermally activated band conduction and variable range hopping conduction in Cu2ZnSnS4 thin films. *Journal of Applied Physics*, 117(2):025706, 2015.

[236] Gil-Ho Lee, Dongchan Jeong, Kee-Su Park, Yigal Meir, Min-Chul Cha, and Hu-Jong Lee. Continuous and reversible tuning of the disorder-driven superconductor-insulator transition in bilayer graphene. *Scientific Reports*, 5, 2015.

[237] Jeongho Park, W. C. Mitchel, Said Elhamri, and Tyson C. Back. Effect of in-situ oxygen on the electronic properties of graphene grown by carbon molecular beam epitaxy. *Applied Physics Letters*, 100(13):133107, 2012.

[238] A L Efros and B I Shklovskii. Coulomb gap and low temperature conductivity of disordered systems. *Journal of Physics C: Solid State Physics*, 8(4):L49, 1975.

[239] Ping Sheng, E. K. Sichel, and J. I. Gittleman. Fluctuation-Induced Tunneling Conduction in Carbon-Polyvinylchloride Composites. *Phys. Rev. Lett.*, 40:1197–1200, 1978.

[240] Ping Sheng. Fluctuation-induced tunneling conduction in disordered materials. *Phys. Rev. B*, 21:2180–2195, 1980.

[241] Zheyong Fan, Andreas Uppstu, and Ari Harju. Anderson localization in two-dimensional graphene with short-range disorder: One-parameter scaling and finite-size effects. *Phys. Rev. B*, 89:245422, 2014.

[242] Gerald Schubert, Jens Schleede, and Holger Fehske. Anderson disorder in graphene nanoribbons: A local distribution approach. *Phys. Rev. B*, 79:235116, 2009.

[243] Y. Naitou and S. Ogawa. Anderson localization of graphene by helium ion irradiation. *Applied Physics Letters*, 108(17):171605, 2016.

[244] R. P. Khosla and J. R. Fischer. Magnetoresistance in Degenerate CdS: Localized Magnetic Moments. *Phys. Rev. B*, 2:4084–4097, 1970.

[245] W. E. Boyce and R. C. DiPrima. *Elementary Differential Equations and Boundary Value Problems.* John Wiley and Sons Ltd, 2012.

[246] R.P. Feynman and A.R. Hibbs. *Quantum mechanics and path integrals.* International series in pure and applied physics. McGraw-Hill, 1965.

[247] N. Otsu. A Threshold Selection Method from Gray-Level Histograms. *IEEE Transactions on Systems, Man, and Cybernetics*, 9(1):62–66, 1979.

[248] Christophe Fiorio and Jens Gustedt. Two linear time Union-Find strategies for image processing. *Theoretical Computer Science*, 154(2):165 – 181, 1996.

List of publications

Peer-reviewed publications of the author

[1] **J. Lehnert**, J. Meijer, C. Ronning, D. Spemann, and E. Vittone, Ion beam induced charge analysis of diamond diodes, Nuclear Instruments and Methods in Physics Research Section B: Beam Interactions with Materials and Atoms, Vol. 404, pp. 259–263, 2017,

Contribution: Preparation of the pin-diodes within the diamond by ion implantation, optical and electrical characterisation of the diodes, evaluation of the results

[2] R. John, **J. Lehnert**, M. Mensing, D. Spemann, S. Pezzagna, and J. Meijer, Bright optical centre in diamond with narrow, highly polarised and nearly phonon-free fluorescence at room temperature, New Journal of Physics, Vol. 19, No. 5, p. 053 008, 2017,

Contribution: Discovery of the new colour centre and first measurements, optical characterisation, evaluation of the experiments, support in writing the manuscript

[3] **J. Lehnert**, D. Spemann, H. Hatahet, S. Mändl, M. Mensing, A. Finzel, A. Varga, and B. Rauschenbach, Graphene on silicon dioxide via carbon ion implantation in copper with pmma-free transfer, Applied Physics Letters, Vol. 110, No. 23, 2017,

Contribution: Preparation of the templates for graphene growth, optical characterisation of the graphene, evaluation of all results, writing the manuscript

[4] **J. Lehnert**, D. Spemann, S. Surjuse, M. Mensing, C. Grüner, P. With, P. Schumacher, A. Finzel, D. Hirsch, and B. Rauschenbach, Preparation and characterisation of carbon-free cu(111) films on sapphire for graphene synthesis, Journal of Physics: Conference Series, Vol. 992, No. 1, p. 012 024, 2018,

Contribution: Thermal treatment of the samples, optical characterisation, evaluation of the experiments, writing the manuscript

[5] C. Laube, T. Oeckinghaus, **J. Lehnert**, J. Griebel, W. Knolle, A. Denisenko, A. Kahnt, J. Meijer, J. Wrachtrup, and B. Abel, Controlling the fluorescence properties of nitrogen vacancy centers in nanodiamonds, Nanoscale, Vol. 11, pp. 1770–1783, 4 2019,

Contribution: Raman measurements and evaluation, support in writing the manuscript

[6] P. With, **J. Lehnert**, L. Seifert, S. D. H. Krautscheid, S. Naumov, A. Prager, B. A. L. Prager, and U. Helmstedt, Photochemical low-temperature synthesis of iron(iii) oxide thin films, Surface Science, Under review 2019,

Contribution: Raman measurements and evaluation of the results, support in writing the manuscript

Conference contributions of the author

[1] **Poster** Presentation at Diamond Conference Hasselt, Belgium, 2014

[2] **Poster** Presentation at 15th Int. Conference on Nuclear Microprobe Technology and Applications, Lanzhou, China, 31.07-05.08.2016

[3] **Talk**, Untersuchung Elektrischer Transporteigenschaften Diamant Basierter Bauelemente, XXIII. Erfahrungsaustausch Oberflächentechnologie mit Plasma- und Ionenstrahlprozessen, Mühlleithen / Vogtland, Germany, 15. - 17. März 2016

[4] **Talk**, Large area graphene on silicon by carbon ion implantation in copper and subsequent transfer, XXIV. Erfahrungsaustausch Oberflächentechnologie mit Plasma- und Ionenstrahlprozessen, Mühlleithen / Vogtland, Germany, 7. - 9. März 2017

[5] **Poster** Presentation at DPG-Tagung 2017, Dresden, Germany

[6] **Poster** Presentation at ECME in Dresden, Germany, 2017

[7] **Talk**, graphene on silicon dioxide by carbon ion implantation in copper and subsequent transfer, Twentieth International Summer School on Vacuum, Electron and Ion Technologies, Sozopol, Bulgaria, 25-29.09.2017

[8] **Talk**, Structured graphene films on silicon dioxide synthesised by carbon ion implantation, XXIV. Erfahrungsaustausch Oberflächentechnologie mit Plasma- und Ionenstrahlprozessen, Mühlleithen / Vogtland, Germany, 20.-23.03.2018

[9] **Poster** Presentation at DPG-Tagung 2018, Berlin, Germany

[10] **Poster** Presentation at Flatlands-conference, Leipzig, Germany, 2018

Danksagung

Selbstverständlich ist es einer einzigen Person nicht möglich, die Herausforderungen beim Erstellen einer Arbeit allein zu bewältigen. Deshalb möchte ich meinen Dank an die folgenden Personen richten.

Als erstes möchte ich mich bei Prof. Dr. Dr. h.c. Bernd Rauschenbach bedanken. Er gab mir die Möglichkeit, dieses Thema zu bearbeiten und bot dafür ein optimales Arbeitsumfeld sowie optimale Arbeitsbedingungen. Außerdem bot er viele Freiheiten im Bezug auf die Vorgehensweisen zur Bearbeitung des Themas. Selbstverständlich stand er mit Ratschlägen und schneller Hilfe jederzeit zur Verfügung.

Ein ganz besonderer Dank gilt Herrn Dr. Daniel Spemann. Er machte mich auf die ausgeschriebene Stelle aufmerksam und meinte während eines heiteren Guinness-Abend im Pub ich solle mich darauf bewerben. Die Erzählung seiner positiven Erfahrungen nach seinem Wechsel zum IOM machten mir die Entscheidung, die Doktorarbeit nach 2 Jahren noch einmal mit neuem Thema und neuem Betreuer zu beginnen sehr leicht. Da das Thema in seiner Arbeitsgruppe angesiedelt war und er dadurch als direkter Betreuer fungieren würde, musste ich nicht lange zögern. Sein umfangreiches Wissen zu allen möglichen Themen war überaus bereichernd und vor allem hilfreich. Wenn es hieß ”Wie funktioniert das eigentlich?” ist die beste Antwort ”Ruf mal Daniel an.”. Ich danke Dir für die Zusammenarbeit, bei der Forschung wieder Spaß gemacht hat.

Weiterhin danke ich Dr. Stephan Mändl und Dr. Darina Manova, die mich bei der Ionenimplantation unterstützten. Darina fungierte oft als ”Mutter” der Arbeitsgruppe, die sich um alles mögliche kümmerte, und dies mit großen Engagement.

Hamza Hatahet danke ich für die Unterstützung beim Transfer der Graphenproben. Dies war sehr spontan und kurzfristig möglich.

Philipp Schumacher danke ich ebenfalls für zahlreiche AFM Messungen. Außerdem war er einer der Personen, die auch nach der Arbeit bei Ausflügen in die Innenstadt dabei waren.

Letzteres gilt auch für Christoph Eichhorn. Zahlreiche Abende in der Leipziger Innenstadt bleiben unvergessen.

Frau Dr. Annemarie Finzel danke ich ebenfalls für AFM Messungen, die mittels des ”fastscan” durchgeführt wurden.

Christoph Grüner stellte die Cu-Dünnschichten mittels Ionenstrahlsputtern bereit, wofür ich ihm ebenfalls danke.

Herr Hirsch habe ich ebenfalls für die Herstellung der Cu-Dünnschichten mittels Magnetronsputtern zu danken. Außerdem half er mir bei der Konzeption und beim Einbau der Heater-stage um Kupferschichten bei höheren Temperaturen herzustellen. Außerdem war er ein sehr kompetenter Ansprechpartner was die Analytik angeht.

Herr Marco Müller war für die Elektronik zuständig. Probleme dahingehend löst er mit sehr viel Leidenschaft. Außerdem kann man bei ihm alles erfahren was man bzgl. Elektronik gern wissen möchte.

Herrn Michael Mensing danke ich für zahlreiche XRD-Messungen. Außerdem ist er immer ein kompetenter Ansprechpartner, wenn es um Programmieren geht. Leider konnten wir unsere gemeinsame Bürozeit von der Universität nicht fortsetzen, aber es wird sicher einen Grund haben warum es hieß "wir wären ein sich selbst verstärkendes System und es sei deshalb besser, wenn wir getrennte Büros hätten". Ich denke jedoch, dass der gemeinsame Wechsel zum IOM für uns beide eine gute Wahl war. Außerdem war es immer interessant, seinen kritischen Fragen während Vorträgen beizuwohnen.

Meiner Lebensgefährtin Ulrike danke ich natürlich ebenfalls. Auch wenn wir bis heute stets eine Fernbeziehung über erst 20 km, dann 8269 km, dann 609 km und aktuell knapp 250 km führen, bist du immer in meinem Herzen. Zum Glück geht es unseren Schildkröten immer genauso.

Zum Schluss möchte ich noch meiner Familie danken, zu der leider nur noch meine Mutter Silke, mein Vater Frank und meine Tante Kerstin gehören. Durch den Rückhalt, der stets vorhanden war, konnte ich sehr unbeschwert meinen Weg bis zum heutigen Tage gehen. Bei uns ist es selbst in schwierigsten Zeiten stets lustig. Ohne eure Unterstützung wäre ich mit Sicherheit nicht so weit gekommen.

Selbstständigkeitserklärung

Hiermit versichere ich, dass ich die vorgelegte Arbeit mit dem Titel "*Large area graphene on silicon dioxide by carbon ion implantation in copper and subsequent transfer*" ohne unzulässige Hilfe und ohne Benutzung anderer als der angegebenen Hilfsmittel angefertigt wurde und dass die aus fremden Quellen direkt oder indirekt übernommenen Gedanken in der Arbeit als solche kenntlich gemacht wurden.

Ich versichere, dass alle Personen, von denen ich bei der Auswahl und Auswertung des Materials sowie bei der Herstellung des Manuskripts Unterstützungsleistungen erhalten habe, in der Danksagung der vorliegenden Arbeit aufgeführt sind.

Ich versichere, dass - außer den in der Danksagung genannten - weitere Personen bei der geistigen Herstellung der vorliegenden Arbeit nicht beteiligt waren. Insbesondere versichere ich, nicht die Hilfe eines Promotionsberaters in Anspruch genommen zu haben und weitere Personen von mir oder in meinem Auftrag weder unmittelbar noch mittelbar geldwerte Leistungen für Arbeiten erhalten haben, die im Zusammenhang mit dem Inhalt der vorgelegten Dissertation stehen.

Ich versichere, dass die vorgelegte Arbeit oder Teile daraus weder im Inland noch im Ausland in gleicher oder in ähnlicher Form einer anderen Prüfungsbehörde zum Zwecke einer Promotion oder eines anderen Prüfungsverfahrens vorgelegt wurde.

Ich teile mit, dass keine früheren erfolglosen Promotionsversuche stattgefunden haben.

Jan Lehnert

Leipzig, den 8. April 2019

Jan Lehnert

Lebenslauf

Geburtsdatum	16.06.1989
Geburtsort	Borna
Familienstand	Ledig
Staatsangehörigkeit	Deutsch

Akademischer Werdegang

Seit 03/2016	Promotion an der Universität Leipzig, Arbeit angefertigt am Leibniz-Institut für Oberflächenmodifizierung (IOM) Leipzig, Thema: *Synthesis of graphene using carbon ion implantation in copper*
03/2013 - 02/2014	Fortsetzung Studium der Physik (Master) an der Universität Leipzig, **Abschluss: Master of Science (M.Sc.)**; Thema: *Untersuchung elektrischer Transporteigenschaften diamantbasierter Bauelemente*
09/2012 - 02/2013	Urlaubssemester, Bildungsreise (Indien, Nepal, Vietnam)
10/2011 - 08/2012	Studium der Physik (Master) an der Universität Leipzig
10/2008 - 09/2011	Studium der Physik (Bachelor) an der Universität Leipzig, **Abschluss Bachelor of Science (B.Sc.)**; Thema: *Bestimmung der Prozessparameter für die Herstellung von Mikrostrukturen in Zinkoxid mittels Protonenstrahlschreiben*
09/2007 - 05/2008	Zivildienst, Helios-Klinikum Borna, Gefäßchirurgie
09/1999 - 08/2007	Gymnasium Am Breiten Teich Borna, **Abschluss: Abitur**
09/1995 - 08/1999	Grundschule Großzössen/Lobstädt

Lehrerfahrungen

WS 2014 - WS 2016	Universität Leipzig, Seminare zur Experimentalphysik I/II
SS 2014	Universität Leipzig, Betreuung physikalisches Anfängerpraktikum für Chemiker

Leipzig, 8. April 2019

Jan Lehnert